The Impact Of Stellar Feedback On The Host Star-Forming Clouds

Elizabeth J. Watkins

A Thesis submitted to
Cardiff University
for the degree of
Doctor of Philosophy

February 2020

"Journey before destination."
Brandon Sanderson

ACKNOWLEDGEMENTS

I have no idea how to thank all the people who made this thesis possible. These words are genuinely not enough to express my gratitude, but here it goes anyway...

Firstly, I would like to thank my amazing supervisor, Nicolas Peretto, for the awesome opportunity to do real research, for all the support and encouragement, and for guiding my journey towards becoming a scientist. I cannot thank you enough. Secondly, I would like to thank Ant Whitworth and Claudia Cyganowski, for being patient examiners, and for making the viva fun.

Next, I would like to thank all the people who did star formation with me. You guys made the last 3.5 years truly special. Thank you for all your LoTR references, animal videos, science discussions, and shouts of "CAKE!". In particular, I would like to thank: Andy Rigby, Michael and Gerwyn, for encouraging my creativity in making beautiful puns and plots. Also, without you guys, I would ignorant to the wonders of 'aa', 'borborygmus', 'cromulent', 'largen', and 'meldrop'; Alex, for being a great and supporting friend, and for popping into the office to offer a well needed distraction; Sarah and Emily, for all the random conversations; Gwen and Zeinab, for your calming influence in the office; Andy Hannington, for being just as spontaneous and as random as me; Rachael, for getting my jokes and to Camilo, for getting confused by my jokes.

To all my friends, thank you for keeping my social life alive for the past 3.5 years. Your friendships stopped me turning into a hermit, and gave me something to look forward to every week.

To Curtis, thank you for being a pillar I could lean on throughout these past years. You made each day fun and exciting.

Finally, I would like to thank my family, my Mam, my Dad, and my brother, Will. Thank you, for always believing in me, caring for me, laughing with me, crying with me, and pushing me to be the best I can be. Without you, I would not be an astrophysicist.

ABSTRACT

Stellar feedback from high-mass stars shapes the interstellar medium, and thereby impacts gas that will form future generations of stars. However, due to our inability to track the time evolution of individual molecular clouds, quantifying the exact role of stellar feedback on their star formation history is an observationally challenging task. Therefore, in the first part of this thesis, I perform a detailed study of the impact of feedback on a single high-mass star forming region. For this purpose, I take advantage of the unique properties of the G316.75-00.00 massive-star forming ridge to determine how stellar feedback from O-stars impacts the dynamical stability of massive filaments. The G316.75 ridge is 13.6 pc in length and contains 18,900 $M_\odot$ of H_2 gas, half of which is infrared dark and half of which infrared bright. The infrared bright part has already formed four O-type stars over the past 2 Myr, while the infrared dark part remains quiescent. Therefore, by assuming the star forming properties of the infrared dark part represent the earlier evolutionary stage of the infrared bright part, I can quantify how feedback impacts these properties by contrasting the two.

I used publicly available *Herschel*/Hi-GAL and molecular line data to measure the ratio of kinetic to gravitational energy per-unit-length, $\alpha_{\mathrm{vir}}^{\mathrm{line}}$, across the ridge. By using both dense (i.e. N_2H^+ and NH_3) and more diffuse (i.e. ^{13}CO) gas tracers, I was able to compute $\alpha_{\mathrm{vir}}^{\mathrm{line}}$ over a range of gas volume densities ($\sim 1\times10^2$–1×10^5 cm^{-3}). This study shows that despite the presence of four embedded O-stars, the ridge remains gravitationally bound (i.e. $\alpha_{\mathrm{vir}}^{\mathrm{line}} \leqslant 2$) nearly everywhere, except for some small gas pockets near the high-mass stars. In fact, $\alpha_{\mathrm{vir}}^{\mathrm{line}}$ is almost indistinguishable for both parts of the ridge. These results are at odds with most hydrodynamical simulations in which O-star-forming clouds are completely dispersed by stellar feedback within a few cloud free-fall times. From simple theoretical calculations, I show that such feedback inefficiency is expected in the case of high-gas-density filamentary clouds.

I conclude that the discrepancy between numerical simulations and the observations presented here originates from different cloud morphologies and average densities at the time when the first O-stars form. In the case of G316.75, I speculate that the ridge could arise from the aftermath of a cloud-cloud collision, and that such filamentary configuration promotes the inefficiency of stellar feedback. This does very little to the dense gas already present, but potentially prevents further gas accretion onto the ridge. These results have important implications regarding, for instance, how stellar feedback is implemented in cosmological and galaxy scale simulations.

To place G316.75 in the larger context of the rest of the galaxy, I investigate how expanding HII regions may affect the star formation efficiencies (SFEs) of molecular clouds. For this purpose, I build a catalogue of dense molecular clouds from the Galactic plane using the *Herschel* Hi-GAL data, determine the number and luminosity of embedded young protostellar objects as a proxy for their SFE, and characterise their association with known HII regions and HII region candidates. Finally, I determine how infrared dark each cloud is and use this as a tracer of their evolutionary stage. I define three categories of clouds: i. clouds that are not associated with any HII regions; ii. clouds that have an embedded HII region; ii. clouds that lie within the boundary layer of an HII region. When comparing boundary layer clouds taken at a similar evolutionary stage with HII and non-HII region related clouds, I find that the boundary layer clouds exhibit SFEs that are more similar to clouds with embedded HII regions than those without. This suggests that boundary layer clouds must have been already present before finding themselves in the proximity of an HII region. Moreover, I find there is little difference in SFEs between boundary layer clouds and clouds with embedded HII regions at all evolutionary stages. The implication, along with the fact that only 20% of clouds are presently being influenced by HII regions, is that star formation triggered by expanding HII regions is not a major contributor to the Milky Way star formation rate as a whole.

PUBLICATIONS

Feedback from OB stars on their parent cloud: Gas exhaustion rather than gas ejection—E. J. Watkins, N. Peretto, K. Marsh, and G. A. Fuller, 2019, 628, A21 A&A

CONTENTS

LIST OF FIGURES

CHAPTER 1

A SHORT INTRODUCTION TO STAR FORMATION[*]

1.1 THE FEEDBACK LOOP OF STAR FORMATION

Star formation is the processes that converts diffuse interstellar gas into stars. As star formation proceeds in galaxies, each generation gradually removes gas from them until there is little gas remaining and star formation stops. But before this occurs, stars return energy, momentum and matter back into the surroundings, thereby reshaping the initial conditions that led to star formation in first place. High-mass stars ($>8\ \mathrm{M}_{\odot}$) have the greatest impact on star forming processes, despite only comprising 1% of the number of stars that are born. They ionise their surroundings, drive powerful winds, and at the end of their lives, they undergo supernova explosions. During these explosions, the supernovae expels nuclear synthesised material into its surroundings. These heavier elements then provide pathways to cool interstellar gas more efficiently and provide the elements necessary for rocky planet formation and complex, carbon-based life. In comparison to high-mass stars, the impact of low-mass stars on the physics and chemistry of the interstellar medium is arguably not as important. They

---

[*] Part of the work presented here is published in Watkins et al. 2019, A&A, 628, A21

radiate less energy ($L_*\propto M_*^{3.5}$) despite living much longer ($\tau\propto M_*^{-2}$). A complete theory of star formation therefore requires us to understand how stellar feedback from high-mass stars impacts star formation. This is the primary goal of my thesis.

1.2 The interstellar medium

The stars and structures we observe in the Milky Way are created from, and exist within the diffuse material present between the stars, called the interstellar medium (ISM). Because the ISM is diffuse, it was only discovered in 1930 (Trumpler 1930) though its existence was alluded to over 100 years before this as sudden and localised decreases in star counts compared to the surrounding stellar distribution, "a hole in the heavens"—(Herschel 1785; Barnard 1919). The region being referred to was catalogued as B 68 in Barnard (1919) and is a region of the ISM that has reached sufficient densities and low enough temperatures that it significantly extincts background stars in the visible spectrum (see fig. 1.1). These regions were particularly noticeable to early astronomers when the background stellar density was high. Compared to when the ISM was first discovered, we now have a much better understanding of the main components of the ISM (see Eddington (1926) for a historic comparison).

In terms of mass, the ISM consists of 70.4% hydrogen, 28.1% helium and 1.5% of everything else (Ferrière 2001), generalised as "metals" (Spitzer 1978). Almost all of these elements are in the gas phase, but when not, they usually take the form of dust in the solid phase (~1–1.5%). The distribution of matter in the ISM is inhomogeneous (e.g fig. 1.1), with the number density of the ISM spanning over 8 orders of magnitude (10^{-3}–10^{5+} cm^{-3}) due to the complex processes within the ISM. Therefore, ascribing an average value to the ISM's density does not capture the full complexity of the ISM. At a minimum, a 2-phase model describing thermal global pressure equilibrium (between its heating and cooling mechanisms, see fig. 1.2) is needed for a basic understanding of the ISM properties (Field et al. 1969), though a

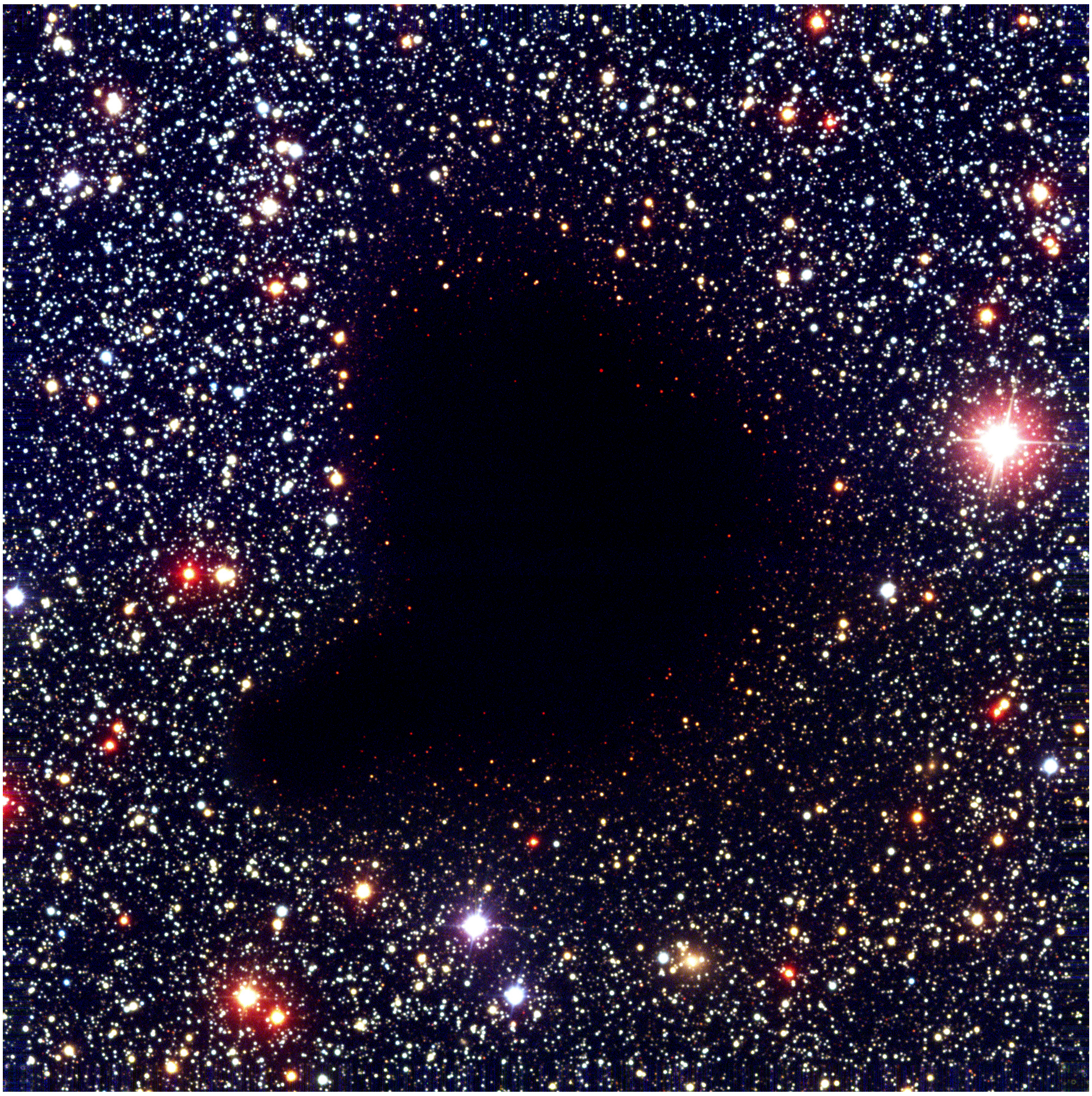

Figure 1.1. Dark nebula Barnard 68 (Barnard 1919) at RA: 17h 22m 38.2s, DEC:$-23°49'34''$. Image data from Alves et al. (2001). Image credit: ESO.

REDACTED

Figure 1.2. 2-phase cooling curve of the ISM amended from Dalgarno & McCray (1972) with cooling mechanisms from Suchkov & Shchekinov (1984).

better description includes a third phase. McKee & Ostriker (1977) were the first to use a 3-phase model to describe the ISM. Below, I give a brief summary of this.

The hottest and most diffuse component of the ISM is the ionised material created by supernovae and stellar winds, called the Hot Ionised Medium (HIM). These processes are able to heat the gas to $> 10^6$ K and drive the gas 3 kpc above the plane of the galaxy as large bubbles. Driven to large scale heights, the HIM occupies 50% of the volume of the ISM as a galactic corona (Spitzer 1956). This phase cools via free-free emission. The next largest component is the Warm Neutral Medium (WNM) and the Warm Ionised Medium (WIM). These phases are usually considered together since they are both maintained by UV photons. This phase occupies ∼50% of the volume of the ISM, with number densities of ∼0.2-0.5 cm^{-3} and temperatures of ∼8000 K. The warm medium cools via Lyman alpha cooling and by fine structure cooling of ionised metals. The final phase contains all the cold non-ionised material called the Cold Neutral Medium (CNM). It has a filling factor of ∼1%, but is significantly colder and denser than the other phases, with densities of ∼50 cm^{-3} and temperatures of 100 K. Consequentially, the CNM contains ∼50% of the mass of the ISM even though it contains the least volume. The CNM is maintained by fine structure cooling of neutral and ionised metals, such as CII and OI and is heated by UV photons. The 2-phase model on fig. 1.2 contains the CNM and the WNM only.

The ISM also contains a molecular gas component. It is the coldest and densest component of the ISM, with densities exceeding >100 cm^{-3} and temperatures that reach ∼15 K and lower. Molecular gas forms out of the CNM so its filling factor is included within the filling factor for the CNM, and is usually destroyed by UV photons. Even though it is distinct in density and temperature compared to the CNM, it is not represented as a 4th phase in this model. It is a continuation of the CNM until the large densities and cold temperatures allow the molecular gas to become self-gravitating. At this point, the molecular gas is no longer in a thermal global pressure equilibrium with the other phases because its evolution is instead dictated by its own self-gravity. Therefore gravitationally bound molecular gas exists outside of the 3-phase (global pressure equilibrium) model.

The definition of the ISM also includes the electromagnetic radiation, magnetic fields, and cosmic rays contained within the ISM, all of which contribute to the structure of the ISM. Cosmic rays and the interstellar radiation field (ISRF) are important sources of heating needed for the existence of the 3-phase model and, the Galactic magnetic field, while relatively weak, is argued to provide an important pressure balance to the ISM (Evirgen et al. 2019) and channels cosmic rays (Zweibel 2013). When all the components of the ISM are considered together, one can see that the ISM is not a simple medium of gas that transforms into stars. Instead, it is a complex, interlinked machinery that continually cycles energy and matter. In this system, stars are a by-product of the ISM but are also needed to sustain the ISM.

1.3 Molecular clouds: stellar nurseries

Molecular gas is the coldest and densest part of the ISM. H_2 is the main component of molecular gas and even though it was predicted to exist in the ISM (Eddington 1937; Spitzer 1949), it was not detected directly until 1970 (Carruthers 1970). H_2 is a homonuclear, symmetric molecule with a small moment of inertia. Direct emission from H_2 is therefore weak so can only probe conditions more energetic than it forms at (probes >2000 K). Such events include protostellar outflows that shock the gas to cause collisionally excited emission (Bally & Lane 1982), and UV radiation, which causes the H_2 to fluoresce (Black & van Dishoeck 1987). To measure cold H_2, we rely on indirect methods, such as dust emission/absorption or emission from other molecules, such as ^{12}CO (1–0).

As H_2 primarily forms on the surfaces of dust grains, its formation rate is a function of density, where the higher densities cause more collisions between the H_2

and the dust (Gould & Salpeter 1963; Sternberg et al. 2014). But because H_2 is dissociated by UV radiation, any incident UV photons must be absorbed before reaching the H_2. This can be achieved if there are enough intervening H_2 molecules between the H_2 and the UV radiation, and if H_2 forms quicker than it is depleted. Since its formation rate is a function of density and only 10–15% UV excitations results in dissociation (Stecher & Williams 1967; Sternberg et al. 2014), H_2 quickly becomes self-shielded when it reaches the densities to do so ($\sim$1–100 cm^{-3} (van Dishoeck & Black 1986; Wakelam et al. 2017)). Therefore the properties of molecular gas are sensitive to H_2 column density. UV photons are the main heating mechanism of molecular gas and their depletion by H_2 changes the balance between the heating and cooling mechanisms. The more column between the UV photons and the H_2, the colder and denser the gas can become. The depletion of UV radiation, and over-abundance of H_2 then allows additional, photo-sensitive molecules to form (such as ^{12}CO), which helps to cool the gas to 10–20 K via rotational line emission (de Jong et al. 1980).

When molecular gas is observed in the ISM, it is found to reside in large complexes called molecular clouds. These clouds are $\sim$1–100 pc in size, and have masses ranging from $\sim 10^{2-6}$ $M_\odot$ (Solomon et al. 1987) but the mechanisms needed to generate clouds of this size are not currently agreed upon. Most theories require that some form of dynamic action to bring the gas together, such as supersonic flows driven by supernovae or galactic dynamics (Ballesteros-Paredes et al. 1999; Koyama & Inutsuka 2000; Dobbs 2008). Although, some theories predict that molecular clouds can coalesce directly from the ISM via galactic-scale gravitational instabilities (Tasker & Tan 2009).

If the densities increase and the temperatures drop enough (either as a result of turbulence or due to cooling), parts of molecular clouds can become self-gravitating (gravitationally bound) causing them to contract and fragment. This changes the structure of molecular clouds and causes the formation of sub-structures, such as

REDACTED

Figure 1.3. *Herschel* column density map of the molecular cloud, IC5146, which contains filamentary structures. The filaments have been traced in cyan and blue. Image from Arzoumanian et al. (2019).

high-aspect ratio filaments (see fig. 1.3) (Schneider & Elmegreen 1979; Bally et al. 1987; Klessen & Burkert 2000). After the launch of the *Herschel* space observatory, filaments were found to exist concurrently within star forming molecular cloud complexes (Molinari et al. 2010a). Typically, filaments are characterised using ridge finding algorithms (e.g., DisPerSE, FilFinder and second derivative techniques Sousbie (2011); Koch & Rosolowsky (2016)). Filaments are found to contain almost all the dense gas within molecular clouds (André et al. 2010a; Arzoumanian et al. 2019) and contain a much higher proportion of stellar precursors (i.e., clumps and cores) compared to the rest of the molecular cloud (Molinari et al. 2010a; André et al. 2010a; Smith et al. 2011) (see Table 1.1 for definitions and properties). Therefore, filaments have been studied extensively to understand what properties influence their star forming ability. In general, filaments are extended structures and can be defined as regions where their aspect ratios are > 3 (Arzoumanian et al. 2019). Their density structure (perpendicular to their long axis) typically appears flat in the centre and tapers away radially with a power-law index $p = 2$ (Arzoumanian et al. 2011). This type of density profile, $n(r)$, can be described using a 3D Plummer-like profile, given by:

$$n(r) = \frac{n_{\mathrm{c}}}{(1 + (\frac{r}{R_{\mathrm{flat}}})^2)^{p/2}} \tag{1.1}$$

where r is the radial position, n_{c} is the central density, R_{flat} is its characteristic width, and p is the density power-law index. As the density increases, the gas temperature drops towards the centre of the filament. Arzoumanian et al. (2011) also found that the filaments they identified have a characteristic width of R_{flat}=0.1 pc. Since 0.1 pc corresponds to the size-scale at which decaying turbulence becomes subsonic, it might imply that filaments form from the dissipation of large-scale turbulence. Although, it has been shown that filaments can have a range of widths both larger and smaller than 0.1 pc (Hill et al. 2011; Fernández-López et al. 2014; Panopoulou et al. 2017; Monsch et al. 2018; Williams et al. 2018; Howard et al. 2019).

Observations also revealed that protostars are mostly found in filaments that are gravitationally unstable (André et al. 2010a; Howard et al. 2019). Therefore, the star forming ability of filaments is usually linked with their stability. By modelling filaments as infinite, isothermal cylinders in hydrostatic equilibrium, there exists a simple analytical solution describing their radial stability against collapse. This is described with a critical line mass, $M_{\mathrm{line}}^{\mathrm{crit}}$, (Ostriker 1964):

$$M_{\mathrm{line}}^{\mathrm{crit}} = \frac{2\sigma_{\mathrm{gas}}^2}{G} = 16.5\Big(\frac{T}{10K}\Big)\mathrm{M}_{\odot}\,\mathrm{pc}^{-1} \tag{1.2}$$

where T is the gas temperature, G is the gravitational constant and σ_{gas} is the velocity dispersion of the gas. For thermally supported gas, σ_{gas} is equal to the thermal sound speed ($\sigma_{\mathrm{th}} = [k_{\mathrm{B}}T/(\mu m_{\mathrm{H}})]^{1/2}$) of H_2, where μ is the mean molecular weight and m_{H} is the atomic mass of hydrogen. Therefore, Eq. 1.2 describes the point at which thermal pressure is unable to support this cylinder against radial collapse. While these simple assumptions lead to an analytical solution, the true radial stability will likely differ from Eq. 1.2 since filaments are not isothermal, infinite and might not be self gravitating. Therefore Eq. 1.2 only represents an estimate of filament stability.

Finally, observations show that dense fragments tend to form at regular intervals along the length of filaments (Beuther et al. 2015; Williams et al. 2018). Therefore it is usual to compare the spacing and mass of these fragments to theoretical predictions to determine if additional supportive mechanisms are present in the filament. For an isothermal cylinder in hydrostatic equilibrium (where the long axis is much larger than the radius) the size of the fragments, λ_{cyl} is given by (Nagasawa 1987):

$$\lambda_{\mathrm{cyl}} = 22.1\sqrt{\frac{\sigma_{\mathrm{gas}}^2}{4\pi G\rho_{\mathrm{c}}}} \tag{1.3}$$

where ρ_{c} is the central mass density of the cylinder.

Generally, the lifetime of filaments and substructures contained within them indicates the rate that stars can form. However, to estimate the efficiency of this star formation, one needs a reference timescale estimating the smallest possible lifetime of these structures. The minimum lifetime of these structures can be estimated by calculating their free-fall time i.e., the time needed for a region to collapse to a single point under its own self-gravity unopposed. For spherical structures, such as the clumps within filaments, the free-fall time is given by:

$$t_{\mathrm{ff}}^{\mathrm{sph}} = \sqrt{\frac{3\pi}{32G\rho}} \tag{1.4}$$

where t_{ff} is the free-fall time and ρ is its mass density, assuming uniform density. For filamentary clouds, the free-fall time is larger than $t_{\mathrm{ff}}^{\mathrm{sph}}$, and is dictated by its aspect ratio (Clarke & Whitworth 2015):

$$t_{\mathrm{COL}} = (0.49 + 0.26A_{\mathrm{O}})(G\rho)^{-0.5} \tag{1.5}$$

where $t_{\rm COL}$ is the collapse time of the filament along its long axis and $A_{\rm O}$ is the aspect ratio of the filament.

1.4 Star forming structures and processes

Table 1.1. Summery of molecular structures in the ISM.

Name of structure	Typical size[a] (pc)	Mass ($M_\odot$)	Density, n_{H_2} (cm^{-3})	Life times (Myr)	Notes
Molecular cloud	1–100+	$\sim 10^{2-6}$	$\sim 10^{2-4}$	~2-100+	Scoville & Hersh (1979); Solomon et al. (1987) Elmegreen (2000); Murray (2011) Vázquez-Semadeni et al. (2018); Kruijssen et al. (2019)
Filament	0.3–100+	$\sim 10^{2-5}$	$\sim 10^{2-4}$	~1-10+	Ragan et al. (2014); Arzoumanian et al. (2019)
Clump	0.1–1	$\sim 10^{1-4}$	$\sim 10^{4-6}$	0.01–0.1	Motte et al. (2018)
Pre-stellar core	0.05–0.1	$\sim 10^{-1-2}$	$\sim 10^{5-6+}$	0.01–1	Motte et al. (2018)
Protostar	<0.05	$\sim 10^{-1-1}$	$\sim 10^{6+}$	0.01–3	André & Montmerle (1994); Motte et al. (2018)

[a] Length of longest axis

As alluded to in the previous Section, molecular clouds contain a hierarchy of density structures within which star formation occurs. These structures have specific names, though their properties are loosely defined within the literature. In Table 1.1 I summarise these structures and their properties. Jeans (1902) was the first to investigate the smallest structure that can form by calculating the fragmentation and gravitational collapse of an infinite, isothermal medium. He found that it exists a length scale above which the amplitude of density perturbation exponentially increases with time. In this particular configuration, the fastest growing perturbation mode is that with the largest length scale, that is to say, clouds that are Jeans unstable should globally collapse. The Jeans length, $\lambda_{\rm J}$, is given by:

$$\lambda_{\rm J} = \sqrt{\frac{\pi \sigma_{\rm gas}^2}{G\rho}} \tag{1.6}$$

where ρ is the density of the medium and $\sigma_{\rm gas}$ is the thermal sound speed. In molecular cloud conditions, as the region collapses globally, it remains, optically thin to its own radiation so the collapse occurs isothermally. Consequentially, the $\lambda_{\rm J}$ decreases as the density increases. This allows the region to fragment again, and so forth (Hoyle 1953). The smallest, gravitational bound fragments that forms are called pre-stellar cores. These are small (< 0.1 pc) in size and are dense ($n_{\rm H2} > 10^6$) but contain no central condensed object (e.g protostars). After this point, further contraction results in the formation of a protostar. Protostars are optically thick to their own radiation, therefore the heat generated by their collapse raises the Jeans length. This stops further fragmentation (Larson 1985).

1.4.1 Low-mass star formation

For the formation of low-mass stars, the collapse continues until their thermal pressure becomes comparable to gravitational forces. At this point, the collapse stops and a hydrostatic core is formed (Larson 1969). This stage is short lasting since material outside of the optically thick radius is still able to collapse onto the core (Tsitali et al. 2013). As a result, the core temperature continues to increase until it can dissociate molecular hydrogen at 2000 K. In doing so, the energy is absorbed and the core undergoes a second collapse until a new hydrostatic equilibrium is reached. When the core reaches this stage, it is now deemed a protostar. The heat from the protostellar collapse results in infrared (IR) emission, where its spectral energy distribution of this evolves as the protostar evolves. Hence, observers usually use the shape of the IR excess to determine the evolutionally state of the protostar (André & Montmerle 1994; Dunham et al. 2014). There are 4 proto-stellar stages (0, I, II, III) detectable. A description of the protostellar stages along with how and why their IR excess changes are shown in fig. 1.4, and are summarised following André & Montmerle (1994); Dunham et al. (2014):

The second hydrostatic core is called a class 0 protostar. At this stage, the IR emission is hard to detect because the protostar is still surrounded by a thick circumstellar envelope (which absorbs the IR emission and re-radiates it at sub-mm wavelengths). As the collapse continues, the protostar forms an accretion disk and is deemed to be a class I protostar. The emission of the accretion disk melds with the radiation from the protostar's photosphere to produce a stronger IR excess. Eventually, the circumstellar material is dissipated by the heat and the stellar outflow output by the protostar, leaving behind the protostar and its disk Now that the emission is no longer absorbed by the envelope, the measured IR excess is much larger, leading to the new protostellar classification (class II protostar). Without the envelope, the disk becomes thin in its final stages and the IR emission is now dominated by the protostar. These are class III protostars.

When the accretion disk is all but gone, the protostar collapses in quasi-hydrostatic equilibrium due to Kelvin-Helmholtz contraction, and it evolves onto the pre-main sequence (PMS). The luminosity and temperature of the PMS stars evolve along Hayashi and Henyey tracks, though the exact track it follows depends

REDACTED

Figure 1.4. Figure illustrating the evolution of a protostar and its expected spectral energy distribution at IR wavelengths. Image from André (2011).

on its mass (Henyey et al. 1955; Hayashi 1961). When the temperature and density at the centre of the PMS star reaches the threshold for hydrogen fusion, the star is born its luminosity is provided by hydrogen fusion; the star settles onto the main-sequence, where it resides on a narrow band in luminosity–temperature space (where luminosity–temperature plots are commonly referred to as a Hertzsprung–Russell diagram).

1.4.2 HIGH-MASS STAR FORMATION

Conceptually, the formation of high-mass stars presents two additional levels of complexity compared to low-mass stars. First, due to much shorter Kelvin-Helmholtz timescales, high-mass stars enter the main sequence while still accreting (Appenzeller & Tscharnuter 1987). When this occurs, the stars exerts a radiative force on the infalling gas, halting the growth of the star at M $\sim$10 $M_{\odot}$assuming spherical accretion. But stars greater than 150 $M_{\odot}$ (even >300 $M_{\odot}$) have been observed (Crowther et al. 2016), so clearly stars can form with masses >10 $M_{\odot}$. Second, the typical Jeans mass of a molecular cloud is $\sim$1 $M_{\odot}$, which is the typical mass of a low mass pre-stellar core. A 100 $M_{\odot}$equivalent would require a significantly larger fragment. Therefore, for high-mass stars to form, they need much larger accretion rates (to overcome the radiative force of the star), and need to exist within much larger fragments. Currently, there are two main models for high-mass star formation that try to answer these issues: monolithic collapse and competitive accretion.

The monolithic collapse scenario is similar to low-mass star formation except that turbulence and/or magnetic fields helps to support the core against fragmentation (Stahler et al. 1980; McKee & Tan 2003; Myers et al. 2013). This increases the mass reservoir available for the star to form from by increasing the Jean's length and, for spherical accretion, allows for higher accretion rates (since the accretion can be approximated to $\dot{M} = \sigma_{\rm gas}^3/G$ where $\dot{M}$ is the accretion rate Shu (1977)). The high accretion rate is then large enough to overcome the radiative pressure exerted by the star after reaching the main sequence. However, turbulence dissipates within a few crossing times, and so it must be continually driven to support the core. Stellar feedback from surrounding proto-stellar outflows are predicted to be able to provide this support. (Krumholz & McKee 2005; Krumholz & Tan 2007; Federrath 2013). Although the mass limit can be remedied by accounting for non-spherical accretion (Yorke & Sonnhalter 2002; Krumholz et al. 2005), the stars still need a larger accretion rates to grow to some of the extreme values seen, beyond what is possible via thermally supported disks.

In the competitive accretion model (Bonnell et al. 2001), cores have access to material from the entire molecular cloud via Bondi-Hoyle accretion (Bondi & Hoyle 1944) and/or the gravitational inflow of material from the surrounding collapsing cloud (Smith et al. 2009). In this scenario, cores compete for the material and by doing so, the largest stars form at the centre of the potential well, where they have access to more mass. Due to the large in-flow of material, the ram pressure is large enough to overcome the radiation pressure of the stars at the centre. Additionally, the in-falling material can be clumpy and contain accreting cores, which in-fall onto the centre of the potential well. This can starve the massive star at the centre of the potential well but naturally explains the clustered nature of high-mass start formation (Peters et al. 2010).

To determine between the two models, the nature of how high-mass stars accrete mass needs to be determined. Monolithic collapse requires the existence of high-mass pre-stellar cores with steep centrally-concentrated density profiles (McKee & Tan 2003). But evidence of their existence remains elusive. This has led observers to hunt for high-mass pre-stellar cores candidates (Motte et al. 2007; Sanhueza et al. 2017, 2019), but under further scrutiny most candidates found are shown to be sub-fragmented (Bontemps et al. 2010; Duarte-Cabral et al. 2013; Svoboda et al. 2019). To date, there are only a small handful of high-mass pre-stellar core candidates left (Cyganowski et al. 2014; Molet et al. 2019; Svoboda et al. 2019).

REDACTED

Figure 1.5. Three panels depicting the Vela C complex. **Panel a**: *Herschel* single temperature H_2 column density map of the Vela C region, tracing large amounts of H_2, **Panel b**: *Herschel* RGB image of the RCW 36 region within the Vela C ridge using the 250 μm (red), 160 μm (green) and 70 μm maps (blue). **Panel c**: RGB images of RCW 36 showing the *Herschel* column density (red), *Herschel* dust temperature (green) and Hα emission (blue). Image from Minier et al. (2013).

Competitive accretion instead requires the entire cloud to be globally bound (virial ratio that is $\geqslant$1) to produce an initial mass function (IMF) similar to observations (Clark et al. 2008). However, it remains uncertain what percentage of molecular clouds are gravitationally bound.

1.4.3 High-mass star-forming complexes

Ridges are high aspect ratio clouds that have similar dimensions of filaments ($\sim$10 pc but are significantly denser (10^5 cm^{-3}); therefore ridges contain >10,000 M$_\odot$ in a small volume of space. They also form high-mass stars with large star formation efficiencies, analogous to a star burst event (Nguyen Luong et al. 2011) and so contain a wealth of young, high mass objects. As a result, ridges contain multiple features indicating that they have been impacted by stellar feedback, such as HII regions, and displaced molecular gas (the molecular ring in the Vela C ridge, fig. 1.5) (Minier et al. 2013). This makes ridges ideal sites to investigate the formation of high-mass stars, and the impact that stellar feedback has on star forming conditions. Although, these extreme conditions make ridges are rare and only a few ridges have been investigated within the Milky way. How ridges form is not well understood but initial investigations indicate that they could form via the collision of two molecular clouds (Nguyen Luong et al. 2011; Hill et al. 2011; Hennemann et al. 2012; Watkins et al. 2019), and follow-up observations substantiate this scenario (Sano et al. 2018; Dobashi et al. 2019). Cloud-cloud collisions seem a promising origin scenario since it provides the turbulence needed to support the cloud again collapse, whilst also triggering high-mass star formation.

1.5 FEEDBACK

Throughout their lifetime, high-mass stars (>8 $M_{\odot}$) affect their surroundings via ionisation, radiation pressure, stellar winds, proto-stellar outflows, and, at later evolutionary stages, supernova explosions. These processes feed energy and momentum back into the surrounding gas and, by doing so, influence its ability to form future generations of stars. The relative importance of each mechanism is a function of the temporal and spatial scales that are taken into consideration (Krumholz et al. 2014). At larger scales, feedback from OB-type stars has been shown to play a central role in regulating the low star formation efficiencies in galaxies. (Stars form at a rate that is ~1% of the amount that should result from the free-fall collapse of gas Murray 2011). This implies that either star formation is efficient, but is disrupted by feedback after a few free-fall times (Elmegreen 2007; Dobbs et al. 2011; Vázquez-Semadeni et al. 2009), or star formation occurs in quasi-stable objects that live for

10s of free-fall times (Krumholz & Tan 2007; Federrath 2013). Here, molecular clouds are maintained by the turbulence that is generated by feedback.

However, from an observational perspective, measuring the impact that feedback has within a given high-mass star-forming cloud is challenging since usually one cannot measure what the gas properties were before feedback occurred, nor track the time evolution of these properties. These observational hurdles have always limited the scope of any study investigating high-mass star formation and stellar feedback. As a result, such studies are often limited to outflow feedback (Arce et al. 2010; Duarte-Cabral et al. 2012; Maud et al. 2015; Yang et al. 2018b) and triggered star formation (Zavagno et al. 2007; Deharveng et al. 2015; Liu et al. 2017; Lim et al. 2018; Deb et al. 2018). In the following, I summarise the main stellar feedback mechanisms, from the perspective of both simulations and observations.

1.5.1 OUTFLOW FEEDBACK

The earliest stage in which stars feed energy and momentum back into their surroundings is the proto-stellar stage. Since the momentum ejected is linearly proportional to the mass of the protostar, low-mass stars dominate outflow feedback (99% of stars are low-mass stars i.e., $<8\ \mathrm{M}_{\odot}$) (Bontemps et al. 1996; Beuther et al. 2002). As a protostar forms, the interaction of the accretion disk and magnetic fields produces collimated bipolar outflows called jets (Frank et al. 2014) (see fig. 1.6). These jets redistribute momentum back into the cloud that birthed them. The rate that momentum, $\mathrm{d}P/\mathrm{d}t$, is injected into its surroundings can be approximated by (Nakamura & Li 2011):

$$\frac{dP}{dt} = \mathrm{SFR} \times f_{\mathrm{out}} v_{\mathrm{out}} \tag{1.7}$$

where SFR is the star formation rate in $\mathrm{M}_{\odot}\ \mathrm{yr}^{-1}$, f_{out} is the fraction of the final star's mass injected in the outflow, and v_{out} is the velocity of the outflow. When averaged

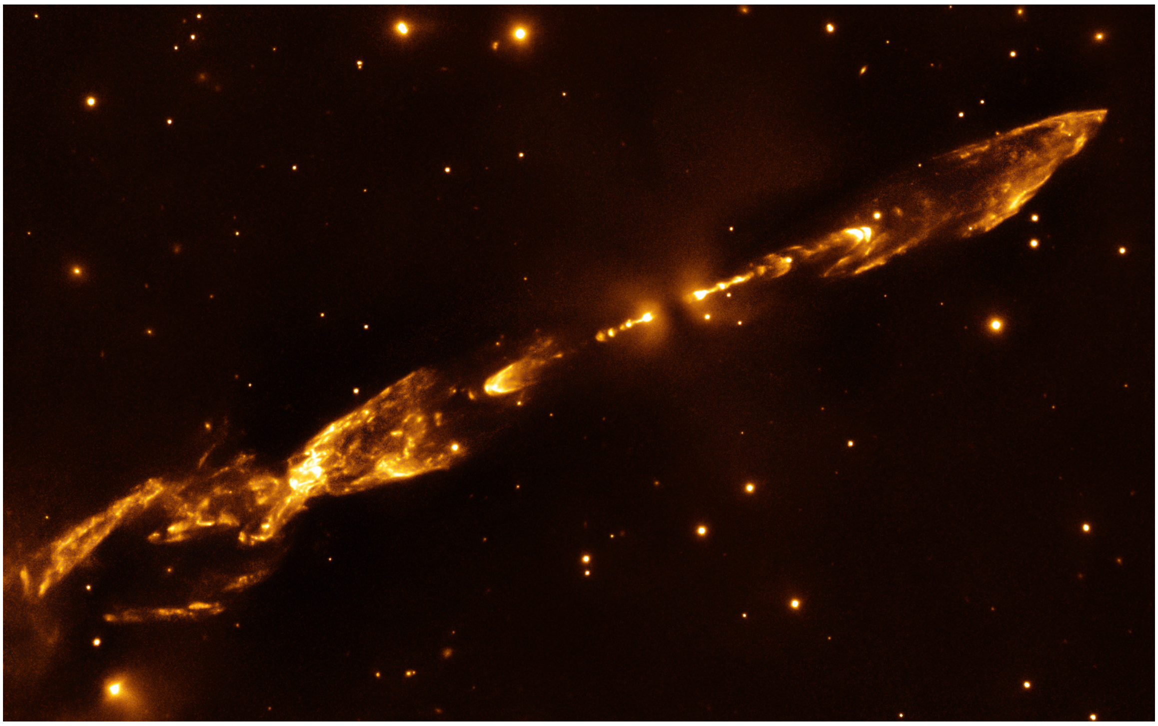

Figure 1.6. Protostellar jet of object HH212 in Orion measured using the H_2 rovibrational 2.12 μm infrared line. The jet was measured using the Infrared Spectrometer And Array Camera (ISAAC) onboard the Very Large Telescope (VLT). Image data from Zinnecker et al. (1997). Image credit: ESO/M. McCaughrean

values are used, one gets a value close to the rate of turbulent momentum dissipation, indicating that outflows could provide the turbulence needed for supporting against collapse. Although, the exact amount of momentum and energy which is effectively deposited into the host clouds is still highly debated (e.g. Arce et al. 2010; Duarte-Cabral et al. 2012; Plunkett et al. 2015; Nakamura 2015; Maud et al. 2015; Drabek-Maunder et al. 2016; Yang et al. 2018b; Seifried et al. 2018)

1.5.2 IONISING FEEDBACK AND HII REGIONS

High-mass stars are responsible for almost all the UV radiation in the ISM. UV radiation destroys molecules, ionises atoms, and heats the gas to over ∼10,000 K. As a result, high-mass stars undo the conditions that led to their formation in the first place (i.e., cold, dense molecular gas) (Fatuzzo & Adams 2008). In molecular clouds, the sudden injection of UV creates HII regions (i.e., a large volume containing ionised hydrogen, see Fig. 1.7). Due to the strong impact ionisation has on star forming conditions, ionising feedback has been extensively studied in theory, simulations and observations. Strömgren (1939) was the first to calculate how stars ionise their surroundings. He showed that the volume of gas a star can ionise is limited because hydrogen is able to recombine within the ionised region. As a result, additional UV photons are used up re-ionising the hydrogen. Eventually, a point is reached when all of the ionising photons produced by the star are consumed maintaining HII region. This occurs when the recombination rate equals the ionisation rate. The point where this occurs determines the size of the HII region. For hydrogen gas, this ionisation rate is given by:

$$N_{\mathrm{ly}} = \int_{\nu_{\mathrm{ion}}}^{\infty} \frac{L(\nu)}{h\nu}\,\mathrm{d}\nu \tag{1.8}$$

where N_{ly} is the number of ionising photons emitted by the star per second, ν_{ion} is the lowest frequency able to ionise hydrogen, h is the Planck constant and $L(\nu)$ is the

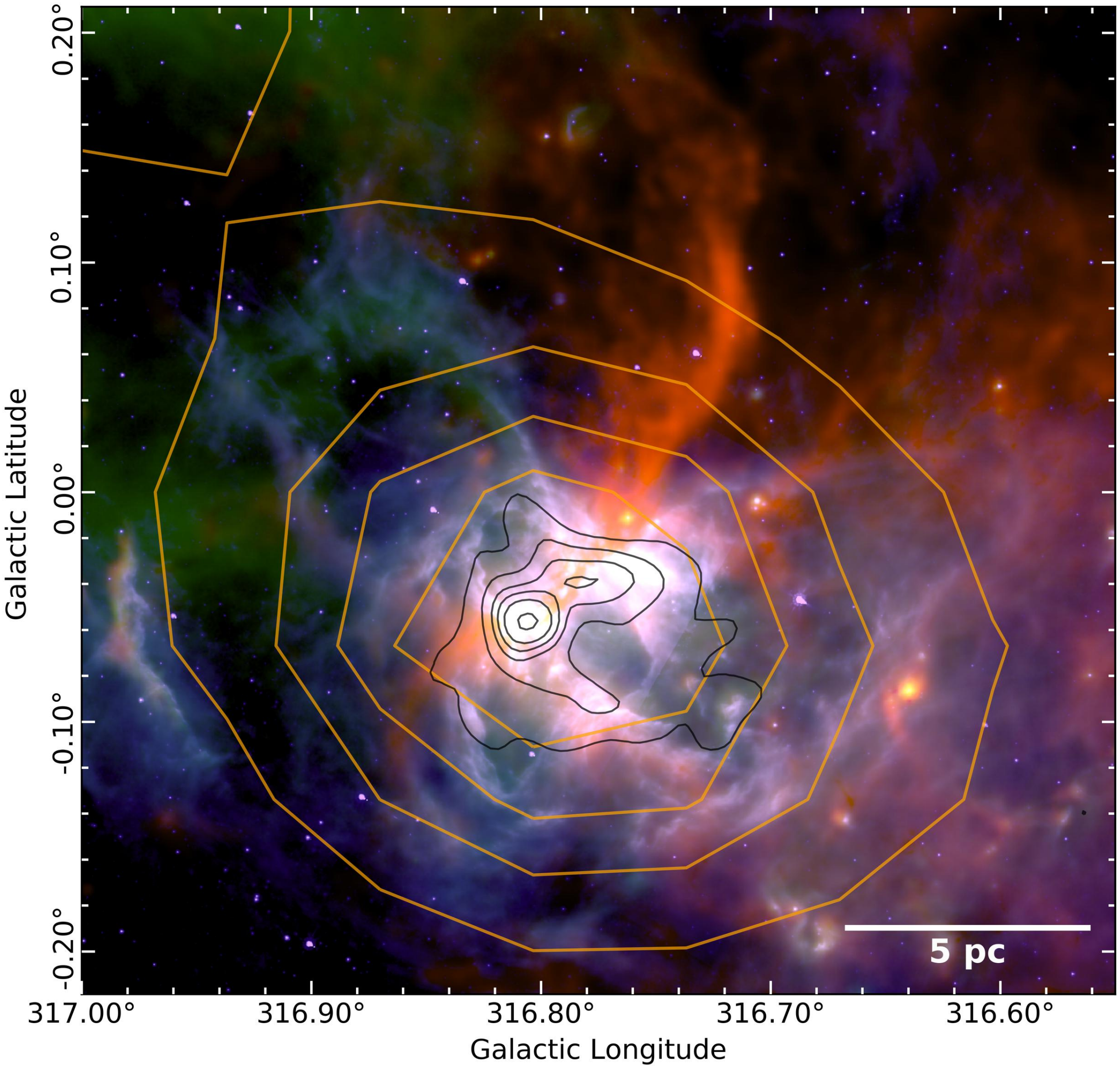

Figure 1.7. False-colour image showing an HII region in the molecular cloud G316.75 made using *Spitzer* (Churchwell et al. 2009) and *Herschel* (Molinari et al. 2010b) observations. Blue and pink: *Spitzer* 8 μm emission tracing hot dust (>50 K) and polycyclic aromatic hydrocarbons heated by high-mass stars stars; Green: *Herschel* 70 μm emission tracing hot dust and protostellar heating; Red: *Herschel* 250 μm emission tracing cold dust ($\sim$15 K, which traces cold and dense molecular hydrogen). The black isocontours at 1.6, 8.0, 17.7, 27.3, 40.1 and 64.2 MJy sr^{-1} represent SUMSS 843 MHz radio emission, which traces the location of ionising stars. The beam size of this emission is 45″. The orange isocontours at 1.6, 2.0, 2.3, 2.5 MJy sr^{-1} represent CHIPASS 1.4 GHz emission, which traces the total size of the HII region present. The beam size of this emission is 14.4′. The white line indicates a physical scale of 5 pc (Watkins et al. 2019).

luminosity of the star. The recombination rate, $\mathcal{R}$ is given by the volume integral:

$$\mathcal{R} = \int_V \alpha_{\mathrm{B}} n_{\mathrm{e}}^2 \,\mathrm{d}V \tag{1.9}$$

where n_{e} is the number density of electrons and α_{B} is the recombination rate to excited states of hydrogen equal to $2.59 \times 10^{-13} (T_{\mathrm{e}}/10^4\,\mathrm{K})^{-0.7}$ cm^3 s^{-1} (Osterbrock 1989) and T_{e} is the electron temperature, which is $\approx 10^4$ K within HII regions. Equation 1.9 implicitly assumes that number density of protons, n_{p}, (i.e., the number density ionised hydrogen particles) is $n_{\mathrm{p}} = n_{\mathrm{e}}$). Equations 1.8 and 1.9 thus show that a volume exists where the flux of ionising photons equals the rate of recombinations. Assuming the surrounding hydrogen is isotropic, the balance of the two implies that the maximum radius of an HII region is given by:

$$R_{\mathrm{S}} = \left(\frac{3 N_{\mathrm{ly}}}{4 \pi \alpha_{\mathrm{B}} n_{\mathrm{e}}^2} \right)^{\frac{1}{3}} \tag{1.10}$$

where R_{S} is the maximum radius of the HII known as the Strömgren radius. However, molecular gas also contains helium and metals. When these are taken into consideration, additional ionisation layers and secondary ionisations play a role in determining the size of the HII region (Peimbert et al. 2017). For a more comprehensive treatment of HII regions that consider these additional ionisations, models such as CLOUDY are used (Ferland et al. 2017). But to understand the full impact HII regions have on realistic molecular clouds, numerical hydrodynamic simulations are needed (Geen et al. 2016; Kim et al. 2018) (see fig. 1.8). Generally these simulations show that molecular clouds are quickly dispersed when ionising source forms except for particularly high surface density clouds (>1000 M$_\odot$ pc^{-2} Grudić et al. 2018; Kuiper & Hosokawa 2018). In these simulations, high surface density clouds are better able to shield their gas from ionising photons due to high recombination rates. Even though HII regions are complex to model, evolved HII regions are easily observed since they are a hot (∼10,000 K) ionised (Churchwell et al. 2009; Beaumont et al. 2014; Yang

REDACTED

Figure 1.8. Simulation modelling the time evolution of the impact of ionising feedback on a the properties of a molecular cloud. Specificity shown here is the impact on the surface and number density of neutral gas (top two rows), the electron density (middle row) and the energy density of ionising and non-ionising radiation (bottom two rows). Modelled cloud has a mass of 1×10^5 $M_\odot$, radius of 20 pc, initial surface density of 79.6 $M_\odot$ pc^{-1}, a neutral gas density of 86.2 cm^{-3}, an initial free-fall time of 4.7 Myrs and an escape velocity of 6.6 km s^{-1}. The dots found within the subplots indicate the location the stars present. The label and colour-bar on top of the figure indicates the age (colour) and mass (size) of the stars present. The white contours shows the where density of neutral gas is = 10 cm^{-3}. This shows that the cloud is quickly dispersed after the formation of high-mass stars. Image from Kim et al. (2018)

et al. 2018a) regions. With large catalogues, the properties and ages of HII regions can be estimated, and galaxy wide surveys can even be used to estimate the timescales of star formation (Kruijssen et al. 2019).

Triggered star formation

As the HII region expands into the material around a young massive star, a shock front is formed and a dense layer of gas forms behind it (see Fig. 1.9). The triggering of the formation of stars with that layer is what is usually referred to as "triggered star formation"

Typically, HII regions expand at the sound speed of the ionised gas at $\sim$10 km s^{-1}. Any cold neutral material that comes into contact with the bubble is shocked since it only have a sound speed of 0.2-1.0 km s^{-1}. As the expansion slows, the shock front can decouple from the ionisation front, driving a shock-wave which propagates ahead of the ionisation front. As a result, the neutral gas is compressed between the ionisation front and the shock-wave, increasing the gas density of both pre-existing dense structures (Bertoldi 1989), and the shell of gas to the point it becomes gravitationally unstable and collapses (Elmegreen & Lada 1977; Whitworth et al. 1994).

The collapse of pre-existing dense structures is usually called radiation driven implosion (RDI). This usually occurs to the dense structures (i.e., cores and clumps) that still exist after the expanding HII has disrupted the surrounding molecular cloud. The implosion occurs since the ionisation front progresses much more quickly at lower densities. Therefore, any surviving dense structures are pinched inwards, which causes them to implode. As the shock-front passes through the dense structures, the density is enhanced allowing them to collapse into cores. Visually, RDI objects appear as elephant trunks pointing perpendicularly away from HII regions due to the photo-evaporation of lower density gas (Bisbas et al. (2011), see fig. 1.10). The dense structures implode almost immediately ($\sim$0.1 Myrs) after the first contact with the

REDACTED

Figure 1.9. Star formation within the shell of the Hii region RCW–120 from (Deharveng et al. 2009). Blue is Hα emission, which traces ionised gas (Parker et al. 2005), green is 8.0 μm emission, polycyclic aromatic hydrocarbon fluorescing in the presence of UV (Churchwell et al. 2009) and red is 24 μm emission which traces hot dust (>50 K) heated by stars. Image from Carey et al. (2005).

ionisation front and do not collect additional material due to the pinching. Consequentially, RDI cores usually form lower mass stars (Bisbas et al. 2011).

HII regions can also form stars as they expand in a process called collect and collapse (Elmegreen & Lada 1977; Whitworth et al. 1994). Here, the compressed, swept-up gas grows as the HII region expands, forming a shell of gas around the HII region. When column densities through the shell reach 4–8$\times10^{21}$ cm^{-2}, the shell becomes gravitationally unstable and it collapses into regularly spaced, massive fragments. Their large masses match the conditions predicted to allow high-mass star formation and cluster formation to occur (Deharveng et al. 2003; Xu et al. 2017).

I note that the triggering scenarios listed here are formalised as separate theories, but recent observations and simulations show that in reality, a mix of the two theories occurs (Deharveng et al. 2009; Walch et al. 2015).

1.5.3 RADIATION PRESSURE

Radiation pressure is an outward force that is delivered to the gas when photons transfer momentum to dust grains (which are coupled to the gas). Stars generate high luminosities and so they are able to produce large radiative forces. This is especially true for higher mass stars since in general $L_{*}{\propto}M_{*}^{3.5}$ where L_{*} and M_{*} are the luminosity and mass of the star. Although the power reduces slightly to ∼2.5 for the most massive high-mass stars (Reed 2001). If the luminosity is large enough, the outward force can counteract gravity, halting the gravitational collapse of the gas. The effectiveness of radiation pressure (in terms of its ability to limit star formation) has had a long and controversial history in star formation studies, despite the fact that the luminosity needed to balance gravity is simple to derive. Thompson & Krumholz (2016) provide this equation:

$$\frac{GM_{*}}{r^2} = \frac{L}{4\pi r^2 c\Sigma} \tag{1.11}$$

REDACTED

Figure 1.10. Model showing how a pre-existing clump is triggered when an HII region expands into it. The labels in the top right of each panel show the time after first contact in Myr, the colour bar indicates the mass surface density of H_2 in g cm^{-2} and the x and y axes shows the size of the region in pc. Figure shows that the less dense gas is pushed away into a tail, causing the region to have an elongated appearance. Image from Bisbas et al. (2011).

where r is the distance away from the star, L, is the luminosity c is the speed of light and Σ is the gas surface density. On scale of entire molecular clouds Eq. 1.11 can be used to estimate a critical mass surface density, $\Sigma_{\rm gas}^{\rm crit}$, below which the luminosity of star, L_*, is enough to eject the gas. But to estimate $\Sigma_{\rm gas}^{\rm crit}$ for the star formation within an entire molecular cloud, one needs an estimate of the cluster mass, how the cluster mass and luminosity are distributed within a given star forming region and the luminosity of each star using an estimate for light-to-mass ratio (Reed 2001).

Although simple, Eq. 1.11 is deceptive since it neglects the complex inhomogeneous nature of star formation (Thompson & Krumholz 2016). As already discussed in Sec. 1.4.2, treating the radiation pressure isotropically during their formation limits stellar masses to ~10 $M_\odot$. Even now, the role of radiation pressure and how it is implemented in hydrodynamical simulations is a point of contention. Uncertainties include the amount of momentum actually delivered to the gas by photons (lowering the effectiveness of radiation pressure) and how a turbulent medium can provide low surface density avenues for radiation pressure to act upon (increasing the effectiveness of radiation pressure) (Thompson & Krumholz 2016; Haid et al. 2018). However, there is even a debate on the accuracy of simulations themselves where subgrid implementations of radiation feedback leads to wildly varying and inaccurate results (Krumholz 2018; Grudić & Hopkins 2018).

1.5.4 HOT STELLAR WINDS

Stars eject mass from their surfaces at high velocities during their nuclear burning phase, analogous to a wind (Lamers et al. 1999). High-mass stars eject much more mass than low-mass stars, and can lose up to $\sim 1\times 10^{-4}$ $M_\odot$ yr^{-1} reaching velocities >1000 km s^{-1} via the line-driven acceleration of material (Lucy & Solomon 1970; Leitherer et al. 1992; Owocki & Puls 1999). While at these velocities, the winds reach $> 10^7$ K by shocking against colder material. When multiple stars produce winds at the same time, they can combine together to drive the galactic outflows that help maintain the HIM (Bruhweiler et al. 1980). Over their lifetime, the energy and momentum output by winds are comparable to supernova explosions (Castor et al. 1975). But, whether they deposit this as efficiently as supernovae is the key to understanding the impact they have. Although some observations find that winds could drive turbulent support in molecular (Arce et al. 2011), simulations find that they cannot impart much momentum and energy to the molecular cloud. In these simulations, most of the energy is lost due to thermal and turbulent conduction or due to physical leakage of the hot gas via low density channels (Rosen et al. 2014; Dale et al. 2015; Kim et al. 2018).

1.5.5 SUPERNOVA

The importance of supernovae has already been alluded to throughout this introduction. Supernovae shock-waves heat up the ISM to help create the HIM (and in some cases molecular clouds in galaxies Dawson et al. 2013) (McKee & Ostriker 1977) and injects turbulence into the ISM at large scales, limiting star formation (Padoan et al. 2016; Hayward & Hopkins 2017), though this is still debated Seifried et al. (2018)) Within the molecular clouds, the impacts that supernovae have are more unknown. Some authors predict that supernovae occur too late to have a dominant role in destroying their host cloud (Geen et al. 2016; Körtgen et al. 2016), while others predict that the combination of winds and ionising radiation with supernova completely destroys their host molecular clouds (Walch & Naab 2015; Wareing et al. 2017).

1.6 PURPOSE OF THESIS

Throughout this introduction, I have shown that stellar feedback plays an important role in shaping the ISM and influencing star formation. Nevertheless, the role of feedback in regulating star formation is still uncertain. Therefore, this thesis uses observational methods at radio wavelengths to quantify the impact of stellar feedback on scales local to the their parent molecular cloud. For that purpose, I describe the fundamentals of observational astronomy at radio wavelengths in Chapter 2, and explain why radio data are used to measure ionising feedback and molecular gas. Chapter 3 then describes analysis tools and methods that can be used to constrain high-mass star formation and stellar feedback. In Chapter 4, I apply the methods described in Chapter 3 to investigate how feedback impacts the star forming ability of the G316.75 ridge. In Chapter 5, I investigate how stellar feedback affects the star formation efficiencies of molecular clouds that have been significantly disrupted by feedback, compared to clouds that have not been disrupted by feedback. This also puts the work of Chapter four into the context of the star formation occurring in the rest of the galaxy. The final chapter presents the conclusion of this thesis, and discusses future avenues of research.

CHAPTER 2

OBSERVATIONAL TECHNIQUES FOR ASTRONOMY

2.1 FUNDAMENTALS OF RADIATIVE TRANSFER

The flux received from an astronomical source is dependent on its wavelength, the medium between the source and the receiver, and the receiver properties. Therefore, to compare different measurements, one needs to characterise the radiation and define the components that can affect emission. In the absence of an intervening medium, we can calculate the emission received by a detector from an extended source by measuring its monochromatic specific intensity I_ν, given by Wilson et al. (2009):

$$I_\nu = \frac{\mathrm{d}P}{\cos(\theta)\,\mathrm{d}A\mathrm{d}\Omega\mathrm{d}\nu} \tag{2.1}$$

For a small detector, such as a single pixel within an array of pixels, this represents the power received, dP, per area, dA, from source solid angle dΩ projected with respect to the surface normal, $\cos(\theta)$, per frequency bandwidth, dν. For resolved objects, the monochromatic intensity does not depend on the distance to the source because I_ν represents the flow of energy through unit solid angle (See Fig. 2.1). Therefore, in

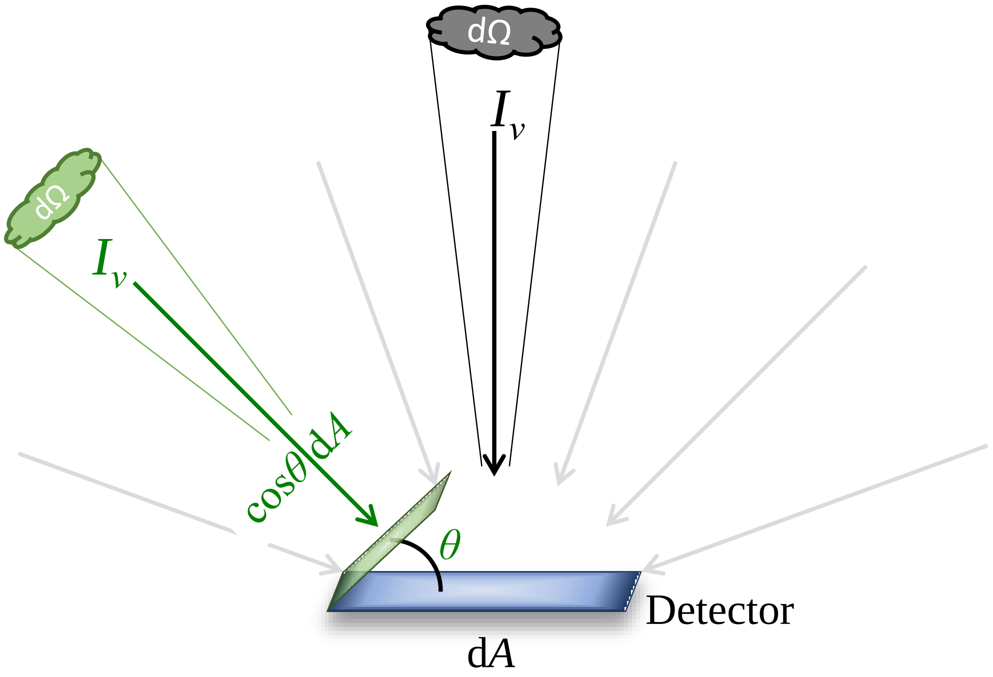

Figure 2.1. Diagram illustrating monochromatic specific intensity (I_ν) received for a small detector of area dA. For a source subtending a solid angle dΩ (the grey and green cones), the power received is dependent on the projected area of the source (the grey and green cloud-like objects) in relation to the detector with respect to the normal of the detector. The blue and green sheets represent the detector area (dA) and the projected detector area (cosθ dA) seen by an on- and off-axis beams respectively. The detector area has been drawn much larger than the incidence beams of radiation to better illustrate the origin of the variables in Eq. 2.1.

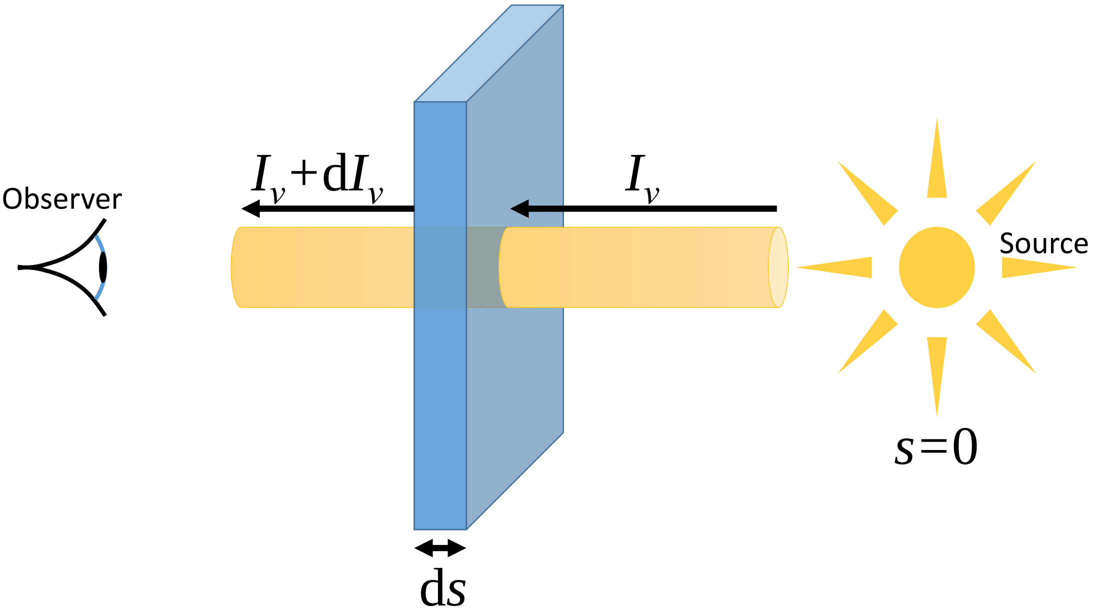

Figure 2.2. Diagram illustrating equation of radiative transfer. I_ν is the monochromatic specific intensity from a source, s is the distance along the beam from the source at $s = 0$, to the observer and dI_ν is change in I_ν as it passes through a medium of thickness ds.

the absence of absorption (and scattering), I_ν is constant along a given beam and can be expressed as:

$$\frac{\mathrm{d}I_\nu}{\mathrm{d}s} = 0 \tag{2.2}$$

where s is the distance along the beam. When an intervening medium exists between the source and the detector, I_ν can both increase and decrease in value. We describe these changes in I_ν using an emission term and an absorption term respectively. Over an infinitesimal distance, ds, the change in I_ν is given by:

$$\frac{\mathrm{d}I_\nu}{\mathrm{d}s} = -\kappa_\nu I_\nu + \epsilon_\nu \tag{2.3}$$

where κ_ν is called the monochromatic absorption coefficient (in Eq. 2.3, the units of κ_ν are per unit length). κ_ν describes the decrease to I_ν due to an absorbing medium present between the source and the detector. With this definition, the inverse of κ_ν

represents the mean free path of a photon. Opposite to this, the monochromatic emissivity coefficient, ϵ_ν, describes the increase to I_ν (see Fig. 2.2) by an emitting medium. ϵ_ν has units of power per unit volume, per unit solid angle per unit frequency.

I_ν can also be affected by scattering mechanisms. Scattering is the name given to an absorption that is immediately followed by emission (usually at the same frequency). However, re-emission usually occurs in a different direction to the incident beam of photons. This reduces the beam intensity. Scattering is dependent on the size and shape of the particles in the medium and the wavelength (λ) of the incoming beam of photons. Usually, when particles have similar sizes to the wavelength of the radiation, they are better able to scatter the light. For example, dust particle have radii on the order of $\sim 10^{-4}$–1 μm (Weingartner & Draine 2001; Hirashita & Kuo 2011) in the ISM, and so the scattering of optical and IR photons is dominated by dust particles. Therefore, the overall impact that scattering will have to a beam of photons is dependent on the frequency ($\propto 1/\lambda$) of the radiation and medium present between the source and the detector. Since these are the same dependencies as absorption, scattering is usually included as an additional term in κ_ν. The total loss of radiation by both processes is now called extinction, where κ_ν represents the monochromatic extinction coefficient instead of the monochromatic absorption coefficient.

We can now represent the loss of photons as the ratio of the distance travelled by a photon over its mean free path. This is given by the monochromatic optical depth, τ_ν:

$$\mathrm{d}\tau_\nu = -\kappa_\nu \, \mathrm{d}s \tag{2.4}$$

Using Eq. 2.4 we can exchange ds with dτ in Eq. 2.3 to get:

$$\frac{\mathrm{d}I_\nu}{\mathrm{d}\tau_\nu} = I_\nu + \frac{\epsilon_\nu}{\kappa_\nu} \tag{2.5}$$

where ϵ_ν/κ_ν is called source function since it describes how photons travelling through a medium are absorbed and emitted. If the source function, S_ν is uniform throughout the medium, Eq. 2.5 has the solution:

$$I_\nu(s) = I_\nu(s=0)e^{-\tau_\nu(s)} + S_\nu(1 - e^{-\tau_\nu(s)}) \tag{2.6}$$

$$I_\nu(s) \approx \begin{cases} S_\nu, & \tau \gg 1 \\ I_\nu(s=0) + \tau_\nu(s)S_\nu, & \tau \ll 1 \end{cases}$$

where the bottom equations describe the optically thick and thin solutions. If the intervening medium is isothermal and collisions dominate within the medium (and so the emission is in local thermodynamic equilibrium (LTE)), S_ν is equal to the Planck function. When in LTE, the optically thin and thick solutions for radiative transfer become:

$$I_\nu(s) \approx \begin{cases} B_\nu, & \tau \gg 1 \\ I_\nu(s=0) + \tau_\nu(s)B_\nu, & \tau \ll 1 \end{cases}$$

Another important quantity used to measure radiation is the monochromatic flux density, F_ν and can be expressed as:

$$F_\nu = \int_\Omega I_\nu \cos(\theta)\, \mathrm{d}\Omega \tag{2.7}$$

F_ν represents the monochromatic specific intensity integrated over the source solid angle dΩ, Unlike S_ν , F_ν is not constant with distance. The final quantities used to measure radiation are the monochromatic and bolometric luminosities emitted from a source. The monochromatic luminosity is the power emitted by the source over the bandwidth dν and is given by:

$$L_\nu = 4\pi d^2 F_\nu \tag{2.8}$$

where L_ν is the monochromatic luminosity, and d is the distance from the source to the observer. Sometimes however, it is more useful to sum the luminosity over all frequencies:

$$L_{\mathrm{bol}} = \int_0^\infty L_\nu \, \mathrm{d}\nu \tag{2.9}$$

This allows one to understand the total power emitted by the source (such as the total luminosity emitted by a black body radiation source).

2.2 INTRODUCTION TO SINGLE-DISH RADIO ASTRONOMY

Radio emission is unique in its ability to trace a large range of star formation processes. At the longer wavelengths, radio emission reveals the locations of HII regions and old supernova remnants (See Fig. 2.3 Heywood et al. (2019)). At 21 cm, radio emission can trace atomic hydrogen, and at millimetre wavelengths, molecules can emit via rotational transitions, tracing a range of molecular gas conditions and properties. In addition, radio emission is less affected by intervening processes that typically affect short wavelength radiation (i.e., extinction) and most radio emission between 1 mm–20 m is easily observed at ground level via a large transparent atmospheric window that exists at this wavelength range (See Fig. 2.4). Although, the quality of radio observations are limited by diffraction (especially when compared to shorted wavelength observations, such as optical wavelengths). For a circular aperture, the relationship between the angular resolution (θ) for a given wavelength (λ) is:

$$\theta = \frac{1.22\lambda}{D} \tag{2.10}$$

where D is the diameter of the collecting area. Equation 2.10 shows that the only way for single-dish radio telescopes to match the resolutions of shorter wavelength observations (e.g, optical, 400–700 nm) is to use large collecting areas. But, to reach

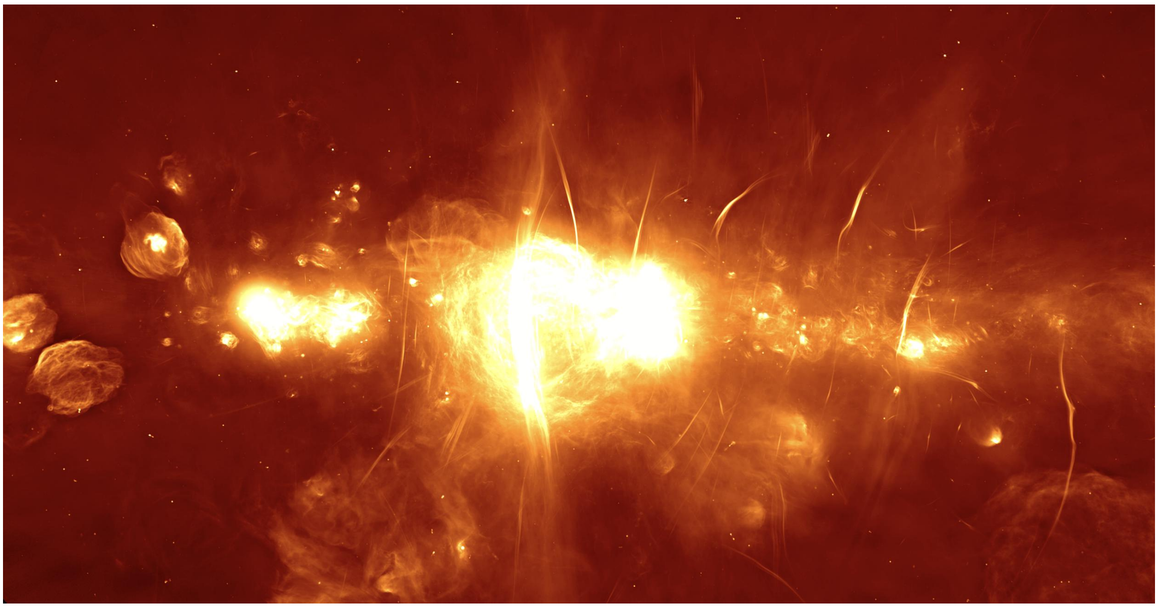

Figure 2.3. Radio emission taken with MeerKAT covering 2° × 1° of the galactic centre at 1284 MHz with resolution $6''$ (Heywood et al. 2019). In the image, circular emission features show the locations of HII regions and supernova remnants. Image credit: The South African Radio Astronomy Observatory.

$\theta = 0.02''$ at 1 mm, a 2 km diameter dish is needed, which is unfeasible to build). Interferometry, (the combination of signals from two or more spatially separated receivers) can create higher resolution images but the data products are much more complex and still comes with their own limitations. Interferometric observations usually contain artefacts from the imaging process, and unless combined with single-dish data, interferometers cannot recover larger-scale, extended emission. The latter makes interferometry unsuited for studying entire molecular clouds and filamentary structures when uncorrected (but is perfectly fine for studying small star forming features such as cores).

I note that the resolution of single-dish radio telescopes are slightly worse than predicted in Eq. 2.10 due to the properties of radio waves and the large observatories needed to achieve modest resolutions. For example, a large collecting area increases the difficulty in minimising surface errors. Even the smallest surface errors can misdirect signal enough to noticeably reduce the angular resolution. Additionally, radio telescopes usually under illuminate their dishes to minimise power that is missed by the dish (spillover). This effectively reduces the diameter of the dish. Overall, these limitations cause the effective collecting area to be smaller than the true geometric area of the dish, which affects the resolution of the telescope (Wilson et al. 2009). Despite being limited by resolution, the range of star formation processes traced by radio emission makes radio observations critical for characterising star forming regions. Therefore, this thesis makes use of radio measurements to investigate star formation processes. For the rest of this chapter, I describe techniques used in single-dish radio observations and define the emission one expects to receive from high-mass star forming regions.

To detect radio emission, the radiation must be collected, transmitted and converted into measurable quantities. Usually this is done via a parabolic reflector onto a secondary mirror and into a detection unit. The emission measured from star forming regions will be $\sim 1\times10^{-26}$ $\mathrm{Wm^{-2}Hz^{-1}}$. With such small intensities, radio emission is given in units of Jy (1 Jy $= 1\times10^{-26}$ $\mathrm{Wm^{-2}Hz^{-1}}$), but a more convenient unit to use is brightness temperature T_B given by:

$$T_\mathrm{B} = \frac{I_\nu c^2}{2k_\mathrm{B}\nu^2} \tag{2.11}$$

The brightness temperature comes from the Rayleigh-Jeans approximation for black-body radiation:

$$B_{\nu,T} = \frac{2h\nu^3}{c^2}\frac{1}{\exp(h\nu/(k_\mathrm{B}T)) - 1} \approx \frac{2k_\mathrm{B}T\nu^2}{c^2}, \text{ for } k_\mathrm{B}T \gg h\nu \tag{2.12}$$

As a result, the brightness temperature is the temperature I_ν would have if it was the result of blackbody emission. A radio source does not need to be in LTE to use brightness temperature as a measure of intensity. However, if the radio source is in LTE, the brightness temperature will equal the kinetic temperature when $\tau >> 1$.

To detect weak radio emission, especially when systematic, intrinsic and background noises dominate over the emission, the emission needs to be amplified and the

REDACTED

Figure 2.4. **Top**: Image illustrating atmospheric transmission v.s wavelength, indicating large transparent window exists at radio wavelengths. Image amended from NASA **Bottom**: Image illustrating atmospheric transmission at millimetre wavelengths. Transmission is highly dependent on water vapour, so the spectrum shown is at the Chajnantor plateau in the Chilean Andes (altitude of ∼5000 m) when the Precipitable Water Vapour (PWV) is 0.5 mm. Image amended from Lundgren (2012).

noise characterised. The first way to increase the signal is by increasing the collecting area of the telescope either by increasing the geometric collecting area, $A_{\rm g}$, or by increasing the aperture efficiency, $\eta_{\rm A}$ of the telescope. As previously mentioned, the efficiency of the antenna area is always less that 100% due to the reflectivity of the antenna surface, positioning errors, signal blockage, spillover and illumination efficiency. Each process reduces the aperture efficiency multiplicatively, therefore each process needs to be minimised or they will seriously reduce aperture performance (Wilson et al. 2009).

The effective collecting area of the telescope can be expressed as $A_{\rm e} = \eta_{\rm A} \times A_{\rm g}$, or as the monochromatic power received, compared to the monochromatic flux density incident on the antenna:

$$A_{\rm e} = \frac{2P_\nu}{F_\nu} \tag{2.13}$$

where P_ν is the power received and the factor of 2 accounts for the fact that radio antennae are sensitive to one polarisation of light at a given time; assuming that the light is unpolarised, the antennae can only ever detect half the flux incident upon it.

Radio antennae are also able to receive power from angular scales over a full sphere, not just the direction the telescope is pointing at, as indicated in Fig. 2.5. However, this makes it difficult to know the exact power received from a single source in the sky. A radio signal can be boosted by concentrating the power received to a smaller area, and by minimising side lobes. The performance of the telescope can now be defined as the fraction of power in the main beam compared to the full beam pattern:

$$\eta_{\rm mb} = \frac{\Omega_{\rm mb}}{\Omega_{\rm A}} \tag{2.14}$$

where $\Omega_{\rm A}$ total beam solid angle and $\Omega_{\rm mb}$ is the main beam solid angle. Higher values for $\eta_{\rm mb}$ indicate that the antenna has a better directionality. As a result, the angular

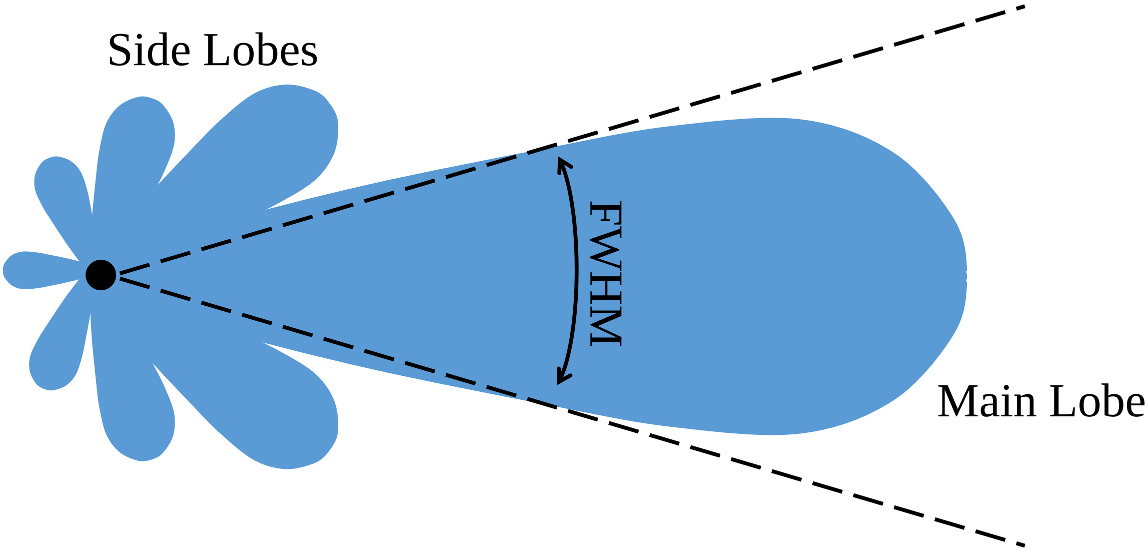

Figure 2.5. Schematic indicating the beam pattern of a radio antenna. The diagram shows that a radio antenna can collect power from all direction. Well designed telescopes concentrate the power pattern to a small angular scale in the frontward facing lobe. The angular scale where the power received drops to half is the half beam full power (HBFP). By approximating the power as a Gaussian, HBFP≈FWHM of a Gaussian.

extent of the main beam controls the angular resolution. Assuming that the beam is well approximated by a Gaussian, the angular resolution can be given by:

$$\Omega_{\mathrm{A}} = \frac{\pi}{4\ln(2)}\theta^2_{\mathrm{FWHM}} \tag{2.15}$$

where θ_{FWHM} is the angular resolution. Analogous to brightness temperature, the monochromatic power measured can be described using its antenna temperature, T_{A} given by:

$$T_{\mathrm{A}} = \frac{P_\nu}{k_{\mathrm{B}}} = \frac{A_{\mathrm{e}}F_\nu}{2k_{\mathrm{B}}} \tag{2.16}$$

Just like blackbody radiation, Eq. 2.16 represents the temperature that P_ν would have if it was the result of a resistor in LTE, under the condition that $k_{\mathrm{B}}T \gg h\nu$ (i.e., its Johnson noise). As a result, T_{A} is a convenient measure of the power received because one can easily relate it to the brightness temperature. However, $T_{\rm A}$ is a measure of all the flux incident on the antenna from all directions, including flux from the ground (see Fig. 2.5). Therefore, for a source confined to small angular scales $\leqslant 2'$ (i.e where the emission from the source emission falls within the main beam and nulls, but not significantly within side lobes), one can use the main beam efficiency to calculate a more appropriate measure of flux, given by:

$$T_{\rm mb} = \frac{T_{\rm A}}{\eta_{\rm mb}}, \tag{2.17}$$

where $T_{\rm mb}$ is called the main beam temperature. For very extended sources, the skyward facing lobes will receive power from the source. By defining, $\eta_{2\pi}$, which is equivalent to $\eta_{\rm mb}$ but for skyward facing lobes, the flux from extended sources is given by:

$$T_{\rm A}^{*} = \frac{T_{\rm A}}{\eta_{2\pi}}. \tag{2.18}$$

Due to the calibration process, which includes a sky subtraction, $T_{\rm A}^{*}$ is usually the quantity measured by telescopes (Wilson et al. 2009). Sky subtraction is done by switching between an observation of the source with the telescope, to an observation of an empty patch of sky. Because the sky emits over a semi-sphere, a telescope pointing at the sky (both on or off a source) receives power over 2π steradians. Therefore when the sky contribution is subtracted from a source, all power over 2π steradians needs to be removed, which results in the quantity $T_{\rm A}^{*}$.

To convert $T_{\rm A}^{*}$ into $T_{\rm mb}$, one can use $\eta_{2\pi}$ and $\eta_{\rm mb}$:

$$T_{\rm mb} = \frac{\eta_{2\pi}}{\eta_{\rm mb}} T_{\rm A}^{*} \tag{2.19}$$

2.3 CONTINUUM EMISSION

2.3.1 DUST EMISSION AND ABSORPTION

Dust particles within the ISM absorb around 30-50% of the short wavelength radiation emitted by stars and re-emit it at longer wavelengths (Bernstein et al. 2002). Since dust is much colder than the colour temperature of stellar light, with typical dust temperatures of ∼10–100 K, dust emits at mid/far-infrared and millimetre wavelengths. The size of dust particles varies from ∼0.0001–1 μm in size, though the exact grain size distribution depends on the model used and the environment being measured. (Weingartner & Draine 2001; Hirashita & Kuo 2011). For example, the dust found in proto-planetary disks tends to be larger due to grain growth, and can reach mm–cm size scales (Natta et al. 2007). In general, the denser and more shielded the dust is, the larger the dust can grow, though there are a few exceptions to this rule (i.e., dust creation in supernova remnants Chawner et al. (2019)).

When a significant amount of cold dust exists in the foreground between an observer and some bright background emission, the observer will see the affect of dust absorption as dark extinction features against this bright background. The affect of dust absorption is best seen at IR wavelengths, since the background emission at IR wavelengths is high (especially along the Milky Way plane Peretto & Fuller 2009). Due to their appearance these features are called “infrared dark clouds”. The more dust that is present between an observer and the background, the darker, and more extinct these clouds appear. Therefore, the extinction value measured can be used to trace the mass of molecular clouds, assuming dust traces the molecular mass present (Bohlin et al. 1978).

Using Eq. 2.6, optically thin dust emission, I_ν is given by:

$$I_\nu = \kappa_\nu \Sigma_{\rm dust} B_{\nu,T_{\rm dust}} \tag{2.20}$$

where $\Sigma_{\rm dust}$ is the mass surface density. To reduce the number of steps needed to calculate $\Sigma_{\rm dust}$, κ_ν is redefined here as the extinction cross-section per mass (whereas it was previously defined as the inverse of the mean free path of a photon in Eq. 2.4). Both definitions represent the same concept, which is the probability that a photon will be interrupted along its path. However, one represents this probability in terms of the distance travel by a photon, and the other represent the probability in terms of the medium's ability (in this example, the dust's ability) to affect the photon. This implies that dust extinction is dependent on the size, shape, and composition of the dust grains, but because these three properties are not known, we usually approximate the dust as spherical grains and parametrise the average properties using a power law, β, given by (Hildebrand 1983; Beckwith et al. 1990):

$$\kappa_\nu = \Sigma_{\rm dust} \left(\frac{\nu}{1000 \text{ GHz}} \right)^{\beta} \text{cm}^2\text{g}^{-1} \tag{2.21}$$

Depending on the model, or on observations, β can vary from 0.2–3 (Rowan-Robinson et al. 1986; Agladze et al. 1996; Smith et al. 2012; Rigby et al. 2018; Whitworth et al. 2019). High values of β typically represent small dust grains found in diffuse ISM conditions whereas lower values of β are found in denser ISM conditions such as molecular clouds (though this property is reversed in proto-planetary disks).

In the Milky Way, 1% of the mass of the ISM is contain with dust particles (Bohlin et al. 1978). This percentage is seen to decrease radially from the centre of the Milky Way, but recent simulations and observations indicate that the ratio of gas-to-dust does not significantly fluctuate on small spatial scales (Giannetti et al. 2017; Tricco et al. 2017; Kreckel et al. 2019). Therefore dust emission can be used to determine the H_2 present, given by:

$$N_{\rm H_2} = \frac{100\Sigma_{\rm dust}}{\mu m_{\rm H}} \tag{2.22}$$

where $N_{\rm H_2}$ is the column density of H_2 and $\mu m_{\rm H}$ is the the mass of hydrogen and μ is the mean mass associated with each hydrogen molecule (μ=2.8 for molecular hydrogen).

At the temperatures of molecular clouds, the dust emission peaks at $\sim 250\ \mu$m, which is well into sub-mm wavelengths. Although, the Earth's atmosphere is opaque at these wavelengths, except for some small bands at 850 μm and 450 μm (See fig. 2.4). Therefore, a telescope outside of Earth's atmosphere is needed to measure dust emission over a larger wavelength range that also includes the peak dust emission (e.g., the *Herschel* space telescope).

2.3.2 FREE-FREE EMISSION

Charged particles are able to emit photons due to the coulomb interaction. When this occurs between a thermalised distribution of electrons and ions, they produce radio continuum emission. No electrons become bound in this interaction and so this type of emission is called free-free emission. The monochromatic emissivity for free-free emission is given by (Oster 1961):

$$\epsilon_\nu = A n_\mathrm{i} n_\mathrm{e} Z^2 T_\mathrm{e}^{-1/2} \ln \frac{b_\mathrm{max}}{b_\mathrm{min}} \tag{2.23}$$

where Z is the proton number of the interacting ion, T_e is the temperature of the electrons, n_i is the number density of interacting ions, n_e is the number density of electrons and b_max and b_min are the maximum and minimum impact parameters (i.e., the distance of interaction). The maximum and minimum impact parameters are controlled by Heisenberg's uncertainty principle, which allows us to approximate $\ln(b_\mathrm{max}/b_\mathrm{min})$ with the gaunt factor for free-free interactions, $\langle g_\mathrm{ff} \rangle$ (Oster 1961). $\langle g_\mathrm{ff} \rangle$ is approximately proportional to $\nu^{-0.1} T_\mathrm{e}^{0.15}$m. A represents all the constants in Eq. 2.23:

$$A = \left(\frac{2m_\mathrm{e}}{3\pi k_\mathrm{B}} \right)^{1/2} \left(\frac{8\pi e^6}{3m_\mathrm{e}^2 c^3} \right) \left(\frac{1}{4\pi\varepsilon_0} \right)^3 \tag{2.24}$$

where e is the charge of an election, ε_0 is the dielectric constant, and m_e is the mass of an electron. To derive I_ν for free-free emission, we can use Kirchhoff 's law, $\kappa_\nu = \epsilon_\nu / B_\nu(T_\mathrm{e})$ to find the monochromatic absorption coefficient. With κ_ν defined, this allows us to define the optical depth as:

$$\tau_\nu = \frac{Ac^2Z^2}{2h} T_\mathrm{e}^{-1/2} \nu^{-3} \langle g_\mathrm{ff} \rangle \left(1 - \exp\left(\frac{-h\nu}{k_\mathrm{B} T_\mathrm{e}}\right)\right) \int_\mathrm{l.o.s.} n_\mathrm{e}^2 \, \mathrm{d}s \tag{2.25}$$

where ds is the distance along the line of sight. Finally, since optically thin emission is given by $I_\nu = \tau_\nu B_\nu(T_\mathrm{e})$ (see Eq. 2.6), the monochromatic specific intensity is given by (Panagia & Walmsley 1978):

$$I_\nu = AZ^2 \exp\left(\frac{-h\nu}{k_\mathrm{B} T_\mathrm{e}}\right) T_\mathrm{e}^{-1/2} \langle g_\mathrm{ff} \rangle \int_\mathrm{l.o.s.} n_\mathrm{e}^2 \, \mathrm{d}s \tag{2.26}$$

In astronomy, the integral in Eq. 2.26 is usually replaced with the emission measure (EM) since EM can be measured independently. The EM is given by:

$$\frac{\mathrm{EM}}{\mathrm{pc\ cm^{-3}}} = \int_\mathrm{l.o.s} \left(\frac{n_\mathrm{e}}{\mathrm{cm^{-3}}}\right)^2 \, \mathrm{d}\left(\frac{s}{\mathrm{pc}}\right) \tag{2.27}$$

where n_e has units of cm^{-3} and the path ds has units of pc.

2.4 LINE TRANSITIONS

Line transitions describe the emission or absorption of photons at quantised energy levels. Rotational transitions, a type of line transition, describe changes in the rotational state of a molecule about an inertial axis (Wilson et al. 2009). These transitions are represented with the quantum number, $J \geqslant 0$, and strong (i.e., electric dipole) transitions only occur when $\Delta J = \pm 1$. For polar molecules with a permanent dipole, rotational transitions can arise either when radiation induces a torque on the molecule, when collisions change the rotational state or due to spontaneous quantum emission. The rates of these processes can be summarised using the Einstein coefficients A, B, and the collisional rates summarised with the coefficient C. Fig. 2.6 illustrates the relationship of these three coefficients.

The A coefficient describe the rate that spontaneous quantum transitions occur. They can only occur from an upper level, u, to a lower level, l, otherwise energy conservation is violated. Spontaneous emissions increase linearly with the number of atoms/molecules in an upper level (i.e., the number density at that level, n_{u}), which is analogous to ϵ_ν. Therefore, the two quantities are related to one another. Given that the energy emitted will equal the energy gap between an upper and lower level, $h\nu_0$, we can write ϵ_ν in terms of A_{ul} as:

$$\epsilon_\nu = \frac{h\nu_0}{4\pi} n_{\mathrm{u}} \phi(\nu) A_{\mathrm{ul}} \tag{2.28}$$

where $\phi(\nu)$ is the intrinsic line profile of the transition, which accounts for the small variation in the band gap due to quantum uncertainty.

The B coefficient describes the probability that a photon, $h\nu_0$, induces a transition, and so the rate the occurs depends on the strength of the radiation field. Unlike spontaneous emission, radiative transitions can occur in both directions. B_{ul} represents stimulated emission, and can occur when an incoming photon equal to the transition energy ($E_{\mathrm{ul}} = h\nu_0$) induces a transition from the upper state to the lower state. B_{lu} describes the probability that an incoming photon, equal to the transition energy, is absorbed. κ_ν is also dependent on the intensity of the incident radiation, therefore, the B coefficients can be used to define the κ_ν. For a species that populates an upper state and lower state with densities n_{u} and n_{l} respectively, the net absorption is given by the energy of the incident photons that equal the transition energy between the two levels, multiplied by difference between the amount of absorption to the amount of induced emission. This can be expressed as:

$$\kappa_\nu = \frac{h\nu_0}{c} \phi(\nu) \Big[n_{\mathrm{u}} B_{\mathrm{ul}} - n_{\mathrm{l}} B_{\mathrm{lu}} \Big] \tag{2.29}$$

The C coefficient represents collisional changes to the energy levels and can

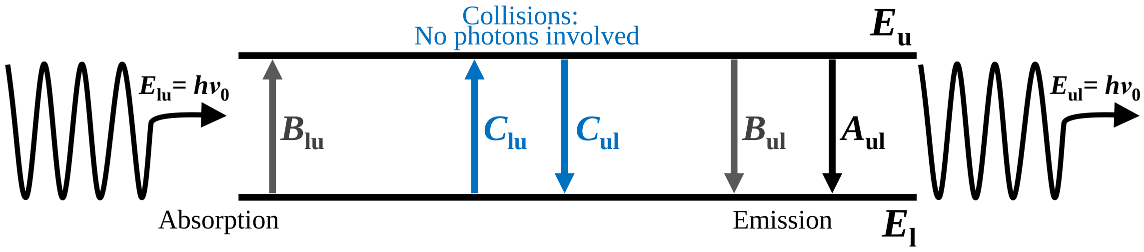

Figure 2.6. Diagram of the five Einstein and collisional Coefficients, A_{ul}, B_{ul}, B_{lu}, C_{ul}, C_{lu}. E_{lu} and E_{ul} shows the photon energy that can be absorbed and emitted respectively and ν_0 is the frequency of the photon, where $\nu_{\mathrm{ul}} = \nu_{\mathrm{lu}}$. Together, these describe the transitional rates.

also occur in either direction (C_{ul} and C_{lu}). A collisional transition does not result in the direct emission or absorption of photons. In statistical equilibrium, the Einstein coefficients and the C coefficients describe the balance between upward and downward transitions and is expressed as:

$$n_{\mathrm{u}}(A_{\mathrm{ul}} + B_{\mathrm{ul}}\overline{u} + C_{\mathrm{ul}}) = n_{\mathrm{l}}(B_{\mathrm{lu}}\overline{u} + C_{\mathrm{lu}}) \tag{2.30}$$

where $\overline{u}$ is the mean radiation energy density of the incident radiation field equal to:

$$\overline{u} = \frac{4\pi}{c}\int_0^\infty I_\nu \phi(\nu)\,\mathrm{d}\nu \tag{2.31}$$

To understand how the transition appears to an observer, we need to know how n_{u} and n_{l} are populated. The easiest way to derive the level populations is to use the principle of detailed balance. Einstein coefficients are constants that describe the atomic/molecular processes of emission and absorption. Therefore, they are independent from the global properties of the medium. This means that any relationships between the coefficients derived must be valid universally, including any relationships derived using thermodynamic equilibrium (TE). For a two level system in TE, the level populations are described by the Boltzmann distribution:

$$\frac{n_{\mathrm{u}}}{n_{\mathrm{l}}} = \frac{g_{\mathrm{u}}}{g_{\mathrm{l}}}\exp\Big(-\frac{h\nu_0}{k_{\mathrm{B}}T}\Big) \tag{2.32}$$

where $g_{\mathrm{u/l}}$ are the statistical weights and T is the kinetic temperature when the system is in TE. In TE, I_ν is equal to $B_{\nu,T}$. By substituting Eq. 2.32 into Eq. 2.30, rearranging for $\overline{u}$ and equating it to Eq. 2.31, the principle of detailed balance requires that:

$$\frac{g_{\mathrm{l}}B_{\mathrm{lu}}}{g_{\mathrm{u}}B_{\mathrm{ul}}} = 1; \tag{2.33}$$

$$\frac{A_{\mathrm{ul}}}{B_{\mathrm{ul}}} = \frac{8\pi\nu_0^3}{c^3}; \tag{2.34}$$

and

$$\frac{C_{\mathrm{lu}}}{C_{\mathrm{ul}}} = \frac{n_{\mathrm{u}}}{n_{\mathrm{l}}}. \tag{2.35}$$

These equations now allow one to express the level populations when the system is not in TE. When the system is no longer in TE, the level populations are dependent on the balance of the incident radiation field and the frequency of collisions. This balance is given by the excitation temperature T_{ex}. At radio frequencies (i.e., when $k_{\mathrm{B}}T >> h\nu_0$), the excitation temperature is:

$$T_{\mathrm{ex}} = \left(\frac{T_0\frac{C_{\mathrm{ul}}}{A_{\mathrm{ul}}} + T_{\mathrm{bg}}}{T_0\frac{C_{\mathrm{ul}}}{A_{\mathrm{ul}}} + T_{\mathrm{k}}}\right)T_{\mathrm{k}} \tag{2.36}$$

where $T_0 = h\nu_0/k_{\mathrm{B}}$ and T_{bg} is the brightness temperature of the surrounding radiation field. Eq. 2.36 shows that the excitation temperature is a mean between the brightness temperature of the incident radiation field and the kinetic temperature of the gas weighted by the radiative to collisional de-excitations. When $A_{\mathrm{ul}} > C_{\mathrm{ul}}$, $T_{\mathrm{ex}} \approx T_{\mathrm{bg}}$, the emission is weak (the upper level is barely populated therefore emission is sparse).

When $A_{\rm ul} < C_{\rm ul}$, $T_{\rm ex} \approx T_{\rm k}$, the line is seen in emission. The collisional rate is dependent on the number density of the colliding partner (usually assumed to be H_2). Therefore, there exists a density where collisional and radiative de-excitations will equal and can be expressed as:

$$n_{\rm crit} = \frac{A_{\rm ul}}{\langle \sigma_{\rm ul} v \rangle} \left(1 + I_\nu \frac{c^2}{2h\nu^3} \right) \tag{2.37}$$

where $n_{\rm crit}$ is the density where collisional equal radiative de-excitations, $\sigma_{\rm ul}$ is the reaction cross-section and v is the gas velocity (Shirley 2015). $n_{\rm crit}$ is the critical density because it indicates the density needed for a line to be seen in emission (i.e., if a line is seen in emission, the density of the collisional partner is $\geqslant n_{\rm crit}$). If $T_0 \gg T_{\rm bg}$, $n_{\rm crit} \approx \frac{A_{\rm ul}}{\langle \sigma_{\rm ul} v \rangle}$ and the transition thermalises close to its critical density ($T_{\rm ex} \approx T_{\rm k}$ when $n = n_{\rm crit}$). When $T_0 \lessapprox T_{\rm bg}$, the surrounding radiation field has a larger impact on the level populations, which means densities larger than $n_{\rm crit}$ are required before $T_{\rm ex} \approx T_{\rm k}$. Additionally, $n_{\rm crit}$ does not take additional physical factors into consideration. For example, when $\tau > 1$, the radiation becomes trapped and re-interacts with the medium through which it is propagating. As a result, photons produced by spontaneous emission are re-absorbed before they can escape, which effectively lowers the rate of spontaneous emission from the medium (Scoville & Solomon 1974). Consequentially, the critical density is reduced by a factor τ when $\tau > 1$. Eq. 2.37 also assumes that H_2 is the only collisional partner. This can underestimate the collisional rates when other species cause collisional transitions and by doing so, overestimate the critical density. Such a situation occurs with HCN rotational transitions, where free electrons play a role in determining $C_{\rm ul}$ and $C_{\rm lu}$ (Faure et al. 2007).

2.4.1 LINE BROADENING

When transitions occur, the band gap between levels are affected by both quantum and macroscopic processes. Radiative emission and absorption is affected by the Heisenberg uncertainty principle, $\hbar \approx \Delta t \Delta E$, due to the probabilistic nature of these processes. Therefore, all transitions have an intrinsic width, given by a Lorentz profile (Wilson et al. 2009). At radio frequencies, natural line broadening is negligible and does not need to be considered. Although, collisions are able to reduce the time spent in a particular level. Since radio transitions come into a steady state via collisions, this affect cannot be neglected. By approximating the width with a Gaussian, the broadening is given by:

$$\phi_{\nu_0} = \left(\frac{\ln 2}{\pi}\right)^{1/2} \frac{2}{\Delta \nu} \tag{2.38}$$

The appearance of emission lines is also affected by gas motions. The radial velocities of the gas particles are proportional to the frequency shift observed along the line of sight to the observer. The relationship between gas velocity and the observed frequency is given by the non-relativistic Doppler equation:

$$v = \frac{c(\nu_0 - \nu_{\rm obs})}{\nu_0} \tag{2.39}$$

where v is the velocity, ν_0 is the rest frequency and $\nu_{\rm obs}$ is the observed frequency. Since the particles can move both away and toward an observer, the line frequency appears broadened. Doppler broadening can occur via thermal and non-thermal processes.

Thermal Doppler broadening occurs due to the random motions of the gas relative to the observer, where the average velocity is proportional to the square root of the gas temperature. The distribution of velocities is described by a Maxwellian distribution. Along the line of sight this appears as a Gaussian distribution. Subsequently, the dispersion of the line indicates the gas temperature if no other motions

REDACTED

Figure 2.7. Diagram modelling optically thick emission lines. Black lines show how the line width changes with opacity and the green lines show the gaussian fit to this black line. Y axis is the intensity and X axis is the velocity. Intensities and velocities are in arbitrary units. Image from Hacar et al. (2016).

are present. However, most molecular clouds contain internal motions. These non-thermal motions increase the line-width observed beyond the thermal value. Non-thermal motions can be caused by turbulence, or, due to the flow of the gas, such as in-fall, outflow and rotation (Myers et al. 1991).

The appearance of emission lines are also affected by the opacity when $\tau > 1$. If $\tau > 1$, the radiation becomes trapped and re-interacts with the medium through which it is propagating. The emission now acts like the background radiation source in Eq. 2.36 and so increases $T_{\rm ex}$ to $T_{\rm k}$. This effect decreases away from the line centre since the optical depth decreases towards the wings. As a result, the width no longer appears Gaussian, but instead appears bloated, as shown in fig. 2.7.

Hyperfine transitions

Molecular lines are sometimes broken up into multiple components by hyperfine splitting. This splitting arises due to the slightly different energies associated with interactions between the spins (and hence the magnetic moments) associated with the constituent electrons and nuclei (Wilson et al. 2009). This can be in the form of magnetic dipole interactions, or electric quadrupole moments. The new quantum number for this interaction is given by F, where $F = J + I$, and I is the nuclear spin. The number of levels, and section rules of transitions are given by $\Delta F \pm 1, 0$ and $\Delta F \neq 0 \rightleftarrows 0$ i.e., a transition involving J=0 to F=0 is not allowed. Hyperfine transitions spread energy over more frequencies and in doing so, the emission is less likely to become optically thick. Moreover, hyperfine transitions are a convenient way to get extra information for the same transition. This extra information then provides a way to estimate additional gas properties, such as opacity and the column density. Although, this also means that hyperfine transitions require more complicated models in comparison to regular rotational transitions.

CHAPTER 3

TECHNIQUES AND METHODS FOR INVESTIGATING HIGH-MASS STAR FORMATION*

In this chapter, I will describe techniques and tools that I have used to measure the mass, density and kinematics of high-mass star forming regions. In particular, I focus on filamentary structures, how to measure feedback mechanisms, and the balance between gravity and feedback.

3.1 CHARACTERISING COLUMN DENSITY AND TEMPERATURE MAPS

The H_2 column density (N_{H_2}) and temperature of a given star forming region can be calculated using dust emission (assuming that $T_{\rm dust} = T_{\rm gas}$). Since the launch of *Herschel*, the standard way to do this is by performing a pixel-by-pixel fit to the dust Spectral Energy Distribution (SED) over the *Herschel* wavebands using Eq. 2.21 (Könyves et al. 2015) (example SED and fit is shown in Fig. 3.1). Typically, the shortest waveband at 70 μm is not used in the fit because it does not necessarily

---

*Part of the work presented here is published in Watkins et al. 2019, A&A, 628, A21

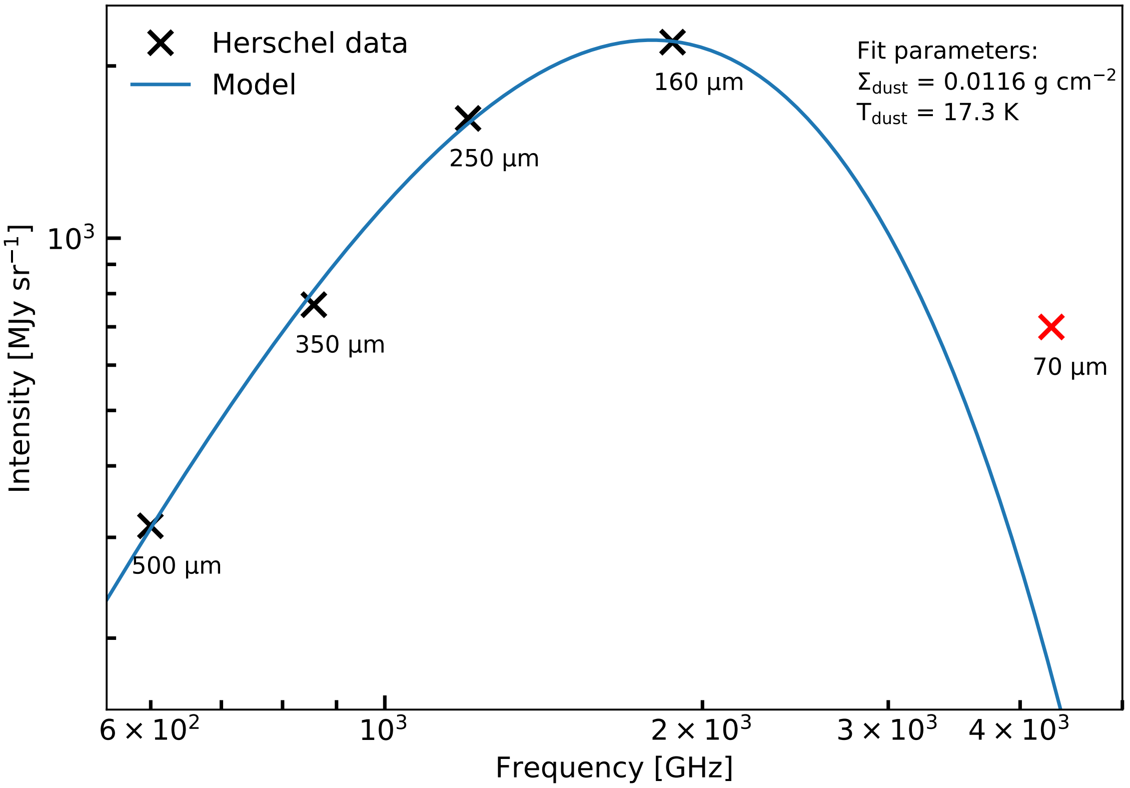

Figure 3.1. Example dust emission made using data from the Hi-GAL survey (data plotted from tile l=316–318). Crosses show the measured intensity and the solid blue line is the model single temperature SED. Typically, only the four longest wavebands (black markers) are used since the shortest waveband (red markers) does not trace cold dust. The observational uncertainties for each waveband are ~5%.

trace cold dust at 10–20 K.

By fixing β in Eq. 2.21, the only variables which the SED depends upon is Σ_{dust} and T_{dust}. Σ_{dust} can be converted to $N_{\mathrm{H_2}}$ by using Eq. 2.22. Before this can be done however, the *Herschel* data needs to be degraded to the coarsest resolution image. Assuming that the beam profiles are Gaussian, each image is degraded by a Gaussian whose FWHM, $\theta_{\mathrm{convolve}}$ is given by:

$$\theta_{\mathrm{convolve}} = \sqrt{\theta_{\mathrm{new}}^2 - \theta_{\mathrm{current}}^2} \tag{3.1}$$

θ_{new} is the angular resolution of the coarsest image, equal to 36″ for the *Herschel* 500 μm band, and $\theta_{\mathrm{current}}$ is the current angular resolution of the data. I note that even

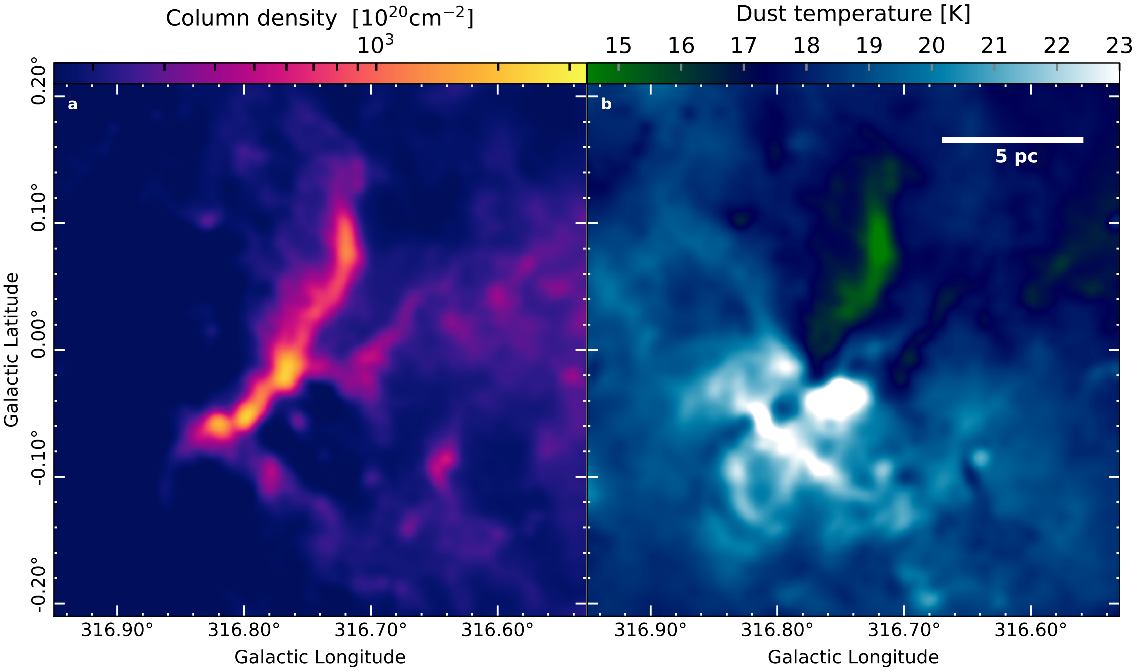

Figure 3.2. H_2 Column density map **(a)** and dust temperature map **(b)** of the G316.75 star forming region derived using pixel-by-pixel SED fitting to convolved *Herschel* observations. The white solid line indicates a physical scale of 5 pc (Watkins et al. 2019).

though the beam patterns of *Herschel* data are not strictly Gaussian, they are close enough that it does not significantly affect the results for this SED fitting method. The resulting 36″ resolution column density and dust temperature maps are shown in Fig. 3.2.

A less standard way of computing H_2 column densities and dust temperatures can be done using Point Process MAPping (PPMAP). PPMAP (Marsh et al. 2015) is a multi-wavelength Bayesian method that derives the H_2 column density emitting at a set of temperature and β bands using dust emission measurements by assuming the emission is optically thin (as does the standard method). For high-mass star forming regions, 12 temperature bands from 8 to 50 K adequately sample the range of temperatures that exists. This produces an H_2 column density cube (differential column density) for the 12 temperature bands, where each 2D slice represents the H_2 column density present at each temperature band. The uncertainty in this model selection is

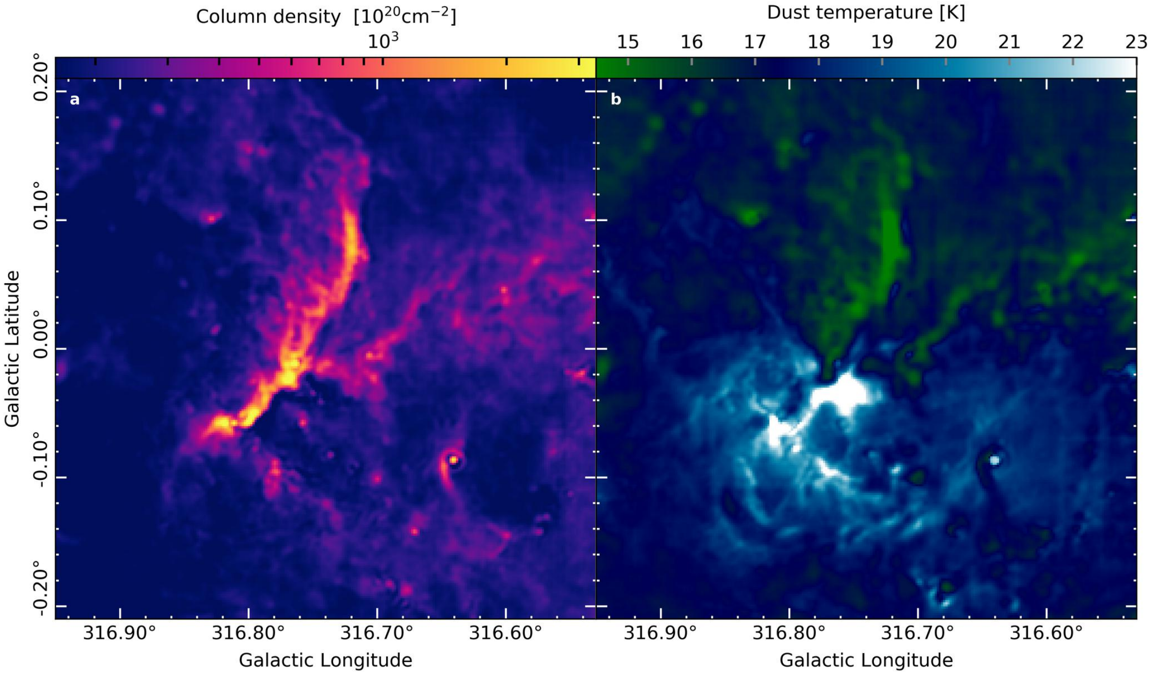

Figure 3.3. H_2 column density map **(a)** and dust temperature map **(b)** of the G316.75 star forming region derived using PPMAP on *Herschel* observations. Image amended from (Watkins et al. 2019).

only a few percent so the uncertainty in H_2 column density is still dominated by the dust emissivity law (Roy et al. 2014).

On simulated data, PPMAP reproduces the column densities a factor of two times better than traditional SED fitting methods (Marsh et al. 2015) and observations used for PPMAP do not need to be convolved to the lowest resolution for this technique to work. Therefore, this method is more powerful than traditional single-temperature SED techniques, not only for its potential to better characterise column densities, but also because PPMAP offers the higher resolutions that are crucial for investigating that impact feedback has at smaller scales, as shown in Fig. 3.3. For a full account of this method see Marsh et al. (2015).

A third way N_{H_2} can be calculated is to use line emission from two isotopologues in LTE, where one is optically thin and one is optically thick. One such isotopologue pair is ^{12}CO and ^{13}CO. Therefore, the following method to measure N_{H_2}, described in detail in Wilson et al. (2009), will be summarised below in relation to ^{12}CO (1–0) and ^{13}CO(1–0).

N_{H_2} can be calculated by relying on the fact that the brightness temperature of an optically thin line in LTE is proportional to the column density. For linear molecules emitting dipole radiation in LTE (which allows one to set $T_\mathrm{k} = T_\mathrm{ex}$), the total column density, N_tot of the molecules along the line of sight is given by:

$$N_\mathrm{tot} \simeq \frac{N_J}{2J+1} \frac{k_\mathrm{B} T_\mathrm{ex}}{h B_0} \mathrm{e}^{\frac{h B_0 J(J+1)}{(k_\mathrm{B} T_\mathrm{ex})}} \tag{3.2}$$

where N_J is the column density measured for the transition $J+1$ to J, B_0 is the rotational constant of the molecule and $k_\mathrm{B} T_\mathrm{ex}/(h B_0)$ is the partition function when $T_\mathrm{ex} \gg h B_0 / k_\mathrm{B}$. N_J can be calculated by integrating Eq. 2.29 over the line of sight, rearranging for N_J and substituting variables using equations 2.32–2.34). Doing this, one gets:

$$N_\mathrm{tot} \approx \frac{8\pi\nu_0^3}{A_\mathrm{ul} c^3} \frac{k_\mathrm{B}}{h B_0} \frac{\mathrm{e}^{\frac{h B_0 J(J+1)}{(k_\mathrm{B} T_\mathrm{ex})}}}{(2J+3)} \frac{T_\mathrm{ex} \int \tau(v)\, \mathrm{d}v}{1 - \mathrm{e}^{-h\nu_0/(k_\mathrm{B} T_\mathrm{ex})}} \tag{3.3}$$

where $\tau(v)$ has been integrated over the line of sight velocity of the emitting gas. When optically thin:

$$T_\mathrm{ex} \tau(v) \approx \frac{\tau_0}{1 - \mathrm{e}^{-\tau_0}} T_\mathrm{B}(v) \tag{3.4}$$

where τ_0 is the optical depth at the centre of the line and T_B is the brightness temperature. Therefore to measure the column density, one needs a measurement for T_B, T_ex, and τ_0.

When observing a radio source, T_B is given by:

$$T_\mathrm{B}(\nu) = T_\mathrm{B}(0) \mathrm{e}^{-\tau_\nu(s)} + T\left(1 - \mathrm{e}^{-\tau_\nu(s)}\right) \tag{3.5}$$

where Eq. 3.5 is the brightness temperature equivalent to Eq. 2.6. The brightness temperature from the source only is given by:

$$T_{\mathrm{B}}(\nu) = T_0\left[\frac{1}{\mathrm{e}^{T_0/T_{\mathrm{ex}}}-1} - \frac{1}{\mathrm{e}^{T_0/T_{\mathrm{bg}}}-1}\right]\left(1-\mathrm{e}^{-\tau_\nu(v)}\right) \tag{3.6}$$

where $T_0 = h\nu/k_{\mathrm{B}}$ and T_{bg} is the background temperature, which is usually set equal to the CMB temperature, 2.73 K. The simplest way to measure T_{ex} using Eq. 3.6 requires that the emission is optically thick. But to measure the optical depth, the simplest method requires that the emission is optically thin. Since emission from a single rotational transition cannot be both optically thin and thick from the same volume of gas, a compromise is made by using isotopologue pairs such as ^{13}CO (1–0) and ^{12}CO (1–0). If one assumes that ^{12}CO and ^{13}CO are in LTE, are emitting from the same volume of gas, that the excitation temperature is the same for both isotopologues, and that ^{12}CO is always optically thick while ^{13}CO is always optically thin, ^{12}CO (1–0) and ^{13}CO (1–0) can be used to calculate T_{ex} and τ_0 respectively. Therefore, this method works best when studying velocity coherent, isothermal, homogenous objects.

When optically thick, Eq. 3.6 is no longer dependent on τ_ν. Therefore, after substituting the known properties of ^{12}CO (1–0) in Eq. 3.6 and rearranging for T_{ex}, T_{ex} is given by:

$$T_{\mathrm{ex}} = 5.53\,\mathrm{K}\Big/\ln\left[1+\frac{5.53\,\mathrm{K}}{T_{\mathrm{b,peak}}^{^{12}\mathrm{CO}}+0.84}\right] \tag{3.7}$$

where T_0=5.53 K for the transition ^{12}CO (1–0), $T_{\mathrm{b,peak}}^{^{12}\mathrm{CO}}$ is the peak brightness temperature measured for ^{12}CO (1–0) at the line centre and $T_0/[\mathrm{e}^{T_0/T_{\mathrm{bg}}}-1]$=0.84 assuming that T_{bg} is described by the CMB radiation field only.

When optically thin, Eq. 3.6 can be rearranged for the opacity. For ^{13}CO (1–0), the line centre opacity is given by:

$$\tau(\nu_0) = -\ln\left[1-\frac{0.189T_{\mathrm{b,peak}}^{^{13}\mathrm{CO}}}{(\mathrm{e}^{5.29/T_{\mathrm{ex}}}-1)^{-1}-0.17}\right] \tag{3.8}$$

where T_0=5.29 K for ^{13}CO, $1/T_0$=0.189, $1/[e^{T_0/T_{\rm bg}}-1]$=0.17 and $T_{\rm b,peak}^{\rm 13CO}$ is the peak brightness temperature of ^{13}COat the line centre.

With both of these defined, the column density in Eq. 3.3 can be calculated for ^{13}CO (1–0):

$$N_{^{13}\rm CO} \cong 2.5 \times 10^{14}\ \rm cm^{-2}\ K^{-1}\ (km/s)^{-1} \frac{\tau_0 \int T_{\rm b}^{\rm 13CO}(v){\rm d}v}{[1-{\rm e}^{-\tau_0}][1-{\rm e}^{-5.29/T_{\rm ex}}]} \tag{3.9}$$

where $N_{^{13}\rm CO}$ is the column density of ^{13}CO in cm^{-2}, τ_0 is the opacity at $T_{\rm b,peak}^{\rm 13CO}$, $\int T_{\rm b}^{\rm 13CO}(v){\rm d}v$ is the integrated intensity and the velocity, v has units km s^{-1}. In this calculation, the values for A_{10} and ν_0 are given in Table 3.1 and B_0=5.51×10^{10} s^{-1} for ^{13}CO. I note that the constant used at the beginning of Eq. 3.9 differs from Wilson et al. (2009) since they use an older value for the electric dipole moment of ^{13}CO when calculating A_{10} in Eq. 15.24. Wilson et al. (2009) use a value of 0.1 debyes, given in Townes & Schawlow (1975), but more recent measurements of this indicate the value is 0.11046 debyes (Goorvitch 1994).

To convert $N_{^{13}\rm CO}$ to $N_{\rm H_2}$, we first convert $N_{^{13}\rm CO}$ to the column density of ^{12}CO ($N_{^{12}\rm CO}$) and then convert this to $N_{\rm H_2}$. It is done this way since the abundance ratio of ^{13}CO to ^{12}CO has been shown to be more dependent on the environment (Langer & Penzias 1990). In local neighbourhood clouds, the ratio 1/60 is most commonly used, however Szűcs et al. (2014) show that the abundance ratio can also vary significantly within a single molecular cloud. Using a hydrodynamical simulation of a young, 10^4 M$_\odot$ molecular cloud (i.e., a cloud without stars and without stellar feedback), Szűcs et al. (2014) show that the abundance ratio can vary from 1/60 to 1/20 due to chemical fractionation. The simulation includes a chemical network and models a surrounding interstellar radiation field (ISRF). Szűcs et al. (2014) show this result over a range of cloud densities (300, 1000 cm^{-3}), metalicities (0.3, 0.6, 1 Z$_\odot$) and incident ISRFs (0.1, 1, 10 G_0). Fortunately, they show that the ratio's variation correlates well with $N_{^{13}\mathrm{CO}}$. By plotting the change in abundance ratio as a function of $N_{^{13}\mathrm{CO}}$, Szűcs et al. (2014) were able to fit a polynomial to the data and give the coefficients of their fit in their Table 3. Therefore, by inputting $N_{^{13}\mathrm{CO}}$ into the polynomial function, an abundance ratio corrected for chemical fractionation can be calculated and used to convert $N_{^{13}\mathrm{CO}}$ to $N_{^{12}\mathrm{CO}}$. After converting $N_{^{13}\mathrm{CO}}$ to $N_{^{12}\mathrm{CO}}$, we can calculate N_{H_2} using the abundance ratio of ^{12}CO to H_2, which is called the X_{CO} factor ($X_{\mathrm{CO}}{\sim}1{\times}10^{-4}$). However, this assumes that ^{12}CO has constant fractional abundance with H_2, but simulations also show the X_{CO} is rarely the constant within young molecular clouds (Peñaloza et al. 2018).

The advantage of using line emission to calculate N_{H_2}, compared to dust continuum, is that it can exclude background and foreground clouds since they exist at separate line of sight velocities. However, when considering that molecular clouds are not velocity coherent, isothermal, homogenous regions, and each conversion, from $N_{^{13}\mathrm{CO}}$ to $N_{^{12}\mathrm{CO}}$ and then finally to N_{H_2}, adds additional uncertainties, one needs to be cautious when analysing N_{H_2} derived with these assumptions. Szűcs et al. (2016) predict that even after correcting for chemical fractionation, N_{H_2} is usually underestimated by a factor of 2. Consequentially, it is usually preferable to use dust continuum to measure N_{H_2} when possible.

3.2 Identifying column density features

Observations with the *Herschel space telescope* have shown that stars preferentially form in filaments (André et al. 2010b; Könyves et al. 2015). Below, I discuss two methods used to identify filaments and fragments using column density measurements. The method for filament extraction is discussed in more depth than fragment identification extraction since I have written the analysis myself.

Filaments can be identified by tracing connected crest points at the centre of a given filamentary structure (Schisano et al. 2014; Williams et al. 2018; Orkisz et al.

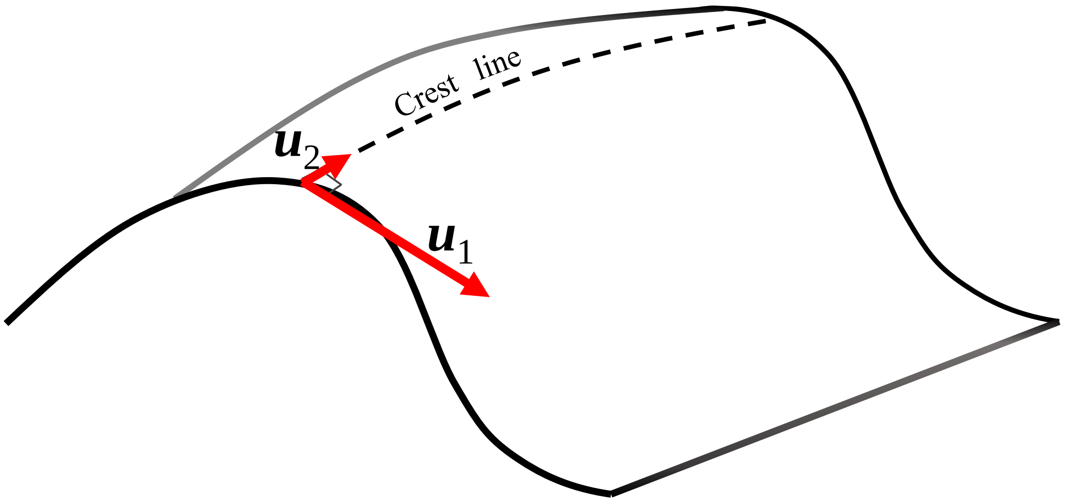

Figure 3.4. Diagram showing the relationship between a 2D surface, the eigenvectors $\boldsymbol{u}_1$ and $\boldsymbol{u}_2$ of this surface and the crest of the surface. $\boldsymbol{u}_1$ points in the direction of maximum curvature and $\boldsymbol{u}_2$ points in the direction of the minimum curvature. $\boldsymbol{u}_1$ and $\boldsymbol{u}_2$ are always perpendicular.

2019; Schisano et al. 2019). The simplest way to do this is to find the maximum and minimum curvature at all points of an image by calculating the Hessian matrix, **H**, at all points:

$$\mathbf{H} = \nabla^2 f(x,y) = \begin{bmatrix} \dfrac{\partial^2 f(x,y)}{\partial y^2} & \dfrac{\partial^2 f(x,y)}{\partial x \partial y} \\ \dfrac{\partial^2 f(x,y)}{\partial y \partial x} & \dfrac{\partial^2 f(x,y)}{\partial y^2} \end{bmatrix}$$

where f is some 2d surface in the x and y directions. The maximum and minimum curvatures are always orthogonal and independent from each other, therefore the directions of the maximum and minimum curvature can be found by finding the eigenvectors ($\boldsymbol{u}_1$ and $\boldsymbol{u}_2$) of **H**. The corresponding eigenvalues (ε_1 and ε_2) then indicate the strength of this curvature and whether the curvature is increasing or decreasing (see Fig. 3.4).

With this, one can identify filaments as regions of a map where at least one of the eigenvalues, for instance ε_1, is < 0 and where $|\varepsilon_1| > |\varepsilon_2|$ (i.e., the curvature along the $\boldsymbol{u_1}$ direction is larger, as indicated in Fig. 3.4). This does not identify the crests, but all points of negative curvature; any increasing slope is identified with this method. To trace just the single spine connecting the crests (i.e., their peaks) a skeletonisation method is needed, such as a medial axis transform.

When applying the Hessian method to a 2D grid of values, $f(x, y)$ (as opposed to a smoothly continuous surface), the 2nd partial derivatives can only be estimated. The simplest way to do this is by performing the central difference approximation to all grid points in f in both the x and y directions, twice. For a grid point ij that has position (x_i, y_j), to first order, directional derivative along the positive x direction can be estimated as:

$$\frac{\partial f}{\partial x} \simeq \frac{f_{\mathrm{i}+1,j} - f_{\mathrm{i}-1,j}}{x_{\mathrm{i}+1} - x_{\mathrm{i}-1,j}} = \frac{f_{\mathrm{i}+1,j} - f_{\mathrm{i}-1,j}}{2\theta} \tag{3.10}$$

where θ is the grid spacing. If instead, the goal is to obtain a reliable skeleton of the main filamentary structures, and not identify the full filament network of a region, one can first convolve the original image to reduce noise. Additionally, one can eliminate small filamentary features by normalising the eigenvalues between -1 to 1, and requiring that the eigenvalue ε_1, is set to a value < 0. This ensures only the most prevalent structures are selected. To see the difference this can make, I show four images, one using the original image and regular conditions, one where the image is convolved to a resolution of $17''$, one where the largest absolute eigenvalue must be < -0.15 and one where the image has been convolved to $17''$ and the largest absolute eigenvalue must < -0.15 on Fig. 3.5

Fragments can be identified using dendrograms (Rosolowsky et al. 2008). Dendrograms are a graph based method that traces the morphological hierarchy of an image based on isocontours. The three possible structures within dendrograms are leaves, branches and trunks. The structures at the top of the hierarchy are called

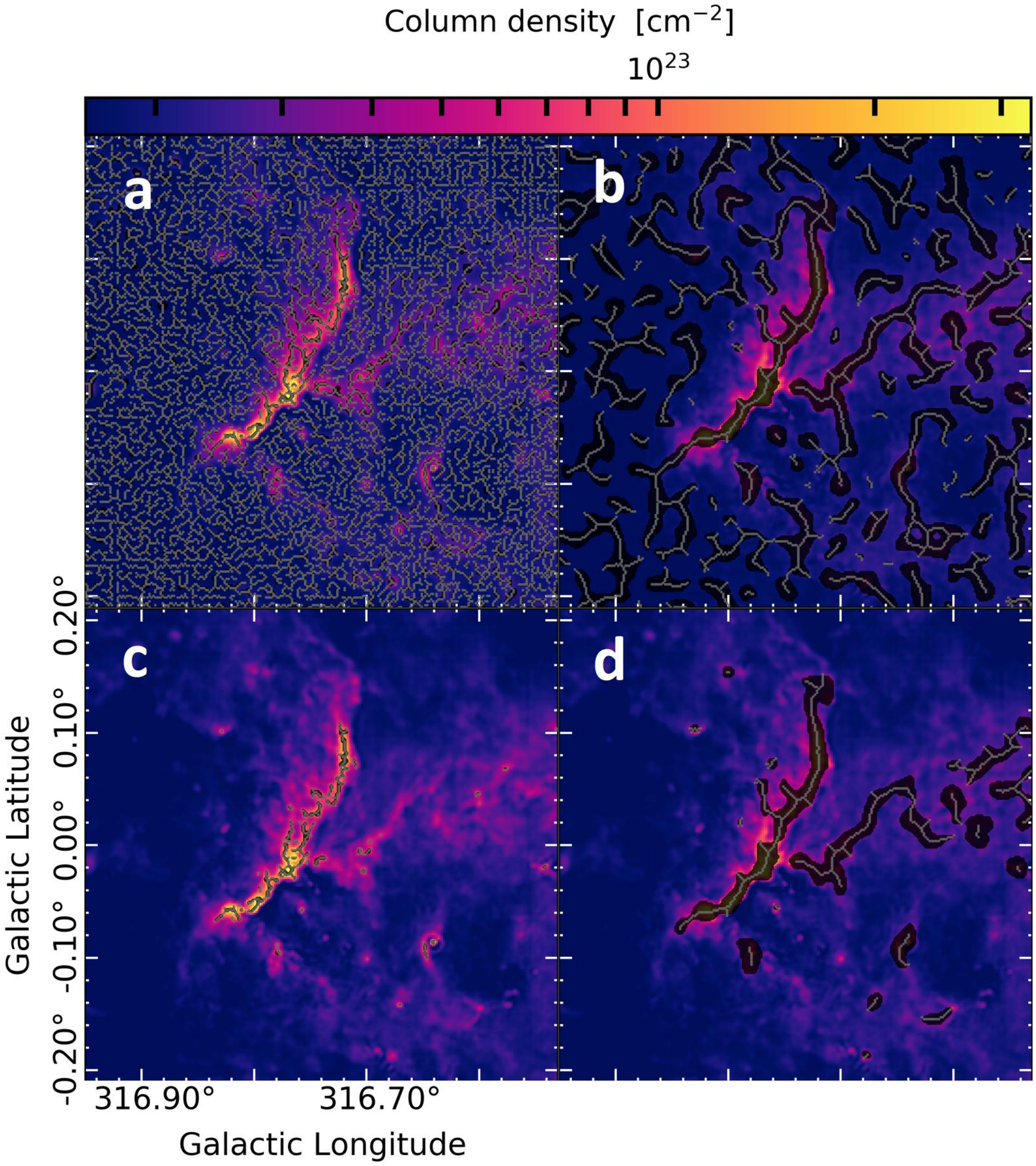

Figure 3.5. Diagram showing how the Hessian method recovers different features due to using different parameters to remove noise. (**a**:) The original image and regular conditions, (**b**:) image is convolved to a resolution of 17″, (**c**:) the largest absolute eigenvalue must be < -0.15 (**d**:) image has been convolved to 17″ and the largest absolute eigenvalue must < -0.15. Black shaded area are identified filaments and grey markers show the skeletonised spines of these filaments.

REDACTED

Figure 3.6. Example dendrogram structure. Each leaf represents the highest morphological structures. The contour than encompasses the leaves is called a branch. The contour that encompasses the entire image is called the trunk. The structures identified are dependent on what is chosen as the value of the lowest isocontour, the lowest amplitude of a significant structure between its local maximum and minimum, and the minimum size of a significant structure. Diagrams from `astrodendro` documentation (Rosolowsky et al. 2008).

leaves, any structure containing multiple leaves are called branches, and the structure containing all branches and leaves is called the trunk (see fig. 3.6). Therefore, leaves represent the position of fragments (i.e., clumps in the context of the G316.75 study). The structure of the dendrogram is controlled by three basic parameters, the value of the lowest isocontour, the lowest amplitude of a significant structure between its local maximum and minimum, and the minimum size of a significant structure. These parameters need to be tuned to the image to correctly identify meaningful structures, otherwise the dendrogram will identify noise peaks or will underestimate the amount of features present. Usually, the three parameters are tuned based on the resolution of the image and the rms noise of the image.

3.3 Measuring Hii related properties

High-mass stars create ionised gas around them which we call Hii regions. If we neglect helium (and all other heavier elements), the rate at which an optically thin Hii region emits free-free photons is proportional to:

$$\int_{\mathrm{H\,II}} n_{\mathrm{e}}(\boldsymbol{r}) n_{\mathrm{p}}(\boldsymbol{r})\, \mathrm{d}(\boldsymbol{r}) = \overline{n_{\mathrm{e}}^2} V_{\mathrm{H\,II}} \tag{3.11}$$

where $n_{\rm p}$ is the number density of protons, $n_{\rm e}$ is the number density of electrons and $V_{\rm H{\small II}}$ is the volume of the Hii region. The expression on the right follows from setting $n_{\rm p} = n_{\rm e}$, where $\overline{n_{\rm e}^2}$ is the volume average of $n_{\rm e}^2(\boldsymbol{r})$. The constant of proportionality is a function of gas kinetic temperature, varying approximately as $T^{3/4}$, i.e., less emission at higher temperatures. Therefore by measuring this emission when it is optically thin, one can determine the properties of Hii regions and thereby the stars needed to reproduce the emission. Furthermore, the size of an Hii region can be used to estimate their age by calculating the time needed for a newly created, over-pressurised region to expand to the size observed.

3.3.1 Stellar cluster mass from radio emission

If one assumes the Hii region has been created by a single ionising source, one can estimate its stellar mass by comparing the number of hydrogen ionising photons ($N_{\rm ly}$) needed to create the Hii region, to a model predicting stellar mass v.s $N_{\rm ly}$ such as Panagia (1973), Vacca et al. (1996) or Sternberg et al. (2003). Using the properties of the Hii region, $N_{\rm ly}$ is given by:

$$N_{\rm ly} = \frac{4\pi}{3}\alpha_{\rm B} R_{\rm S}^3 n_{\rm e}^2 \tag{3.12}$$

This is the equation for the Strömgren radius (Eq. 1.10) rearranged for $N_{\rm ly}$. The only unknown in Eq. 3.12 is $n_{\rm e}$ but the monochromatic flux density of the Hii region, F_ν is $\propto n_{\rm e}^2$.

Therefore $n_{\rm e}$ can be calculated by measuring the flux density, F_ν, of the Hii region, and the expression for F_ν can be calculated by integrating I_ν, given in Eq. 2.26. This leads to the following equation for $N_{\rm ly}$ (Martín-Hernández et al. 2005; Panagia & Walmsley 1978):

$$N_{\rm ly} = 7.603 \times 10^{46} \left(\frac{F_\nu}{1{\rm Jy}}\right) \left(\frac{T_{\rm e}}{10^4{\rm K}}\right)^{-0.33} \left(\frac{d}{1{\rm kpc}}\right)^2 \times b(T_{\rm e}, \nu)^{-1}\,{\rm s}^{-1} \tag{3.13}$$

where $T_{\rm e}$ is the electron temperature, normally $\approx 10^4$ K for ionised gas, d is the heliocentric distance to the region, and $b(T_{\rm e}, \nu)$ is related to gaunt factor, $\langle g_{\rm ff} \rangle$, and is given by:

$$b(T_{\rm e}, \nu) = 1 + 0.3195 \log_{10}\left(\frac{T_{\rm e}}{10^4{\rm K}}\right) - 0.213 \log_{10}\left(\frac{\nu}{1{\rm GHz}}\right) \tag{3.14}$$

This method assumes that the HII region is spherical, optically thin, homogeneous and that all the ionising photons produced are used to ionise hydrogen. However $N_{\rm ly}$ can be absorbed by dust, can ionise other atoms, such as helium, or can escape the HII region (Binder & Povich 2018). Consequently $N_{\rm ly}$ is usually underestimated resulting in a smaller estimate for the mass of the star.

Rather than attributing the $N_{\rm ly}$ to one dominant ionising object, one can instead calculate the cluster mass needed to reproduce this emission. Following Lee et al. (2016):

$$M_* = 1.37 N_{\rm ly} \times 1.6 \times 10^{-47}\, M_\odot \tag{3.15}$$

where 1.37 accounts for dust absorption and 1.6×10^{-47} is the normalisation factor for the number of ionising photons needed for a star cluster to power an HII region. This assumes that the IMF is fully sampled. The IMF used to make in this model is a modified Muench IMF since Eq. 3.15 depends more on the high-mass end of the IMF slope, and the Muench IMF better estimates this slope (Muench et al. 2002; Murray & Rahman 2010).

REDACTED

Figure 3.7. Diagram showing how the pressure in Hii regions change as a function of radius (x axis) and the number of ionising photons (the colour bar). Coloured circular markers show these properties – with – for real Hii regions and dashed coloured line are isolines representing the number of ionising photons. Over-plotted with black dashed lines are age isochromes (in Myr) modelled as a function of the other three parameters. This allows one to determine the age of an Hii region using a combination of its measured size, the number of ionising photons and its pressure. Plot is presented in Tremblin et al. (2014).

3.3.2 Dynamical age from the size of Hii regions

The dynamical age of an Hii region can be estimated by calculating how long it takes an Hii region of radius, r, and internal pressure P_{II}, to expand into a uniform molecular cloud. Analytically, a solution for this is given by: (Spitzer 1978; Dyson & Williams 1980):

$$\frac{c_{\mathrm{II}}t}{R_{\mathrm{S}}} = \frac{4}{7}\left(\left(\frac{r}{R_{\mathrm{s}}}\right)^{7/4} - 1\right) \tag{3.16}$$

where r is the current radius, c_{II} is the sound speed of the ionised gas and t is the time. However, this solution neglects the pressure of the surrounding medium, and so the Hii region never stops expanding in this solution. A more realistic model describing the expansion of HII was calculated in Tremblin et al. (2014). Tremblin et al. (2014) used numerical models to find the impact that a turbulent and clumpy medium has on the expansion of the HII region. Moreover, they use these models to construct isochrones describing the HII region as a function of their radius, pressure, and ionisation rate and show this in fig. 3.7. By doing this, one can calculate the age of an HII region by finding the intersection of the HII region size, pressure and N_{ly} rate on fig. 3.7.

3.3.3 Calculating amount of ionised gas

The amount of gas ionised can be estimated by assuming that the number density of ionised hydrogen atoms equals the number density of electrons. Doing this, the amount of ionised gas is:

$$M_{\mathrm{ion}} = \frac{4}{3}\pi r^3_{\mathrm{H\textsc{ii}}} n_{\mathrm{e}} m_{\mathrm{H}} \tag{3.17}$$

where M_{ion} is the mass of the ionised gas, $r_{\mathrm{H\textsc{ii}}}$ is the radius of the HII region and m_{H} is the mass of hydrogen.

3.3.4 Expansion of HII regions in filaments

In the context of this thesis, I studied the high-mass star forming ridge, G316.75, in which several O-stars were found. It is a high-aspect ratio, filamentary cloud and has formed an HII region with a dynamical age of ~2 Myr. To account for its morphology when modelling the expansion of the HII region present, the gas is modelled as a cylinder of radius R_{cyl} with has a mean density n_{H} within which a point source is embedded. The point source represents the O-star and so emits ionising photons isotropically $\mathcal{N}_{\mathrm{ly}}$ but illuminates only the edges of the cylinder (due to the symmetry of the model, only one edge is modelled). If no recombinations take

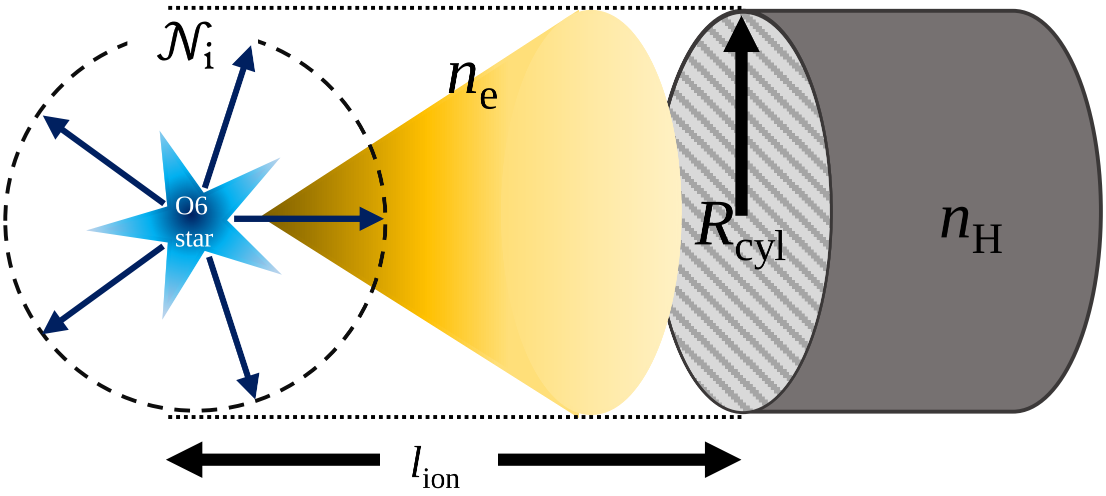

Figure 3.8. Diagram illustrating an ionisation model of a uniformly dense, cylinder. $\mathcal{N}_\mathrm{i}$ is the total amount of ionising photons emitted by an O6 star, l_ion is the length ionised by the O6 star, n_e is the density of electrons, R_cyl is the radius of the filament and, n_H is the mean hydrogen density.

place, the rate of ionising photons that reaches the cross section of the cylinder is given by:

$$\mathcal{N}_\mathrm{ly,cyl} = \mathcal{N}_\mathrm{ly}\frac{\pi R_\mathrm{cyl}^2}{4\pi l_\mathrm{ion}^2} \tag{3.18}$$

where l_ion is the distance between the star and the edge of the cylinder. A more realistic scenario however is one that includes recombination between ionised hydrogen and electrons. From Eq. 1.9, the recombination rate per unit volume is given by $\mathcal{R} = \alpha_\mathrm{B} n_\mathrm{e}^2$ Therefore, for a cylinder, the total recombination rate will equal the product of $\mathcal{R}$ and the conic volume, defined between the position of the ionising source and the surface area of the cylinder edge. Assuming that the electron density between the ionising source and the cylinder cross section is constant, the rate of ionising photons that reaches the cross section of the cylinder is given by:

$$\mathcal{N}_\mathrm{ly,cyl} = \pi R_\mathrm{cyl}^2 \left(\frac{\mathcal{N}_\mathrm{ly}}{4\pi l_\mathrm{ion}^2} - \frac{l_\mathrm{ion}\mathcal{R}}{3}\right) \tag{3.19}$$

In Eq. 3.19, it has has also been assumed that recombinations are instantaneous reionised since the timescale for ionisation is much shorter than for recombination. Finally, one can write the change in $l_{\rm ion}$ as a function of the change in time as:

$$\mathrm{d}l_{\rm ion} = \frac{\mathcal{N}_{\rm ly,cyl}}{\pi R_{\rm cyl}^2 n_{\rm H}} dt = \frac{1}{n_{\rm H}} \left(\frac{\mathcal{N}_{\rm ly}}{4\pi l_{\rm ion}^2} - \frac{l_{\rm ion}\alpha_{\rm B} n_{\rm e}^2}{3} \right) dt. \tag{3.20}$$

where $n_{\rm H}$ is the number density of neutral hydrogen at the cylinder cross section. Using Eq. 3.12, we can simplify Eq. 3.20 to:

$$\mathrm{d}l_{\rm ion} = \frac{n_{\rm e}^2 \alpha_{\rm B}}{n_{\rm H}} \left(\frac{R_{\rm s}^3}{3 l_{\rm ion}^2} - \frac{l_{\rm ion}}{3} \right) \mathrm{d}t \tag{3.21}$$

By using the product rule, Eq. 3.21 reduces to:

$$\frac{\mathrm{d}(l_{\rm ion}^3)}{\mathrm{d}t} \times \frac{1}{R_{\rm s}^3 - l_{\rm ion}^3} = \frac{n_{\rm e}^2 \alpha_{\rm B}}{n_{\rm H}} \tag{3.22}$$

which can now be integrated in order to obtain $l_{\rm ion}(t)$:

$$l_{\rm ion}(t) = R_{\rm s} \left[1 - \exp\left(-\frac{n_{\rm e}^2 \alpha_{\rm B}}{n_{\rm H}} t \right) \right]^{\frac{1}{3}} \tag{3.23}$$

3.4 Assessing the stability of ridges

In this section, I describe the methods used in this thesis to measure the energy balance and the stability of the ridge. In the context of the G316.75 massive star forming ridge, I describe how to calculate its fragmentation and radial stability using a range of gas density tracers. By doing this, one can investigate how these properties change with density. When feedback is present, this allows one to assess the impact that stellar feedback has on the star forming ability of the region over different gas density regimes.

3.4.1 MEASURING STAR FORMING ABILITY OF FILAMENTARY CLOUDS

Fragmentation and the radial stability of a star forming region is determined by the balance of gravity and pressure. If thermal motions are the only contributors to the kinetic pressure of a cloud, then $\sigma_{\mathrm{gas}} = \sigma_{\mathrm{th}} = \sqrt{\frac{k_{\mathrm{B}}T}{\mu m_{\mathrm{H}}}}$, where T is the gas temperature and σ_{th} is thermal sound speed. If turbulence also contributes to the kinetic pressure then $\sigma_{\mathrm{gas}} = \sigma_{\mathrm{eff}} = \sqrt{\sigma_{\mathrm{th}}^2 + \sigma_{\mathrm{turb}}^2}$ where σ_{turb} is the turbulent component of the velocity dispersion. The effective velocity dispersion σ_{eff} can be calculated according to the following equation from Fuller & Myers (1992):

$$\sigma_{\mathrm{eff}}^2 = \sigma_{\mathrm{mol}}^2 + k_{\mathrm{B}}T\left(\frac{1}{\mu m_{\mathrm{H}}} - \frac{1}{m_{\mathrm{mol}}}\right) \tag{3.24}$$

where σ_{mol} is the observed velocity dispersion for a given rotational transition, and m_{mol} is the mass of the corresponding molecule. To see if σ_{eff} changes according to the density traced, one can calculate σ_{eff} for a variety of rotational transitions that cover a range of critical densities, such as ^{13}CO, NH$_3$ and N$_2$H$^+$, which trace low, intermediate and high gas densities.

3.4.2 GAS DENSITY TRACERS

In the context of the study performed on the G316.75 massive star forming ridge, we used ^{13}CO (J=1–0), NH$_3$ (1,1) and N$_2$H$^+$ (J=1–0) to trace low, medium and high density gas respectively. We used ^{12}CO to trace the most diffuse gas, but because it is usually optically thick in high-mass star forming regions, it is unsuitable for tracing the full gas kinematics of such regions.

^{12}CO (1–0)

^{12}CO is a diatomic linear molecule and is the next most abundant molecule to H$_2$. But unlike H$_2$, ^{12}CO is polar, which allows for rotational dipole radiation. The lowest transition, (J=1–0) occurs at T_0=5.53 K and has a low critical density of 2.5×10^3 cm^{-3}

Table 3.1. Summery of rotational transitions and their critical densities calculated using Eq. 2.37 assuming the background radiation field is given by the CMB. Collisional rates for ^{12}CO (J=1–0) and ^{13}CO are calculated in (Yang et al. 2010), collisional rates for N_2H^+ are given in (Schöier et al. 2005), and collisional rates for NH_3 are calculated in (Danby et al. 1988).

Rotational transition	Rest frequency of transition (GHz)	$A_{\rm ul}$ (s^{-1})	$C_{\rm ul}/n$ (s^{-1} cm^{-3})	$n_{\rm crit}$ (cm^{-3})
^{12}CO (J=1–0)	115.271	7.203×10^{-8}	3.249×10^{-11}	2500
^{13}CO (J=1–0)	110.201	6.294×10^{-8}	3.249×10^{-11}	2200
N_2H^+ (J=1–0)	93.174	3.628×10^{-5}	2.3×10^{-10}	1.88×10^{5}
NH_3 (1,1)	23.694	1.712×10^{-7}	8.6×10^{-11}	3300

(see Table 3.1). As a result, ^{12}CO (J=1–0) is useful for tracing cold, diffuse H_2. ^{12}CO (1–0) emission is detected readily throughout the Milky Way and external galaxies (Dame et al. 1987; Nishiyama & Nakai 2001), and its high abundance combined with a low critical density makes ^{12}CO (1–0) ideal for tracing proto-stellar outflows in the line wings of spectra. Although, its large abundance results in ^{12}CO emission becoming optically thick, limiting analysis to the outer surface of molecular clouds, or to molecular clouds with low densities. When optically thick, ^{12}CO (1–0) can trace densities as low as $\sim$ 200 cm^{-3}. Additionally, ^{12}CO it a reactive molecule, and binds strongly to dust at cold temperatures below 15 K. This reduces the abundance of ^{12}CO in the coldest, densest regions and limits our ability to characterise column densities and kinematics of dense cores. So when used as a gas density tracer in a star forming region, it should be used to trace the lowest density gas.

^{13}CO (1–0)

^{13}CO, the next most abundant isotopologue of ^{12}CO is $\sim$60 times less abundant than ^{12}CO in the local neighbourhood (Langer & Penzias 1990). Even though the critical density of ^{13}CO (J=1–0) is approximately the same as ^{12}CO (J=1–0) (see Table 3.1), its lower abundance reduces the chance that the emission will become optically thick. Therefore, ^{13}CO (J=1–0) can be used in place of ^{12}CO to understand the kinematics of diffuse gas and as a probe of column density when ^{12}CO is optically thick. For this thesis, I assume that the ^{13}CO emission traces low density gas and that ^{13}CO (J=1–0) is always optically thin (a good assumption until $\tau \sim 2$) so that the kinematics traced represent the gas motions for the entire column.

N_2H^+ (J=1–0)

N_2H^+ is a triatomic linear cation found in dense molecular gas. The N_2H^+ (J=1–0) transition has a critical density of 10^5 cm^{-3} (see Table 3.1), so it is able to trace densities much higher than CO (1–0) transitions. N_2H^+ has been shown to increase in abundance when CO depletes from the gas phase onto dust particles (Bergin et al. 2001; Pagani et al. 2005). The reason for this is not known, but recent laboratory experiments indicate that the freeze-out of CO can create a thin layer dust, which reduces the binding energy between N_2 and the dust (Nguyen et al. 2018). This, along with the fact that CO is the main destruction pathway of N_2H^+, causes the abundance of N_2H^+ to increase as CO depletes. Therefore, N_2H^+ (J=1–0) is a useful tracer of cold and dense H_2, and can probe gas at densities where CO stops being as useful. Additionally N_2H^+ (1–0) has 15 allowed hyperfine transitions though only 7 are resolvable. This is advantageous for tracing high densities since hyperfine structure can spread the emission over a larger frequency range, which helps keep the emission optically thin even though the densities traced with N_2H^+ are high. Therefore in this thesis, N_2H^+ is used to trace the kinematics of high density gas.

NH_3 (1,1)

Unlike aforementioned molecules, NH_3 is a non-linear molecule, meaning it contains a 3D structure. The nitrogen is connected to three hydrogen atoms in a trigonal pyramidal arrangement. As a result, it has three axes of rotation, though two of these are degenerate where the non-degenerate axis is the rotation of the molecule about the nitrogen atom. As a result, the rotation of NH_3 is represented by two quantum numbers, J for the total angular momentum, and K, which is the projection of J

onto the non-degenerate axis, and is written as (J,K). This leads to two alignments of the nitrogen atom above and below to the hydrogen plane, with identical values for J and K. Although, these orientations exist at slightly different energies and so they can emit or absorb photons. These are called inversion transitions, since when this transition occurs, the nitrogen quantum mechanically tunnels through to the other side of the plane. To denote this transition, we write (J,K) after the molecule. NH_3 also contain hyperfine structure, with 18 components though typically only 5 are resolvable. Just like N_2H^+, this reduces the chance that the emission becomes optically thick. NH_3 traces gas at densities $\sim 3 \times 10^3$ cm^{-3} (see Table 3.1) but because the transition occurs at a low frequency ($h\nu_{(1,1)}/k_{\rm B} < T_{\rm bg}$), higher densities than $n_{\rm crit}$ are needed to thermalise the emission. As a result, NH_3 (1,1) tends to trace $> 10^4$ cm^{-3} (Shirley 2015).

For this thesis, NH_3 is used in place of N_2H^+ to tracer higher density gas when N_2H^+ data is unavailable, but otherwise, NH_3 is used to trace gas at intermediate gas densities.

3.5 PROBING GAS KINEMATICS

Here, I describe the methods and tools one can use to probe the kinematics of a star forming region. In the context of this thesis, the kinematics traced include ^{13}CO (J=1–0), NH_3 (1,1), and N_2H^+ (J=1–0)—low transition rotational data—to probe low, medium and high density gas. By modelling the intensity structure of these datasets, one can study thermal and non-thermal motions in the gas, and changes in line of sight velocity.

3.5.1 GAUSSIAN LINE FITTING

Due to Doppler broadening (both from thermal and non-thermal motions), the appearance of optically thin rotational transitions can be described using a Gaussian

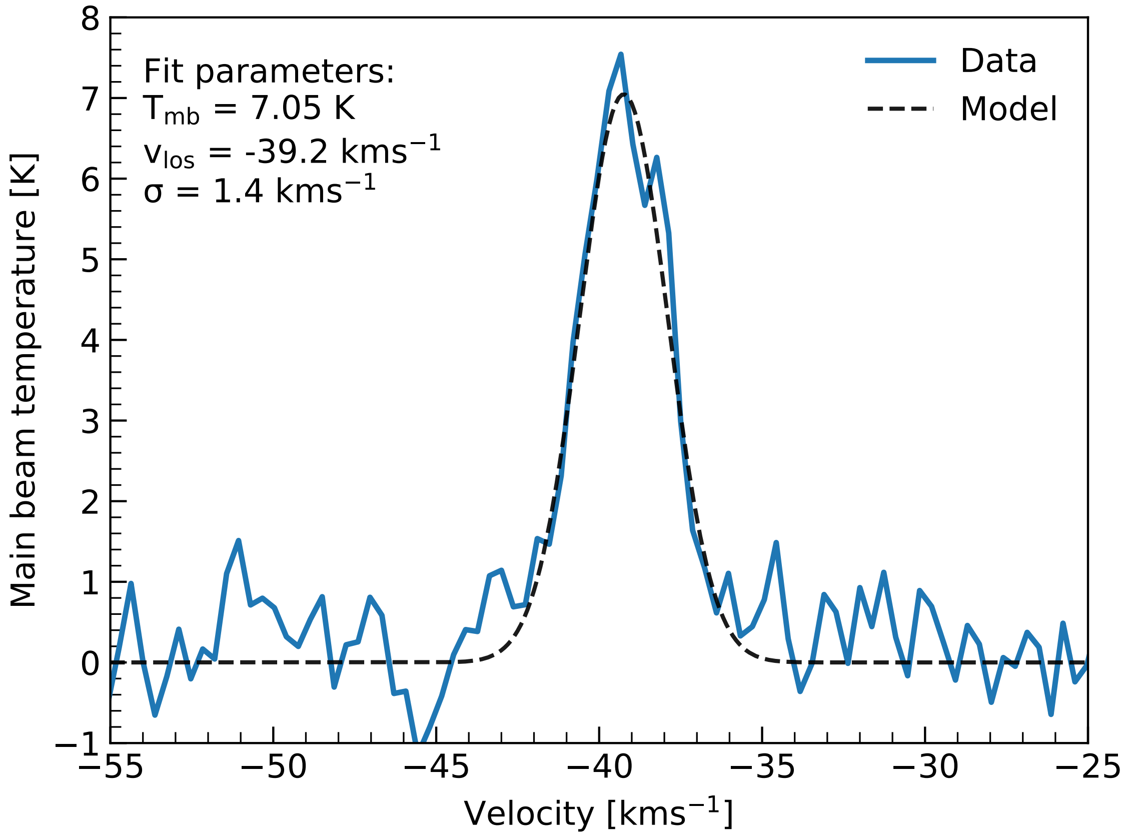

Figure 3.9. Example showing ^{13}CO(J=1–0) data (solid blue line) along with a model single Gaussian fit to the data (dashed black line). $T_{\rm mb}$ is the peak main beam temperature, $v_{\rm los} = v_{\rm peak}$ and is the velocity where $T_{\rm mb}$ peaks and σ is the velocity dispersion.

profile given by:

$$T_{\mathrm{mb}}(v) = T_{\mathrm{mb}}^{\mathrm{peak}} \exp\Big(- \frac{(v - v_{\mathrm{peak}})^2}{2\sigma^2} \Big) \tag{3.25}$$

where T_{mb} is the measured main beam temperature at the velocity v, v_{peak} is the position of the peak value of T_{mb} and σ is the velocity dispersion of the gas. To trace the gas kinematics of a given star forming region, one can use Eq. 3.25 to fit T_{mb}, v_{peak} and σ to every pixel. To fit these parameters, a least squares minimisation routine can be used. This method finds the best fit parameters by finding the nearest local minimum of the residuals between the model spectrum in Eq. 3.25, starting from some initial guess of the parameters. An example fit using this method is shown in Fig. 3.9.

3.5.2 FITTING HYPERFINE TRANSITIONS

Molecules that contain resolvable hyperfine transitions are useful for determining gas properties. The transitions can be measured from a single observation since they are closely spaced in frequency. Therefore, we can safely assume that the transitions occurred within the same gas volume. Additionally, the relative intensities, r_i, and the frequency separation, ν_i between different hyperfine components are fixed by quantum mechanics. Not only does this allow us to better constrain the velocity that the transition occurred at, but also allows us to measure the opacity and excitation temperature (and hence the kinetic temperature and the column density) from the difference in the observed relative intensities to the theoretical relative intensities.

To model the brightness temperature, and thereby the velocity and velocity dispersion of gas molecules containing hyperfine transitions, we assume that the opacity varies as a Gaussian. For optically thin emission, this is a fairly good assumption as $T_{\mathrm{B}}(v) \propto \tau(v)$ when optically thin (and $T_{\mathrm{B}}(v)$ is well approximated by a Gaussian). With this assumption, we can define the opacity of a single component, i, as:

$$\tau_i(v) = \tau_i^{\rm peak}{\rm exp}\bigg(- 4{\rm ln}2\Big(\frac{v - v_i^{\rm peak}}{\Delta v}\Big)^2\bigg) \tag{3.26}$$

where $\tau_i(v)$ is the opacity for the ith component, $\tau_i^{\rm peak}$ is the opacity at the centre of the component and $v_i^{\rm peak}$ is the velocity at the centre of the component. I note that the Gaussian has been defined in terms of its FWHM, Δv. If we assume that Δv is equal for all hyperfine components, and that the components do not overlap, the total opacity can now be defined as a sum of each component:

$$\tau_(v) = \sum_{i=1}^{N} \tau_i(v) \tag{3.27}$$

However, in Eq. 3.27, we know the velocity separation for each component. So rather than fitting each velocity separately, we can fit a single reference velocity and account for the relative velocity offset i.e., we replace $v_i^{\rm peak}$ with $v_i - v_{\rm ref}$, where $v_{\rm ref}$ is the reference velocity and v_i is the offset from this reference velocity for each component. Additionally, we can use the relative heights (r_i, which are also known) of each transition to define a single variable to represent each $\tau_i^{\rm peak}$:

$$C_1 = \frac{\sum_{i=1}^{N} \tau_i^{\rm peak}}{\sum_{i=1}^{N} r_i} \tag{3.28}$$

Therefore C_1 represents the sum of the peak opacities of each component weighted by the relative intensities between the hyperfine transitions. All together, this allows us to write:

$$\tau(v) = C_1 \sum_{i=1}^{N} r_i{\rm exp}\bigg(- 4{\rm ln}2\Big(\frac{v - v_i - v_{\rm ref}}{\Delta v}\Big)^2\bigg) \tag{3.29}$$

With the total opacity defined, we can now model the brightness temperature (given in Eq. 3.6) as:

$$T_{\rm B}(v) = \frac{C_2}{C_1}\big(1 - {\rm e}^{-\tau(v)}\big) \tag{3.30}$$

where we fit C_1, C_2, v_{ref}, and Δv using a minimisation routine. $C_2 = A \cdot C_1$, where A is the amplitude of the brightness temperature:

$$A = T_0 \left[\frac{1}{\mathrm{e}^{T_0/T_{\mathrm{ex}}} - 1} - \frac{1}{\mathrm{e}^{T_0/T_{\mathrm{bg}}} - 1} \right] \tag{3.31}$$

C_2 is defined this way to improve the fitting routine for small ($\tau < 1$) opacities. If the opacities are large, it is better to fit A, C_1, v_{ref}, and Δv instead. Assuming each hyperfine component has the same T_{ex}, A allows us to calculate the T_{ex} by rearranging Eq. 3.31 for T_{ex}.

3.5.3 Fragment scales and masses in filamentary clouds

The first aspect of the analysis concerns the development of gravitational instabilities via linear perturbation. The slowest growing mode for an infinite, isotropic, isothermal medium is given by the Jeans length, defined in Eq. 1.6. The Jeans mass can then be expressed as the mass contained within a sphere of diameter λ_{J}:

$$M_{\mathrm{J}} = \frac{4\pi}{3}\rho \left(\frac{\lambda_J}{2}\right)^3 = \frac{\pi^{5/2}}{6G^{3/2}} \frac{\sigma_{\mathrm{gas}}^3}{\rho^{1/2}} \tag{3.32}$$

The situation is very different when considering infinite cylinders in hydrostatic equilibrium. The slowest growing mode is instead one with an intermediate length scale. For star forming filaments that resemble cylinders, the fragmentation scale is given by Eq. 1.3 and the fragmentation mass is given by:

$$M_{\mathrm{cyl}} = 22.1 r^2 \sqrt{\frac{\pi \sigma_{\mathrm{gas}}^2}{4G\rho_{\mathrm{c}}}} \tag{3.33}$$

where r is the radius of the cylinder. To calculate λ_{cyl} and M_{cyl}, one needs an value for the central density of the filament, ρ_{c}, which can be calculated if the 3D density profile is known. In observations however, only the 2D density profile can be measured. To estimate the 3D density profile of observed filaments, we can use a by Plummer-like profile, given by Eq. 1.1 (see Sec. 1.3) assuming the filament is infinitely long, isothermal and in hydrostatic equilibrium. We can then fit n_c, $R_{\rm flat}$ and p, thereby estimating $\rho_{\rm c}$, by generating a series of 3D cylindrical models over various values for n_c, $R_{\rm flat}$ and p and collapse the result into 2D. Then using a χ^2 minimisation, each model can be compared to observed mean column density profiles to find the best fit. The mean profiles are calculated by finding the crests along the filament length using H_2 column density measurements (see Sec. 3.2) and interpolating the data perpendicular to the crests to trace the profiles along the filament. The average profile is then the mean of the perpendicular profiles. Note, this assumes that the filament has zero inclination along the line of sight, which simplifies the 2D interpolation but overestimates the derived central density. If turbulent motions are present, they are also able to provide an additional pressure that can increase the fragmentation scales, thereby the mass of the fragments. To calculate fragmentation scales for turbulent motions, one must replace $\sigma_{\rm gas}$ with $\sigma_{\rm eff}$.

With these quantities defined, one can now compute the length and mass scales using Jeans and cylindrical fragmentation and their respective variations from the thermal case to the effective case. By comparing these values to the fragments within a given star forming region, one can determine the dominant fragmentation mode and if turbulence plays a significant role in determining the fragment sizes and masses.

3.5.4 Radial stability of filamentary structures

To determine radial collapse of cylinders, one first needs to define the mass-per-unit-length ($M_{\rm line}$). Unlike spherical geometries, cylinders are only symmetric about one axis, therefore the $M_{\rm line}$ has to be used in place of point source approximations. The $M_{\rm line}$ is determined by dividing the total filament mass by the length of the filament. Defined like this, the $M_{\rm line}$ is analogous to point sources used in spherical geometry;

all of the mass measured has been condensed to a 1D line element about the cylinder centre. Rather than using a single measurement for M_{line}, one can instead calculate the M_{line} using smaller length intervals along the filament to understand how the M_{line} changes locally. This has been done for the G316.75 ridge to trace where and how feedback impacts the ridge.

With M_{line} defined, one can calculate the virial theorem for a self-gravitating infinite cylinder with internal kinetic pressure. If such a cylinder is in equilibrium, in the absence of magnetic field, it can be shown that the virial theorem is given by (Chandrasekhar & Fermi 1953):

$$\frac{4}{3}U_{\mathrm{line}} - GM_{\mathrm{line}}^2 = 0 \tag{3.34}$$

where U_{line} is the kinetic energy per unit length. It is worth noting that the second term on the left side of Eq. (3.34), GM_{line}^2 is proportional to Ω_{line}, that is to say, the gravitational energy per unit length. The constant of proportionality is a function of the normalisation of the gravitational potential (Ostriker 1964). For thermal motions, the kinetic energy per unit length can be written as:

$$U_{\mathrm{line}} = \frac{3}{2}\frac{k_{\mathrm{B}}T_{\mathrm{k}}}{\mu m_{\mathrm{H}}}M_{\mathrm{line}} = \frac{3}{2}\sigma_{\mathrm{th}}^2 M_{\mathrm{line}} \tag{3.35}$$

The kinetic energy per unit length U_{line} can be computed for both the thermal and turbulent support values if one assumes that all non-thermal dispersion is caused by turbulent motions. From Eq. 3.34 one can derive the expression of the virial ratio for a cylinder $\alpha_{\mathrm{vir}}^{\mathrm{cyl}}$ as:

$$\alpha_{\mathrm{vir}}^{\mathrm{cyl}} = \frac{M_{\mathrm{line}}^{\mathrm{crit}}}{M_{\mathrm{line}}} \tag{3.36}$$

where $M_{\mathrm{line}}^{\mathrm{crit}}$ is obtained by combining Eq. (3.34) and Eq. (3.35):

$$M_{\rm line}^{\rm crit} = \frac{2\sigma^2}{G} \tag{3.37}$$

Equation (3.36) can therefore be rewritten as:

$$\alpha_{\rm vir}^{\rm cyl} = \frac{2\sigma^2}{GM_{\rm line}}. \tag{3.38}$$

$M_{\rm line}^{\rm crit}$ corresponds to the mass per unit length needed for a cylinder to remain in virial balance. $M_{\rm line}^{\rm crit}$ can also be computed for the thermal and turbulent case using $\sigma_{\rm eff}$.

CHAPTER 4

THE IMPACT OF STELLAR FEEDBACK WITHIN THE HIGH-MASS STAR FORMING RIDGE, G316.75[*]

Here, I present the analysis of the G316.75 massive-star forming ridge whose morphology and current evolutionary stage allow us to circumvent the hurdle of time evolution.

4.1 INTRODUCTION

The G316.75 ridge (Fig. 1.7) is located at a distance of 2.69±0.45 kpc from the Sun (using the Reid et al. 2009 Galactic rotation model). It consists of a 13.6 parsec-long ridge with an extended bipolar HII region emerging from the south end while the north part remains infrared dark and nearly free of young stellar objects. and so has been classified as an infrared dark cloud (SDC316.786-0.044 Peretto & Fuller 2009). The high column densities and lack of significant 70 μm emission from the

---

[*] The work presented here is published in Watkins et al. 2019, A&A, 628, A21

infrared dark part of the ridge made it a target to characterise the initial conditions that potentially lead to high-mass star-formation in a few surveys in the past (Ragan et al. 2012; Vasyunina et al. 2011). However, only the bright IRAS source (IRAS14416−5937) has attracted much of attention in the past 20 years, often as part of large surveys investigating the early stages of high-mass star formation (Shaver & Goss 1970b,a; Caswell & Haynes 1987; Bronfman et al. 1996; Harju et al. 1998; Juvela 1996; Walsh et al. 1998, 2001; Pirogov et al. 2003; Purcell et al. 2006; Pirogov et al. 2007; Longmore et al. 2007; Beuther et al. 2008; Longmore et al. 2009; Longmore & Burton 2009; Purcell et al. 2012; Anderson et al. 2014a; Caratti o Garatti et al. 2015; Longmore et al. 2017; Samal et al. 2018). These studies have shown that G316.75 is a very active and young star-forming region, harbouring water (22.24 GHz), hydroxyl (1665 MHz 1667MHz, 22 GHz) and class I/II methanol (6.67 GHz, 12.18 GHz, 44.07 GHz, 95.17 GHz) masers, HII and UCHII regions, a compact X-ray source, and very dynamic gas conditions.

So far, only three published studies focus on the G316.75 ridge. Shaver et al. (1981) were the first to confirm that G316.75 is located at the near kinematic distance, and determined that the source of the HII region is likely to be an O6-type star. The second study, Vig et al. (2007), estimated that not one, but two O-type stars of mass 45 $M_\odot$ and 25 $M_\odot$ are responsible for most of the infrared bright luminosity of G316.75 by performing radiative transfer modelling on the dust emission. Based on 2MASS colour-magnitude and colour-colour diagrams they also conclude that a relative large number of early type B stars are present in the region. They claim that as many as six of these stars are directly associated with the ridge (though, with no velocity information there is no certainty that they really are part of the ridge). Finally, Dalgleish et al. (2018) studied the kinematics of the ionised gas using radio recombination line emission, and conclude that the strong velocity gradient they observe could be the relics of the cloud's initial angular momentum. In all of these studies however, the infrared dark part remained largely ignored. However, the stark differences between the two halves of the G316.75 ridge provide us with the unique opportunity to quantify the exact impact of O-type stars on the gas properties of their host cloud. Indeed, it seems reasonable to assume that the gas properties, and in particular the gas velocity dispersion, within the active part of G316.75 before the formation of high-mass stars must have been very similar to that of the quiescent part. By comparing and contrasting the ridge properties in both halves, we are able to derive robust conclusions on the feedback's ability to destroy the cloud, and the star formation history of the ridge. I note that this methodology makes the additional implicit assumption that the differences between the two parts of the ridge as observed today (i.e., one is actively forming stars the other one is quiescent) are not due to differences in the initial velocity dispersion of the gas or initial mass-per-unit-length of the two parts of the ridge, but rather a consequence of some asymmetries in the converging flows that led to the formation of the ridge in the first place.

This chapter is structured as followed. Section 4.2 introduces the data available on the G316.75 ridge. Sections 4.3–4.5 present the results, Section 4.6 analyses the results and Section 4.7 discusses potential explanations and scenarios that best explain the data.

4.2 OBSERVATIONS

This chapter makes use of a large set of publicly available data. In the following I provide details on each of these datasets.

4.2.1 HI-GAL DATA

The Hi-GAL Galactic plane survey is a key project of the *Herschel* mission (Molinari et al. 2010b). The survey mapped ~1° above and below the Galactic plane over a 360° view at 70 μm, 160 μm, 250 μm, 350 μm, and 500 μm with resolutions of 7″, 12″, 18″, 24″, and 36″ respectively. The observations were split into ~2.2 deg^2 fields.

The G316.75 ridge was observed on the 21 August 2010 as part of the Hi-GAL survey of the galactic plane. The archived data is already reduced with the ROMAGAL pipeline, which has been optimise for the Hi-GAL observations (Molinari et al. 2016). Hi-GAL observations are here used to determine the H_2 column density and dust temperature structure of G316.75.

4.2.2 MOPRA SOUTHERN GALACTIC PLANE CO SURVEY

The *Mopra* Southern Galactic Plane CO Survey (MSGPCOS) is a millimetre molecular line survey of the Galactic plane (Burton et al. 2013/ed; Braiding et al. 2018/ed). The data were taken with the 22 m Mopra radio telescope, located in Australia. The MSGPCOS survey mapped the ^{12}CO, ^{13}CO, C^{17}O C^{18}O and rotational transitions from J=1→0 between $b = \pm0.5°$ and $l = 270°$–$360°$. The data cubes have an angular resolution of 33″ and span a velocity range of ∼200 km s^{-1} with a spectral resolution of ∼0.1 km s^{-1}. The ^{12}CO and ^{13}CO cubes are used in this study to extract kinematic information about the low and medium density gas respectively. The ^{13}CO data has an rms of 1.3 K/channel and the ^{12}CO data has an rms uncertainty of 2.7 K/channel ($T_{\rm mb}$).

4.2.3 THRUMMS

The THRee-mm Ultimate *Mopra* Milky way Survey (ThrUMMS) is another millimetre molecular line survey of the Galactic plane (Barnes et al. 2015) taken with the 22 m Mopra radio telescope. The survey mapped the ^{12}CO, ^{13}CO, C^{18}O and CN rotational transitions from J=1→0 and cover $b = \pm1°$ and $l = 300°$–$360°$ with an angular resolution of 72″ (which is lower than MSGPCOS due to ThrUMMS using a faster mapping speed), a velocity range of ∼150 km s^{-1}, and a spectral resolution of ∼0.36 km s^{-1}. As a result of its under-sampling and lower integration time per pixel, ThrUMMS is superseded by MSGPCOS i.e., the ThrUMMS ^{12}CO data has an rms of 1.5 K/channel in $T_{\rm mb}$ scale at an angular resolution of 72″. Additionally, when the spectral resolution of the two surveys are matched, the rms of MSGPCOS becomes ∼1.6 K/channel. Therefore, we only use the ThrUMMS ^{12}CO data only when we need to view emission that extends beyond the latitude range covered by MSGPCOS.

4.2.4 MALT90

The Millimetre Astronomy Legacy Team 90 GHz (MALT90) survey (Foster et al. 2011, 2013; Jackson et al. 2013) investigates the chemistry, evolutionary and physical properties of a random sample of high-mass dense-cores, identified in the ATLASGAL survey (Schuller et al. 2009) over a range of different evolutionary stage. MALT90 mapped 16 transitional lines at ∼3 mm, including the cold dense tracer N_2H^+(1–0). These data were taken with the *Mopra* radio telescope by individually observing each of the ∼2000 targeted clumps in a 3′ × 3′ data cube. The data cubes have an angular resolution of 38″ and a spectral resolution of ∼0.11 km s^{-1}with an rms noise of 0.2 K/channel ($T_{\rm A}^*$). To convert to $T_{\rm mb}$, one needs to divide $T_{\rm A}^*$ by the extended main beam efficiency of *Mopra* which is 0.55. Four MALT90 observations were taken towards G316.75, covering most of the ridge but leaves a significant section of the infrared dark part unobserved. The four corresponding data cubes were mosaicked together using Starlink (Currie et al. 2014) in order to build a single N_2H^+ (1–0) dataset of G316.75. These data are used to characterise the kinematics of the dense gas.

4.2.5 HOPS

The H_2O Southern Galactic Plane Survey (HOPS) (Walsh et al. 2011; Purcell et al. 2012; Longmore et al. 2017) observes 12 mm data including NH_3 (1,1) and NH_3 (2,2) using the Mopra telescope. This blind survey was undertaken from l = 30–290°, 0.5° above and below the galactic plane. The beam size of this survey was ∼ 2.2′ with a velocity resolution of 0.52 km s^{-1} between 19.5–27.5 GHz and a velocity resolution of 0.37 km s^{-1} between 27.5–35.5 GHz. The median rms of the data is 20±0.05 K ($T_{\rm mb}$). The HOPS data are used to analyse the kinematics of the dense gas. Given its lower critical density compared to N_2H^+ (1–0), the NH_3 (1,1) emission is more extended and so probes gas down to lower densities, which are intermediate between between those traced by ^{13}CO (1–0) and N_2H^+ (1–0).

4.2.6 RADIO CONTINUUM OBSERVATIONS

SUMSS survey

The Sydney University Molonglo Sky Survey (SUMSS) (Mauch et al. 2003) is a southern sky radio continuum survey at 843 MHz measured using the Molonglo Observatory Synthesis Telescope (MOST). The MOST telescope comprises two cylindrical paraboloids each 778×11.6 m in size. The telescope has a FWHM resolution of $\sim 45'' \times 45''$ cosec$|\delta|$ (where δ is the source declination) (Mills 1981). The rms flux sensitivity at the location of G316.75 is 6 mJy beam^{-1}. Due to the higher resolution images reconstructed by this interferometer (compared to single dish radio data), we use this data to locate the brightest ionising sources.

CHIPASS survey

Continuum HI *Parkes* All-Sky Survey (CHIPASS) is a single dish radio continuum and HI survey at frequency of 1.4 GHz observed with the 64 m Parkes telescope (Calabretta et al. 2014). The survey covers declinations less than $+25^\circ$ with a $14.4'$ beam and reaches an rms sensitivity of 40 mK (∼6 mJy). Even though these single dish observations have a low resolution, they recover the extended emission that is lost in the SUMSS interferometric data. Therefore the CHIPASS radio continuum data has been used to estimate the total mass of the stellar cluster.

Table 4.1. Table containing properties describing the clumps within G316.75.

ID #	l ($^\circ$)	b ($^\circ$)	Area[a] (pc^2)	$R_{\rm eff}$[b] (pc)	$\lambda_{\rm sep}$[b] (pc)	$\overline{N}_{\rm H_2}$ ($\times 10^{23}$ cm^{-2})	Mass[a] (M$_\odot$)	$\overline{T}_{\rm Dust}$ (K)	Notes
1	316.81785	-0.05777	0.21	0.26	0.31	2.41	820	19.6±1.3	In active half
2	316.81119	-0.05777	0.03	0.01	0.31	2.03	87	28.9±0.7	In active half
3	316.79952	-0.05611	0.35	0.33	0.55	2.51	1507	19.8±1.6	In active half
4	316.78785	-0.03944	0.19	0.25	0.96	1.44	357	19.8±0.5	In active half
5	316.76784	-0.02443	0.17	0.23	0.65	3.18	748	16.8±0.8	In active half
6	316.75784	-0.01443	0.04	0.12	0.35	1.36	71	18.4±0.2	In active half
7	316.76451	-0.01110	0.09	0.17	0.35	3.13	404	17.0±1.2	In active half
8	316.74451	0.02891	0.29	0.31	0.72	0.75	311	15.0±0.3	In quiescent half
9	316.74117	0.04391	0.09	0.17	0.72	0.65	72	14.9±0.1	In quiescent half
10	316.72450	0.05391	0.06	0.14	0.91	0.93	71	14.6±0.1	In quiescent half
11	316.71950	0.07725	0.10	0.18	0.47	1.78	225	13.5±0.2	In quiescent half
12	316.71950	0.08725	0.08	0.16	0.47	1.69	166	13.5±0.1	In quiescent half

[a] Error propagated from the distance error and is equal to a fractional error of 1/3

[b] Error propagated from the distance error and is equal to a fractional error of 1/6

ID # corresponds the the clump identification number from the most southernly position (see Fig. 4.4 and 4.7a-c). l and b are the galactic coordinates of the peak intensity of the clump. Area is calculated from the number of pixels contained within the isocontour extracted using `astrodendro`. $R_{\rm eff}$ is the effective radius, $R_{\rm eff} = \sqrt{{\rm Area}/\pi}$. $\lambda_{\rm sep}$ is the minimum separation to the peak intensity of the neighbouring clump. $\overline{N}_{\rm H_2}$ is the mean column density contained within the `astrodendro` isocontour for each clump. Mass is the average of the bijective and clipped mass contained within the `astrodendro` isocontour for each clump. $\overline{T}_{\rm Dust}$ is the mean *Herschel* dust temperature within the clumps isocontour where the uncertainty quoted equals the standard deviation, and Notes specifies whether the clump is located in the active or quiescent region.

4.3 Stellar masses and Hii region dynamical age

In order to quantify the impact of the embedded G316.75 stellar cluster on its parent molecular cloud, one first needs to compute its cluster mass, and provide constraints on its age. For this purpose, we use CHIPASS single dish data to estimate the cluster mass. The CHIPASS emission is shown on Fig. 1.7 using contours, where the final contour roughly equals the extent of the 8 μm data. Inner contours were chosen to have have similar angular separations. By integrating intensity over the entire Hii region (i.e., the intensity within the final radio contour on Fig. 1.7), we measure a total flux density of 61.3±4.0 Jy. According to Eq. (3.13), this corresponds to $\log_{10}(N_{\rm ly}[s^{-1}]) = 49.63 \pm 0.11$ given that the electron temperature, $T_{\rm e}$, is equal 6600 K (where $T_{\rm e}$ has been estimated in Shaver et al. (1983)).

When $\log_{10}(N_{\rm ly}[s^{-1}]) = 49.63 \pm 0.11$, the cluster mass $M_{\rm cl} = 930 \pm 230$ M$_\odot$, which includes four O-type stars one of which has a mass larger than 48 M$_\odot$. This number of high-mass stars is comparable to the six B0 stars, or earlier, identified by Vig et al. (2007) using near-infrared colour-colour diagrams. To pinpoint the strongest ionising sources, we instead used the SUMSS observations. These observations resolve the emission into two separate radio continuum peaks (see Fig. 1.7). By splitting the emission into two halves, I estimated the radio flux densities of the two sources are 23±2 and 12±1 Jy. These fluxes correspond to $\log_{10}(N_{\rm ly}[s^{-1}]) = 49.1 \pm 0.1$ and $\log_{10}(N_{\rm ly}[s^{-1}]) = 48.8 \pm 0.1$, respectively. Depending on the stellar model used (Panagia 1973; Vacca et al. 1996; Sternberg et al. 2003), the two high-mass stars have spectral types between O8.5 and O7 V with a stellar mass of 28-38 $M_\odot$, and O6.5 and O6 V with stellar mass 34-55 $M_\odot$ for the small and large intensity peaks respectively. These stellar masses are consistent with the cluster mass estimated using the CHIPASS data.

Finally, one can estimate the dynamical age of the HII region using fig. 3.7 from Tremblin et al. (2014). A G316.75-like HII region with a radius of 6.5 pc and $N_{\rm ly} = 10^{49.63} s^{-1}$ is estimated to be $\sim$ 2 Myr old using this method. The lifetime for O6 stars is $\sim$ 4 Myr (Weidner & Vink 2010), therefore this is consistent with the estimated dynamical age of the HII region. It also indicates that in a couple of Myr a supernova explosion should occur in G316.75, which might drastically change the star formation history of the ridge.

4.4 H_2 COLUMN DENSITY AND DUST TEMPERATURE MAPS

The dust temperature and H_2 column density maps (Fig. 4.1) were derived using PPMAP (Marsh et al. 2015) using 12 temperature bands from 8 to 50 K on all five *Herschel* images. As a result, the angular resolution of the maps are 12″ with a pixel size of 6″, which corresponds to 2 pixels along the beam. The resulting differential column density (i.e., the column density per temperature band) has been shown on Fig. 4.2. Fig. 4.2 reveal a range of features for the cold and hot column density gas. For instance the column density of hot dust outlines the shape of multiple bipolar lobes, which coincide with the bipolar lobes shown in Spitzer 8 μm on Fig. 1.7 Additionally,

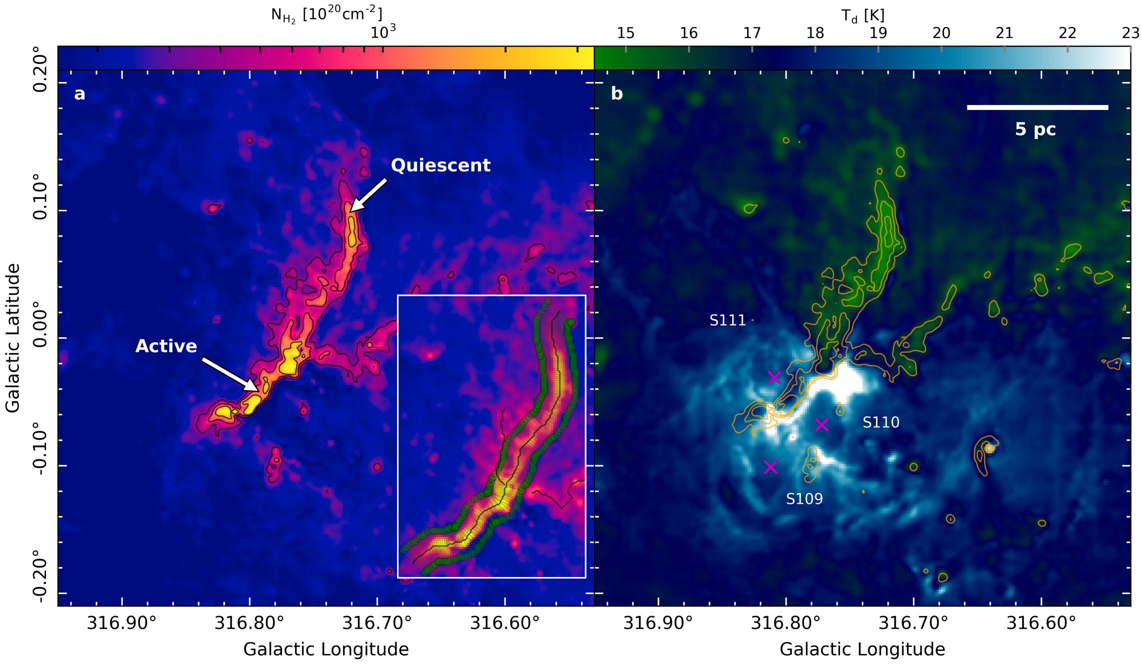

Figure 4.1. H_2 Column density map **(a)** and dust temperature map **(b)** derived using PPMAP. The black contours on **(a)** and the orange contours on **b** show H_2 column density contours at 400, 800 and 1600 $\times 10^{20}$ cm^{-2}. Inaxes figure shows the three spines traced by Hessian methods as solid black lines. Green-dashed lines show the perpendicular cuts along the ridge offset from the spine centre by 0.63 pc. Theses are used for further analysis. Labelled arrows point toward the active and quiescent parts of the filament and labelled magenta crosses show the location of three bubbles, S109, S110, and S111, catalogued in Churchwell et al. (2006). The white solid line indicates a physical scale of 5 pc.

the 38.94–46.00 K temperature band in Fig. 4.2 reveals the location of $\sim$ 10 hot sources, some of with are co-spatial with cold clumps present in colder temperature bands.

The differential column density cube created by PPMAP was collapsed to output the total H_2 column density (Fig. 4.1a) and the mean H_2 column density weighted dust temperature (Fig. 4.1b). Focusing on the ridge, one can already see some basic differences between the quiescent and active regions as the latter exhibits higher H_2 column density and dust temperatures compared to the quiescent region. Furthermore, the H_2 column density and dust temperature are anti-correlated in both the active and quiescent regions except near the SUMSS radio peak. Here, both the dust temperature and H_2 column density increase together. Additional notable features are three warm bubbles of gas swelling from the active region in the dust temperature map, resembling the same features in 8 μm Spitzer emission (see Fig. 1.7). One can also see that some diffuse dust emission around the active part reaches temperature of 50 K (see Fig. 4.2).

The H_2 column density map also shows that the ridge is surrounded by diffuse emission from the galactic plane. This material is composed of a large number of unrelated diffuse clouds that are accumulated along the line of sight across the entire Galaxy, and consequently, can reach large column density values (e.g. Peretto et al. 2010, 2016). At $\sim 0.23 \pm 0.03 \times 10^{23}$ cm^{-2}, this emission becomes comparable to the extended emission from the ridge itself (see Sec 4.4.2). Below this value, it is impossible to disentangle what fraction of the diffuse dust emission is associated to the ridge itself. We therefore used this column density value of $0.23 \pm 0.03 \times 10^{23}$ cm^{-2} to define the borders of the dense inner part of the ridge and remove it from subsequent calculations. As a result, we estimate that G316.75 has a total gas mass of 18900±6500 $M_\odot$ of which 11200±3800 $M_\odot$ (59%) is located in the active region and 7700±2700 $M_\odot$ (41%) in the quiescent. These masses were calculated by averaging the clipped and bijective masses within the first isocontour located three standard deviations above

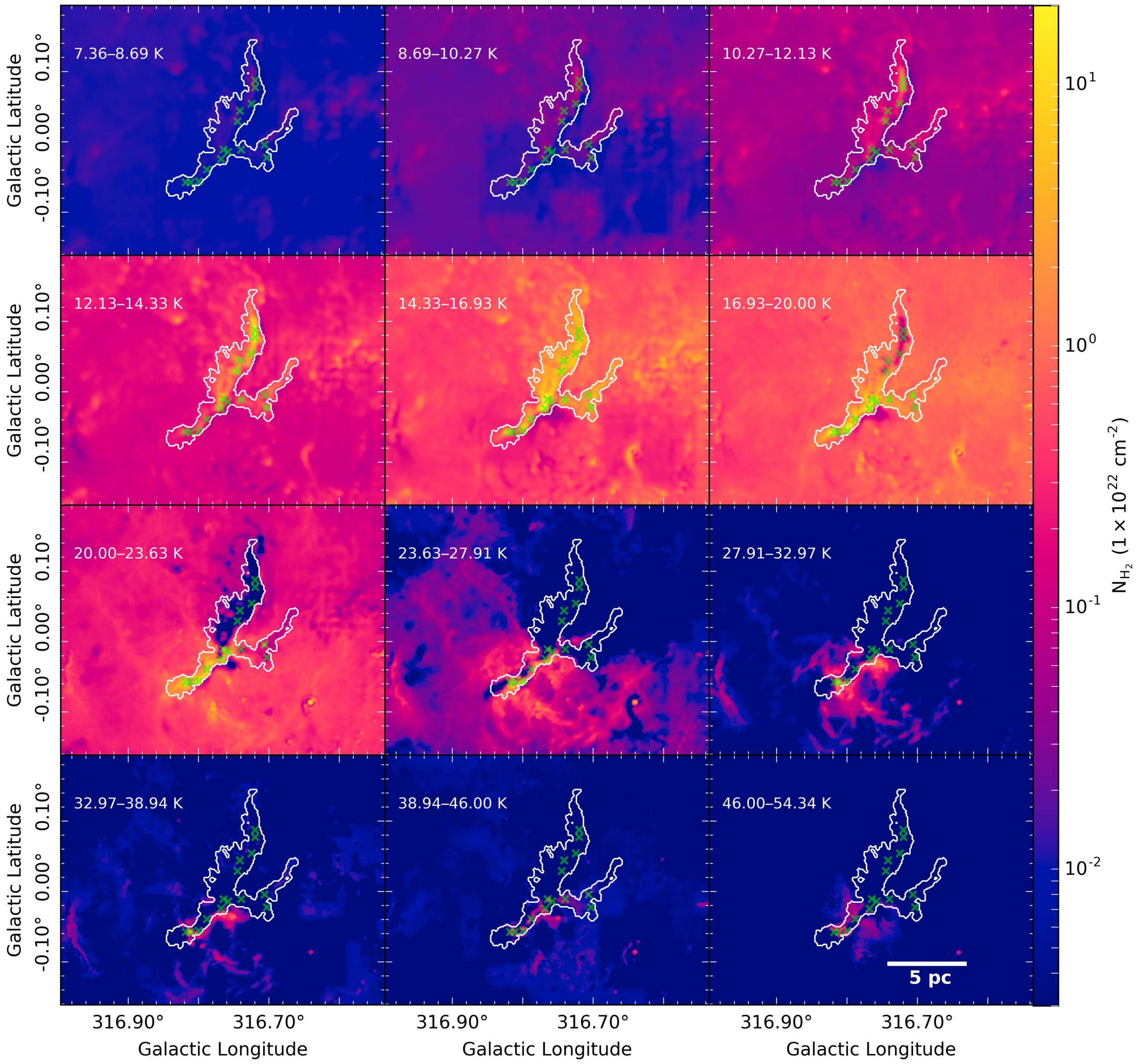

Figure 4.2. Differential column density of G316.75 over 12 temperature bands. The temperature bands used are logarithmically distributed from 8 to 50 K. Each subplot has been labelled with the temperature band the column density represents. The white contour indicate where the total H_2 column density is $> 0.31\times10^{23}$ cm^{-2} Fig 4.7. Green crosses mark the location of the clumps present in the the total H_2 column density. Physical scale is 5 pc = 0.106°

the background value ($\sim$3.1 $\times 10^{23}$ cm^{-2}). The bijective mass is defined as the mass within the full column for a given isocontour whereas the clipped mass subtracts the contribution from column less than the given isocontour (Rosolowsky et al. 2008). The relatively high background column density underestimates the ridge mass but ensures that measured properties are those of the dense gas. The mass uncertainties cover the spread resulting from the clipped and bijective schemes propagated with the distance error. The same isocontour was used to calculate a mean dust temperature of 19.6±2.3 K in the active region and 15.6±0.8 K in the quiescent region. The quoted uncertainties measure the spread of dust temperatures for the active and quiescent regions.

4.4.1 CLUMP IDENTIFICATION

The H_2 column density map reveals a number of local density peaks i.e., clumps. To identify these clumps and estimate their masses, I used the dendrogram package `astrodendro` (Rosolowsky et al. 2008). I use a minimum isocontour of 0.23 $\times 10^{23}$ cm^{-2} to match the galactic background, with a minimum trough between structures set to 0.2 $\times 10^{23}$ cm^{-2}. This ensues only well defined clumps are identified. The smallest size considered significant was based of the PPMAP resolution of 12$''$, resulting in a minimum of five pixels (equal to an area of 0.03 pc^2). This dendrogram extracts seven clumps in the active region and five in the quiescent region. The clump properties are given in Table 4.1, numbered from 1 to 12 from south to north. Clump masses provided in Table 4.1 are also calculated by averaging the clipped and the bijective masses. The minimum separation distance, λ_{sep} between the peak clump masses are also calculated in Table 4.1.

Table 4.2. Average properties the active and quiescent parts of the ridge within the 3.1 $\times 10^{23}$ $cm^{-2} H_2$ column density contour. This represents the isocontour that is is 3-sigma larger than the background value (see Sec. 4.4.1).

Region	Area[a] (pc^2)	Length[b] (pc)	Width[c] (pc)	$\overline{N}_{H_2}$ ($\times 10^{23}$ cm^{-2})	M_{ridge} ($M_\odot$)	$\overline{T}_d$ (K)	$\overline{\lambda}_{sep}$ (pc)	$\overline{M}_{clump}$ ($M_\odot$)
Active	5.86	6.0	0.63±0.08	0.85	11200±3800	19.6±2.3	0.50±0.22	570±470
Quiescent	10.08	7.6	0.63±0.08	0.34	7700±2700	15.6±0.8	0.66±0.17	170±90

[a] Error propagated from the distance error and is equal to a fractional error of 1/3

[b] Error propagated from the distance error and is equal to a fractional error of 1/6

[c] The width the two regions are equal due to the method used to calculated them (see Fig. 4.3).

4.4.2 Ridge tracing

G316.75 is a single continuous filamentary structure, therefore its properties are best described in the context of its filamentary structure. For this purpose, a self-developed Hessian method was used to extract the filament skeleton (spine) and the perpendicular angles of the skeleton. Since the goal here is to obtain a reliable skeleton of the G316.75 ridge, not to calculate the filament network of the unrelated gas present in the *Herschel* image (such as in Arzoumanian et al. 2019), we convolved the H_2 column density image before applying the Hessian method. Additionally, we required that the largest absolute normalised eigenvalues need to be < -0.15 rather than < 0 to extract only the most prominent structures. With these conditions, the Hessian method identified three structures in the vicinity of G316.75: the G316.75 ridge; a small filament left of the ridge; and a third filament immediately right to the ridge (see in-axis plot in Fig. 4.1). The third filament does not connect to the main ridge due to an absence of H_2 column density on the right side of the ridge. Using the spine found for the G316.75 ridge, I calculate that the ridge is 13.6 pc long, assuming zero inclination towards our line of sight for the entire region. In reality, the ridge is likely to have a non-zero inclination. Therefore our assumption will cause us to underestimate the length of G316.75 and overestimate the volume densities in future calculations.

Using the eigenvectors calculated during the Hessian method, shown in Fig. 4.1, the transverse dust temperature and H_2 column density profiles have been calculated

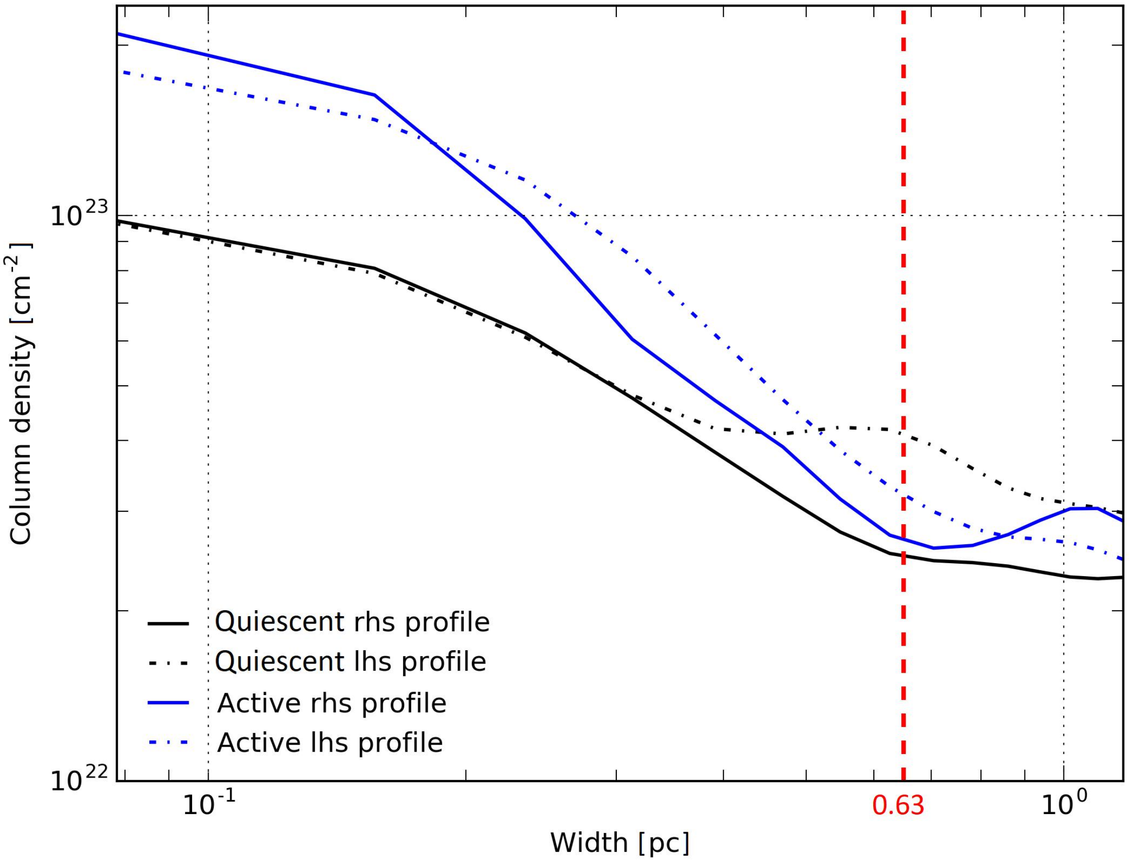

Figure 4.3. Mean transverse H_2 column density profiles averaged in the longitudinal direction from 0 and 6 pc for the active region, and from 6 to 13.6 pc for the quiescent region. The left-hand-side (lhs) and right-hand-side (rhs) profiles denotes the eastern (i.e., from 0 to -0.63 pc) and western (from 0 to +0.63 pc) offsets from the spine centre. The red dashed line marks the position of a power-break that fits best the four profiles. I interpret this as the transition between the compact ridge and the more diffuse material surrounding the ridge.

for every position along the ridge skeleton by interpolating the maps across the perpendicular direction to the spine. Using these individual transverse profiles, the mean H_2 column density profile for the active and quiescent regions have been calculated as a function of the ridge's width and are shown in Fig. 4.3 using a log-scale. Figure 4.3 shows that the average column densities and the power-law gradient in the active region are larger than the quiescent region. Additionally, the left hand side profiles have slightly higher column densities compared to the right hand side profiles as a function of width. In particular, the left hand side in the quiescent region has more extended emission at larger distances away from the centre compared to the active region. However, where the gradients follow a constant power law, both the left and right sides have similar gradients. The profiles also all exhibit a power-break at $\sim$0.23 $\times 10^{23}$ cm^{-2} at a distance of $\sim$0.63 pc from the centre of the ridge. This matches the point where emission from the galactic plane becomes comparable to the extended emission from the ridge (see beginning of this section). Therefore, the differences between the left and right sides likely represent the remaining diffuse gas flows responsible for the formation of the ridge, but the similar gradients and the power-break indicate the dense gas towards the centre of the ridge has evolved at a similar rate on both sides. As a result, I only consider the gas >0.63 pc from the centre (which represents the dense part of the ridge) and treat both the left and right sides equally when analysing the ridge in this chapter.

In Figs. 4.4 and Fig. 4.5, I plot the interpolated straightened projections, and the mean longitudinal profiles of the dust temperature and H_2 column density profiles and also over-plot the clump positions. These provide a new perspective of the ridge and show a clear view of the correlation and anti-correlation between column density and temperature. One particular feature to notice is the decrease of column density in combination with strong temperature peaks around clump #3 and between clump #4 and #5. These locations are coincident with the two radio continuum peaks observed in SUMSS observations, (see Fig. 1.7) which strongly suggests that here

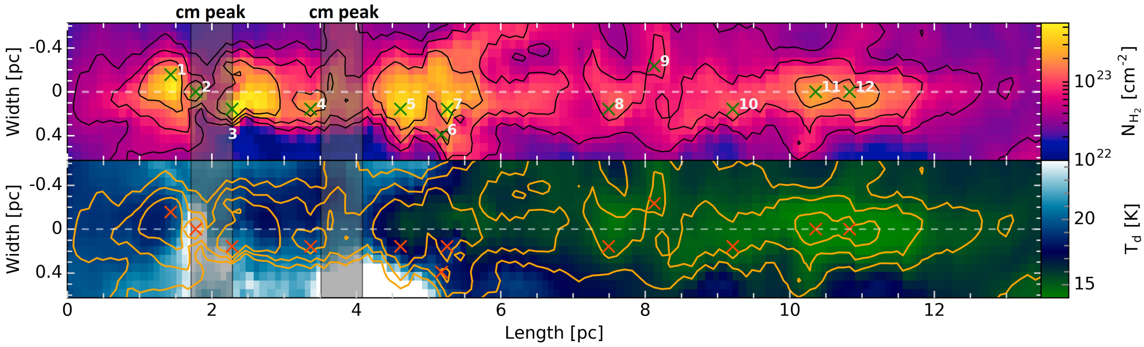

Figure 4.4. Straightened H_2 column density map **top** and dust temperature map **bottom** with a width of 2×0.63 pc and length of 13.6 pc. Negative values along the y axis corresponds to the eastern offset from the spine centre, while along the x axis 0 pc corresponds to the most southern position of the spine. The black contours on **(a)** and the orange contours on **b** show H_2 column density contours at 0.4, 0.8 and 1.6 $\times 10^{23}$ cm^{-2}. Green and orange crosses mark the locations of the peak column density for each clump along with their ID #. Due to the projecting affects, some crosses are slightly offset from the column density peaks in this image. White-dashed line shows where the centre of the spine is. The grey-shaded regions labelled 'cm peak' correspond to the radio continuum peaks seen in SUMSS (see Fig. 1.7).

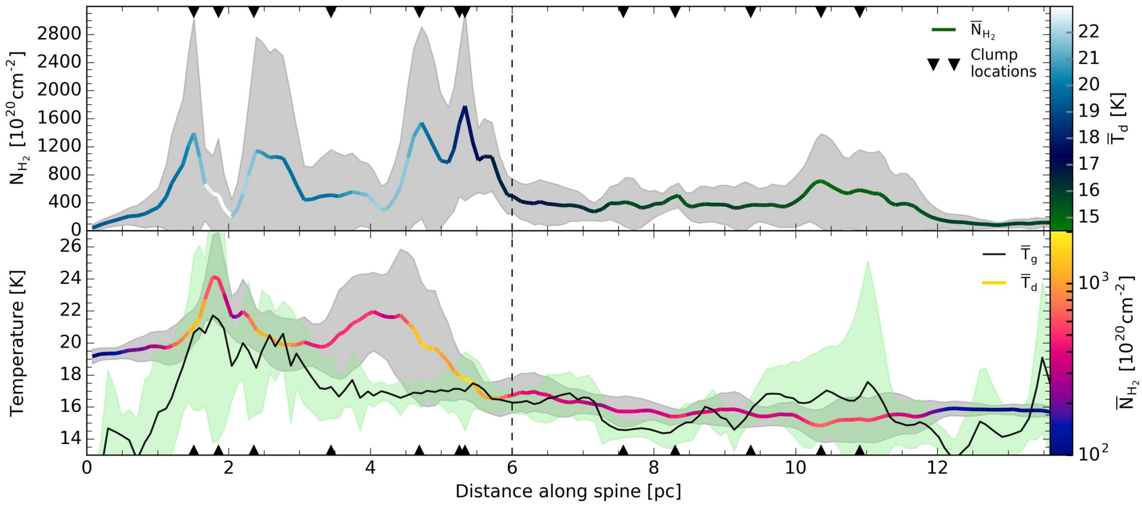

Figure 4.5. Background subtracted longitudinal column density **(top)**, and longitudinal dust temperature (solid coloured line) and the gas temperature (solid black line) **(bottom)** between 0 and 13.6 pc and averaged over 2×0.63 pc (i.e. 0.63 pc either side of the spine). The thin black vertical dashed line marks the separation between the active half of the ridge (left) and the quiescent half (right). The colour of the solid line in the **top** panel corresponds to the dust temperature longitudinal profile of the **bottom** panel and the colour of the dust temperature line in the **bottom** panel corresponds to the H_2 column density longitudinal profile in the **top** panel. Black triangles mark the clump positions. Translucent regions show the 1-sigma uncertainty range for the values (i.e., the standard deviation of each value).

feedback from embedded O-stars are impacting the ridge. On the other hand, the temperature and column density profiles of the quiescent part of the ridge do not show any sign of embedded star formation activity. Furthermore, when plotting the mean perpendicular of the dust temperature and H_2 column density profiles of the active and quiescent regions, one can see that the temperature minimum in the active part is offset with respect to the ridge spine, unlike the H_2 column density maximum (see Fig. 4.6). This shows that the temperature offset is a genuine physical effect and not the result of the skeletonisation process, which would offset the H_2 column density maximum and temperature minimum equally.

Figures 4.4 and 1.7 shows that the peak of the radio emission coincides with clump #2. Potentially, the free-free emission present might be strong enough here to significantly contribute to the intensity measured at *Herschel* wavelengths. Using an aperture of radius $45''$ over clump #2, I use the SUMSS data to calculate that the radio emission present equal 2190 MJy sr^{-1} at 843 MHz. Since optically thin free-free emission is approximately proportional to $\nu^{-0.1}$ (See Sec. 2.3.2), I can estimate that the flux contribution at 500 μm is 1140 MJy sr^{-1}. Over the same area in the *Herschel* 500 μm map, I measure an intensity of 0.11×10^6 MJy sr^{-1}. Therefore the free-free contribution is only represents 1%. I note however that the dust column density is more sensitive to 250 μm emission. Repeating the above calculations for 250 μm, I estimate that the free-free contribution is 1060 MJy sr^{-1}, and the *Herschel* intensity is 3.04×10^6 MJy sr^{-1}. The free-free emission contribution 0.03% at 250 μm confirming that it is safe to ignore this contribution.

4.5 KINEMATICS AND GAS TEMPERATURE

The main goal of the present study is to evaluate the impact of OB stars on their parent cloud. However, the effect that feedback has on the surrounding gas is most likely a function of its density (Thompson & Krumholz 2016). Here, we analyse

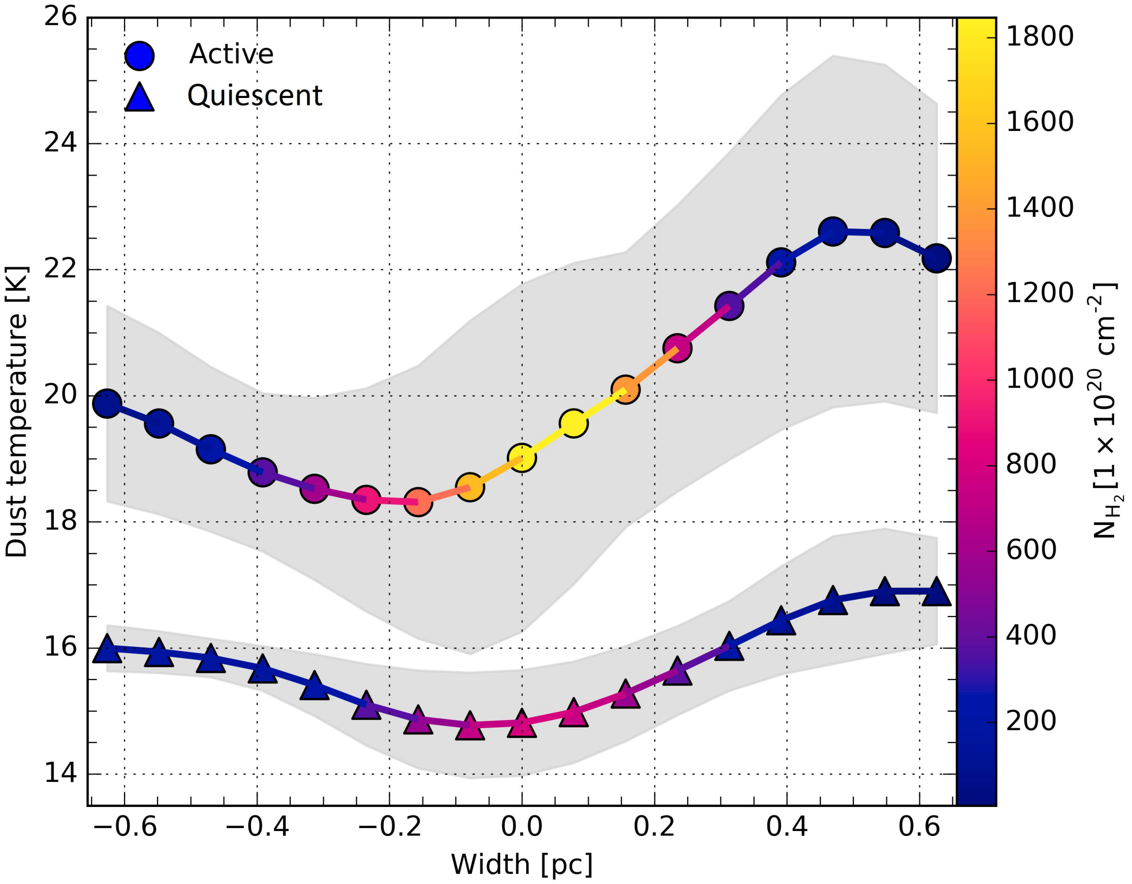

Figure 4.6. Mean transverse temperature profile averaged over the same limits as Fig. 4.3. The colour of solid line denotes the mean *Herschel* H_2 column density profile where the circle and triangle markers show the dust temperature profile for the active and quiescent regions respectively. The translucent region shows the 1-sigma uncertainty range for the dust temperature.

Table 4.3. Table showing the average kinematic properties and gas temperature of the ridge calculated within using the masked datasets in Fig. 4.7. Unless specified, average values are calculated using the mean, and uncertainty represents the statistical uncertainty (i.e., the standard deviation).

Region	$\overline{v}_{\rm lsr}$ N_2H^+ (km s^{-1})	$\overline{v}_{\rm lsr}$ NH_3 (km s^{-1})	$\overline{v}_{\rm lsr}$ ^{13}CO (km s^{-1})	$\overline{\sigma}$ N_2H^+ (km s^{-1})	$\overline{\sigma}$ NH_3 (km s^{-1})	$\overline{\sigma}$ ^{13}CO (km s^{-1})	$\overline{T}_{\rm gas}$ (K)
Active	-38.7±1.1	-39.0±0.6	-39.1±1.0	1.7 ±0.6	1.5 ±0.3	2.3±0.5	17.4±2.6
Quiescent	$-38.7^{+1.1}_{-1.0}$ [a]	-38.8±0.5	-39.4±0.3	$1.0^{+0.3}_{-0.4}$ [a]	1.5±0.2	1.8±0.5	14.4±2.4

[a] Median and interquartile ranges are used to estimate average values

line data from four different molecules, each tracing relatively different gas density regimes, as indicated in Table 3.1 but to summarise: ^{12}CO (1–0) and ^{13}CO (1–0) trace gas at $\sim 1 \times 10^2$ cm^{-3}; NH_3 (1,1) traces gas at $\sim 1 \times 10^3$–10^4 cm^{-3}; and N_2H^+ (1–0) traces gas at $\sim 1 \times 10^4$–10^5 cm^{-3} (see Shirley 2015). Overall, these data probe gas that span more than 2-3 orders of magnitude in density.

4.5.1 N_2H^+ (J=1–0)

The kinematics of the dense gas are investigated using the MALT90 N_2H^+ (J=1–0) data (see Sec. 4.2.4). The velocity channels were first smoothed to 0.22 km s^{-1} to improve the signal-to-noise ratio, after which the seven hyperfine components of the N_2H^+ (J=1–0) were fitted using the HFS routine within GILDAS. At every position, one velocity component has been fitted. The resulting integrated intensity, centroid velocity, and velocity dispersion maps are shown in Fig. 4.7a-c. The full ridge has not been observed by the MALT90 survey, but, from the coverage we have, one can see that the integrated intensity has a similar morphology to the H_2 column density and has a number of peaks that coincide with *Herschel* clumps (see Sec. 4.4.1). However, the N_2H^+ (J=1–0) emission in the active region is asymmetrically concentrated to the west side of the H_2 column density, which might be a sign that the relative abundance of N_2H^+ is affected by the different physical conditions of the ridge at this location. This is somewhat reminiscent of what has been observed in the SDC335 massive star-forming infrared dark cloud (Peretto et al. 2013).

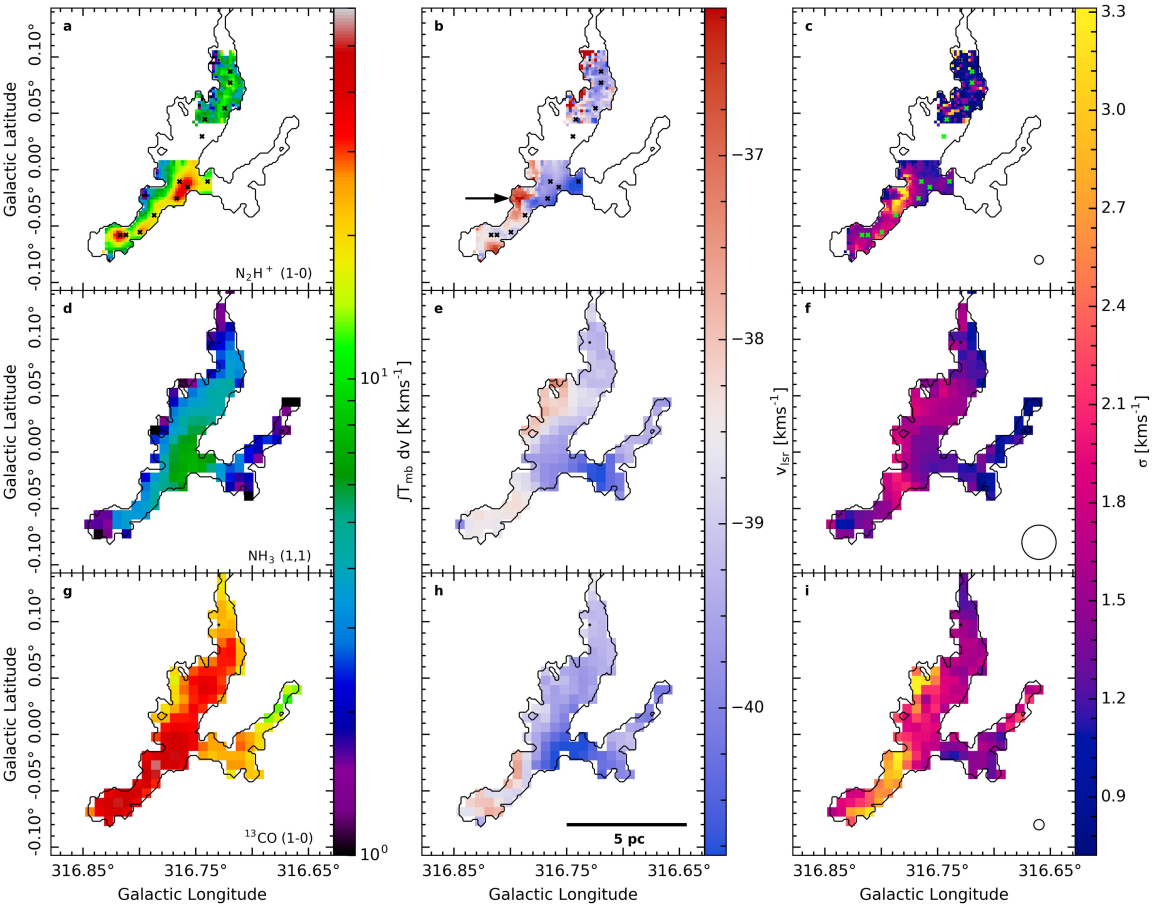

Figure 4.7. Molecular transition analysis for N_2H^+ (J=1–0) **(top)**, NH_3 (1,1) **(middle)** and ^{13}CO (J=1–0) **(bottom)**. First column shows the integrated intensity between -42.5 to -33 km s^{-1}. The second column shows the radial velocity and the third column shows the velocity dispersion. The over-plotted contour corresponds to an H_2 column density of 0.312 $\times 10^{23}$ cm^{-2} (see Sec. 4.4.1). Each dataset has been masked according to this contour and is used to estimate the properties of G316.75 in Table 4.3. The molecular transition used has been labelled in the bottom right of of the first column. The open black circle in the last column shows the FWHM beam size of the observations. The crosses in the first row show the positions of the clumps and the black arrow in **b** show the location and the direction along which the N_2H^+ spectra presented in Fig. 4.9 were taken.

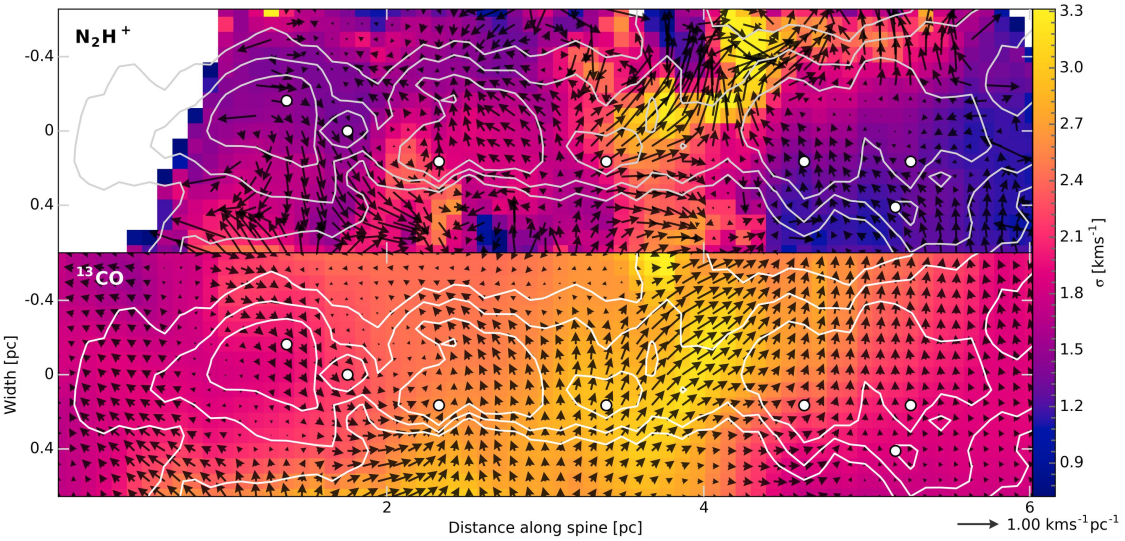

Figure 4.8. Two panels showing the straightened velocity dispersion of N_2H^+ (J=1–0) **(top)** and ^{13}CO (J=1–0) **(bottom)** along the active part of the ridge. The length and width and contours used are identical to Fig. 4.4. Over-plotted on each panel are the velocity gradient vectors calculated across a beam size for each corresponding data set. The magnitude scale of the gradient vectors is indicated at the bottom right of the plot. The white dots denote the positions of the clumps.

The centroid velocity map in Fig. 4.7b reveals a very dynamic environment, in particular towards the active part of the ridge where large velocity gradients and dispersions' coincide ($|\nabla v| > 5$ km s^{-1} pc^{-1} and $\sigma > 3$ km s^{-1} respectively). More specifically, on small spatial scales, one can see large velocity gradients perpendicular and parallel to the ridge in the active region. For a more quantitative comparison between the velocity gradients and velocity dispersion, I constructed a vector plot of these gradients using the centroid velocity map for each tracer on Fig. 4.8. The velocity gradient was estimated using the central difference method over the beam size for each tracer (i.e., using Eq. 3.10 with a grid spacing, θ, equal to the FWHM of the observations in the x and y directions). I straightened the plots in the same way as Fig. 4.4 to emphasise the spatial correlation between these two quantities. On Fig. 4.8, one can see that the velocity dispersion in the active region is large, with a non-weighted average of 1.7 km s^{-1}, reaching peaks of 3.9 km s^{-1}. These velocity dispersion peaks correlate spatially with velocity gradient peaks of $\sim$ 10 km s^{-1} pc^{-1}.

This strongly suggests that unresolved gas flows are present the ridge. In fact, a closer inspection of the N_2H^+ (J=1–0) spectra around where the largest velocity gradients are located, near clumps #2 and #4 (see Fig. 4.9), reveals that they could be the result of two overlapping velocity components (one at ∼-36.5 km s^{-1} and one at ∼-40 km s^{-1}). More unresolved velocity structures might be present in the ridge, potentially contributing to the measured velocity dispersion along the ridge. As far as the ridge stability analysis is concerned, such gas flows will, in the case where gravity is responsible for their development, lead to an overestimate of the kinetic pressure term. Therefore, their presence can only strengthen the results presented in Sec. 4.6.3.

The centroid velocity within the quiescent region is relatively uniform, despite being noisier. Visual inspection of the spectra indicates that they have low signal-to-noise ratios (S/N). These low S/N results in poor fits and so when discussing the quiescent region I only use the median centroid velocity and median velocity dispersion, along with their corresponding interquartile ranges(see Table 4.3). Median values are less impacted by erroneous fits.

4.5.2 NH_3 (1,1) AND (2,2)

The NH_3 (1,1) and NH_3 (2,2) HOPS observations cover all of the G316.75 ridge, allowing us to investigate the dense gas that is not mapped in N_2H^+. The velocity channels were smoothed to 1 km s^{-1}. As for N_2H^+, both datasets were fitted using the HFS routine of GILDAS, using one velocity component. The integrated intensity, centroid velocity and dispersion maps resulting from the fit of the NH_3 (1,1) transition are shown in Fig. 4.7d-f. I do not show the (2,2) maps in this thesis since they trace the same structures as to the (1,1) maps (but at lower S/N).

Overall, all these maps resemble the N_2H^+ maps but at a lower resolution. It is interesting to see that the quiescent region has a significant velocity gradient across the ridge where the N_2H^+ observations were not mapped (1.5–2.5 km s^{-1} pc^{-1}).

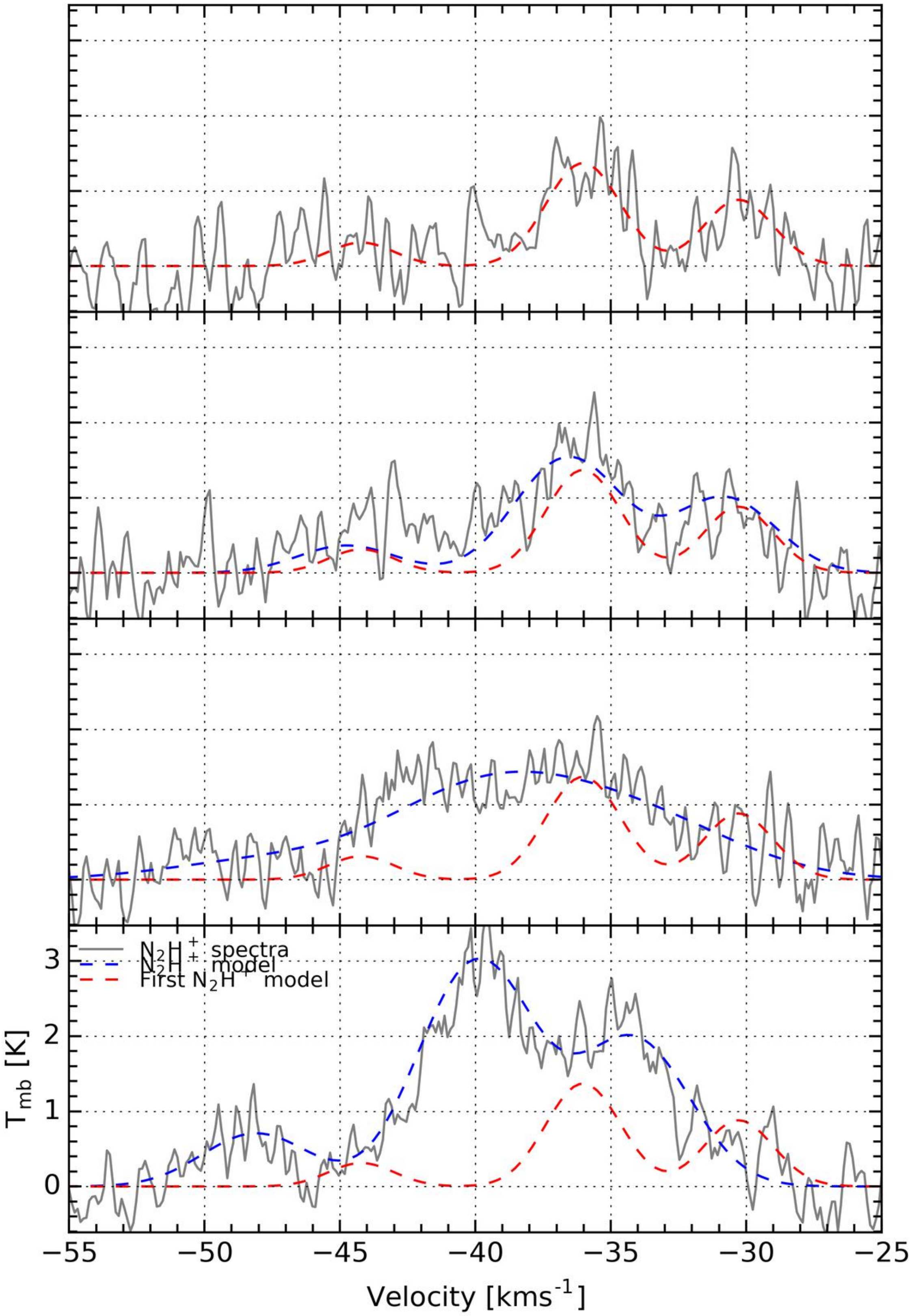

Figure 4.9. Four vertical panels showing N_2H^+ (J=1–0) spectra and corresponding fitted models at four different positions from left to right as indicated by the arrow in Fig. 4.7b. The solid grey line are the observed spectra at each location. The red dashed line corresponds to the best fit model of the top panel spectrum, which has then been over-plotted on the bottom three panels for reference. The dashed blue lines correspond to the best fit models to the bottom three spectra. All fits have been calculated using GILDAS.

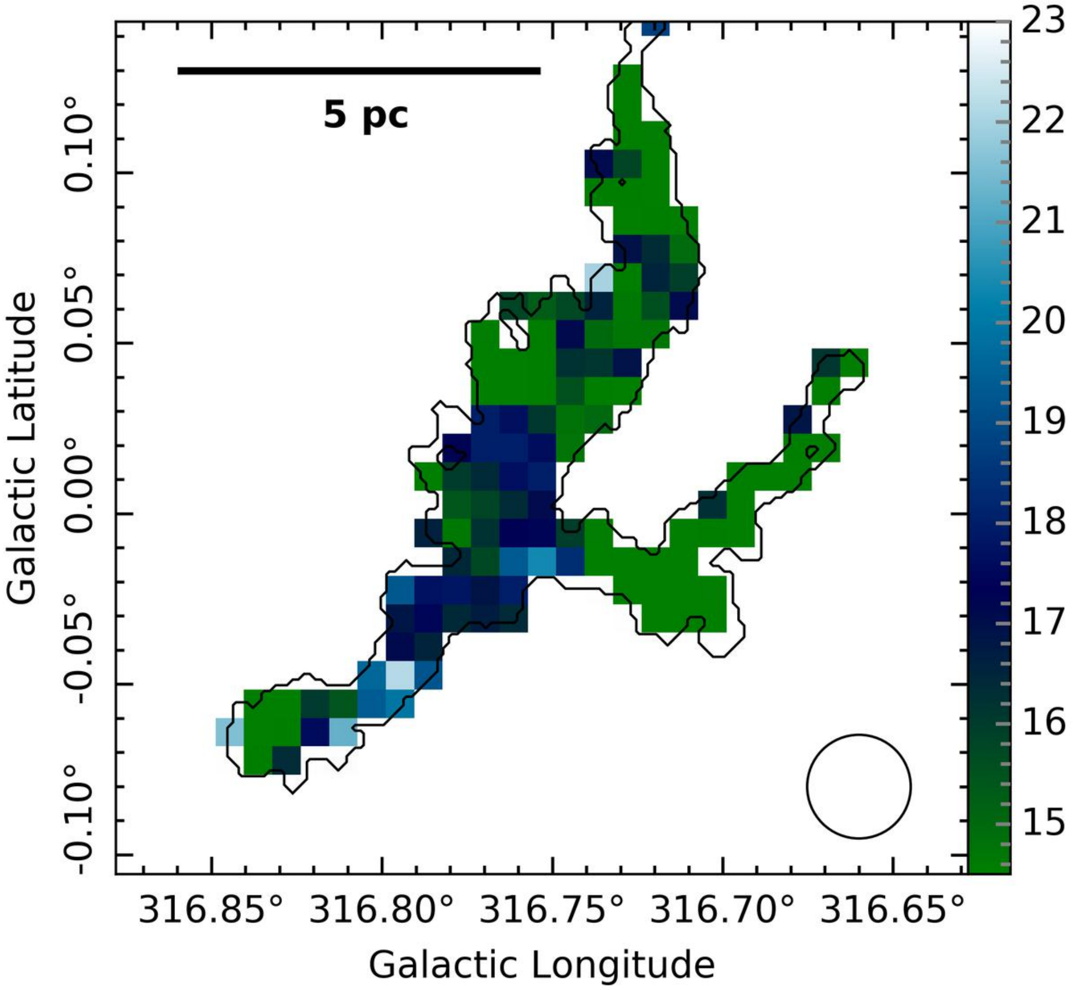

Figure 4.10. Rotation temperature map derived from NH_3 (1,1) and (2,2) observations. Limits of the colour map are equal to the limits of the dust temperature in Fig 4.1. The black contour and mask used are identical to Fig 4.7. The open black circle shows the beam size of the observations.

See Fig. 4.7). Visual inspection of the NH_3 spectra do not show multiple velocity components.

The excitation of the ammonia inversion lines is dominated by collisions at low temperatures. One can therefore use ammonia to derive the temperature of the gas (Ho & Townes 1983). Following the same method as that presented in, for example, Ho & Townes (1983) and Williams et al. (2018), I compute the ammonia rotational temperature map on see Fig. 4.10. This shows that the general morphology of the gas temperature matches that seen in dust temperature; the active region is warmer than the quiescent with mean gas temperatures of 17.4±2.6 K and 14.4±2.4 K respectively. In Fig. 4.5 I plot the longitudinal gas temperature to better illustrate the matching features in both the gas and the temperature maps. One can see that both temperatures are consistent with each other along most of the ridge, and differences can be explained by the order of magnitude difference in angular resolution between HOPS maps and PPMAP datasets.

4.5.3 ^{13}CO (J=1–0)

The MSGPCOS ^{13}CO (J=1–0) integrated intensity, centroid velocity, and velocity dispersion maps were calculated by fitting a single Gaussian at each position after the velocity channels were smoothed to 0.37 km s^{-1} (see Fig. 4.7g–i). The integrated intensity of ^{13}CO (J=1–0) resembles the dust derived H_2 column density and unlike NH_3 and N_2H^+, the integrated intensity peaks along the spine of the ridge. The centroid velocity map looks relatively similar to that of the NH_3 centroid velocity map, even though the perpendicular gradient observed in the quiescent region is not as apparent in the ^{13}CO (J=1–0) data. To check this gradient I have produced a position-velocity diagram along the spine of the ridge in Fig. 4.11. Indeed, this shows that there is a velocity gradient present. The black line within the figure indicates that the gradient steepens toward the centre. This feature could indicate gas infall towards the centre of the ridge (Hacar et al. 2017; Inoue et al. 2018) but the complexity of

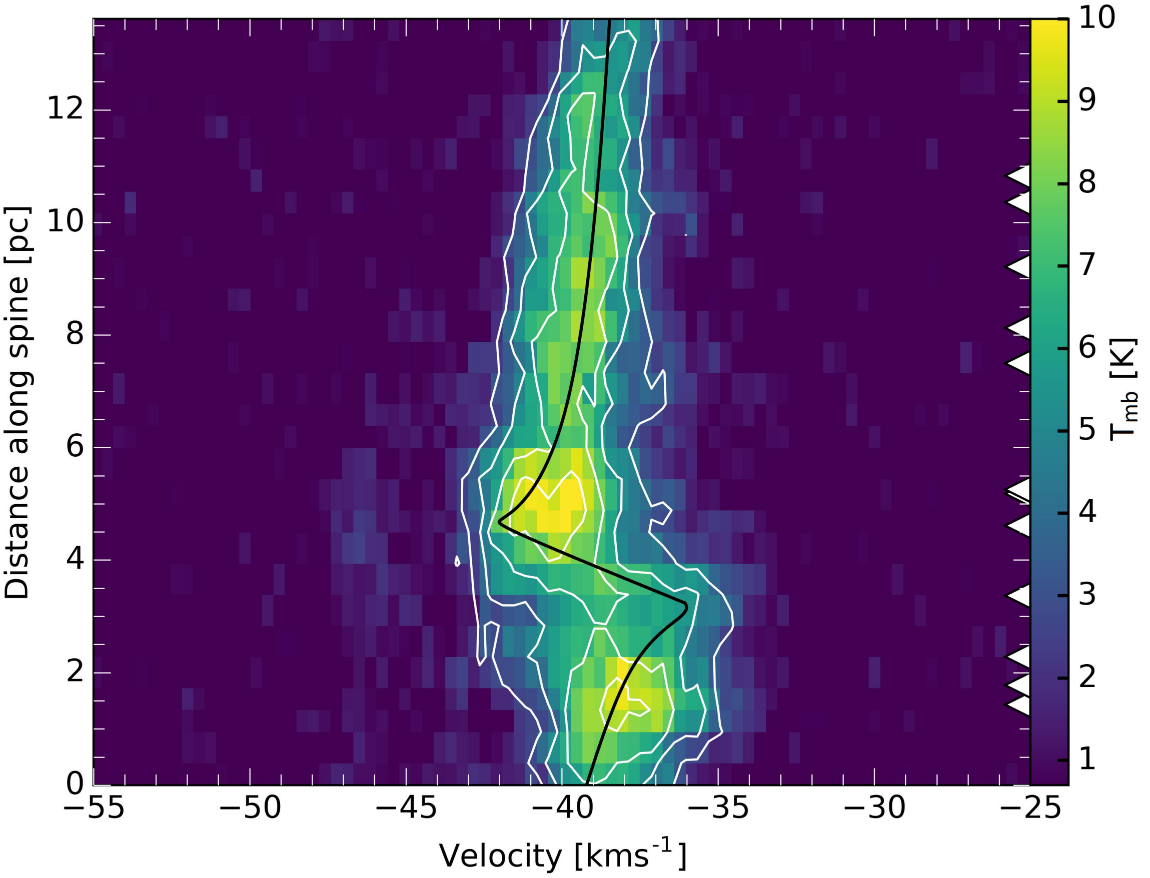

Figure 4.11. Position-velocity diagram of ^{13}CO along the spine centre from 0 and 13.6 pc. The solid black line traces the centre of the emission and the solid white contours mark the intensity of the emission at 3, 5, 7 and 9 K. White triangles mark the clump positions.

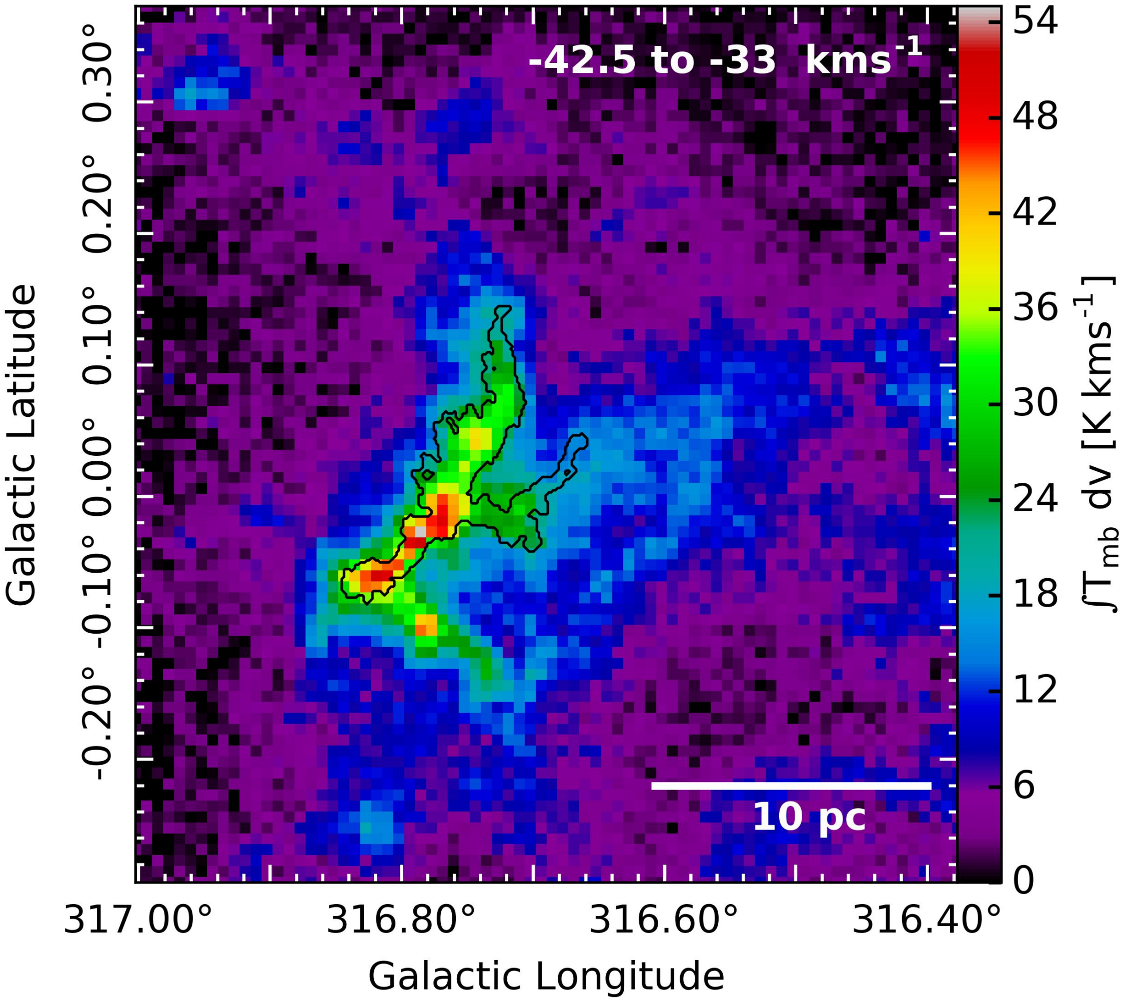

Figure 4.12. ^{13}CO (1–0) integrated intensity of G316.75 between -42.5 and -33 km s^{-1}. The black contour is identical to that in Fig. 4.7.

the region stops us from making robust conclusions about the origin of this velocity gradient. The ^{13}CO (J=1–0) velocity dispersion map exhibits, with the exception of a couple of pixels with unresolved NH$_3$ (1–0) velocity components, larger values than any of the other two tracers. One can observe with values as high as σ = 3.5 km s^{-1} in the active region. As for the other two tracers, large velocity dispersion peaks are also matched by large velocity gradients (Fig. 4.8).

In Fig. 4.12 I show the integrated intensity of the ^{13}CO (J=1–0) line over a larger field than that shown in Fig. 4.7d. On this image, one can see that there is a significant amount of diffuse emission surrounding the ridge, with a clear asymmetric

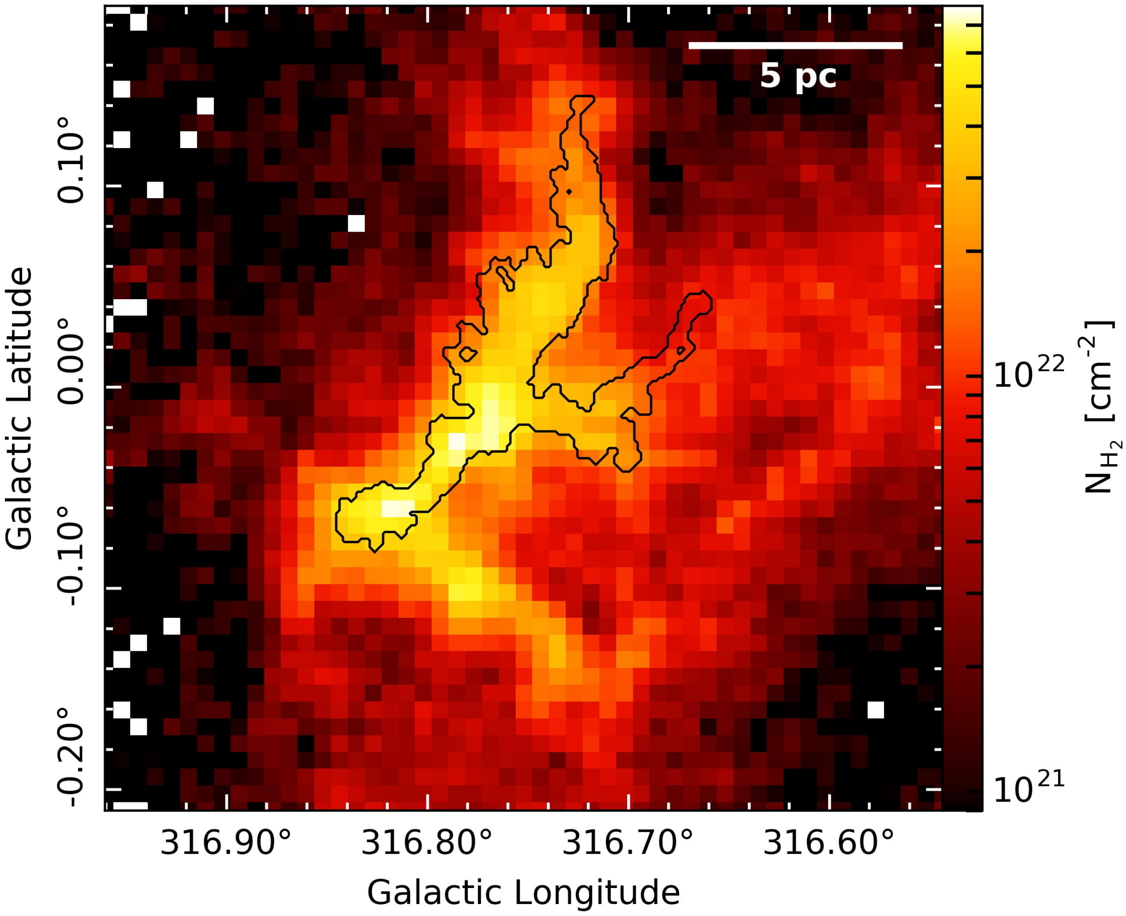

Figure 4.13. H_2 column density map derived assuming LTE approximation using ^{13}CO and ^{12}CO. The black contour and mask used are identical to Fig 4.7.

morphology of the emission with respect to ridge's spine, most of it being located south of the ridge. This map also reveals an additional filamentary structure extending perpendicularly to the southern end of the active part of the ridge. This is not seen in the dense gas tracers, but does match a warm and low column density structure present in the *Herschel* column density map (see Fig. 4.1). The ^{13}CO (J=1–0) spectra observed along this structure have low intensities but spread over a large velocity range > 10 km s^{-1}. To characterise emission that cannot be disentangle from the background galactic plane emission using dust continuum, I calculate the H_2 column density from ^{13}CO using LTE, following the methodology presented in Sec. 3.1. The H_2 column density map calculated by this method has been shown in Fig. 4.13.

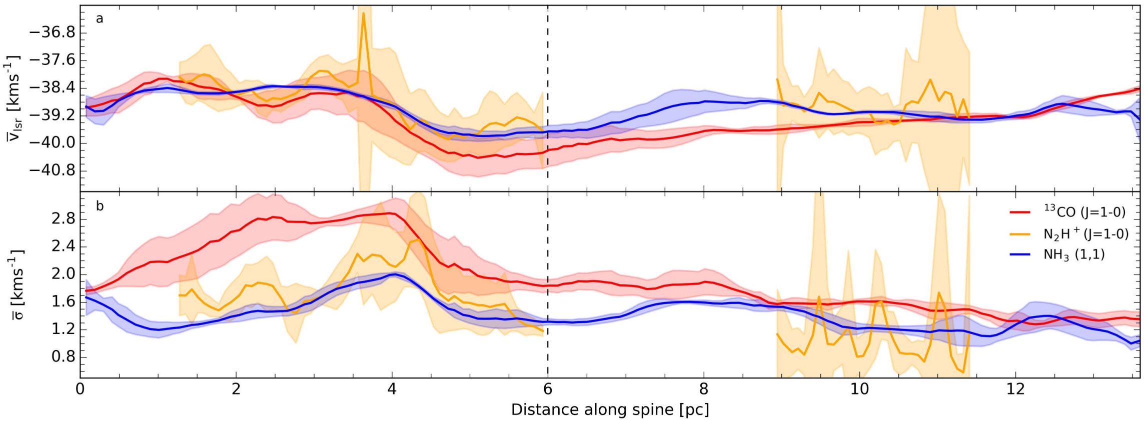

Figure 4.14. Longitudinal centroid velocity **(a)**, and velocity dispersion **(b)** in km s^{-1} for the molecular transitions shown in Fig. 4.7 averaged over the same width and length as Fig. 4.5. The solid red line is ^{13}CO (1–0), the solid yellow is N_2H^+ (1–0) and the solid blue is NH_3. The thin black vertical dashed line marks the separation between the active half of the ridge (left) and the quiescent half (right). Translucent regions shows the 1-sigma uncertainty values.

4.5.4 Comparison of the gas kinematics

In order to get a more concise view of the ridge kinematics, I computed the centroid velocity and velocity dispersion profiles of ^{13}CO (1–0), NH_3 (1,1) and N_2H^+ (1–0) in both longitudinal and transverse directions. The longitudinal profiles (see Fig. 4.14) for the centroid velocity show a mostly smooth velocity gradient along the ridge that steepens at around 4-5 pc (see also Fig. 4.11). Owing to its higher angular resolution, the N_2H^+ profile shows more small-scale structures that are not recovered in the other two profiles. Regarding the velocity dispersion, it is quite clear that the velocity dispersion traced by ^{13}CO (1–0) is larger than the other two dense gas tracers everywhere in the ridge. NH_3 (1,1) and N_2H^+ (1–0) also show larger velocity dispersions in the active part of the ridge, however not to the same extent as ^{13}CO. The transverse profiles (see Fig. 4.15) are less structured than the longitudinal ones. The active region displays a small transverse velocity gradient, mostly evident in ^{13}CO, while its quiescent counterpart seems to be flat. Regarding the velocity dispersion, the transverse profiles show similar trends as the longitudinal ones for both parts of the ridge.

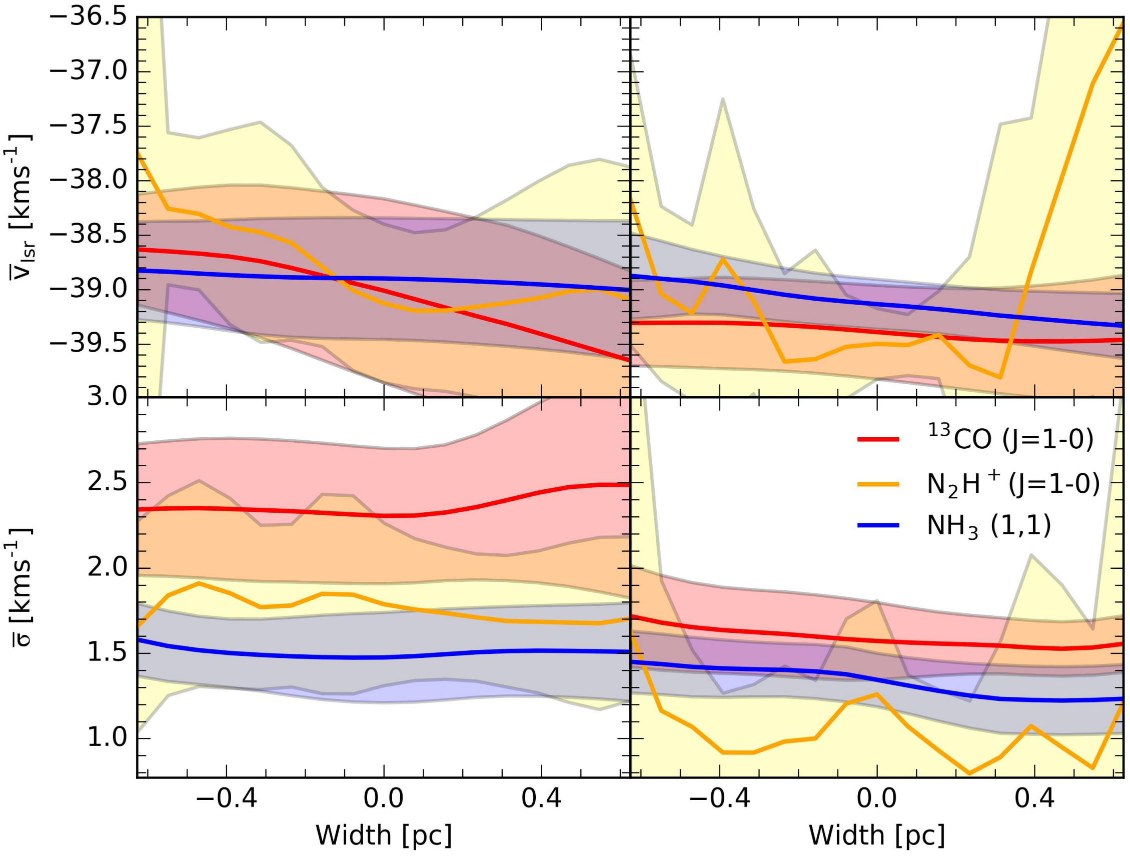

Figure 4.15. Transverse centroid velocity (**top**), and velocity dispersion (**bottom**) profiles are shown using the same molecular transitions and line colours shown in Fig. 4.14. Profiles are averaged over the same range as Fig. 4.6 for the active region (**left** column) and quiescent regions (**right** column). Translucent regions describes the 1-sigma uncertainty values.

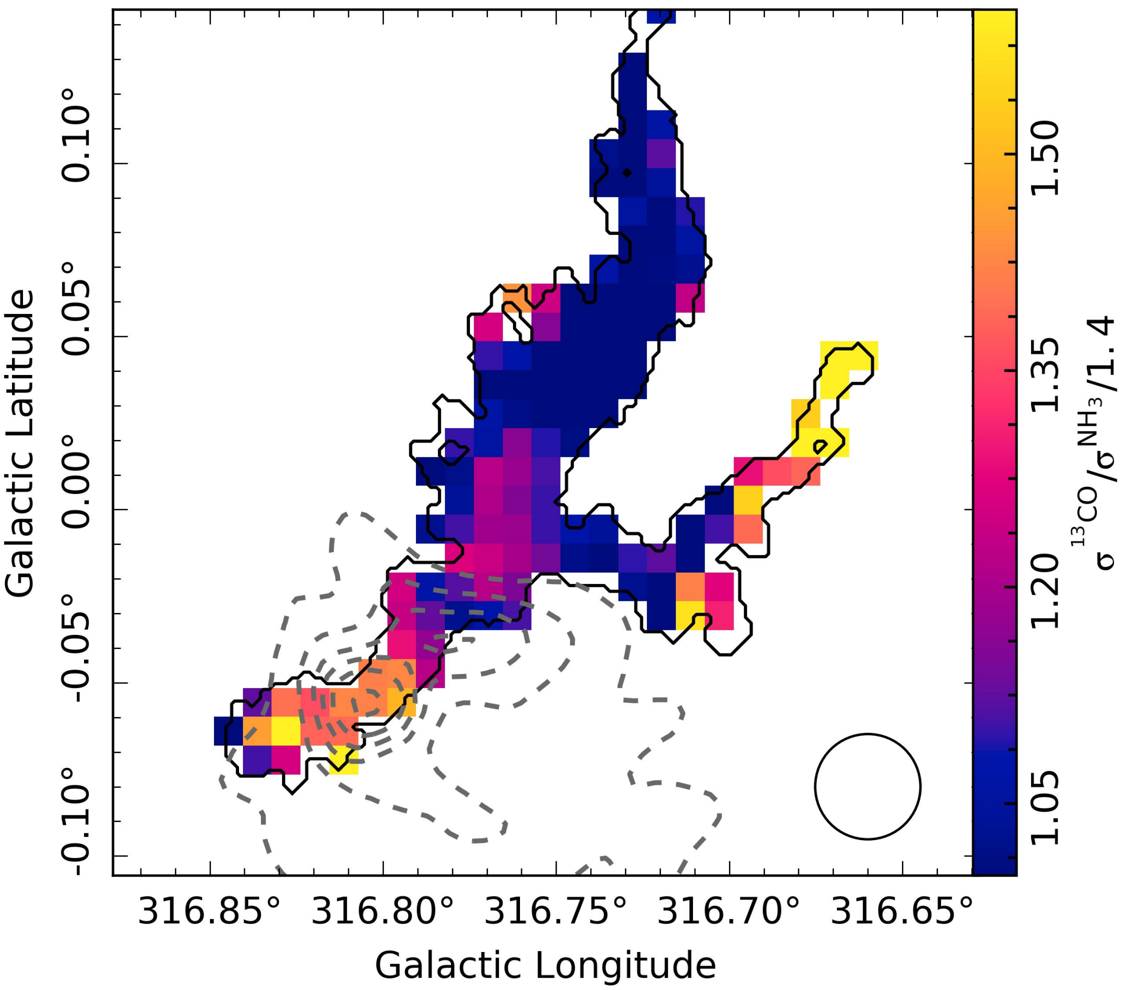

Figure 4.16. Ratio map of ^{13}CO against NH_3 velocity dispersion divided by the mean value of the ratio in the quiescent region, (i.e 1.4). The black contour and mask used are identical to Fig 4.7. Dashed grey contours show SUMSS radio emission using the same contour levels presented on Fig. 1.7. The open black circle shows the beam size of the ratio map. Large values seen on the right side of the image are due to low S/R.

The measured ^{13}CO velocity dispersion is, on average, larger than the dense gas tracers. This is generally the case in any star-forming cloud as ^{13}CO tends to tracer more diffuse gas. However, one would like to evaluate to what extent feedback from the embedded O-stars are contributing to this increase. For that purpose, I convolved the ^{13}CO (1–0) data to the NH_3 (1,1) resolution, and regridded the data to the same grid. The velocity dispersion map was then recalculated for ^{13}CO to compute the ratio of ^{13}CO (1–0) to NH_3 (1,1) velocity dispersion (see Fig. 4.16). On average, the ^{13}CO (1–0) velocity dispersion was found to be 1.4 times larger than the NH_3 (1,1) velocity dispersion in the quiescent part of the ridge where feedback from O-stars is minimal. This confirms that ^{13}CO includes large velocity dispersion gas that is not probed with dense gas tracers. Taking the ratio, 1.4 as the non-feedback-contaminated velocity dispersion ratio between the two tracers, one can then evaluate what is the contribution of feedback on the ^{13}CO (1–0) velocity dispersion by dividing the velocity dispersion ratio map by 1.4. The resulting map is shown in Fig. 4.16. Here, one can see that the active part of the ridge exhibits up to 65% larger velocity dispersion ratios than the average value of 1.4. The spatial correlation of this increase with respect to the location of the embedded O-stars strongly suggests that the increase is due to stellar feedback.

Table 4.4. Table with derived average values for both parts of the ridge. Except for ^{13}CO-based measurements, the averages tabulated use the straightened values over the same width and length as in Fig. 4.5, whereas ^{13}CO-based values are averaged over a 2.82 pc scale (i.e. 1.41 pc either side of the ridge). All mean values use 1-sigma errors. The remaining errors are calculated using error propagation unless otherwise stated.

Region	$\overline{\sigma}_{\mathrm{eff}}$ ^{13}CO (km s^{-1})	$\overline{\sigma}_{\mathrm{eff}}$ NH$_3$ (km s^{-1})	$\overline{\sigma}_{\mathrm{eff}}$ N$_2$H$^+$ (km s^{-1})	n_{c}^{a} (10^4 cm^{-3})	$\overline{n}$ (10^4 cm^{-3})	λ_{J} (pc)	λ_{cyl} (pc)	M_{J} (M$_\odot$)	M_{cyl} (M$_\odot$)	$\lambda_{\mathrm{J}}^{\mathrm{eff}}$ (pc)	$\lambda_{\mathrm{cyl}}^{\mathrm{eff}}$ (pc)	$M_{\mathrm{J}}^{\mathrm{eff}}$ (M$_\odot$)	$M_{\mathrm{cyl}}^{\mathrm{eff}}$ (M$_\odot$)
Active	2.4±0.4	1.5±0.2	1.5±0.4	17±4	2.0±0.9	0.18±0.04	0.21±0.02	4±1	450±90	1.10±0.31	1.33±0.27	971±531	2803±739
Quiescent	1.8±0.2	1.3±0.2	0.6±0.5	7±2	1.0±0.4	0.21±0.05	0.29±0.02	4±1	302±55	1.38±0.36	1.83±0.30	925±462	1888±443

[a] Uncertainty estimated from 1-sigma confidence in χ^2 residuals in Sec. 4.6.

$\overline{\sigma}_{\mathrm{eff}}$ is the mean effective dispersion for the transitions listed, n_{c} is the central number density and $\overline{n}$ is the mean number density. λ and M refers to fragmentation length and mass, where the subscript J refers to Jeans values and cyl refers to cylindrical fragmentation values. Any superscripts with eff show that the fragmentation scale was calculated using $\overline{\sigma}_{\mathrm{eff}}$ rather than the thermal dispersion.

4.6 Analysis

In the following section we evaluate the ability of the G316.75 ridge to collapse and fragment and explore if current feedback has the capacity to disrupt the ridge.

4.6.1 Density, mass-per-unit-length, and effective velocity dispersion

In order to determine the global stability and fragmentation ability of the ridge, one needs to compute a number of key physical quantities, the first of which is the average volume density of the ridge, $\overline{\rho}$. Assuming that the ridge is cylindrical, $\overline{\rho} = M/(\pi R^2 L)$, where L is the length, M its mass, and R its radius. Radius of the cylinder is $R = 0.63 \pm 0.08$ pc to match the transition between the dense filament and the diffuse emission. The mass within this cylinder is calculated using the transverse H_2 column density shown in Fig. 4.4. In observations, the number density, $\overline{n} = \overline{\rho}/(\mu m_{\mathrm{H}})$, of H_2 is often preferred to the mass density. All quantities for both quiescent and active parts are given in Table 4.2. I note that $\overline{n}$ is 2×10^4 and 1×10^4 cm^{-3} for the active and quiescent regions respectively, which are high average values over such a large structure.

A second important quantity to compute is the mass-per-unit-length (M_{line}) of the ridge. The M_{line} has been calculated using the transverse H_2 column density shown in Fig. 4.4. For this analysis, we compute the M_{line} at every pixel along the Hessian derived spine and summed the mass out to a radius of 0.63 pc (width of 1.26 pc). This gives us the local mass-per-unit-length. Figure 4.4 provides a visual representation of the each profile used when when calculating the M_{line}. The M_{line} was computed twice, once using the *Herschel* H_2 column density map, $M_{\mathrm{line\text{-}dust}}$, and once using a H_2 column density map computed from the ^{13}CO (1–0) integrated intensity, $M_{\mathrm{line\text{-}13CO}}$ (see Fig. 4.13 and Sec. 4.5.3 for details on how the ^{13}CO-based H_2 column density map is obtained). The reason behind these two sets of M_{line} is that, as

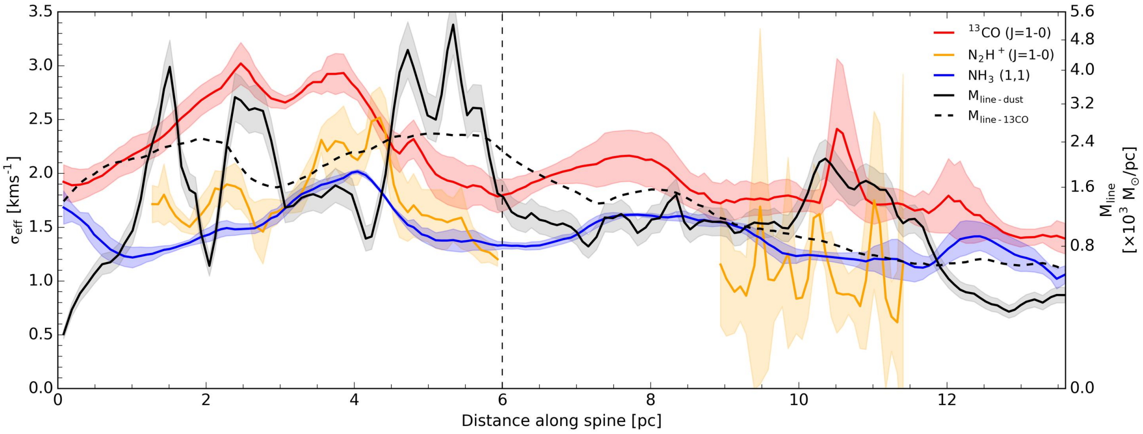

Figure 4.17. Longitudinal effective velocity dispersion and corresponding $M_{\text{line}}^{\text{crit}}$ are shown using the same molecular transitions and line colours as shown in Fig. 4.14. Also plotted are $M_{\text{line-dust}}$ and $M_{\text{line-13CO}}$ (and corresponding $\sigma_{\text{eff}}^{\text{crit}}$). Except for ^{13}CO-based measurements, the values are averaged over the same width and length as in Fig. 4.5, whereas ^{13}CO-based values are averaged over a 2.82 pc scale (i.e. 1.41 pc either side of the ridge). The y axis on the left portrays the velocity dispersion and the y axis on the right is the M_{line}. The axis appears stretched by a square root scale since, in the critical case, $\sigma_{\text{eff}} \propto M_{\text{line}}{}^{0.5}$. Translucent regions describes the 1-sigma uncertainty values each molecular line tracer. Uncertainty values are not shown for $M_{\text{line-13CO}}$ since the LTE method used in calculating $M_{\text{line-13CO}}$ result in uncertainties of a factor of $\gtrsim$2. These error bounds are large and reduce the clarity of the plot.

seen in ^{13}CO, the G316.75 ridge extends beyond the dense part characterised using *Herschel* data (R = 0.63 pc for the dense part, while R = 1.41 pc when including the diffuse gas traced by ^{13}CO). This implies that the measured ^{13}CO velocity dispersions include diffuse gas which is not included in the *Herschel*-based M_{line}. Therefore, for a fair comparison of the kinetic and gravitational energies of the ridge (see Sec. 4.6.3), ^{13}CO-based velocity dispersions have to be compared to ^{13}CO-based mass-per-unit-length measurements. I note that the $M_{\text{line-13CO}}$ does not require any background subtraction (whereas the dust derived H$_2$ column density map does, as explained in Sec. 4.4) since the LTE method allows us to only include emission over the velocity channels containing emission from the ridge (see Fig. 4.12).

Figure 4.17 shows how both M_{line} measurements vary along the ridge. The uncertainty shown for the dust derived M_{line} values is calculated from the distance error. Both $M_{\text{line-dust}}$ and $M_{\text{line-13CO}}$ are, on average, twice as large in the active part compared to the quiescent part. Interestingly we see that $M_{\text{line-13CO}}$ is not much different from the $M_{\text{line-dust}}$ despite encompassing about double the area. This is most likely due to a combination of two factors. First, in order to compute the ^{13}CO-based H_2 column density map, we used the local thermodynamic equilibrium (LTE) approximation which is known to underestimate column densities by a factor of ~ 2 (Szűcs et al. 2016). Second, cold dense regions such as within infrared dark clouds cause CO to deplete onto dust grains, which also leads to an underestimate of the H_2 mass (Hernandez et al. 2011). The significance of underestimating the mass in context of the analysis is discussed in the following Sections.

The third important quantity for stability analysis is the effective velocity dispersion of the gas, which can be calculated using Eq. (3.24). In Fig. 4.17 we plot the variation of σ_{eff} along the ridge for ^{13}CO (1–0), NH_3 (1,1) and N_2H^+ (1–0) and present their mean values for the active and quiescent regions in Table 4.4. For a matter of consistency with the M_{line} measurements, velocity dispersions have been averaged up to R=0.63 pc either side of the spine for both dense gas tracers, while up to R=1.41 pc for ^{13}CO. I note that the observed velocity dispersions can also contain contributions from unresolved systematic gas flows generated by collapse and rotation, and so it is unclear what fraction of the observed velocity dispersion is due to this or due the internal pressure of the cloud (Traficante et al. 2018). Therefore the effective velocity dispersion represents an upper limit for the kinetic pressure with the lower limit provided by the thermal sound speed.

Finally to characterise the fragmentation of the ridge, one needs to derive the central density of ridge n_c. For this purpose, the density of G316.75 has been modelled as a cylinder using a Plummer-like profile with $R = 0.63 \pm 0.08$ pc. Following the method described in Sec. 3.5.3 the Plummer-like profile has been modelled over the parameter space, n_c: 4–40×10^4 cm^{-3}; R_{flat}: 0.1–0.4 pc; p: 1–4 to obtain a best fit of the parameters. Dor the active and quiescent regions $n_c = 17\pm2\times10^4$ cm^{-3} and $n_c = 7\pm2\times10^4$ cm^{-3} respectively (see Table 4.4) where errors represent the 1-sigma

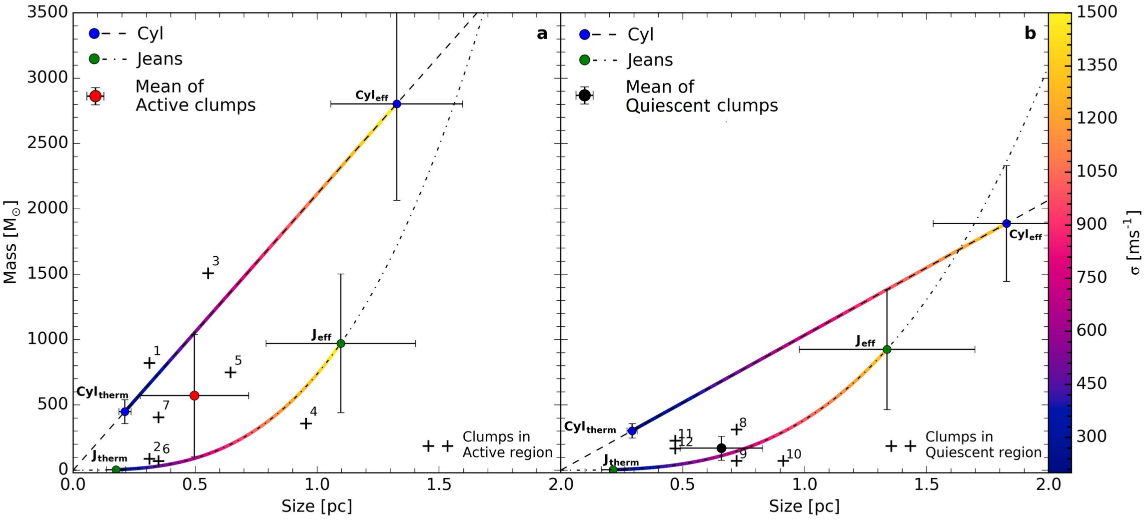

Figure 4.18. Fragmentation scales (both mass and length) for increasing values of velocity dispersion for the active **(a)** and quiescent **(b)** regions calculated using *Herschel* column density. The dashed-black line shows the cylindrical fragmentation case, while the dashed-dotted-black line shows the Jeans fragmentation case. The mass and length calculated for thermal and effective fragmentation modes are shown as blue and green circles. The coloured lines show how the mass and length fragmentation scales change with increasing velocity dispersion (from thermal to effective velocity dispersion (240–1520 km s^{-1}). The black pluses show the mass and minimum separation of the clumps tabulated in Table 4.1. The numbers ascribed to the clumps match the numbering given in Table 4.1. The red circle marks the mean mass and minimum separation of the clumps for the active region, and the black circle marks the mean mass and minimum separation of the clumps for the quiescent region. The errorbars for the mean show the 1-sigma spread in values.

confidence in the χ^2 residuals to estimate the spread of values. Doing this, I note that, even though n_c is well characterised, R_flat and p are degenerate (i.e., the data does not have enough angular resolution to properly characterise R_flat). However, since only n_c is needed, this is not an issue.

4.6.2 RIDGE FRAGMENTATION

With both n_c and $\overline{n}$ characterised, we follow Sec. 3.5.3 to compute the length and mass scales using Jeans fragmentation and cylindrical fragmentation for the active and quiescent regions, and their respective variations from the thermal case to the effective case. By doing this, one can investigate what fragmentation mode better represents the fragmentation occurring within the ridge, and whether this changes between the active and quiescent regions. We present this fragmentation analysis in Fig. 4.18. On the same figure we over-plot the observed clump masses vs the distance to their nearest neighbour $\lambda_{\rm sep}$ (see Table 4.1) where $\lambda_{\rm sep}$ is assumed to be a reasonable estimate of the fragmentation length scale, albeit the inclination angle of the ridge with respect to the line of sight is not taken into account). All quantities presented in Fig. 4.18a and Fig. 4.18b are also given in Table 4.4 and Table 4.2. From these plots, one can see that the fragmentation of the G316.75 ridge into clumps is better explained by the thermal case than by the effective case. This indicates that the large velocity dispersion measured does not greatly contribute to support the gas against fragmentation. It is also interesting to note that all the clumps in the quiescent region are compatible with Jeans fragmentation while it is not necessarily the case for the clumps in the active region. Even though we expect changes in the fragmentation scale of filaments with changing gas properties (Kainulainen et al. 2013), one has to keep in mind that the limited angular resolution of our H_2 column density map prevents us from drawing robust conclusions from this fragmentation analysis. For a correct assessment of fragmentation, one would need to resolve down to the scales of individual cores (θ = 0.75$''$=0.01 pc).

4.6.3 RADIAL STABILITY OF THE RIDGE

The three variables that determine the radial stability are the mass, kinetic energy and the potential energy. However, the G316.75 ridge is a 13.6 pc long filamentary cloud with an aspect ratio of $\sim$ 11. Therefore when trying to determine how likely it is that the ridge will globally collapse or expand, models that approximate interstellar filaments as cylinders are the most appropriate. This can be achieved by defining the radial stability against collapse in terms of per unit length. Doing this, the stability is determined by the mass per unit length ($M_{\rm line}$), the kinetic energy per unit length ($U_{\rm line}$) and the potential energy ($\Omega_{\rm line}$).

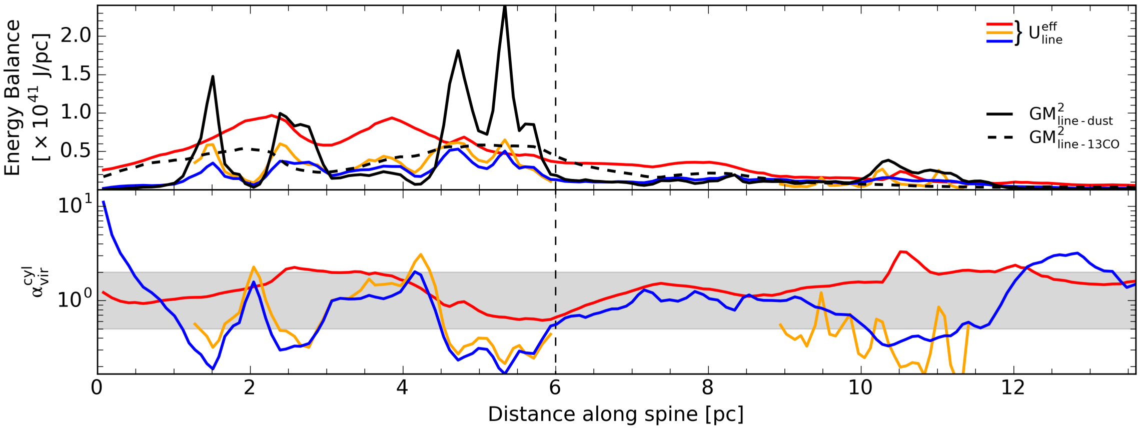

Figure 4.19. Top panel: Kinetic energy per unit line as estimated using the same molecular transitions and line colours as shown in Fig. 4.14. Also plotted is $GM^2_{\rm line}$ (which is proportional to the potential energy per unit line Ω_{line}) calculated using *Herschel* (black solid line) and ^{13}CO (1-0) (black dashed line). **Bottom panel:** Virial ratio as estimated using the same three molecular transitions. The grey shaded region highlights where the gas has a virial ratio between 0.5 to 2, which indicates where the gas is bound.

The derivation for these quantities has been shown in Sec 3.5.4 and show that in order to characterise the energy balance of the ridge, one needs $\sigma_{\rm th}$, $\sigma_{\rm eff}$, and $M_{\rm line}$ at every position along the spine of the ridge. These quantities are presented in Fig. 4.17 (see Sec. 4.6.1)

The kinetic energy per unit length $U_{\rm line}$ has been computed six times in total, thrice for thermal support case $U^{\rm th}_{\rm line}$ and thrice for the turbulent support case $U^{\rm turb}_{\rm line}$, using $\sigma_{\rm eff}$ from ^{13}CO (1–0), NH$_3$ (1,1) and N$_2$H$^+$ (1–0) as a function of the position along the ridge spine and has been shown in the first panel of Fig. 4.19. This allows one to track how $U_{\rm line}$ varies for different density regimes and if turbulence plays a role in determining the stability of the ridge. I note that the thermal cases for the dispersion and for the kinetic energy are a lot smaller than the turbulent case, so much so that they cannot be seen on Fig. 4.17 and Fig. 4.19 respectively. This already suggests that the entire cloud is either rapidly collapsing radially, or that another source of support, beyond thermal support, is preventing the global collapse of the ridge.

Additionally, after plotting $GM_{\rm line}^2$ on the first panel of Fig. 4.19, which is proportional to $\Omega_{\rm line}$, one can see that $GM_{\rm line}^2$ is comparable to $U_{\rm eff}$ for almost the entire ridge. This is despite the large differences in average properties of both halves of the ridge. The uniformity of the ridge energy budget between active and quiescent halves of the ridge is emphasised when computing its virial ratio, $\alpha_{\rm vir}^{\rm cyl}$, across three density regime (using $\sigma_{\rm eff}$ for ^{13}CO, NH$_3$ and N$_2$H$^+$). The viral ratio assesses how bound the ridge is as a function of density and position along the ridge and by using 3 different density tracers, one can assess how the boundedness changes as the gas measured is more or less diffuse. In Fig. 4.19 $\alpha_{\rm vir}^{\rm cyl}$ as a function of length. Here, one can see that both halves are very similar, and when only considering $\alpha_{\rm vir}^{\rm cyl}$, it is not obvious which half contains the four O-type stars. The only distinguishing feature between the active and quiescent regions is that $\alpha_{\rm vir}^{\rm cyl}$ varies slightly more in the active region with a dex of 0.6 compared to 0.3 in the quiescent region (as measured in NH$_3$ (1,1)), which could be the result of local compression or ejection of matter due to the local injection of momentum and energy by the surrounding young high-mass stars (Fukuda & Hanawa 2000). Additionally, in contrast to the previous section (Sec. 4.6.2), non-thermal motions have been shown to play a dominant role in determining the radial stability of the ridge compared to its role in setting the fragmentation scale. All this strongly suggests that the physical process that sets the ratio of kinetic to gravitational energy is global to the ridge, and not set by local stellar feedback.

Furthermore, the ridge can be seen to be gravitationally bound (i.e., within the grey band on the bottom panel of Fig. 4.19) nearly everywhere, and in all tracers. Even the gas traced by ^{13}CO (1-0) is gravitationally bound, despite having larger velocity dispersions with visual signs indicating that this is somewhat powered by stellar feedback (see Sec. 4.5.4 and Fig. 4.16). The situation is compounded by the fact that the mass estimated from ^{13}CO is likely to be underestimated.

Finally, the $\alpha_{\rm vir}^{\rm cyl}$ traced with NH$_3$ significantly increases in value between a longitudinal offset of 0 and 1 pc. This can be explained by two scenarios. The upturn could be where H_2 column density is currently being pushed away by feedback, however this would be opposite to the observed trend everywhere else in the ridge. Or, it could be a consequence of having subtracted a too large H_2 column density background. This would reduce the ridge mass measured and would result in an overestimate of the virial ratio. This scenario is supported by the fact that $M_{\text{line-13CO}}$ in that part of the ridge (see Fig. 4.17) is 1.5 to 8 times larger than $M_{\text{line-dust}}$, the largest difference between the two M_{line} measurements.

4.6.4 Gas expulsion

It is often assumed that stellar feedback from OB stars is powerful enough to destroy the cloud in which they formed. Two important mechanisms that can cause this disruption are photo-ionisation of the gas and radiation pressure on dust grains. Depending on the cloud properties, these mechanisms can transfer enough momentum and energy to the gas and dust to counteract the gravitational potential of cloud. With four O-type stars already formed, one would expect that a significant fraction of mass within the G316.75 ridge is being pushed away by stellar feedback. In the following, I investigate what fraction of the ridge mass is currently being affected by these mechanisms.

Radiation pressure

As discussed in Sec. 1.5.3, one can use a critical mass surface density $\Sigma_{\text{gas}}^{\text{crit}}$ to determine where radiation pressure is able to disrupt the gas, given one has an estimate for radiation pressure present and has a measurement of the gas surface density, Σ_{gas}. In G316.75, only the active region contains high-mass stars hence we only model radiation pressure in this part of the ridge. To estimate the radiation pressure, we randomly inject a fully sampled IMF of a ~1000 $M_\odot$ cluster across length of the active region. Since locations containing large dust temperatures and H_2 column densities are likely to host more stars, the injection location was weighted using dust temperature and H_2 column density maps. More specifically, the dust temperature and H_2 column density maps were normalised together so that high dust temperatures and H_2 column densities had a higher injection probability compared to low dust temperatures and H_2 column densities. Since we know there are two O-stars near the radio emission peaks at 2 and 4 pc, these stars are manually injected at these locations rather than being randomly injected (See Fig. 4.20).

Figure 4.20 shows only 8–11% of the mass in the active region is super-Eddington showing that the momentum injected by the stars' radiation is not enough to destroy G316.75, except in the immediate vicinity of the O-stars. Here the lower mass surface density is likely a side-affect of previous gas expulsion. I also show $\Sigma_{\rm gas}^{\rm crit}$ in the case where a 30 $M_\odot$ star is present in every pixel along the ridge (the same is also displayed for 20 and 10 $M_\odot$ stars). Even though this extreme scenario is unrealistic, it illustrates that the already present dense clumps would still remain bound, and in the case of 20 $M_\odot$ stars (which is still unrealistic) most of the ridge mass would remain bound. The large mass surface density of G316.75 protects the dense gas it from radiation pressure and only unrealistic numbers of high-mass stars would manage to change this.

In making these calculations, a number of assumptions were made that can over or underestimate $\Sigma_{\rm gas}^{\rm crit}$. Firstly, it was assumed that the IMF is fully sampled. If there are fewer stars, or a few very massive stars, this can over and underestimate $\Sigma_{\rm gas}^{\rm crit}$ respectively. Secondly, the potential of the ridge itself has been neglected, and it has been assumed that the stars are all located at the centre of the filament where all the luminosity of a star is absorbed by the line of sight column density at the centre. This could underestimate the impact the stars could have.

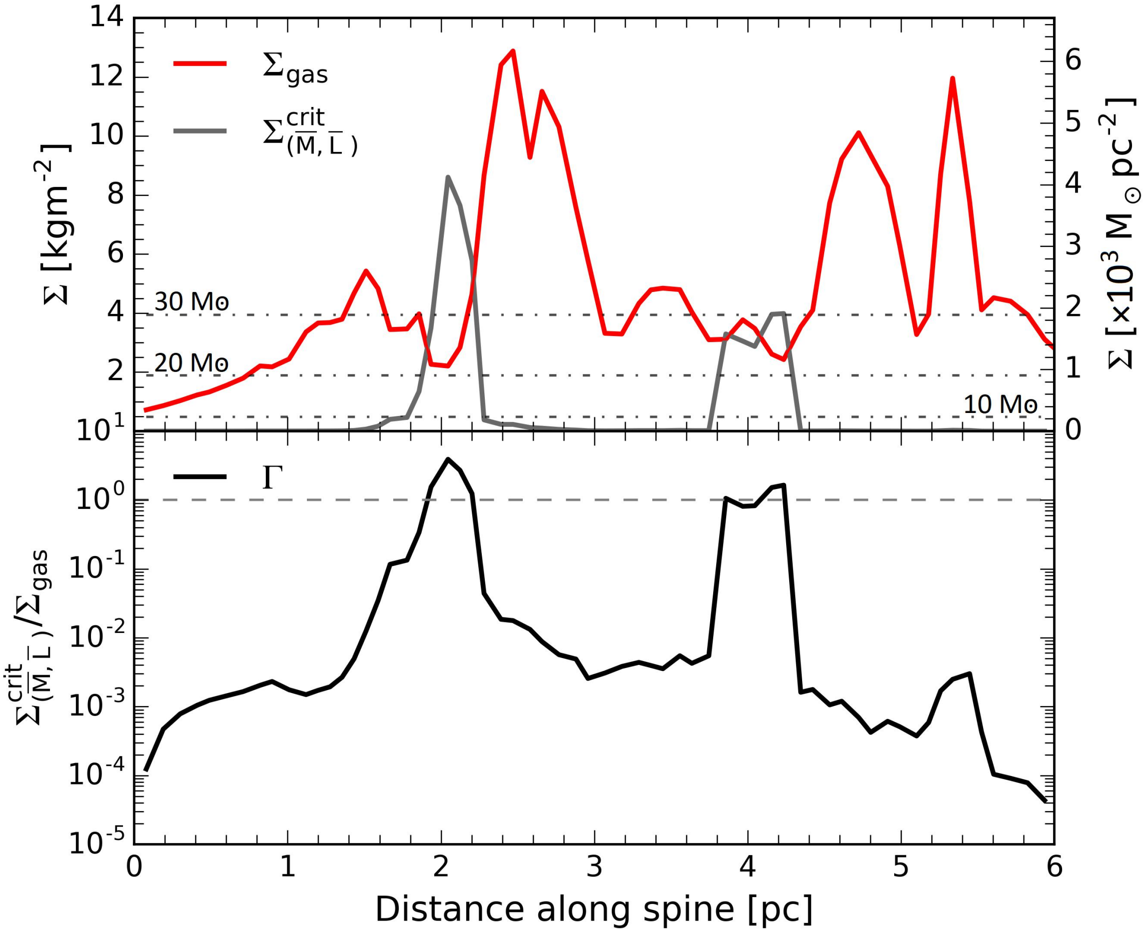

Figure 4.20. Gas surface density (solid red) and estimated critical gas surface density (solid grey) for the active part of G316.75 **(top)**, and corresponding Eddington ratio **(bottom)**. I note that here, the gas surface density is only half of the observed G316.75 mass surface density as massive stars are assumed to be located at the centre of the ridge. Grey dash-dotted lines in the **top** panel labeled as 30, 20 and 10 $M_\odot$ show the critical gas surface density if a star of that mass were placed every ∼ 0.08pc (in every pixel) along the ridge spine. The horizontal grey-dashed line in the **bottom** panel shows where the Eddington ratio is equal to 1.

Ionised gas

As a result of their large UV luminosities, OB stars efficiently ionise the surrounding gas. The sound speed of this newly ionised gas is often larger than the escape velocity of the parent molecular cloud, leading to its photoevaporation. Here we calculate the ability of the G316.75 O-stars to ionise the ridge, and compare this to observed ionised gas mass.

Using Eq. 3.17 we first estimate that the amount of gas that has already been ionised is 1700 ± 500 M$_\odot$ using Eq. 3.17, where the uncertainty has been estimate using Monte-Carlo error propagation using the distance uncertainty the rms uncertainty of the radio observations. This only represents $\sim$ 8% of the ridge mass, which is far from the high ionisation mass fractions found in a number of numerical simulations (Geen et al. 2016; Kim et al. 2018) (though I note that these simulations model turbulent spherical clouds). Obviously, we can invoke the fact that this cloud is at a very early stage of its evolution, but the dynamical age of the HII region (see Sec. 4.3) suggests that at least one of the most massive stars has been around for a couple of Myr. Another explanation could be that the ionisation front is quickly stalled by large recombination rates. In order to check whether this scenario is viable, Eq. (3.23) was used to calculate how long it takes for an HII region to expand into the active part of G316.75 using the ionisation parameters derived in Sec. 4.3, but using a range of electron densities (i.e. $\overline{n}_{\rm H} = 2 \times 10^4$ cm^{-3} – $\mathcal{N}_{\rm i} = 1.26 \times 10^{49}$ s^{-1}– $\alpha_{\rm B} = 3.47 \times 10^{-13}$ cm$^3 s^{-1}$). $\overline{n}_{\rm H}$ is not varied since $\overline{n}_{\rm H}$ represents the neutral hydrogen present at the cross-section of the cylinder, which we know from the column density. However, the exact value of $n_{\rm e}$ (and $n_{\rm p}$, which is assumed to equal $n_{\rm e}$) is not known in between the ionising star and the cylinder cross-section since $n_{\rm e}$ is not confined to a cylindrical geometry (and so does not necessarily equal $\overline{n}_{\rm H}$)

For an ionising source placed within the filament, the total length of gas ionised either side of the source (i.e. $2 \times l_{\rm ion}$) in time is given in Fig 4.21. The case where

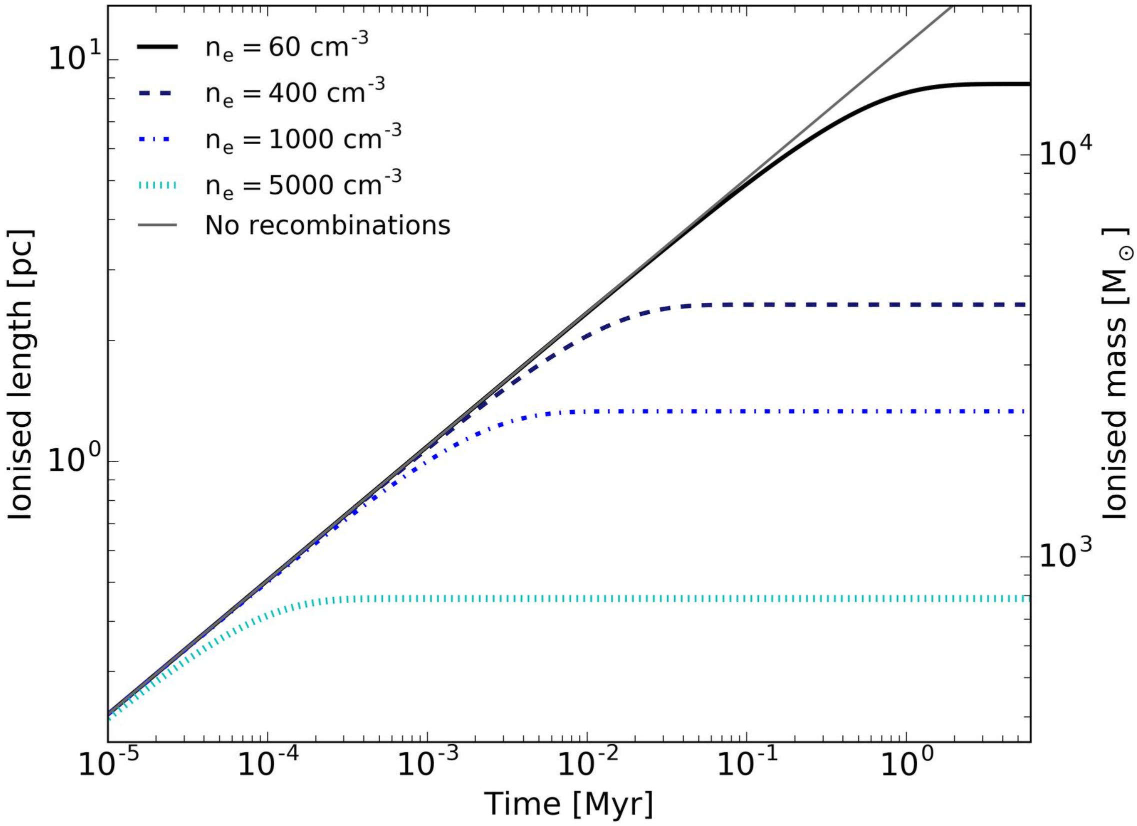

Figure 4.21. Time evolution of ionised length ($2\times l_{\rm ion}$) of a filament of density n=2×10^4 cm^{-3} exposed to the ionisation rate from an embedded O6 star. This calculation has been done for four different electron density values as indicated on the plot and for the case when there are no recombinations

.

recombinations are ignored are also plotted to show the role that recombinations have.

Figure 4.21 shows that when recombinations are ignored, or when $n_{\rm e}$ is low, an O6 type star will ionise the entire length of G316.75 by 2 Myr. Since we do not see the level of ionisation suggested by these calculations, this plot suggests that the electron density in between the ionising source and the filament cross section is closer to the density of the ridge. For instance, for $n_{\rm e}$=5000 cm^{-3}, 800 M$_\odot$ of gas is predicted to be ionised over a length of 0.5 pc, which better matches the ionised mass and length scales that are observed in G316.75. We therefore propose that the small ionised gas fraction of G316.75 is caused by large electron densities, which are the result of the large H_2 gas densities in the direct vicinity of the ionising high-mass stars. As a result, the ridge itself remains mostly unaffected by ionisation.

4.7 DISCUSSION

In the following discussion we compare and contrast the properties of the two halves of the G316.75 ridge. By assuming that the gas properties of the quiescent half provide a reasonable proxy for those of the active half before the formation of OB stars, we are able to draw some conclusions on the impact of stellar feedback. We will also briefly discuss a possible mechanism for the formation of the ridge itself.

4.7.1 THE STAR FORMATION HISTORY OF G316.75

As discussed in Sec. 4.3, the radio continuum emission observed in the G316.75 ridge is compatible with the presence of a ~ 1000 $M_\odot$ embedded cluster in the active part of the ridge. If one uses the dynamical age of the HII region (2 Myr) as a proxy for the age of the cluster, one can infer a star formation rate (SFR) of $\sim 5\times10^{-4}$ $M_\odot$ yr^{-1} (which matches cloud with similar masses to G316.75 Lada et al. (2010)). By assuming that the present embedded cluster in the active region formed within clumps similar to those currently present in the quiescent region, one can obtain a star formation efficiency per free-fall time, $\epsilon_{\rm ff}$. In the quiescent part of the ridge, the total clump mass identified was 845 $M_\odot$ ($\sim$ 11% of the mass of the quiescent half) with an average volume density and free-fall time of 0.86×10^5 cm^{-3} and 0.11 Myr, respectively. This implies a SFR per free-fall time, $SFR_{\rm ff}$ of $\sim$ 8.0×10^{-3} $M_\odot$ yr^{-1}, resulting in a $\epsilon_{\rm ff} \simeq 5 \times 10^{-4}/8.0 \times 10^{-3} = 6.3\%$ on the clump scale. If one instead assumes that the total clump mass present 2 Myr ago in the active region scales with either the length or the mass of the ridge, we obtain a range of total clump mass between $845 \times 6.01/7.58 = 670$ $M_\odot$ and $845 \times 11200/7700 = 1229$ $M_\odot$ respectively. Using

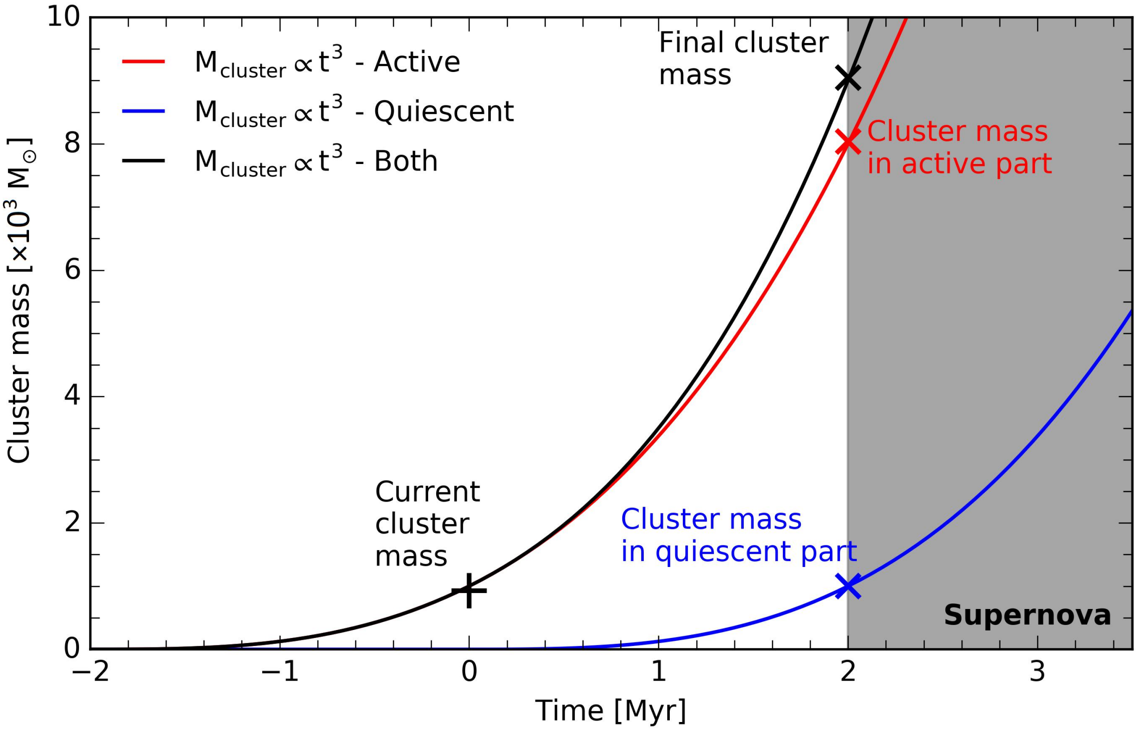

Figure 4.22. Illustrative figure of how the G316.75 stellar cluster mass might evolve in time. Time $t = 0$ Myr is now. The solid red, blue and black lines shows the time evolution of the cluster mass in the active region, the cluster mass in the quiescent region and the combined cluster mass respectively. Grey shaded region labeled as 'supernova' indicates when a supernova explosion is expected. Labeled markers indicate current and predicted cluster masses as discussed in Sec. 4.7.1.

these scaled masses, the revised clump-scale star-formation efficiency per free-fall time is: $\epsilon_{\rm ff}= 6.3^{+1.6}_{-2.0}\%$.

What we now observe in the active region is a total clump mass of 3994 M$_\odot$. It is these clumps that will form the next generation of stars therefore, with an average density and free-fall time of 2.46×10^5 cm^{-3}, 0.06 Myr respectively, the SFR$_{\rm ff}$ for this second generation of clumps is $\sim 64.3 \times 10^{-3}$ M$_\odot$ yr^{-1} showing that the total clump mass and SFR$_{\rm ff}$ are 3.4 and 8 times larger than in the quiescent region. As shown by Ginsburg et al. (2017) in the W51 region, it is very likely that the change in these clump properties is the result of stellar feedback via increased gas temperature and local gas compression (see clumps #1 and #3 in Fig. 4.4). Given the feedback's inefficiency at unbinding the dense gas (see Sec. 4.6), it is reasonable to assume that

$\epsilon_{\rm ff}$ will, at the bare minimum, remain constant. In fact, some studies suggest that $\epsilon_{\rm ff}$ increases with time as $\epsilon_{\rm ff} \propto t^2$ (Lee et al. 2016). The implication of a constant $\epsilon_{\rm ff}$ would be that in the next 2 Myr, another $\sim$ 9000 $\mathrm{M}_\odot$ worth of stars could form, assuming that the currently present clumps in the quiescent region evolve in a similar way to the active clumps. Assuming the current cluster remains bound, this would lead to a total stellar mass of $\sim 10,000$ $\mathrm{M}_\odot$, matching the mass definition limit for young massive clusters of 10^4 $\mathrm{M}_\odot$ (Portegies Zwart et al. 2010). These results are summarised in Fig. 4.22 where the G316.75 cluster mass is plotted as a function of time. In addition to these masses, we have added a $M_{\rm cluster} \propto t^3$ relationship, which fits the admittedly rather limited observational data rather well. Such accelerated SFR has also been derived by Lee et al. (2016) in order to explain the large dispersion of $\epsilon_{\rm ff}$ values observed in galactic giant molecular clouds. In the case of G316.75, the accelerated SFR would be the result of the increased mass fraction of the dense star-forming clumps in the active region due to gas accretion onto the clumps.

4.7.2 THE INEFFICIENCY OF STELLAR FEEDBACK AND RIDGE ORIGIN

When looking at the mid- to far-infrared composite image of G316.75 presented in Fig. 1.7, it is immediately obvious which part of the cloud is currently being affected by the vast amount of energy and momentum released by the embedded OB stars. However, when looking at the virial ratio profile along the ridge (Fig. 4.19), it is not obvious any more—the active part looks very similar to the quiescent part. This suggests that the process setting the ratio of kinetic to gravitational is global to the ridge and not due to local stellar feedback. An obvious candidate for such global process is radial gravitational collapse. Indeed, collapse is the expression of the conversion of gravitational energy into kinetic energy, and therefore naturally ensures that both quantities remain close to equipartition (Lee & Hennebelle 2016)

The inefficiency of stellar feedback at dispersing the ridge mass is further evidenced through our calculation of the ionised mass in the region. As shown in Sec. 4.6.4 only $\sim$8% of the ridge mass has been ionised so far. This is much lower than reported in simulations of cloud evolution with ionisation feedback, where fractions of 30–95% are reported at the extreme limits of their parameter space (e.g., Kim et al. 2018). In these simulations, the average cloud is expected to ionise $\sim$ 80% of their parent cloud mass after a couple of initial cloud free-fall times. Using Clarke & Whitworth (2015) to estimate the longitudinal free-fall time of G316.75, assuming the volume density in the quiescent region in Table 4.4, represents the initial density, the age of G316.75 is only 0.5 t_{ff}. However in this time, 5% of the mass in G316.75 has been converted into stars. Only after 1 cloud free-fall time are similar efficiencies observed in Kim et al. (2018) but $\sim$30% of the initial mass has also been ionised. The most likely explanation for the difference between our results and such numerical simulations lies in the difference in density structure at the time when the first ionising star was born. In these simulations, the cloud is modelled as a sphere of gas and ionising sources are created when the cloud is still in a porous state (where the clouds have not had time to collapse into single, dense structure). What this study suggests is that the ridge was already a single high-gas-density filamentary structure with a large aspect ratio before the OB stars began to ionise their environment. With such initial conditions, ionising photons are only able to ionise a very small fraction of the ridge mass (as explained in Sec. 4.6.4, where only 8% of the ridge mass is ionised), which limits the damage caused by ionisation when compared numerical simulations that use spherical initial conditions and low densities (n $\sim$100-1000 cm^{-3}).

A possible mechanism to rapidly compact a lot of mass into a ridge-like structure could be cloud-cloud collision. In order to test this idea in G316.75, ThrUMMS ^{12}CO (1–0) data was used in order to look for signatures in the most diffuse molecular gas observable. Figure 4.23 shows the ^{12}CO (1–0) spectrum averaged over the ridge. This spectrum shows two components, the one associated to the ridge in a

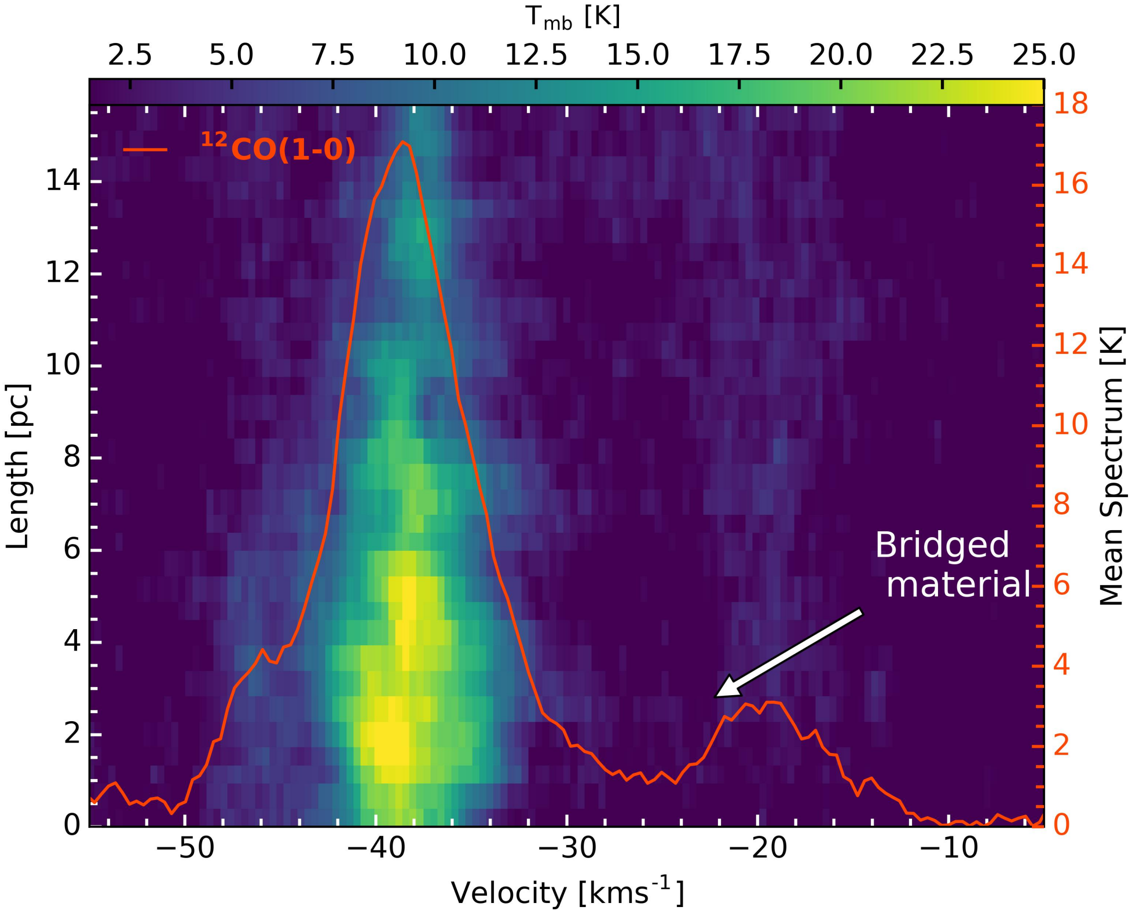

Figure 4.23. ^{12}CO (1–0) position-velocity diagram calculated using the same distance as Fig. 4.11. Over-plotted in orange is a ^{12}CO (1–0) spectrum calculated by averaging the ^{12}CO (1–0) spectra associated with G316.75, as defined by the black contour shown in Fig. 4.7. The y axis on the right side corresponds to the mean spectrum. Arrows indicate a possible bridge feature.

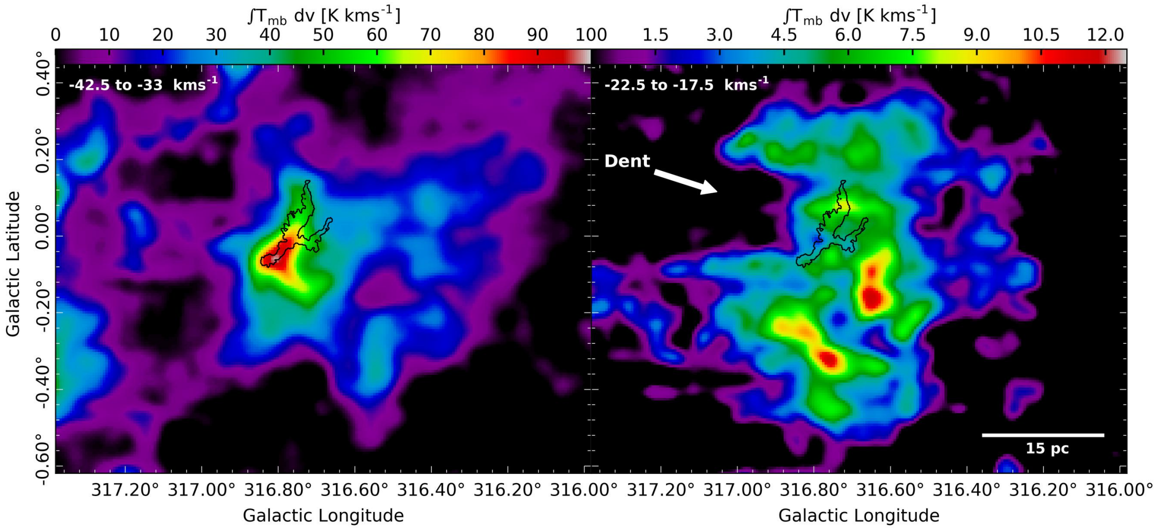

Figure 4.24. ^{12}CO (1–0) integrated intensity between -42.5 and -33 km s^{-1} (**left**) and -22.5 to -17.5 km s^{-1} (**right**). The black contour is identical to that in Fig. 4.7. Both maps have been convolved by a Gaussian of σ=1 arcmin to increase the signal to noise ratio.

velocity range -42.5 to -33 km s^{-1}, and a weaker one at velocities between -22.5 to -17.5 km s^{-1}. In Fig. 4.24 I show the integrated intensity maps of both components, convolved with a Gaussian of σ=1 arcmin to increase the signal to noise ratio. One can immediately see that the two clouds are spatially coherent in projection suggesting that they could be physically connected to each other. One can also see a drop in intensity morphologically similar to the G316.75 ridge, that may be the 'dent' left by the collision of the two clouds (Fukui et al. 2018). By taking the projected distance between the centre of the ridge and the dent, ∼20 pc, and the velocity difference between the two clouds, 18 km s^{-1}, we can determine that the collision may have happened $t_{\rm pcc} \simeq 1$ Myr ago. This estimate is biased by projection, where $t_{\rm pcc}$ represents the time when the two clouds collided. The true collision time is given by $t_{\rm cc} = t_{\rm pcc}\frac{\cos(\alpha)}{\sin(\alpha)}$, where α is the angle between the line of sight and the collision axis. In order to get a collision time $\geqslant 2$ Myr, that is to say, the dynamical age of the cluster (assuming the cluster age equals the dynamical age of the Hii region), $\alpha \leqslant \pi/7$ (i.e $\sim$ 27 deg).

Observational signatures of cloud-cloud collisions have been investigated in detail (e.g., Haworth et al. 2015; Bisbas et al. 2017). One key signature is the presence of bridges, that is to say, low column density gas at intermediate velocities between the systemic velocities of the two colliding clouds. These bridges are best seen in position-velocity diagrams (PV). For this reason, a ^{12}CO (1–0) PV diagram was computed along the spine of the ridge (see Fig. 4.23). On this figure, one can see the presence of a faint strip of emission connecting the two clouds that are reminiscent of bridging features seen in the aforementioned studies.

Finally, in their recent work, Inoue et al. (2018) and Whitworth et al. (2018) showed how massive filaments, such as ridges, may form via cloud-cloud collision using numerical and analytical methods, respectively. It is interesting to note that both studies predict properties that are similar to those observed in G316.75. In Inoue et al. (2018) the velocity and density profiles that develop along their simulated filament has many similarities with that of G316.75. In particular, their modelled filament shows a velocity gradient that flips near the centre of the ridge, which also coincides with large densities, reminiscent to what was observed at 4–5 pc along G316.75. On the other hand, Whitworth et al. (2018) predict the formation of bipolar HII regions similar to what is observed in G316.75. Even though we cannot be certain that cloud-cloud collision is the mechanism that led to the formation of G316.75, evidence presented here seems to point towards such a mechanism.

4.8 CONCLUSIONS

I used archive data of the G316.75 massive-star-forming ridge to determine how feedback from high-mass stars impacts the star forming properties. The G316.75 ridge is unique in the sense that half of the ridge is currently actively forming stars, while the other half is quiescent. Comparing and contrasting these two halves gives us the opportunity to quantify the impact of stellar feedback on the surrounding gas. By studying both halves in detail, I showed that despite the presence of four embedded

O-types stars, feedback is unable to unbind most of the ridge's mass over a large range of gas densities. Indeed, when looking at the ridge virial ratio there is very little difference between the active part (i.e., where the massive stars are), and the quiescent part. This is compelling evidence for feedback being inefficient at ionising and pushing away the ridge mass. From theoretical calculations, I showed that such feedback inefficiency is actually expected given the large average density and elongated morphology of the ridge. Due to this inefficiency and the sharp increase of the total clump mass over time (assuming the clumps in the quiescent region represent the active clumps at earlier evolutionary stage), I predict that G316.75 will continue producing stars to form a massive stellar cluster until a supernova explosion changes the star forming environment in the coming 2 Myr. After this point, the impact the supernova will have on the star forming ability of the ridge cannot be predicted.

I conclude that the initial morphology of a massive star-forming cloud plays an important role in its future evolution, especially with respect to the impact of the high-mass stars it will form. It is likely that a filamentary configuration strongly reduces the disruptive effects that feedback might have on the gas, and that such morphology could be the result, at least in the case of G316.75, of cloud-cloud collision. As shown in this study, in such configuration, stellar feedback from high-mass stars does very little to the dense gas already present, but is probably able to stop extended lower density gas from accreting onto the ridge. As shown in Fig. 1.7, a large volume around the ridge is directly being exposed to the ionising radiation of the G316.75 O-stars, and therefore the possibility for further gas accretion onto G316.75 is drastically reduced. In other terms, the main impact of feedback in G316.75 is gas exhaustion rather than gas ejection. These results have strong implications as to how feedback is implemented in cosmological and galaxy-scale simulations. In particular simulations reaching parsec-scale resolutions by using star-formation recipes (i.e., isotropic subgrid implementations of stellar feedback) might have to be revised to account for reduced impact of stellar feedback has in dense filamentary structures.

CHAPTER 5

TRIGGERED STAR FORMATION IN THE VICINITY OF HII REGIONS*

In this chapter, I use Galactic wide surveys to investigate whether expanding HII regions are able to enhance star formation efficiencies. The work presented here is part of ongoing work in Watkins, E., J., Peretto, N. & Zavagno, A. in prep.

5.1 INTRODUCTION

Determining the importance of triggering in setting Galactic star formation rates has been, and still is actively debated. This is due to the fact one cannot observationally track the time evolution of an individual cloud, nor track how it would have evolved without the presence of feedback. To overcome this observational limitation, we can instead compare the properties of a large sample of objects that potentially contain triggered star formation, to objects that are not triggered (Thompson et al. 2012; Kendrew et al. 2016; Palmeirim et al. 2017).

By investigating the number of dense clumps and young stellar objects (YSO's)

---

[*] The work presented here is part of ongoing work in Watkins, E., J., Peretto, N. & Zavagno, A. in prep

located near and away from HII regions over a large fraction of the Galactic plane, these authors all determine a similar increase (13–30%) in the number density of YSO's near HII regions. Thompson et al. (2012) and Palmeirim et al. (2017) also compared the dynamical age of HII regions to the age of the surrounding YSO's to show that the YSO's are younger than the HII regions, indicating they formed after the formation of the HII region. Although, the authors warn that they cannot distinguish YSOs whose formation is actually triggered from those that pre-existed within the gas.

A potential problem with these methods is they only compare clumps in the direct vicinity of HII regions to young, less evolved clumps (i.e., clumps that have no HII regions associated with them). If one wants to determine how the star formation efficiency (SFE) is affected by the expansion of HII regions and how triggering impacts the star formation rate in the Milky Way, one needs to use a large, unbiased sample, which includes objects that are more evolved and/or have developed their own HII regions. With the existence of *Herschel* Hi-GAL data (Molinari et al. 2010b) combined with the WISE HII catalogue Anderson et al. (2014b), the most comprehensive catalogue of Galactic HII regions, one is in the best position to undertake such a study.

For that purpose, this chapter makes use of a wide range of public datasets to determine how the SFE of clouds bounding HII regions differs from non-boundary clouds as a function of their evolutionary stage.

5.2 OBSERVATIONS AND CATALOGUES

Here, I provide details on each dataset used that is not already described in Chapter 4.

5.2.1 HI-GAL SOURCE CATALOGUES

The Hi-GAL catalogues contain 123210, 308509, 280685, 160972, and 85460 compact sources at 70, 160, 250, 350 and 500 μm respectively (Molinari et al. 2016). The catalogues currently covers Galactic longitudes of $|l| \leqslant 70^\circ$ out to a Galactic latitude of $\pm 1^\circ$. Sources were extracted using CuTEx to detect sources over a large range of background emission. The CuTEx algorithm locates sources by using a Hessian transform and calculates the flux of the sources by fitting a 2D Gaussian to the source along with a 2D surface to account for the background. The detection threshold has been defined using the second order derivative maps rather than constant flux brightness maps to account for the local curvature of the flux brightness maps. Using an RMS of 2 in the second order derivative maps, Molinari et al. (2016) estimate 90% of sources are successfully recovered.

Distance catalogue

Along with a source catalogue, the Hi-GAL team has a distance catalogue to 150226 sources (A. Traficante, private communication). These distances were assigned by cross examining all available distance tracers for each object, similar to how distances were assigned in the ATLASGAL 850 μm source catalogue Urquhart et al. (2018). If maser parallax measurements were available, the source distance could be determined with a high degree of accuracy. Otherwise, radial velocity measurements from molecular line emission or from HI surveys were used to in a Galactic rotation model to assign a distance. To break the near/far ambiguity, the distance is compared to dust extinction, HI absorption features and its calculated Galactic scale height when these options are available. If an object is only seen in extinction/absorption, or its scale height at the far distance is higher than the scale height of the Milky Way, the object is unlikely to be at the far distance and so it is assigned the near distance value.

The distance catalogue contains 22 columns, including its sky position, its radial velocity, how the distance was assigned (i.e., maser parallax, molecular line emission etc.), the probability that the assigned distance is correct, and both the near and far distances. The last three values are given if a radial velocity measurement was used to estimate the distance.

5.2.2 GLIMPSE I/II

The Galactic Legacy Infrared Mid-Plane Survey Extraordinaire (GLIMPSE) (Churchwell et al. 2009) is a near-to-mid IR Galactic plane survey taken with the InfraRed Array Camera (IRAC) onboard of the *Spitzer* space telescope (Fazio et al. 2004; Werner et al. 2004). The survey covered Galactic longitudes of $|l| \leqslant 65^\circ$ and Galactic latitudes $|b| \leqslant 1^\circ$ (extending to 1.5° between $|l|$=5–2° and extending to 2° for longitudes $|l| \leqslant 2^\circ$). The survey imaged the sky in 3.6, 4.5, 5.8, and 8.0 μm. At 8.0 μm, the survey traces both internal heating from proto-stellar objects and traces Hii regions via the fluorescence of polycyclic aromatic hydrocarbons (PAH's), caused by UV emission. The angular resolution, pixel resolution and the average rms uncertainty are 1.9″, 1.2″ and 0.3 MJy sr^{-1} respectively at 8.0 μm for this survey. For this chapter, the amount of 8.0 μm emission is used to indicate how much of a given cloud is currently forming stars.

5.2.3 WISE Hii region catalogue

The WISE Hii region catalogue (Anderson et al. 2014b) covers the entire plane of the Galaxy between Galactic latitudes of ±8°. The survey catalogue contains a range of information concerning each Hii region identified, such as their sky position, radii, and distances (from radial velocities and maser parallax measurements). Although, only 1413 Hii regions were able to have their distance measured. The survey was compiled by visually inspecting data from the Wide-Field Infrared Survey Explorer (WISE) at

12 and 22 μm (Wright et al. 2010). At 12 μm, PAH's emit at the edge of HII regions whereas 22 μm traces small heated dust grains within HII regions. The overlapping of the two can thus indicate the location of HII regions. Each HII region identified was cross-matched with radio surveys, radio recombination lines (RRL), and Hα emission to verify whether it is real. In total, they identify 8399 HII regions, where 1524 coincide with known HII regions (due to the presence of either radio recombination lines or Hα). They further identify 1986 HII regions coinciding with radio emission but no RRL or Hα emission. These are deemed as candidate HII regions. Anderson et al. (2014b) estimate that ∼95% of candidate HII regions are real. Finally, they also detect 4124 HII regions that have no corresponding radio continuum, RRL or Hα, so deem these radio quiet. The majority of these sources (60%) sources are usually small in radius ($< 1'$) and coincide with cold dust measurements (∼15 K) from either the ATLASGAL survey Schuller et al. (2009), or the BGPS survey Aguirre et al. (2011), leading them to suggest that the majority of radio quiet sources trace young HII regions (i.e., UCHII regions) that are optically thick at low radio frequencies. In some cases they also expect these objects to represent low surface brightness HII regions, such as those created by weaker sources, (i.e., late OB stars), or if the region in very extended in size, represent a population of old HII regions. Finally, they also detect 115 objects that could not be cross checked with radio data due to missing or poor quality radio observations.

5.3 METHODS

Here I discuss how I identify and categorise a large sample of molecular clouds, how to cross-correlate survey data, and large data catalogues and how to use mid-IR emission to trace the relative evolutionary stage of molecular clouds. I note here that I exclude all data between ±4° in Galactic longitude since distance measurements in the Galactic centre are less reliable compared to the rest of the Galactic plane.

5.3.1 CLOUD IDENTIFICATION

To trace molecular gas, I use the background subtracted H_2 column density maps calculated in Peretto et al. (2016), which have an angular resolution of $18''$. The higher resolution was maintained by taking the ratio of the 160 μm to 250 μm maps to estimate the dust temperature. With this, one can then calculate the H_2 column density using the 250 μm fluxes (assuming β=2 and $\kappa_{250\mu\mathrm{m}}$= 0.012 $\mathrm{cm}^2\mathrm{g}^{-1}$ (Ossenkopf & Henning 1994)). I note that it was shown in Chapter 4, Sec. 4.4.2 that the free-free contribution at the centre of a bright HII region at 250 μm is negligible.Therefore, I can ignore free-free contribution for all column densities measurements in this chapter.

With these maps, I identify and catalogue[†] all the molecular gas between $|l| = 70°$, $|b| \leqslant 1°$ that are above an isocontour of $1{\times}10^{22}$ cm^{-2} and have solid angles larger than the $18''$ beam. $1{\times}10^{22}$ cm^{-2} has been selected to represent the cloud boundaries since it is close to observed threshold for star formation (André et al. 2014). Most clouds identified above this contour should therefore represent a population of clouds capable of forming stars and HII regions. With these criteria, I identify 22851 objects.

On some occasions, the high column density threshold causes some molecular clouds to be split into multiple objects, i.e., clumps (see Fig. 5.1). As a result, they were identified as separate clouds. In most cases however, these clumps exist as part of a larger molecular cloud complex. Lowering the column density threshold would help in some cases, but would also allow new, lower density objects to be catalogued. At lower densities, these new objects are less likely to contain the conditions necessary for star formation. Under these conditions, I perform a friends-of-friends like (FoF) method to combine closely neighbouring objects. When performing the FoF, rather than merging clouds based on their centroids and effective radii, one can instead take advantage of the morphology of each cloud. To do this, all masked pixels were convolved with a small Gaussian kernel (see example top panel of Fig. 5.1). All

---

[†] Image segmentation has been performed using the Python package `skimage.measure`

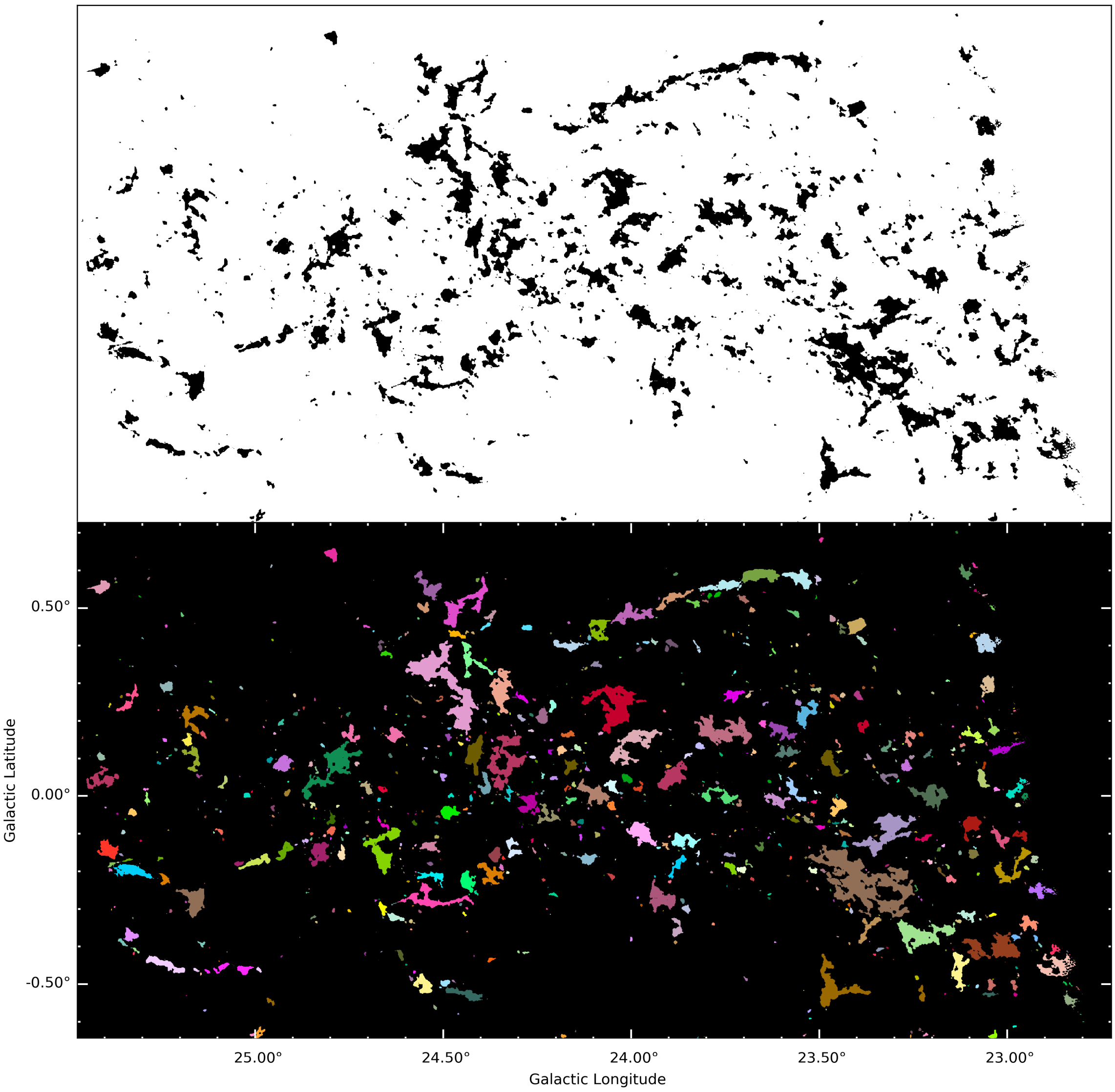

Figure 5.1. Figure illustrating molecular cloud identified in *Herschel* column density data between 23–25.5° longitude. **Top** panel shows all pixels $\geqslant 1\times10^{22}$ cm^{-2} (solid black colour), where each pixel is 4.5″ in size. **Bottom** panel shows each individual regions identified, where each colours indicates the ID's of clouds identified. One can clearly see that some large-scale filaments have been split into multiple individual clumps.

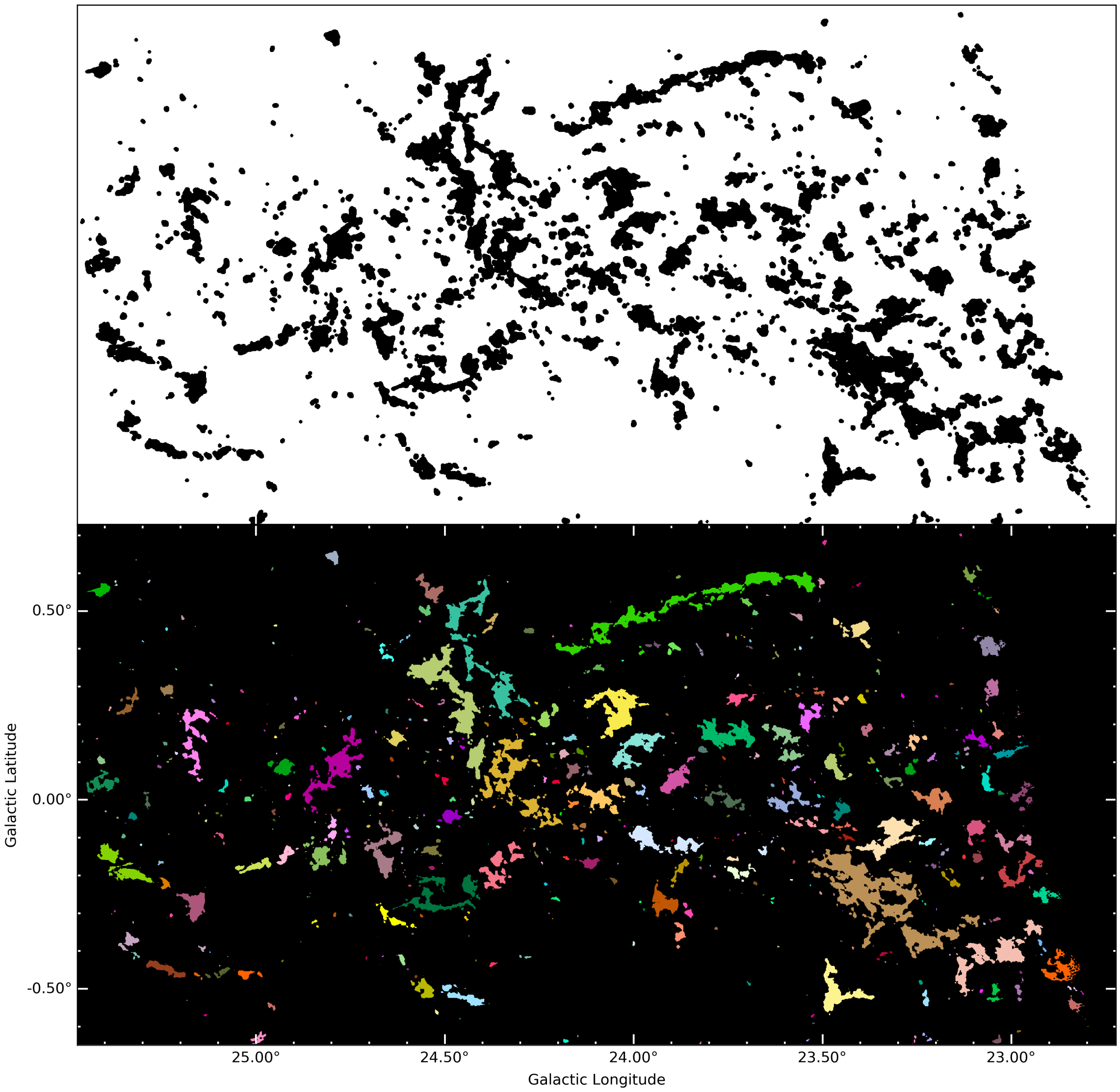

Figure 5.2. Figure illustrating a friends-of-friends like merging strategy to combine neighbouring molecular clouds, between 23–25.5° longitude. **Top** panel illustrates how clouds are merged by convolving the masked data to 21″. **Bottom** panel shows the clouds identified after they have been merged. The colours indicates the ID's of each object in both panels.

regions that now touch in the convolved image are merged into a single cloud, as indicated on Fig. 5.2. To avoid over-merging clumps, I convolve the masks to 21″. 21″ was used over larger and smaller kernels by visually comparing how known star forming regions were merged using different values between 18″ –30″. While it was not rigorously tested for all values between this range, I found that larger kernels would over-merged clouds in parts of the Galactic plane, resulting in unphysical cloud sizes (i.e., most clouds in Fig. 5.2 become merged together and when merged, their masks would span over 1° in size). The smaller kernels did not merge many masks. For the size scales important for this chapter (cloud-scale objects), a value of 21″ was able to join most of the gas in known star forming regions (e.g., NGC6334, see Fig. 5.3), without over-merging crowed part of the Galactic plane.

In total, I identify 16212 molecular clouds after merging. Although, some neighbouring clumps might not be physically related to each other, but appear so along the line of sight. Therefore, I only retain clouds where more than 50% of their associated clumps have similar distances (see next Section for more details), which reduces the number of clouds identified to 12149 clouds. This number is comparable to the number of clouds found in (Peretto et al. 2016).

I note that in this study, it is vital to assign an accurate estimate for the evolutionary stages of the identified clouds so that the SFE's of clouds in different environments are compared with similar evolutionary stages. Otherwise, differences in SFE's between two clouds could just be a product of their differing evolutionary state, and not due to an environmental factor. In this regard, the evolutionary stage of just one clump, out of context of the star formation occurring in the rest of the complex, provides a poorer estimate of its evolution (i.e., a cloud containing five clumps, where only one contains YSO's is likely to be younger than a similar cloud but has YSO's in all five clumps). Therefore, if a clump exists as part of a larger molecular cloud complex, a better estimate of its evolutionary stage can be made by considering its evolution alongside the rest of the clumps present. It is for this reason

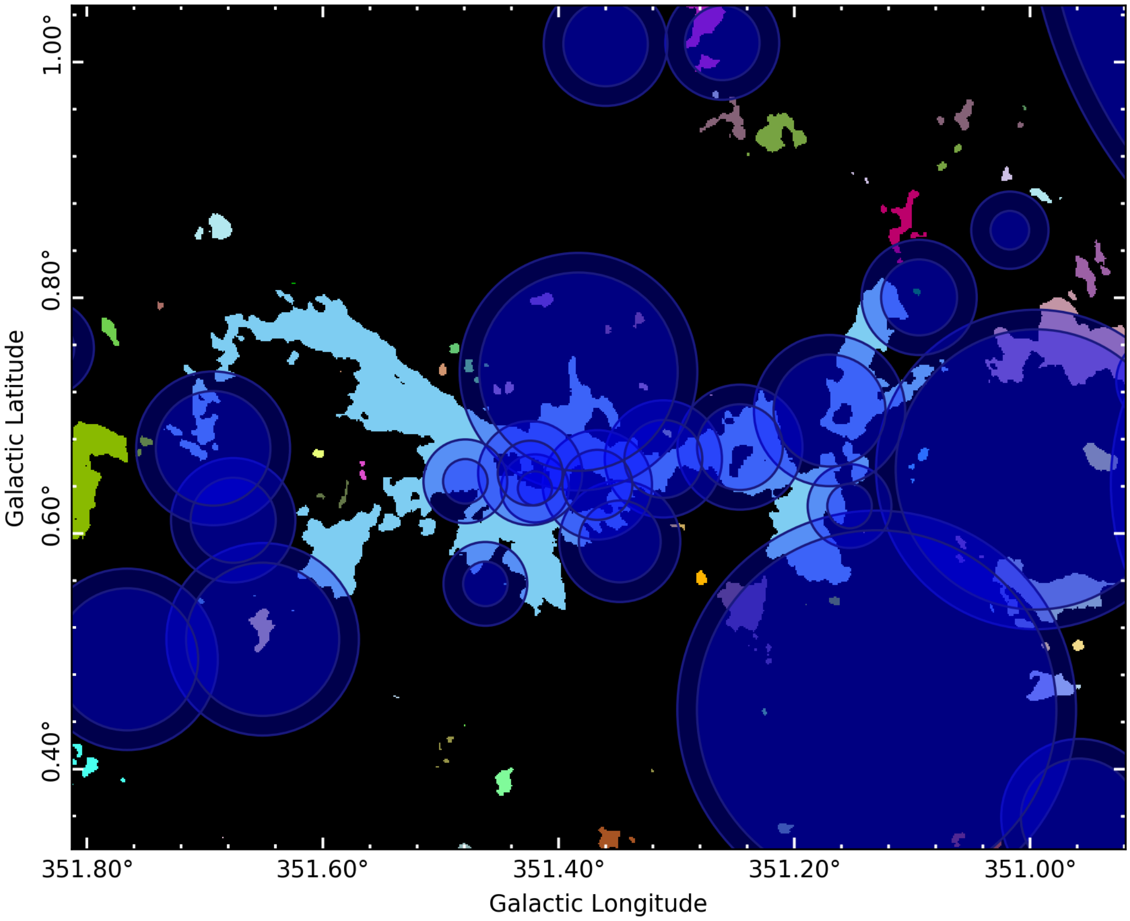

Figure 5.3. Plot illustrating the star forming region NGC6334 (light blue mask in the centre of the image) where the majority of unconnected masks are merged (and so appear light blue) after performing a FoF-like method. Blue circles represents HII regions from the WISE catalogue (see Sec. 5.2.3), and outer dashed blue annuli represent HII region boundaries calculated in Sec. 5.3.5. Masks that are not light blue represent separate molecular clouds identified in Sec. 5.3.1.

that entire cloud complexes are analysed, rather than individual clumps, if a larger complex is present.

Cross-catalogue matching

For cross-catalogue matching, one can take advantage of the morphology of each cloud (rather than relying on the cloud centroid and major and minor axes) by cross-matching catalogues with the mask of each cloud. By doing so, a match can be made only when a catalogued entry falls within the cloud mask. However, cross-matching multiple catalogues over the entire Galactic plane survey is computationally slow. Therefore, the boundary (i.e., contour) enclosing each cloud is also catalogued in Galactic coordinates, along with the cloud ID number. By doing so, one can quickly map molecular clouds to different co-ordinate systems without the need to re-grid entire 2D maps. Additionally, contours allow one to account for duplicate entries where neighbouring *Herschel* tiles overlap without the need for re-gridding or mosaicking tiles (tiles overlap by $\sim 0.2°$).

5.3.2 ASSIGNING DISTANCES TO MOLECULAR CLOUDS

The Hi-GAL distance catalogue contains 150226 velocities and distances for point sources. Consequentially, cloud masks can contain multiple distance values within its boundary, some of which have different velocity and distance values (either due to uncertainties in the data, or because multiple objects exist along the line of sight). Other times, clouds have identical velocities values, but the distances are near/far confused (i.e., the distances agree when just the near (or far) distances are used). Under these circumstances, one needs to determine a distance/velocity that represents the majority of distances within the mask if more than one value is present, while eliminating outliers, and rejecting clouds from further analysis when most of the distances are dissimilar. Therefore, I first assign distances to the un-merged catalogue, before applying the same analysis to the merged catalogue. These conditions ensures that only physically coherent structures within the survey are analysed. Additionally, if was found that the final distances/velocities were affected less by outliers when values were assigned to the un-merged masks first.

For both iterations, I assign the median distance after performing sigma clipping if >50% of the distances and the velocities remain after sigma clipping, otherwise, no distance is assigned. Sigma clipping is a statistical method for removing outliers from data to produce a more robust measurement for the central tenancy of the data. Outliers are defined using a statistical measure for the spread of the data, such as the standard deviation, or the median absolute deviation. In this case, outliers correspond to velocities/distances belonging to another cloud along the line of sight. Sigma clipping can be performed iteratively to remove outliers (i.e., after removing outliers, the data spread is recalculated and this new estimate is used to remove outliers). In most cases, all outliers are removed after 3 iterations. Since most masks contain < 5 distance/velocity values, I use the median absolute deviation, (with a 3 sigma confidence level) since the median absolute deviation limits the affect of outliers on small sample statistics compared to the standard deviation.

I therefore use sigma clipping to both improve the robustness of the final average values and to remove clouds if sigma clipping removes over 50% of the distances or velocities found. In doing so, clouds that cannot be be represented by a single, dominant velocity/distance along the line of sight are ignored. If sigma clipping rejects a cloud, I also reperform the test using the near distances only. If the cloud is no longer rejected, I assume that the distance used in the catalogue has been wrongly assigned, and calculate the median using the near distance given in the Hi-GAL catalogue (I use the near distance in these cases since it is more likely the cloud is at the near distance Urquhart et al. 2018).

While sigma clipping worked most of the time, it was common for very coherent values to be clipped accidentally. Therefore, when all the velocities and distances are within $\leqslant$2.5 km s^{-1}and $\leqslant$0.1 kpc of each other, the median distance is assigned without performing sigma clipping. The limits were chosen after inspecting typical velocity and distance values present when sigma clipping failed. Both larger and smaller limits were tested but because the velocities and the distances were already similar enough that sigma clipping failed, increasing the distance and the velocity limit did not significantly increase the number of assigned distances/velocities. However, I note that when larger ranges were used, it was found that final distance/velocity assigned to each cloud were more likely to be skewed towards an incorrect value (i.e., when checking the final distance/velocity of clouds to values found in the literature, larger limits would skew the final distance/velocity away from the literature value). Sigma clipping also fails when an object contains only two distance values (a minimum of three values are needed for sigma clipping). When this occurred, the mean distance was assigned if both the velocities and distances are within $\leqslant$5 km s^{-1}and $\leqslant$0.1 kpc of each other. Otherwise, no distance was assigned. The limits used were chosen to match the limits used previously since these were found to represent an object that is velocity coherent. However, it was found that a velocity limit of 2.5 km s^{-1} was too strict in most cases, and so most clouds were rejected (while increasing the distance limit had much less of an impact). Therefore I doubled the velocity limit, which improved the pass rate significantly. When the velocity was limit was set larger than this, again the final velocity values were more likely to be skewed.

In both of the exceptions above (where sigma clipping could not be used), a much stricter distance limit could be used than the velocity requirement. Typically, while clouds often had very similar distances (coherent within 0.1 kpc of each other), their velocities had a much larger spread in values ($\sim$5 km s^{-1}). This likely reflects how their distances were assigned, (with the majority of objects assigned using their line of sight velocity in a Galactic rotation model).

After performing this method to the un-merged, and then merged catalogues, I was able to assign distances to 12149 clouds, (75% of the catalogue). I note that the method described does not un-merge masks from the final molecular cloud when sigma clipping determined either the velocity or the distance was an outlier compared the rest of the masks. My justification for this relates to the fact most un-merged masks actually represent column density peaks contained within a larger molecular cloud complex. However, masks can contain velocities and distances to multiple objects along the line of sight, or have a mix of near/far distance values. When this occurs, a mask can be assigned a different velocity/distance compared to its neighbours if the mask contained more values at a different distance/velocity, even though the mask does contain some distance/velocity values similar to its neighbours. When investigating the masks affected, I found that this error only occurs to the smallest un-merged masks. Therefore their affect on the final molecular cloud is small so I do not re-assign these clouds.

,

5.3.3 $L_{\mathrm{TOT}}^{70\mu\mathrm{M}}/M_{\mathrm{CLOUD}}$ AS A TRACER OF STAR FORMATION EFFICIENCY IN MOLECULAR CLOUDS

To trace the current (or the instantaneous) SFE in molecular clouds, one must determine the mass of the stars currently forming, and the total mass present. One measurement that can provide this estimate is the bolometric luminosity of a protostar. When evolving, the luminosity of a protostar luminosity is dominated by its accretion luminosity. But the accretion luminosity has been shown to be proportional to the current mass of the protostar present (Ragan et al. 2012). Therefore, the bolometric luminosity can be used to trace the current protostar mass.

The bolometric luminosity is usually difficult to measure since the emission at lower frequencies (those corresponding to wavelengths < 100 μm) are dominated by emission from the cold dust that surrounds the protostar while emission at higher frequencies (corresponding to wavelengths > 100 μm) becomes optically thick and can trace hot ($>$50 K) dust heated by ionising photons. Dunham et al. (2008) and Ragan et al. (2012) show that the 70 μm emission is the least affected by these effects, and because 70 μm emission is present throughout most stages of proto-stellar evolution (see Fig. 1.4), it can be used to trace the bolometric luminosity of protostars (and hence trace protostar mass.)

For this reason, I cross-match the *Herschel* 70 μm compact source catalogue with my cloud catalogue. Using the distances calculated in the previous section, I calculate the total 70 μm luminosity of the sources present within each cloud (integrated over the 25μm bandwidth the PACS 70μm detectors), and use the Hi-GAL H_2 column density maps to calculate the total cloud mass. For the rest of this chapter, I assume that the total 70 μm luminosity from compact sources divided by the total cloud mass ($L_{\rm tot}^{70\mu{\rm m}}/M_{\rm cloud}$) is proportional to the current SFE.

5.3.4 TRACING THE EVOLUTIONARY STAGE OF MOLECULAR CLOUDS

To determine the relative evolutionary lifetimes of molecular clouds, we can measure the fraction of mass within a cloud that is actively forming stars, compared to the fraction that is currently inert. By assuming that the all quiescent gas will eventually develop stars, and that on average, the star formation occurs in a steady state, these fractions provide a relative measurement of the current evolutionary stage of that cloud (Battersby et al. 2017; Kruijssen et al. 2019). If we are able to calibrate this fraction with the lifetime of an object coexisting with one of these categories (such as the ages of UCHII regions, or the dynamical times of HII regions), the cloud lifetimes can also estimated. Battersby et al. (2017) developed such a method using 8 μm emission. The star formation activity within a cloud internally heats the dust around it and ionising photons emitted cause PAH's to fluoresce at mid-IR wavelengths. Therefore, the amount of 8 μm emission can be used to trace the amount of star formation present. However, Battersby et al. (2017) applied this method on a pixel-by-pixel basis, determining the percentage of high-mass pixels (as defined using Hi-GAL data) that are infrared bright/dark to trace the average star forming timescales of high-mass stars in the Milky Way. If we instead determine the fraction of each cloud that is infrared bright, we can calculate a relative evolutionary timeline of star formation on a cloud-by-cloud basis.

For that purpose, we use the GLIMPSE 8 μm survey. For each cloud mask, we find all the 8 μm pixels contained within a given mask boundary (where each 8 μm pixel is $1.2''$ in size). To determine if a given 8 μm pixel within a cloud is IR bright or dark, we compute the difference between the pixel's 8 μm flux with the background flux. The background emission has been defined using a median filter of size $4.8'$, which approximately matches the average size of the structures within the GLIMPSE survey. All positive pixels above the rms noise limit given by the survey (0.3 MJy sr^{-1}) are labelled as IR bright and all negative pixels lower than the rms noise are labelled dark. Any pixels falling under the rms noise limit remain unassigned. Of the remaining clouds in the catalogue, 244 clouds were not covered by the GLIMPSE survey. As a result, I ignore these entries, which leaves 11905 clouds in the catalogue).

5.3.5 CLOUD ASSOCIATION

The clouds identified in this survey will either have no HII regions associated with them, contain HII regions from its own star formation activity or are found within the boundary layer of an HII region. For ease of future discussions, I refer to these three categories as *clear clouds*, *HII clouds*, and *boundary clouds* respectively. For this study, I assume that clear clouds trace the earliest phases of star formation and that HII clouds trace more evolved phases of star formation. By construction, the evolutionary phases traced by these two categories of clouds do not overlap (see Fig. 5.5 for illustration). This is different to the boundary cloud category which, in principle, can contain clouds at all evolutionary stages. By comparing the properties of boundary clouds to those of clear and HII clouds, I can determine whether boundary clouds do indeed trace all stages of cloud evolution or not.

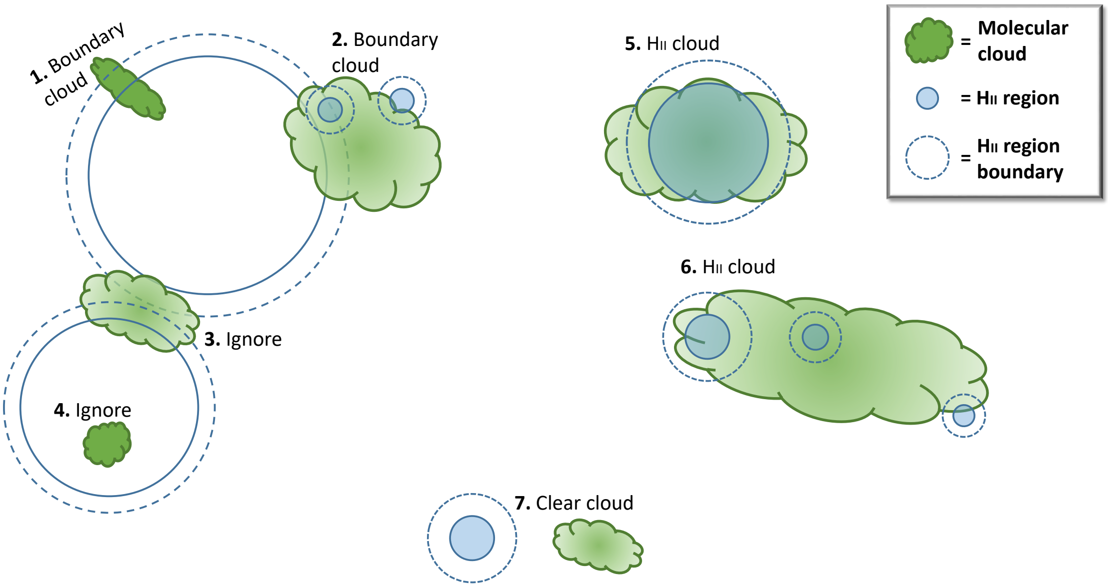

Figure 5.4. Diagram illustrating how clouds are associated with HII regions. Clouds (filled green objects) found mainly in the boundary (dashed blue circle) of a large HII region are categorised as boundary clouds (clouds 1. and 2.) where an HII is considered large compared to a given cloud if its diameter (filled blue circle) is larger than the cloud's major axis (and considered small otherwise). Boundary clouds can contain small HII regions (cloud 2.). Any cloud found with the boundary of two or more large HII regions (cloud 3.), or is only inside a large HII region (cloud 4.) is ignored from further analysis. Clouds only associated with small HII regions are categorised as HII clouds (clouds 5. and 6.). Any cloud without HII regions are categorised as clear clouds (label 7.). See Sec. 5.3.5 for further information about how clouds were categorised.

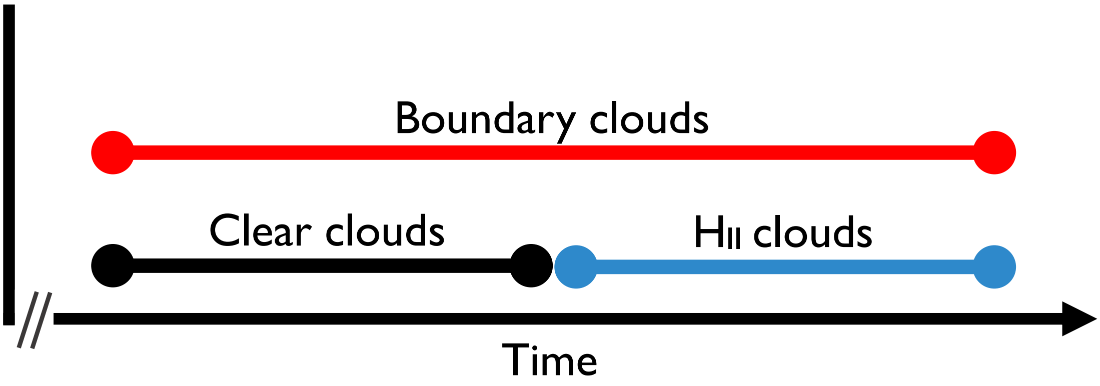

Figure 5.5. Diagram illustrating the relative evolutionary ages of the three cloud classifications used in this study.

To classify clouds into these categories, I use the WISE HII catalogue. This catalogue contains the most complete sample of HII regions over the Galactic plane and not only does it contain large and evolved HII regions, but contains small, and usually radio quiet HII regions most likely tracing very young HII regions. This makes the WISE HII catalogue well suited to this purpose. To associate clouds to the boundary layer of HII regions, I define an annulus around each HII region whose inner radii always equal the radii assigned within the catalogue ($r_{\rm HII}$). The outer radii is set to be double $r_{\rm HII}$ when $r_{\rm HII} \leqslant 60''$ and $r_{\rm HII} + 60''$ when $r_{\rm HII} > 60''$. A relatively small thickness has been chosen in an attempt to minimise coincidental associations while retaining a large enough sample of clouds. With both the HII region and boundary layer defined, I cross-match the mask catalogue to the HII catalogue, and calculate the percentage area of the HII region and the boundary layer that is occupied by each cloud. If a larger percentage of the HII region is occupied compared to the percentage occupied by the boundary layer, the cloud is deemed to be associated with the HII region, else, the cloud is associated with the boundary layer. Classifying clouds this way helps minimise classification bias caused by the difference between the areas of the boundary layer and HII region (see cloud **1.** in Fig. 5.4). I then identify if the HII region is large (or small) compared to the cloud by comparing the diameter of the HII region with the major axis of the cloud. If the diameter is larger than the major axis, the HII region is considered large, otherwise, it is considered small. I note that clouds within the boundary layer of a small HII regions are instead classified as being associated with the HII region, rather than its boundary. After inspecting these small HII regions, I found that traced star formation present from within the cloud.

Additionally, a cloud can also be identified as being associated with the HII region, but fully contained within a large HII region (see cloud **2.** in Fig. 5.4). However, the exact relationship of these clouds in relation to the HII region is difficult to determine, therefore I exclude these clouds from the analysis, which removes 2210 clouds. Additionally, a cloud can sometimes exist within the boundary layer of two,

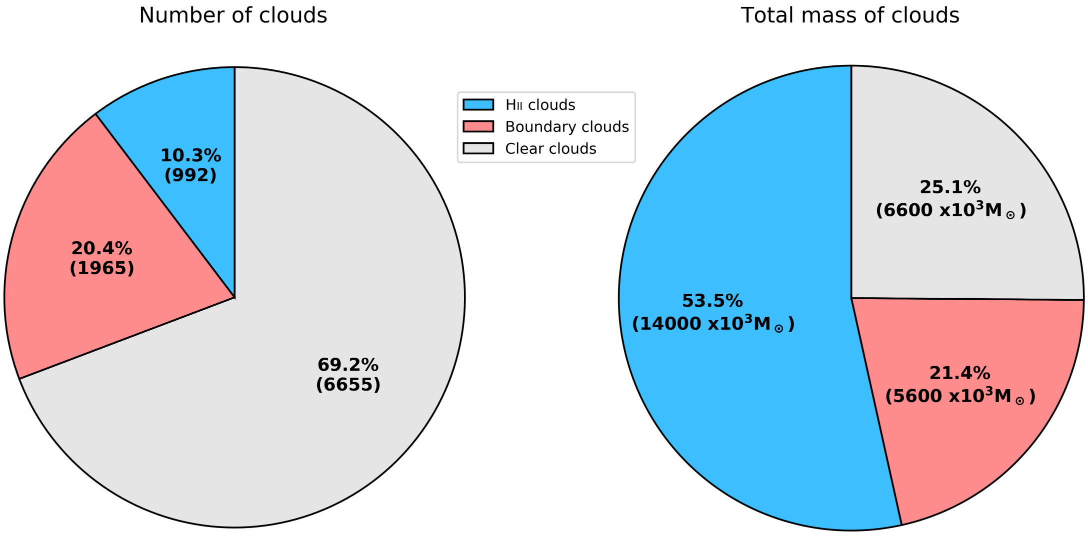

Figure 5.6. Chart illustrating percentage of clouds categorised **left** and the total mass contained within each category **right**. The three cloud categories are clear clouds (solid grey colour), HII clouds (solid blue colour) and boundary clouds (solid red colour).

or more large HII regions. When this happens, I ignore all clouds associated with multiple boundary layers due to complexity in defining the affect it has on the properties of the cloud (cloud **3.** in Fig. 5.4). This occurs to 128 clouds. However, I keep all large clouds (relative to the HII region) that contain multiple HII regions and classify them as HII clouds (cloud **7.** in Fig. 5.4). Furthermore, any clouds within the boundary layer of a large HII region, but has developed small HII regions of its own are classified as boundary clouds (cloud **4.** in Fig. 5.4). This occurs to 195 clouds within my sample. With these definitions, I classify 6655 as clear clouds, 992 as HII clouds, and 1965 as boundary clouds. The total amount of mass within each category is 6600×10^3 M$_\odot$, 14000×10^3 M$_\odot$, and 5600×10^3 M$_\odot$ respectively (see Fig. 5.6).

The WISE HII catalogue presents all HII regions as circles, and does not take eccentricity, nor bipolar morphologies into consideration. As a result, I expect some boundary clouds will be misclassified. To check the extent this occurs, I visually inspect the WISE catalogue compared to the molecular clouds with bubble-like morphologies (i.e., arcs). In general, the WISE catalogue approximates HII regions well,

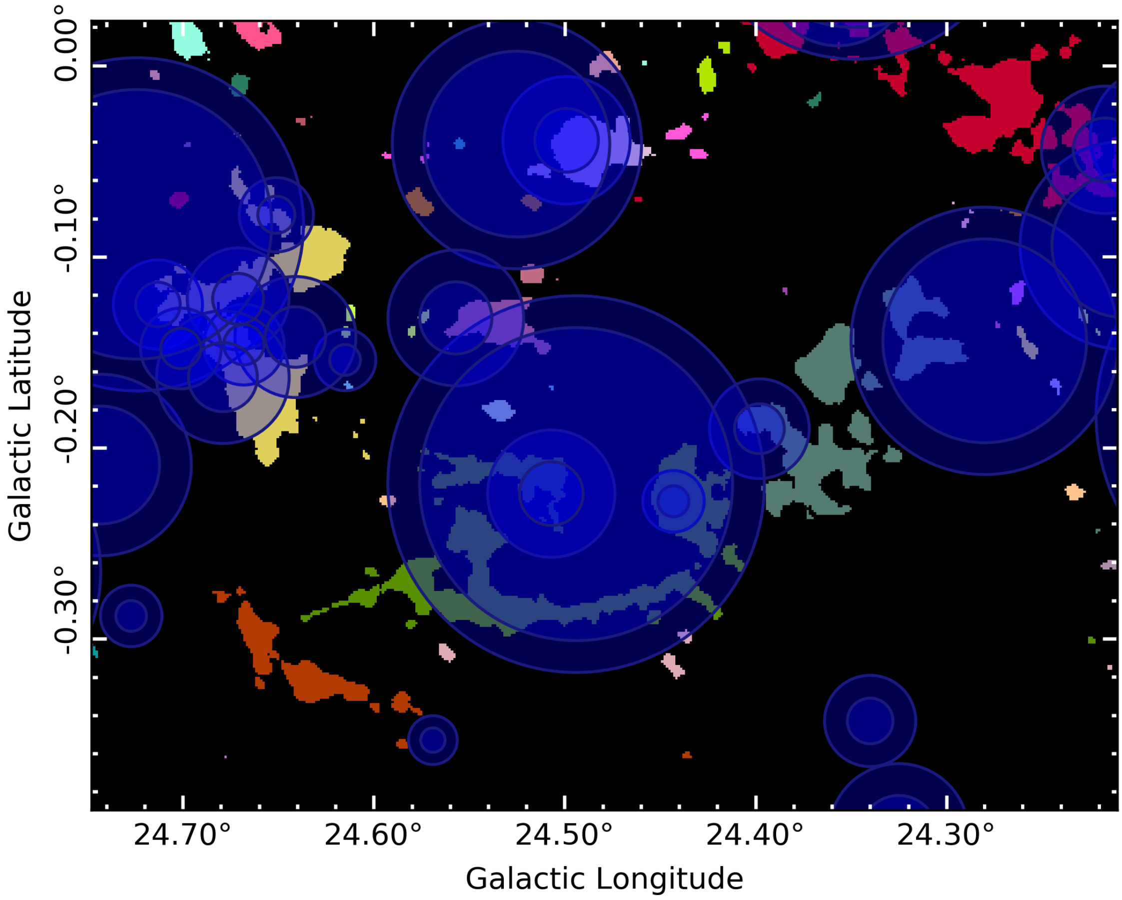

Figure 5.7. Plot illustrating misclassified boundary cloud (green mask in the centre of the image) due to the WISE catalogue approximating HII regions as circular. Blue circles represents HII regions from the WISE catalogue, and outer dashed blue annuli represent HII region boundaries calculated in Sec. 5.3.5. Coloured masked represent molecular clouds identified in Sec. 5.3.1.

and so molecular clouds bounding HII regions are accounted for. Although, there are a few cases where the WISE catalogue overestimates the size HII regions, and so clouds that should be within the boundary of an HII region are found within them instead (see Fig. 5.7 for an example of when this occurs). But from visual inspections, this occurs to a small fraction of objects and so I ignore this error for the rest of the chapter.

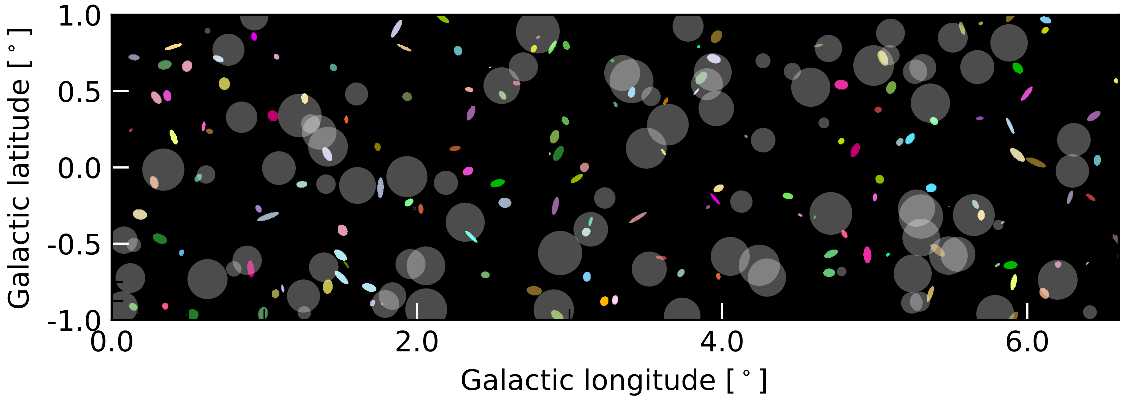

Figure 5.8. Example showing a model of molecular clouds (coloured ellipses) and HII regions (translucent circles) in the Milky Way. The percentage of the model filled with HII regions and molecule clouds was set to equal the same filling factors represented over the Southern Galactic plane. The area of the HII regions and molecular clouds follow a uniform distribution (i.e., a histogram showing the area distribution will be have equally sized bins).

Association bias

By categorising the clouds based on their size and area, it is likely that the cloud classifications contain a size bias. When referring to size bias, I specifically mean a change in the number of clouds classified within each category as a function of their projected area. Therefore, to estimate how often clouds might have been misclassified, I created a small model of the Galactic plane, 13.2° × 2° in size, with 4.5″ sized pixels (to match the pixel resolution of the H_2 column density maps). In this model, I randomly inject molecular clouds and HII regions using the same filling factor observed within the Galactic plane (see Fig .5.8 for model). Excluding the Galactic centre, 3% and 20% of the Galactic plane between $|l| \leqslant 70°$ is covered by molecular clouds ($N_{\mathrm{H}_2} \geqslant 1\times10^{22}$ cm^{-2}) and HII regions respectively. To match the shape of molecular clouds within the Galaxy, I model the clouds as ellipses with aspect ratios sampled from the mask catalogue. This ensures that any bias caused by the morphology of the cloud is included in the model. Finally, to determine if a size bias exists, I used a uniform area distribution to generate HII regions and molecular clouds (i.e., a

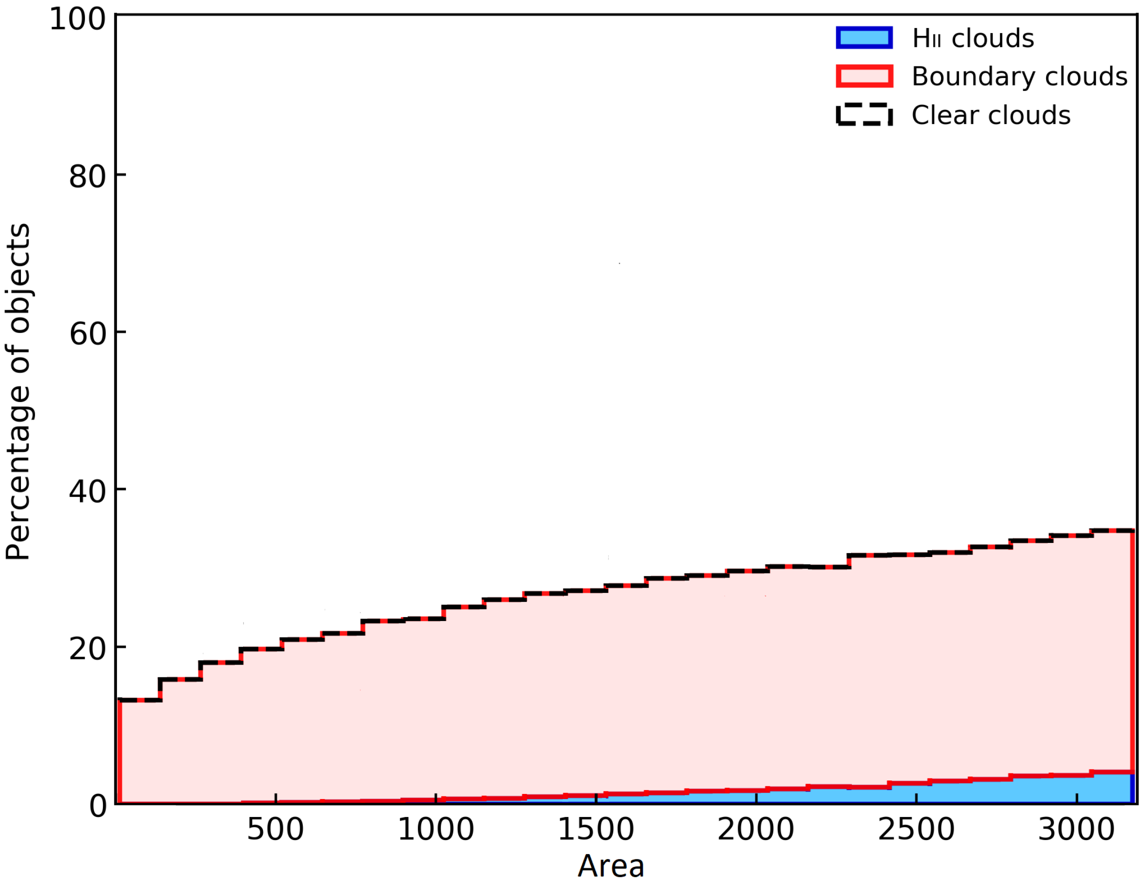

Figure 5.9. Plot showing the modelled cloud distributions as a function of their projected sky area after being categorised as a either a clear cloud (white), a boundary cloud (red) or an HII cloud (blue). If no size bias exists in the categorisation rules, all percentages will be constant with area (area is equal to the number of pixels within each cloud. 1 pixel = 4.5″ in length, which matches the resolution of the H_2 column density maps. An area of 1000 has and angular area of 5.6 arcmin^2).

histogram showing the area distribution will be have bins of equal height). By doing this, any deviation from a uniform distribution after classifying each cloud (using same criteria described in the previous Section) will indicate a bias exists. I create the model 2000 times to improve the reliability of this test, and plot the results in Fig. 5.9. Figure 5.9 shows two important results. Firstly, it shows that up to 15–30% of boundary clouds classified in my sample could occur due to chance alignment. Secondly, it shows that larger clouds are more likely to be classified as either a boundary cloud or an HII cloud. Therefore the classification scheme introduces a size bias to the results.

While 15–30% might seem like a large number, I note that in real observations, we know that dense gas correlates with HII regions. Hence, 15–30% will represents an upper limit to the number of misclassified clouds. To test this assumption, I counted the number of large HII regions in the data and in the model with > 1, > 2, and > 3 clouds associated with it. If there is no spatial correlation, the percentage of HII regions with multiple clouds associated with it should match the random model. If there is a spatial correlation, the difference between the model and the data should increase as the cloud limit (> 1, > 2, and > 3) increases. I find that 32%, 18% and 5% of the real HII regions have > 1, > 2, and > 3 clouds in its boundary respectively, but modelled HII regions only 13%, 2% and 0.2% respectively. There is a greater spatial correlation that is not explained by the model, therefore it is safe to assume that the boundary clouds identified are contain a significant amount of real associations (as opposed to them all having chance alignments). The size bias however will introduce a genuine problem that must be addressed before analysing the results. If more clouds are misclassified as a function of their area on the sky, any property that correlates with the size of the cloud will now exhibit a bias.

To see the extent of the size bias, I plot normalised histograms of the projected area distribution (i.e., number of pixels on the sky) for the real catalogue after categorising them as clear clouds, HII clouds and boundary clouds in Fig. 5.10. The distributions of the HII and the boundary clouds resemble the biased distributions shown in Fig. 5.9. At larger areas, both cloud types are seen to increase in frequency, relative to the number of clear clouds. This strongly indicates that the area distributions contain a bias. Therefore, under the assumption that the projected area distributions of the three cloud types should be similar, I can resample the HII and boundary clouds to the projected area distribution of the clear clouds to minimise the affect of the size bias. This assumption is justified by the fact that it has already been assumed that the clouds within this survey represent the same distribution of clouds at different evolutionary stages. In this assumption, clear clouds are expected to evolve in HII clouds, and boundary clouds evolve from either/both the clear clouds

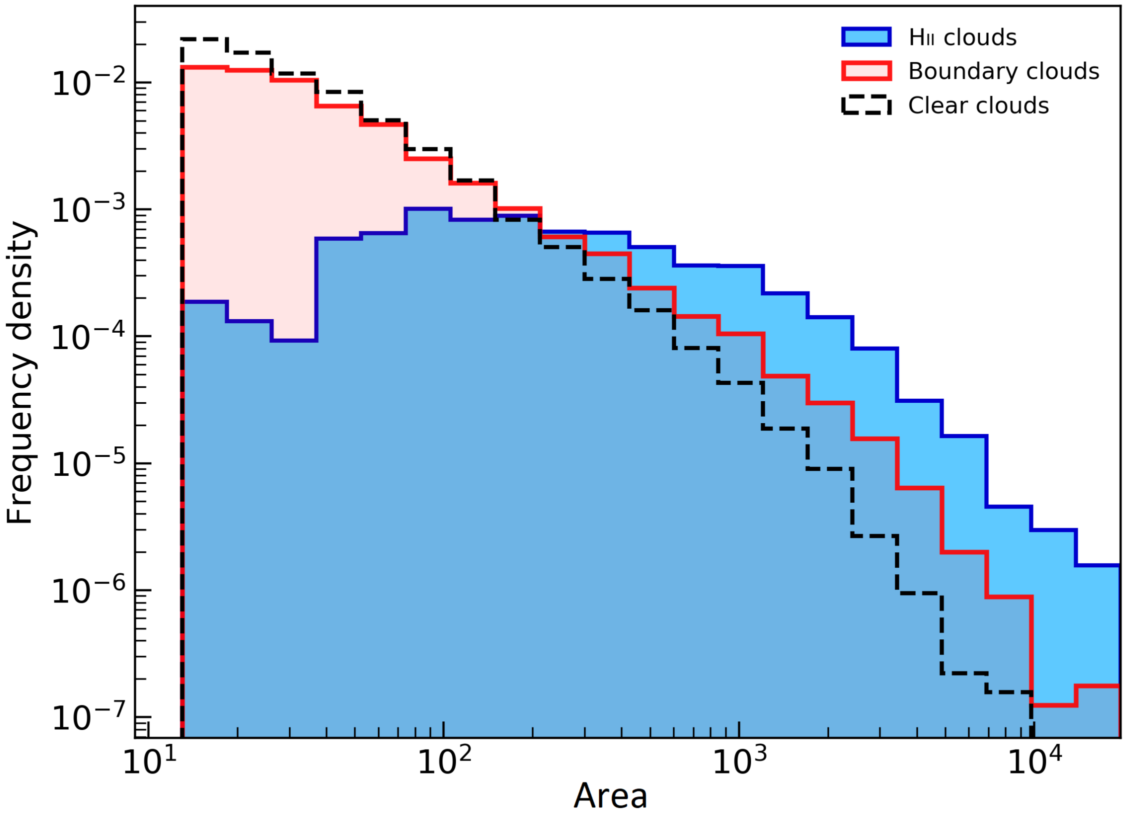

Figure 5.10. Plot showing the normalised histograms of the area distributions for HII clouds (blue), boundary clouds (red) and clear clouds (dashed black line). The y-axis shows the bin frequency normalised to 1 for each category to better compare the distributions.

and the HII clouds. I note that this assumption ignores boundary clouds that might eventually evolve into HII clouds if the bounding HII region is no longer detectable, or the new star formation activity affects the morphology of the bounding HII region. However, in Sec. 5.5, I address the impact of sequential star formation and show that only a small fraction of clouds represent a population that can propagate star formation. Therefore it is safe to assume that the main evolutionary pathway of HII clouds is from clear clouds.

To resample HII and boundary clouds, I bin each area distribution and calculate the percentage difference between each bin in the current distribution, to each bin in the distribution I want to eventually match (i.e., the clear clouds). I then assign a weight, W_i, to each measurement in the current distribution using the percentage difference of the bin it is in, and the number of measurements within that bin so that $\sum_{i=1}^{N} W_i = 1$. Using these weights as probabilities, I can then randomly sample from the current distribution, with replacement, which gives me a new distribution of clouds where the area distribution has been made to match the area distribution of the clear cloud distribution.

In Fig. 5.11, I show the result of the resampling using 665500 samples for the HII clouds, and the boundary clouds. I note that 20 HII clouds, and 2 boundary clouds had areas beyond the largest area present in the clear clouds. As a result, these clouds could not be resampled and have been removed. This leaves 972 HII clouds and 1963 boundary clouds.

To see the impact of the resampling has had on different cloud properties, I plot the old and new mass distributions on Fig. 5.12 and Fig. 5.13 respectively. Without resampling, the mass distributions between the three cloud categories are significantly different from each other, but after resampling, the mass distribution of all three cloud categories are similar (even though it was the area distribution that was resampled). This indicates the mass distributions between the clouds only differed due to the size bias present. Therefore in the following analysis, we will work under

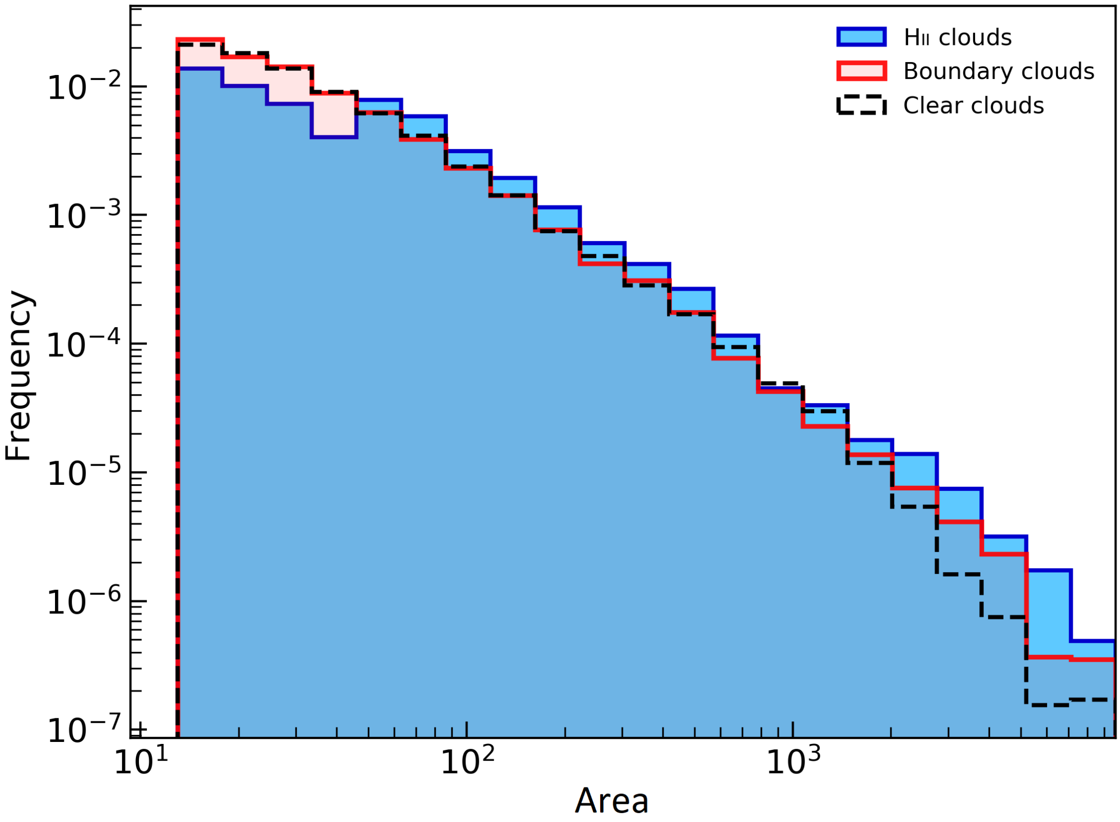

Figure 5.11. Plot showing the normalised histograms of the area distributions for HII clouds (blue), boundary clouds (red) and clear clouds (dashed black line) after resampling their area distributions to match the clear clouds. The y-axis shows the bin frequency normalised to 1 for each category to better compare the distributions.

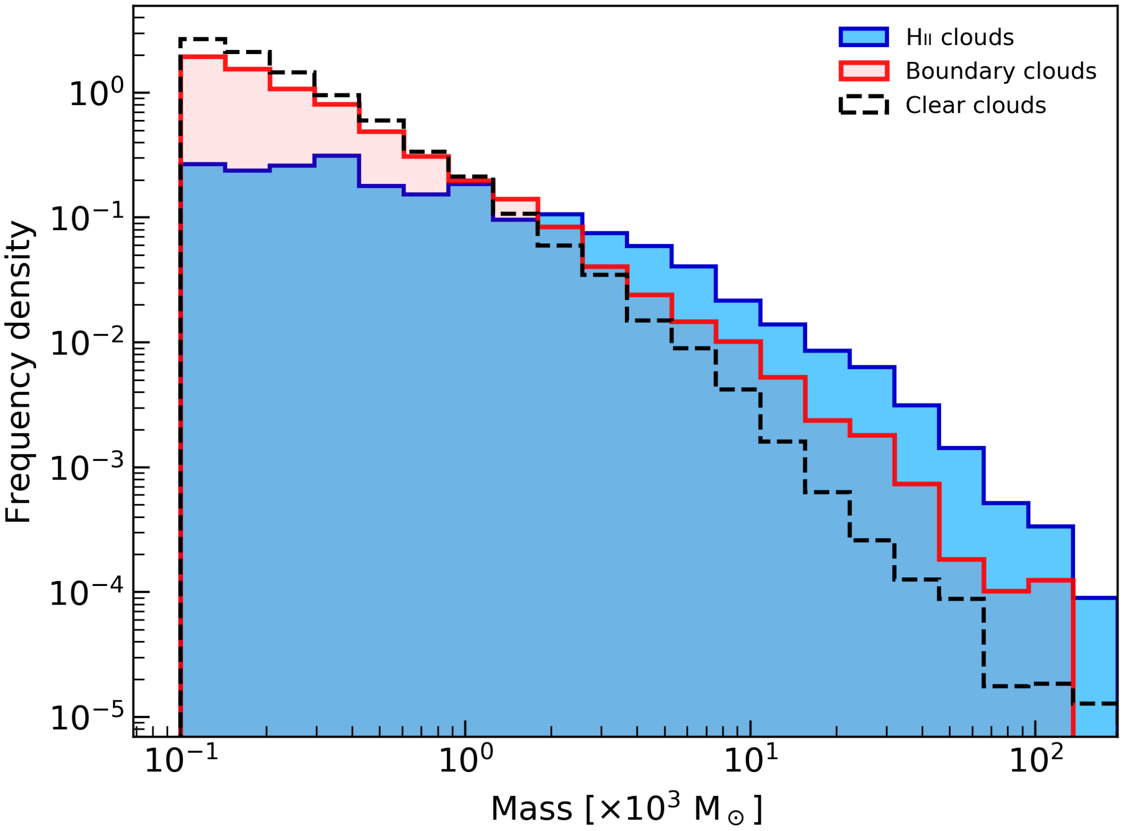

Figure 5.12. Plot showing the normalised mass distributions for HII clouds (blue), boundary clouds (red) and clear clouds (dashed black line). The y-axis shows the bin frequency normalised to 1 for each category to better compare the distributions.

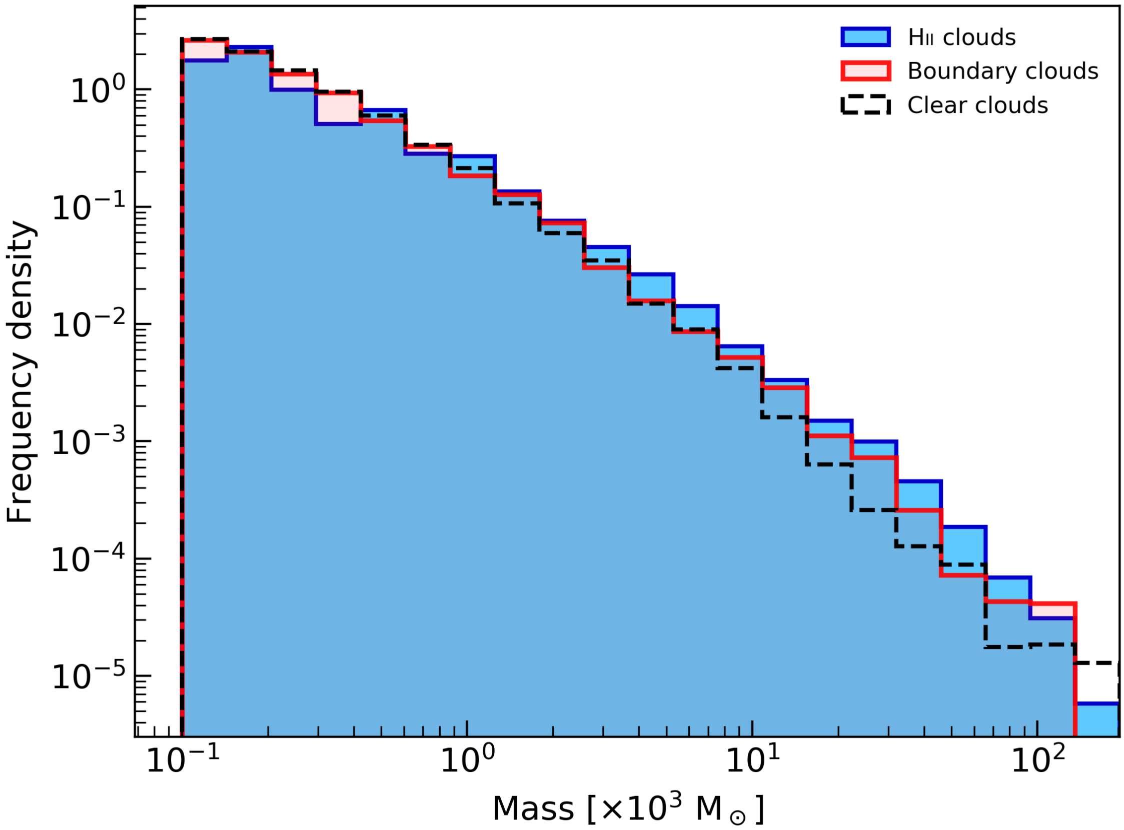

Figure 5.13. Plot showing the normalised mass distributions for HII clouds (blue), boundary clouds (red) and clear clouds (dashed black line) after resampling their area distributions to match the clear clouds. The y-axis shows the bin frequency normalised to 1 for each category to better compare the distributions.

the assumption that the size distributions of all three cloud categories are similar, allowing us to minimise the bias introduced when categorising the clouds. Given the original size distributions presented in Fig. 5.10 and the exposed size-bias discussed above, this seems a reasonable assumption to make.

5.3.6 Distribution matching

Here, we evaluate the statistical differences between the properties of the three cloud categories after resampling has been performed. To determine if two distributions are drawn from the same population of objects, one can use a non-parametric test with the null hypothesis being that both distributions are from the same parent distribution. Two such tests are the Kolmogorov–Smirnov test (KS test) and the Mann–Whitney test (MW test). The KS test works by comparing the differences between the cumulative probability function of the two distributions (i.e., it compares the distance between ranked values). While a powerful statistical method, long-tail distributions tend to influence the statistic towards rejecting the null hypothesis for the KS test. The MW test however, does not compare distributions but instead compares how a random sample taken from the one distribution differs from a random sample taken from a different distribution (i.e., it compares the difference between the medians of each distribution). Since the median is less affected by long tail distributions, the statistic is less likely to reject the null hypothesis due to differing extents of long-tails. Under these circumstances, I use both tests when checking if two distributions are drawn from the parent population. For a robust result, I only reject the null hypothesis if the outputted statistic is significant above 99.94% (which is equivalent to a 3σ detection). This means there is only a 0.6% chance that the distributions come from the same population. Since I have three distributions to compare in this study, I perform the tests three times to compare between each category using the Python package, `scipy.stats`, which outputs both the statistic for each test and its percentage significance.

5.4 Results

5.4.1 Summary of cloud properties

In Table 5.1, I list all the resampled cloud properties calculated in this chapter, along with their median values and their 16–84 percentile values as an estimate for their 1-sigma spread since most distributions contain long tails toward large values.

The impact resampling has on all the values in Table 5.1 is to lower the median values toward the clear clouds, and reduces the 1-sigma spread in the data. Even though the resampling should just minimise size bias, it still has the potential to

Table 5.1. Median values and 16–84 percentiles of all parameters, and results of KS and MW tests if the null hypothesis could not be rejected (i.e the distributions are the same).

Property	Category	Median
Average column density (1×10^{22} cm^{-2})	HII clouds	$1.27\pm^{0.53}_{0.23}$
	Boundary clouds	$1.18\pm^{0.39}_{0.12}$
	Clear clouds	$1.15\pm^{0.29}_{0.11}$
Peak column density (1×10^{22} cm^{-2})	HII clouds	$2.11\pm^{3.53}_{0.78}$
	Boundary clouds	$1.69\pm^{1.82}_{0.44}$
	Clear clouds	$1.57\pm^{1.24}_{0.35}$
Average dust temperature (K)	HII clouds	$17.6\pm^{1.2}_{1.0}$
	Boundary clouds	$17.6\pm^{1.1}_{1.2}$
	Clear clouds	$16.9\pm^{0.9}_{1.1}$
Peak dust temperature (K)	HII clouds	$18.7\pm^{1.6}_{1.2}$
	Boundary clouds	$18.2\pm^{1.7}_{1.3}$
	Clear clouds	$17.4\pm^{1.0}_{1.2}$
Aspect Ratio	HII clouds	$2.75\pm^{1.98}_{1.09}$
	Boundary clouds	$1.69\pm^{0.96}_{0.41}$
	Clear clouds	$1.68\pm^{1.03}_{0.42}$
Cloud mass ($M_\odot$)	HII clouds	$330\pm^{2000}_{260}$
	Boundary clouds	$180\pm^{1100}_{150}$
	Clear clouds	$160\pm^{840}_{140}$
Effective radius (pc)	HII clouds	$0.6\pm^{0.9}_{0.3}$
	Boundary clouds	$0.5\pm^{0.7}_{0.3}$
	Clear clouds	$0.5\pm^{0.7}_{0.3}$
Spherical volume density (cm^{-3})	HII clouds	$4300\pm^{9100}_{2000}$
	Boundary clouds	$6200\pm^{8100}_{3400}$
	Clear clouds	$6200\pm^{8000}_{3400}$
Ellipsoidal volume density (cm^{-3})	HII clouds	$8300\pm^{9300}_{4700}$
	Boundary clouds	$8100\pm^{10700}_{4300}$
	Clear clouds	$8600\pm^{10100}_{3400}$
Free-fall time (Myr)	HII clouds	$0.34\pm^{0.18}_{0.11}$
	Boundary clouds	$0.35\pm^{0.16}_{0.12}$
	Clear clouds	$0.34\pm^{0.17}_{0.11}$
Thermal Jeans mass ($M_\odot$)	HII clouds	$7.8\pm^{3.5}_{2.8}$
	Boundary clouds	$7.4\pm^{3.8}_{2.6}$
	Clear clouds	$6.8\pm^{3.6}_{2.3}$
IR brightness fraction	HII clouds	$0.65\pm^{0.26}_{0.44}$
	Boundary clouds	$0.34\pm^{0.58}_{0.31}$
	Clear clouds	$0.13\pm^{0.44}_{0.12}$
No of 70 μm sources	HII clouds	$1\pm^{2}_{1}$
	Boundary clouds	$0\pm^{2}_{0}$
	Clear clouds	$0\pm^{1}_{0}$
Total 70 μm flux (Jy)	HII clouds	$1\pm^{35}_{1}$
	Boundary clouds	$0\pm^{13}_{0}$
	Clear clouds	$0\pm^{2}_{0}$
Total 70 μm luminosity ($L_\odot$)	HII clouds	$40\pm^{1220}_{40}$
	Boundary clouds	$0\pm^{230}_{0}$
	Clear clouds	$0\pm^{30}_{0}$

remove genuine differences between cloud properties, which could result in a wrong conclusion about the similarity between cloud properties. However, all distributions of cloud properties, except for the cloud properties that are directly proportional to their projected area, are visually quite different, (which is reflected in the cloud's median values); therefore I do not expect that the resampling will significantly impact my conclusions. I note that cloud properties directly proportional to their projected area (e.g., effective radius, volume density) should be similar.

When only considering the median values and sigma ranges of the cloud properties, in general, HII clouds > boundary clouds > clear clouds. Although there are three exceptions to this trend, the median aspect ratios, the median the peak H_2 column densities, and the median spherical volume densities, where HII clouds have much different median values compared to the others two categories (aspect ratio=2.75, peak H_2 column density=2.11×10^{22} cm^{-2} are much larger while the spherical volume density=4300 cm^{-3}, is much smaller). Volume density is a property that only depends of size, therefore the fact that HII clouds have high aspect ratios and high H_2 column densities, but a low volume density indicates that they are more filamentary compared to boundary clouds and clear clouds. Indeed, when looking at the ellipsoidal volume density (which uses the cloud major and minor axis), all cloud categories now have almost identical volume densities around 8000 cm^{-3}. Therefore, the ellipsoidal volume density better represents the average volume density of the molecular clouds in this survey and will be used for the rest of the chapter for any property involving volume density.

Another exception are the peak and average dust temperatures for HII and boundary clouds, which are similar between themselves but larger compared to clear clouds. Typically, molecular gas temperatures increases as the gas is converted into stars. But this also correlates with increased H_2 column densities (Urquhart et al. 2018). The boundary clouds, while having high temperatures similar to HII clouds, have lower column density values. This suggests that the HII regions have affected the molecular gas temperatures in their neighbouring clouds (assuming dust temperatures trace gas temperatures). Table 5.1 also shows that the median values for 70 μm sources and total luminosities are 0 for boundary and clear clouds have. Only 74%, 48%, and 36% of HII, boundary, and clear clouds respectively had detectable 70 μm sources. Therefore, the median values of the boundary and clear clouds are zero.

I note that after performing KS and MW for each parameter for each distribution, all distributions were able to reject the null hypothesis. The distributions were different enough to pass the KS and MW test, including area derived properties. However Table 5.1 shows that the area derived properties have similar median and sigma spreads, and as discussed, they should have similar distributions. Hence, I expected that the KS and MW tests would fail to reject the null hypothesis. When looking at the actual histogram distributions, I see some small differences present at the high and low end values of the distributions. Therefore, it is likely that the tails of the distribution are affecting the reliability of these tests. Considering this, I do not rely on these tests.

5.4.2 PERCENTAGE OF REGIONS THAT CONTAIN TRIGGERED STAR FORMATION

In Fig. 5.14, I estimate the new total cloud mass per category. To do this, I took a 100 subsamples equal to the number of clouds per category from the new distribution, and calculated the average total mass of the subsamples. Doing this I show that only ~20% of clouds, both in number and mass are within the boundary layer of HII regions. This indicates that, at a uniform star formation efficiency (see next sections for a discussion regarding this assumption), boundary clouds can only contribute to a maximum of 20% of the stars currently produced in the Milky Way. Even assuming all boundary clouds have been correctly assigned, this still only accounts for 20% due the overwhelming percentage of mass contained in HII clouds. For triggered star

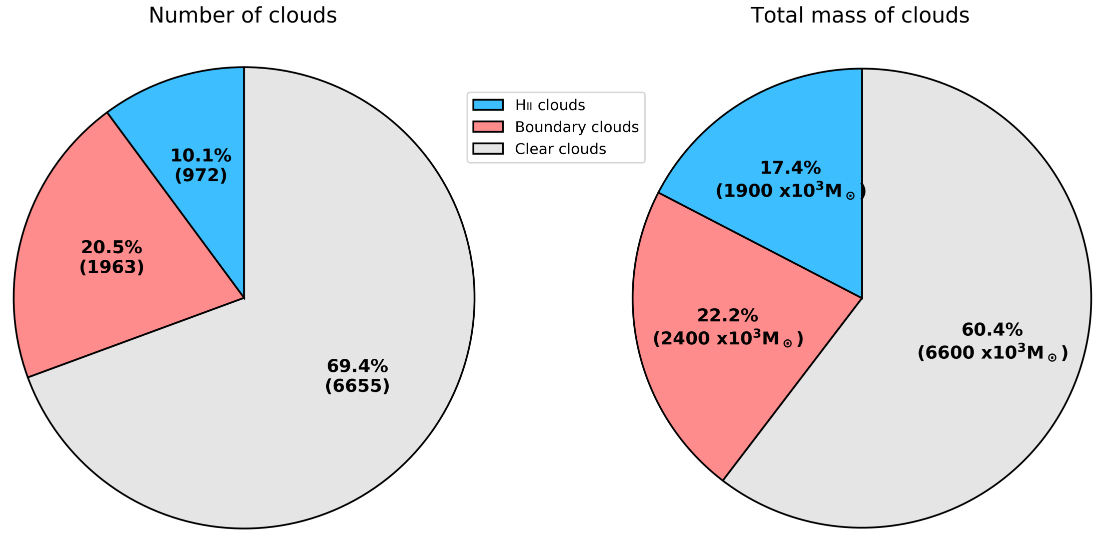

Figure 5.14. Chart illustrating percentage of clouds categorised **left** and the total mass contained within each category **right** after removing the size. The three cloud categories are clear clouds (solid grey colour), HII clouds (solid blue colour) and boundary clouds (solid red colour). The number of HII clouds and boundary clouds decrease compared to Fig. **??** by 20 and 2 clouds respectively since their projected areas were beyond the largest area present in the clear clouds. As a result, these clouds could not be resampled and had to be removed.

formation to play a significant role contributing to the star formation rate in the Milky Way, the recycling time of boundary clouds (i.e., the time it takes to replace the current population of boundary clouds by new ones) needs to be shorter than that for the other two categories. However, this is unlikely to be the case since there is no significant differences in the distribution of volume densities and free-fall times between the three categories, and the mass of boundary clouds are not much different from clear clouds; There is little evidence indicating that clouds that are in the boundary layer of HII regions are able to evolve faster.

5.4.3 CHECKING IR BRIGHTNESS AS A TRACER OF EVOLUTIONARY STAGE

To check that the IR brightness fraction can trace the relative evolutionary stage of clouds, I plot the total 70 μm luminosity measured in each cloud against their

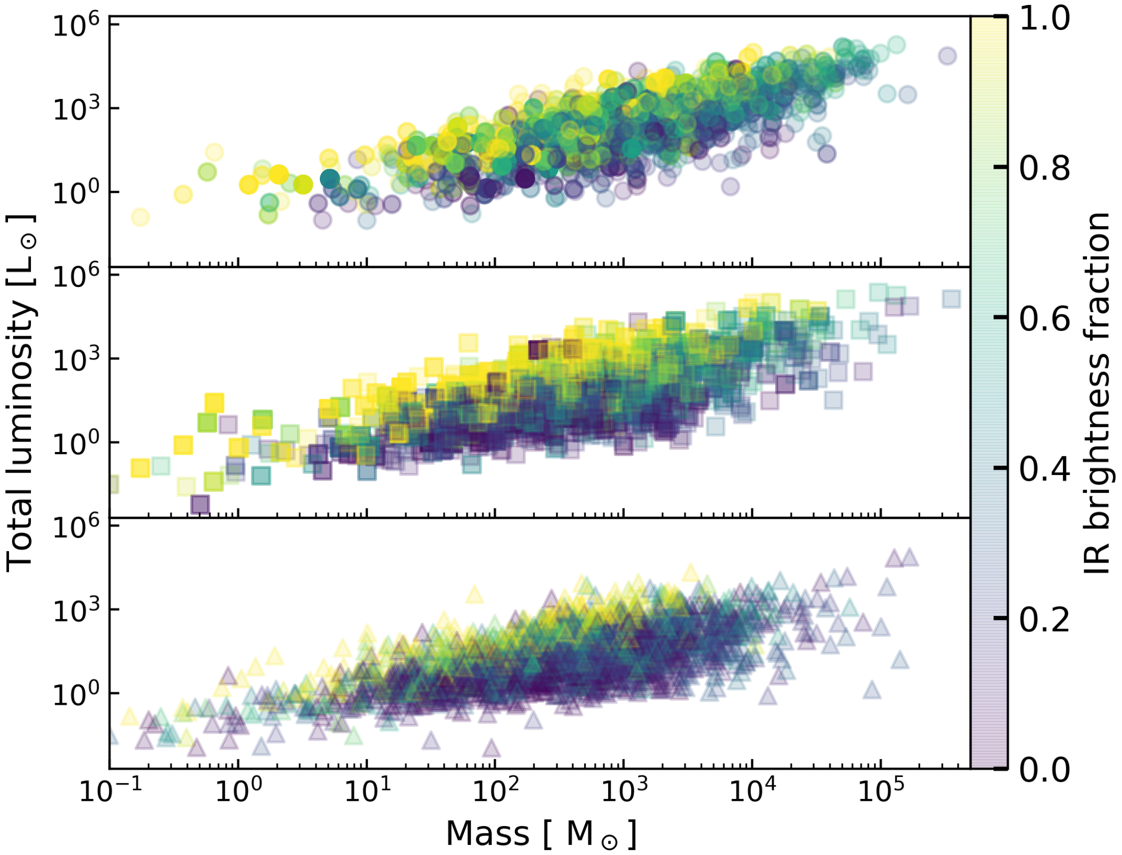

Figure 5.15. Figure showing 70 μm luminosity v.s. the cloud mass for HII clouds (**top**), boundary clouds (**middle**) and clouds with no HII regions (**bottom**). The colour of the points indicate their IR brightness fraction.

mass, and colour each point by its IR brightness fraction for the three classifications on Fig. 5.15. Figure 5.15 shows two important results. Firstly, it shows that the IR brightness fraction increases as the luminosity to mass ratio increases for all three cloud categories. By this, I mean that the luminosity increases in proportion with the IR brightness fraction at constant cloud mass. Assuming that the 70 μm luminosity is an indicator of the stellar mass that is being formed in each cloud, the plot indicates that as more of mass is converted into stars, the IR brightness fraction increases. This result justifies our use of the IR brightness fraction as a tracer of the evolutionary stage of clouds.

Secondly, the plot shows that HII clouds have more clouds with larger IR brightness fractions at lower luminosity to mass ratios compared to clear clouds. Boundary layer clouds are somewhere in between the two. Furthermore, there are almost no HII clouds that intersect with clouds without any HII regions with similar IR brightness fractions in luminosity/mass space. Having shown that the IR brightness fraction can trace the evolutionary stage of clouds, this result is consistent with the idea that HII clouds and clear clouds trace to very different evolutionary stages that do not overlap (see Fig. 5.5). It also demonstrates that boundary layer clouds cover a broader range of evolutionary stages than any of the other two cloud categories.

5.4.4 INVESTIGATING SFE AS A FUNCTION OF EVOLUTIONARY STAGE WITHIN CLOUDS

To investigate how the SFE evolves in time, I use $L_{\rm tot}^{70\mu{\rm m}}/M_{\rm cloud}$ as a proxy for SFE and the IR brightness fraction a proxy for time evolution. For all three cloud classifications, I calculate their $L_{\rm tot}^{70\mu{\rm m}}/M_{\rm cloud}$ and I subdivide the catalogue into the four IR brightness ranges, 0–25%, 25–50%, 50–75% and 75–100% and plot this on Fig. 5.16. I also tabulate the percentage of clouds within these ranges in Table 5.2. I note again that because only 74%, 48%, and 36% of HII, boundary, and clear clouds

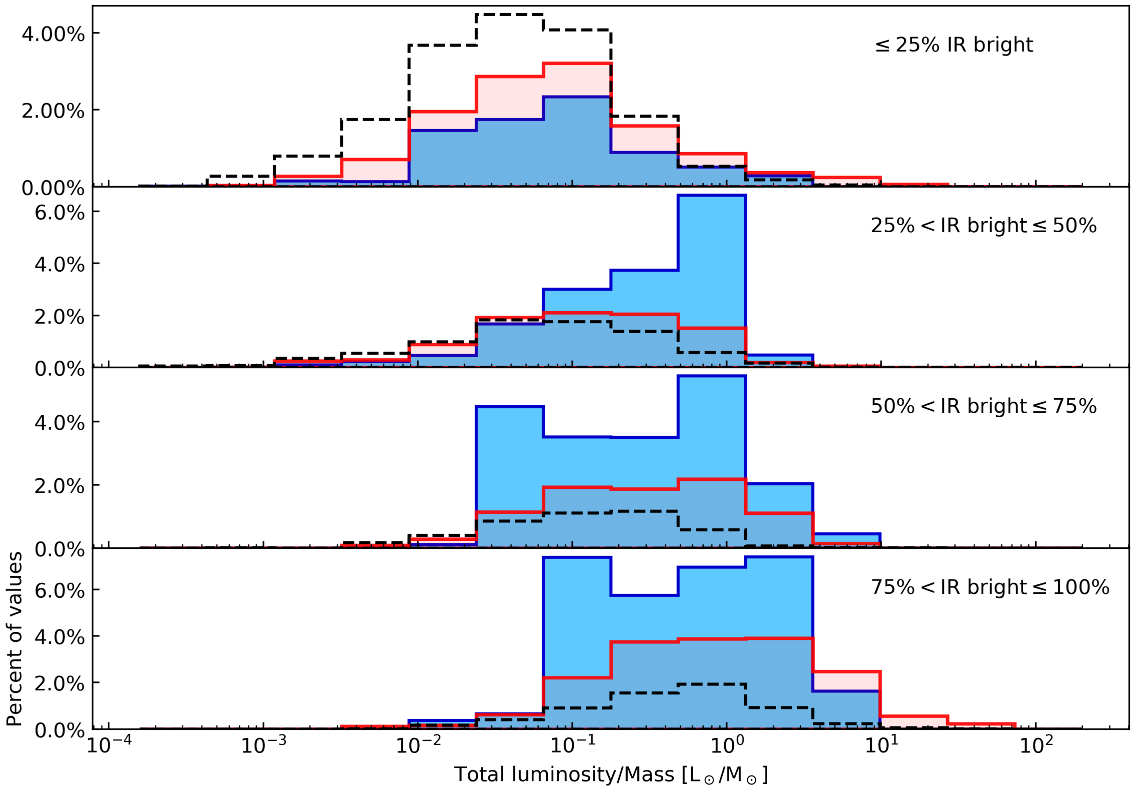

Figure 5.16. Change in IR brightness as a function of luminosity to mass ratio for clear clouds (dashed black line), boundary clouds (solid red line), and HII clouds. (solid blue line). Each panel indicates the IR brightness range of the corresponding distributions. Since only 74%, 48%, and 36% of HII, boundary, and clear clouds respectively had detectable 70 μm sources, the percentages do not add up to 100%, but instead add up to the percentage of clouds with a source per category.

Table 5.2. Percentage of clouds in each category at least one 70 μm that have IR brightness values within the IR range shown in the first column. Only 74%, 48%, and 36% of HII, boundary, and clear clouds respectively had detectable 70 μm sources so their percentages listed add up to these values.

IR brightness fraction	HII clouds	Boundary clouds	No HII region
0–25%	8%	12%	18%
25–50%	16%	9%	8%
50–75%	20%	9%	4%
75–100%	30%	18%	6%

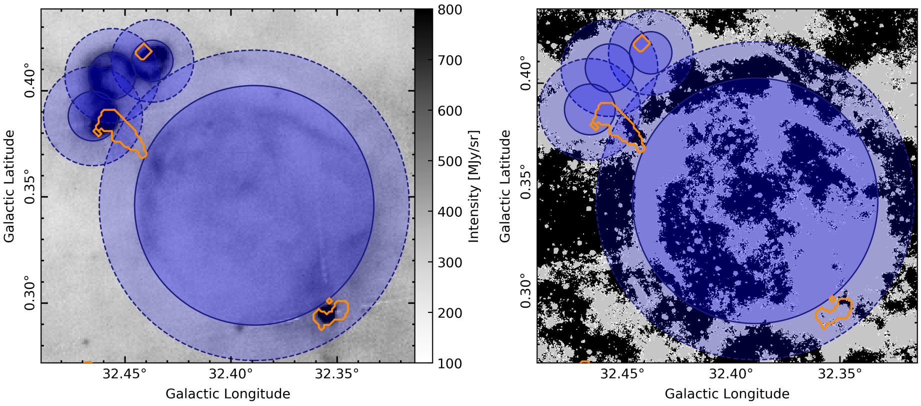

Figure 5.17. Example of molecular clouds (solid orange contours) with high IR brightness (50–100%) found in the boundary of a large HII region (light blue annuli with dashed boarders, see Sec. 5.3.5 for how HII regions are defined as being large) **left** shows the HII regions and molecular clouds over-plotted against 70 μm emission and **right** shows the same objects over-plotted against their IR brightness fractions. Black pixels are IR dark pixels, grey pixels are IR bright pixels and white pixels those that could not be assigned since their value after background subtraction were below the rms limit of the GLIMPSE map. Pixels in IR brightness map are 1.2″ in size.

respectively had detectable 70 μm sources, the percentages shown in Fig. 5.15 add up to these values, rather than to 100%. As shown in the previous subsection, the lowest IR brightness values, and the clouds without any HII regions trace the SFE at the earliest evolutionary stages, while high IR brightness values, and clouds with HII regions trace more evolved evolutionary phases. Therefore, for the following results, I refer to HII clouds and clear clouds as more and less evolved clouds respectively.

Figure 5.16 shows three main results. First, there is a deficiency of boundary layer clouds with low SFEs compared to the least evolved clouds at early evolutionary timescales (i.e when 0–25% IR bright, see top panel of Fig. 5.16). Secondly, the total percentage of clear cloud's at intermediate timescales (that also contain an 70 μm source) drops by 10% compare to the previous evolutionary stage, but the number of boundary clouds barely changes while the percentage of HII clouds at the same stage increases by 8%. This indicates that almost all the young clear clouds evolve into HII clouds, rather than into boundary clouds. Together, this suggests that boundary clouds do not evolve from clear clouds and are created at later evolutionary stages.

Finally, there is a small population of boundary clouds with larger $L_\odot/M_\odot$ compared to Hii at final evolutionary stages (corresponding to 1.5% of boundary clouds on Fig. 5.16). This suggests a small fraction of boundary clouds have higher SFE's compared to Hii clouds. However, these clouds might also represent a fraction of clouds where the neighbouring Hii region has increased the measured IR brightness fraction or even increased the 70 μm flux measured. To test this, I visually inspected a sample boundary clouds masks and the WISE Hii overlayer on top of the Hi-GAL 70 μm and IR-brightness maps and plot some examples on Fig. 5.17. What I find is that IR-brightness measured is normally larger in extent compared to the 70 μm emission for lower column density clouds (where lower column densities also result in lower cloud masses and hence higher $L_\odot/M_\odot$ ratios). Therefore, I expect that the IR fraction of lower column density boundary clouds might be overestimated. Even so, there is still a population boundary clouds with higher SFE's compared to Hii clouds, but since only occurs for 1.5% of boundary clouds, they do not represent a significantly contribute to the overall star formation in the Milky Way.

Tracing top heavy star formation

Some models of triggered star formation predict that triggered stars are more likely to form high-mass stars (Whitworth et al. 1994). To determine if boundary layer clouds are forming a higher proportion of high-mass stars compared to regular molecular clouds, I divide $L_{\rm tot}^{70\mu{\rm m}}/M_{\rm cloud}$ by the number of sources, $N_{70\mu{\rm m}}$ within each cloud to obtain the average luminosity per source vs the total mass of the cloud. In doing this, I assume that high values of $L_{\rm tot}^{70\mu{\rm m}}/(M_{\rm cloud}N_{70\mu{\rm m}})$ trace the clouds that contain, on average, a larger fraction of high-mass stars in relation to the cloud mass present. Small values of $L_{\rm tot}^{70\mu{\rm m}}/(M_{\rm cloud}N_{70\mu{\rm m}})$ thus trace the clouds that contain a larger fraction of low mass stars in relation to the cloud mass present. On Fig. 5.18, I plot $L_{\rm tot}^{70\mu{\rm m}}/(M_{\rm cloud}N_{70\mu{\rm m}})$ at different evolutionary stages (as traced by the IR brightness fraction). In these plots, we see some evidence that the more evolved boundary clouds

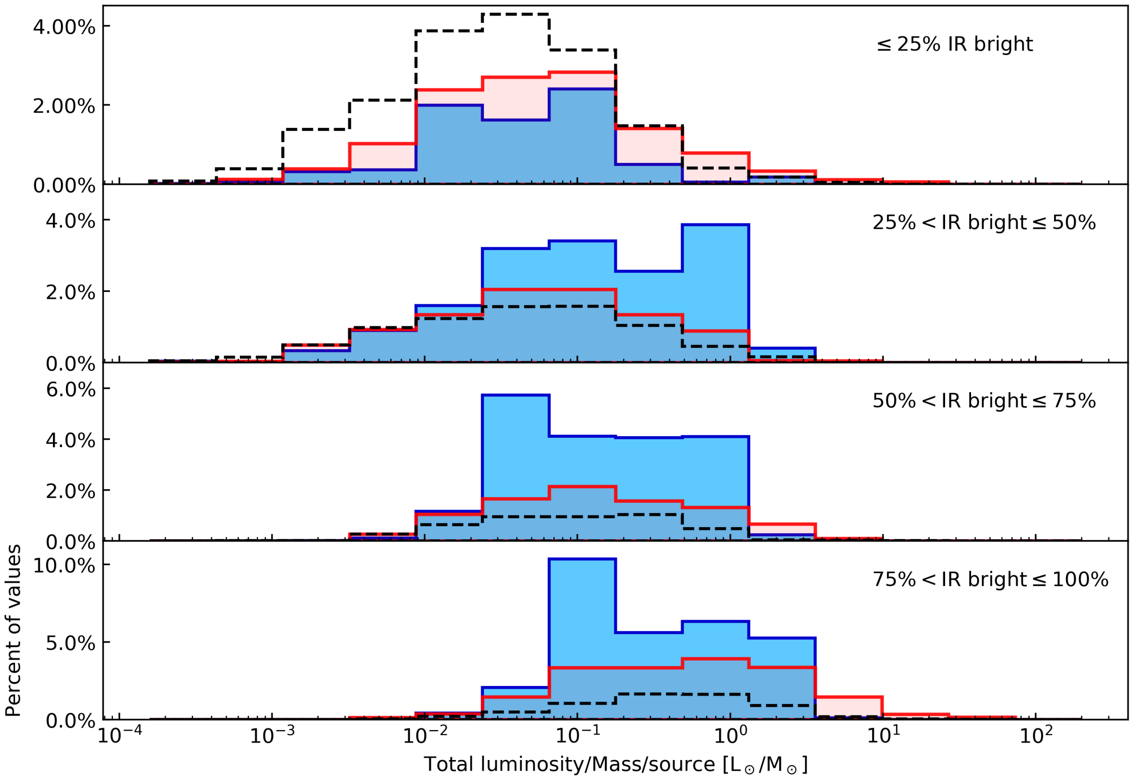

Figure 5.18. Change in IR brightness as a function of luminosity to mass ratio s number of 70μm sources for for clear clouds, (dashed black line), boundary clouds (solid red line) and HII clouds. (solid blue line). Each panel indicates the IR brightness range of the corresponding distributions.

have a fraction (∼3%) of clouds with brighter (i.e., more massive) young stellar objects in relation to the cloud mass present compared to similarly evolved clouds. Except for these clouds, boundary clouds have similar distribution of $L_{\rm tot}^{70\mu{\rm m}}/(M_{\rm cloud}N_{70\mu{\rm m}})$ values to HII clouds, indicating that most boundary clouds form the expected number of high (and low) mass stars.

I note that as clouds evolve (become more IR bright), the total distributions shift towards higher $L_{\rm tot}^{70\mu{\rm m}}/M_{\rm cloud}$ and $L_{\rm tot}^{70\mu{\rm m}}/(M_{\rm cloud}N_{70\mu{\rm m}})$ values. As protostars evolve, their luminosity output changes (see Fig. 1.4). This can make $L_{\rm tot}^{70\mu{\rm m}}/M_{\rm cloud}$ an unreliable tracer of SFE since it is difficult to disentangle SFE from the evolution of the protostar. But by separating the clouds by their evolutionary stage, $L_{\rm tot}^{70\mu{\rm m}}/M_{\rm cloud}$ (and $L_{\rm tot}^{70\mu{\rm m}}/(M_{\rm cloud}N_{70\mu{\rm m}})$), we remove (or limit) the variability in these values, which is why we see a shift towards higher values as a function of IR.

5.4.5 THE ORIGIN OF THE GAS FOUND IN THE BOUNDARY OF HII REGIONS

The gas that assembles around the boundary layer of expanding HII regions originates from:

- Low-density ($\sim 1\times10^{21}$ cm^{-2}), unbounded gas that has been swept-up and gathered by the expanding HII region (Whitworth et al. 1994);
- Nearby, bound gas (i.e., a molecular cloud) that pre-exists the expansion of the HII region (Bertoldi 1989);
- Dense molecular gas that existed within the molecular cloud that hosted the HII region (Dale et al. 2012).

In the following, I refer to these three different origins as (low density-) swept-up gas, pre-existing molecular gas and (dense-)relocated molecular gas respectively. The true origin of boundary layer clouds will contain a mixture of all three scenarios at

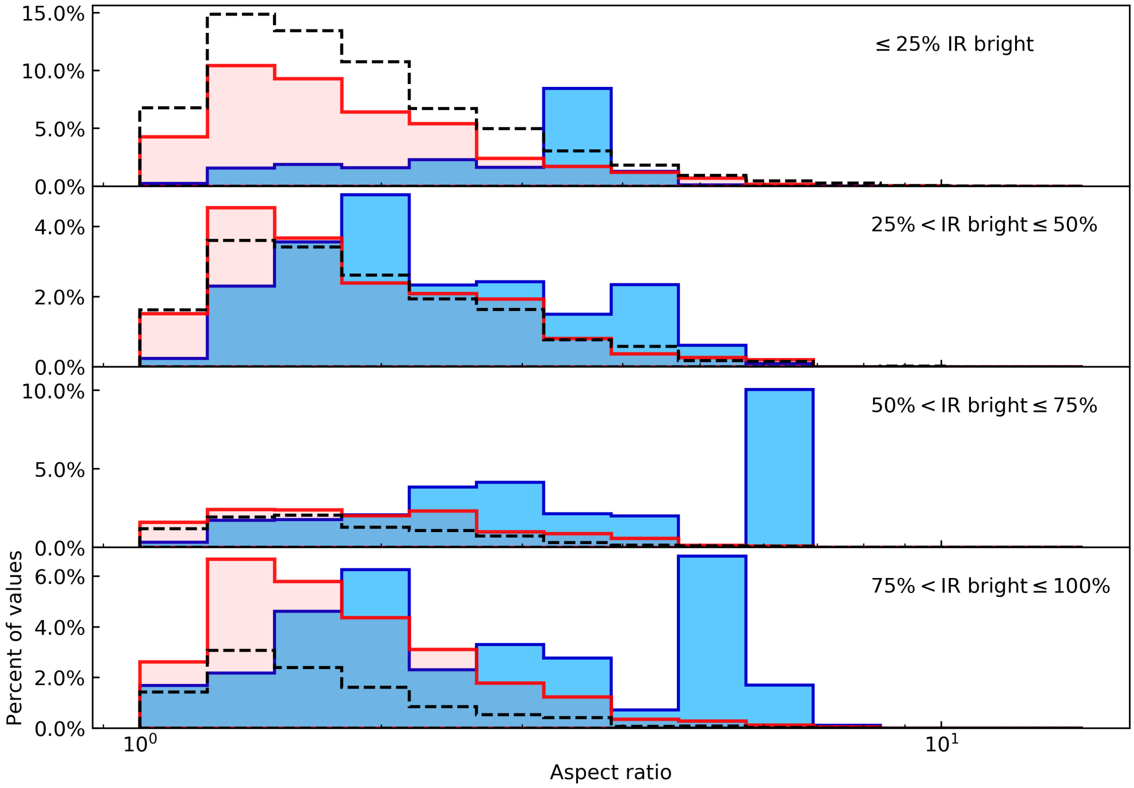

Figure 5.19. Change in IR brightness as a function of aspect ratio for clear clouds, (dashed black line), boundary clouds (solid red line) and HII clouds. (solid blue line). Each panel indicates the IR brightness range of the corresponding distributions.

once (Deharveng et al. 2009; Walch et al. 2015), however, one can determine the dominant one by comparing the cloud and star formation properties predicted by different models to the observations.

Boundary clouds formed from swept-up, low density gas are predicted to remain starless for a long period of time (∼1–3 Myrs, Whitworth et al. (1994); Iwasaki et al. (2011)) until they become dense enough for gravitational instabilities to develop, causing them to fragment. The properties of these swept-up shells are such that the resulting fragments are massive and are likely to lead to the formation of high-mass stars and clusters. If the majority of boundary clouds form by this mechanism, one should see the existence of young, and relatively starless molecular clouds in the shells of HII regions at early evolutionary times. Projected along the line of sight, these clouds will appear as arcs, and so have high aspect ratios. According to this model, as the boundary clouds evolve, they should fragment into massive-star forming clumps of lower aspect ratios. The change in aspect ratio occurs because the fragments form while the HII region is still expanding. This eventually separates the fragments away from each other spatially, causing them to be detected as separate molecular clouds. As a result, I plot the distributions of aspect ratios as a function of IR brightness in a similar way as the previous section to check whether one can see evidence of such a process. Figure 5.19 shows there is a slight increase in median value when clouds are 50-75% IR bright, compared to the other brightness fractions, but this represents later evolutionary stage rather than at earlier evolutionary stage. Additionally, fragmentation is predicted to occur when the column densities through the shell reach 4–8$\times10^{21}$ cm^{-2}, (Whitworth et al. 1994), yet I only investigate clouds $\geqslant 1\times10^{22}$ cm^{-2}. Consequentially, I might not be able to trace the early evolution of these clouds.

However, it was found that the later evolutionary stages of boundary clouds (IR brightness of 50–100%) form more high-mass star than HII clouds in the previous Section (i.e., panel 3–4 on Fig. 5.18). Therefore these clouds might represent a population of objects that formed and evolved via swept-up gas. If I assume that all high $L_{\rm tot}^{70\mu{\rm m}}/(M_{\rm cloud}N_{70\mu{\rm m}})$ are the product of swept-up gas, and that 3% represents the detectable fraction of boundary clouds with higher $L_{\rm tot}^{70\mu{\rm m}}/(M_{\rm cloud}N_{70\mu{\rm m}})$ between IR brightnesses of 50–100%, 6% of boundary clouds formed via swept-up gas. While a crude estimate, it is a low enough percentage to indicate that it is unlikely that the majority of boundary clouds formed from swept-up gas.

Simulations modelling the expansion of an HII region into small pre-existing clouds indicate that the gas within these clouds quickly collapses, and forms low mass stars ~0.1 Myr after the first contact with the HII region. However the achieved SFE within these clouds is only high when the incident ionising flux is low(Bertoldi 1989; Bisbas et al. 2011). If an HII region instead expands into a larger molecular cloud, which already contains clumps, the HII region compresses the cloud, which cause clumps to merge together. With larger masses, these clumps gravitationally collapse to form higher mass stars and star clusters (Elmegreen et al. 1995).

If the majority of boundary clouds evolved from pre-existing gas, one would expect that at early evolutionary stages most of these clouds evolve from clear clouds from a purely statistical argument. If one assumes that all boundary clouds originate from pre-existing molecular gas, and assuming that clouds used in this survey—that are not bounding a HII region—are representative sample of Galactic plane clouds, an HII region will expand into a clear cloud 77% of the time (6655/[1963+6655] =0.77, see Fig. 5.14). Therefore, if this occurs, I expect the properties of the boundary clouds to coincide with clear cloud at early evolutionary stages. At later evolutionary stages however, it is unclear what would be observed since and the ability pre-existing molecular gas to form star is dependent on the incident ionising flux density and the size of the cloud.

Simulations modelling HII regions expanding into its natal cloud often find that star formation continues mostly uninterrupted in the molecular gas, but is relocated to the boundaries of the HII region (Dale et al. 2012). In these simulations, some stars are triggered but the overall impact of the Hii region is to slightly lower SFE's, when compared to molecular cloud that evolves without feedback. Therefore, if the majority of boundary clouds form from dense relocated molecular gas, one would expect that the SFE's within these clouds to trace SFE's of Hii clouds at earlier evolutionary stages, but for SFE's to reduce sightly compared to Hii clouds at later evolutionary stages. Figure 5.16 shows the SFE's of boundary clouds at the earliest evolutionary stages have similar distributions to Hii clouds (where SFE$\propto L_{\rm tot}^{70\mu{\rm m}}/M_{\rm cloud}$). Additionally, the distribution SFE's of at later evolutionary stages also have similar values to Hii clouds (except for a small percentage of boundary clouds, which represents 1.5% of boundary clouds).

While the SFE's align with this origin, the average properties of boundary clouds in Table 5.1 are more similar to clear clouds, than Hii clouds (median mass, peak column densities etc.), except for dust temperatures. This points toward an evolutionary scenario where boundary cloud represent gas that has been relocated by an Hii region quickly after the first ionising sources formed. Therefore, I expect that the majority of clouds in the boundary layer of Hii regions comes from younger Hii clouds where the development of an Hii region was able to unbind the gas from its host molecular cloud.

5.5 Discussion

In the following discussion I attempt to place constraints on the amount of triggered star formation occurring in the Milky Way. I note that when discussing about the evolutionary stages and SFEs of clouds, I am referring to their IR brightness and $L_{\rm tot}^{70\mu{\rm m}}/M_{\rm cloud}$ values.

As shown in Fig. 5.14, only ~20% of clouds (by number and mass) are contained within the boundary layer of Hii regions. Under the assumptions that this gas evolves on a similar timescale and with a similar SFE to the rest of the clouds in the Milky Way, a maximum of 20% of star formation is triggered at any given time. In the previous Section, I predict that the majority of boundary clouds evolve from young HII clouds. This implies that before this gas ended up in the boundary of an HII region, it existed within an HII cloud that has itself evolved from a dense, but quiescent molecular cloud. Therefore, there is no reason to expect that boundary clouds evolve on a quicker timescale. (I note that some HII clouds might have themselves evolved from the boundary of an HII region, but I assess the contribution to SFE's in the next Section).

Even though triggered star formation might only be a minor contributor to the over star formation rate within the Galaxy, one still needs to determine whether or not it is at play. The only way to determine if triggering has occurred is whether, on average, SFE's with boundary clouds are greater than those not currently within the boundary of an HII region. In other terms, I define triggering as a mechanism that locally raises the SFE within clouds over its lifetime. Figure 5.16 shows that almost all boundary layer clouds have a similar SFE's as HII clouds at all evolutionary stages. However the latest evolutionary stage indicates that ∼1.5% of boundary clouds have higher SFE's than HII clouds. Since this increase is only present for the most evolved boundary clouds, this better represents an increase in the SFR rather than the SFE; for the majority of the evolution of the boundary clouds, the SFE was no different than if it was to evolve away from the boundary of an HII region.

The final argument for whether triggered star formation is important within the Galaxy is whether the stars that have formed would have formed without being influenced by a HII region first. With simulations, this value can be estimated by investigating how many stars formed with stellar feedback, and without (Dale et al. 2012). On the other hand, observations represent a single snapshot in time, which restricts our ability to predict how HII regions actually impact star formation. But because this study indicates that most boundary evolved from HII clouds, we can predict how the gas would have evolved if the HII region present was unable to unbind the gas. The Hii clouds represents this sample of clouds that have developed Hii regions, but have not been interrupted by their own star formation activity. Since these clouds have SFEs that are similar to the clouds that were unbounded by an Hii region, the star formation in boundary clouds do not represent an increase to the total star formation rates of the Milky Way (i.e., if this gas had remained bound, it would have evolved a similar number of stars). Therefore, triggered star formation is not an important star formation mechanism in the Milky Way.

Sequential star formation

Sequential star formation is the propagation of star formation due to the repeated triggering of high-mass stars (Elmegreen & Lada 1977). In this regime, high-mass stars that form in the boundary layer of an Hii region create their own Hii region, which propagates the star formation over a larger area where it can influence another generation of molecular clouds. Therefore its ability to set star formation rates is dependant on the number of high-mass stars that form in the boundary layer of Hii regions.

Some clouds classified as Hii clouds might represent a population of sequential star formation after it has evolved to the point that its initial 'triggering' is no longer present. As a result, it will be difficult to identified when this has occurred. I do however know the number boundary clouds currently present that contain Hii regions themselves. Assuming they represent the fraction of clouds that can propagate star formation, I can estimate this number. In Sec. 5.3.5, I found that 195 boundary clouds contain at least 1, or more small Hii regions, which is 10% of boundary clouds. This therefore represents an upper bound for the number of Hii clouds that might have evolved from boundary clouds. For a boundary cloud to appear as an Hii cloud, the initial Hii region must no longer be detected, or appear associated. The WISE catalogue includes large and extended Hii regions where radio emission is no longer detected. Consequentially, most boundary clouds that have evolved their own Hii region should still be classified as a boundary cloud.

To provide an estimate for the maximum number of clouds that might be influenced by sequential star formation, I assume that all boundary clouds containing HII regions will influence a 2nd generation of molecular clouds, in which 10% will influence a 3rd generation of molecular clouds, and so forth. I also assume that the initial sample of boundary clouds have only been influenced once by an HII region. Indeed, it was estimated that 6% of boundary clouds produce, on average, stars with higher mass than in HII clouds (see Sec. 5.4.4. Therefore it is not unreasonable to assume that 10% boundary clouds are able to form another generation of high-mass stars. When summed to infinity, just over 1% of clouds in total are influenced by future cycles of triggered star formation. Therefore, these results indicate that sequential star formation is not a dominant process within the star formation cycle of the Milky Way.

5.6 Summary and conclusions

To determine if triggered star formation plays a role in setting the SFEs in the Milky Way, I cross matched molecular clouds within the Hi-GAL survey to the WISE HII region catalogue to obtain a large sample of molecular clouds bounding HII regions to non-bounding. By tracing the evolutionary stage of each cloud based on their 8 μm IR brightness, I was able to perform a like-to-like comparison of SFEs, without the uncertainties introduced by time evolution. Therefore, changes in SFE could be reliably attributed to the local environment.

This allowed me to determine that most clouds within the boundary of an HII region evolved from the molecular gas present within the host HII region molecular cloud, where star formation was already underway and was evolved enough that at least one high-mass star has already formed. Therefore the SFEs in these clouds are higher than the gas found away from HII regions since the gas exists at a later evolutionary stage and not due the Hii region enhancing SFEs. In fact, when compared to more evolved clouds, clouds in the boundaries of Hii regions do not evolve any differently than if the gas that had developed an Hii region but had remained bound within the host cloud. Though, a small fraction of the most evolved clouds in boundaries of Hii regions have increased SFEs and are able to form larger stars. The implication of this, along with the fact that only only 20% of clouds (both in mass and number) are presently in the boundary of an Hii region, is that triggered star formation does not govern the star formation rate of the Milky Way.

CHAPTER 6

SUMMARY OF THESIS

In this chapter, I summarise the main results and conclusions concerning the impact of stellar feedback and discuss future work to be conducted following this thesis.

6.1 SUMMARISING THESIS PURPOSE

Star formation is a by-product of the processes that govern the ISM, but the energy and momentum generated by high-mass stars affect these processes in a complex feedback loop. Understanding how stellar feedback impacts an individual star forming region is an observationally difficult task when limited to studying their star forming properties from a single snapshot in time. However, without fully understanding the impact that stellar feedback has on regulating star formation within molecular clouds, a complete theory of star formation is impossible to obtain. Therefore, the goal of this thesis is to use observational methods to measure the impact of stellar feedback.

6.2 CONCLUSIONS

Throughout this thesis, I have analysed publicly available datasets tracing molecular gas, kinematics and feedback within molecular clouds to determine how feedback has impacted their star forming conditions locally. The first part of this thesis therefore focused on the G316.75 high-mass star forming ridge. The G316.75 ridge is ideally suited for this study since half of the ridge has already formed 4 O-stars, and has had at least one high-mass star for $\sim$2 Myr. However, the other half of the ridge has yet to form high-mass stars and appears unaffected by the high-mass star formation present within the active half. Therefore, by contrasting the two halves, I am able to quantify the impact of stellar feedback on the star forming ability of the gas. This assumes that the gas properties within the quiescent part were similar to the active part before the formation of high-mass stars. By calculating the local M_{line} along the ridge using Hi-GAL data, combined with ^{13}CO (J=1–0), NH_3 (1,1), and N_2H^+ (J=1–0) to trace low, medium and high gas densities, I show that there is little difference between the active part and the quiescent part when comparing their virial ratios, and expected mass loss over the gas densities measured. This contradicts simulations (Kim et al. 2018) which show stellar feedback destroying molecular clouds after only a few free-fall times after the formation of high-mass stars. This suggests that the process setting the ratio of kinetic to gravitational energy is global to the ridge and not due to local stellar feedback.

Moreover, by using theoretical calculations, I show that such feedback is actually expected to be inefficient given the large average density and elongated morphology of the ridge. Additionally, it is found that total clump mass measured within the active region has increased over time (assuming the clumps in the quiescent region represent the active clumps at earlier evolutionary stage), especially the clumps found in-between the ionising sources. This indicates local gas compression induced by stellar feedback may play a role in enhancing the gas density of clumps. Due to the inefficiency of feedback, and the inferred rapid rate of growth of the clump mass, I suggest that G316.75 will continue producing stars to form a massive stellar cluster until a supernova explosion changes the star forming environment in the coming 2 Myr.

I conclude that the initial morphology of a massive star-forming cloud plays an important role in its future evolution, especially with respect to the impact of the high-mass stars it will form. I suggest that a filamentary configuration strongly reduces the disruptive effects that feedback might have on the gas, and that such a morphology could be the result, at least in the case of G316.75, of cloud-cloud collision. As shown in this study, in such a configuration, stellar feedback from high-mass stars does very little to the dense gas already present, but is probably able to stop extended lower density gas from accreting onto the ridge. In other words, the main impact of feedback in G316.75 is gas exhaustion rather than gas ejection.

To understand the significance of this conclusion, I conducted a galactic wide survey in the second half of this thesis. Here, I investigated how stellar feedback in the form of expanding HII affects the star formation efficiencies of molecular clouds and its relevance for triggered star formation. This was done by cross-matching molecular clouds from the Hi-GAL survey with the WISE HII catalogue to obtain a large sample of molecular clouds bounding HII regions to non-bounding clouds. By tracing the evolutionary stage of each cloud based on their 8 μm IR brightness, I was able to perform a like-to-like comparison of SFEs, without the uncertainties introduced by time evolution. Therefore, changes in SFE could be reliably attributed to the local environment.

I found that most clouds within the boundary of an HII region evolved from the molecular gas present within the host HII region molecular cloud, where star formation was already underway. Therefore the SFEs in these clouds are higher than the gas found away from HII regions since the gas exists at an later evolutionary stage and not due the HII region enhancing SFEs. When compared to more evolved clouds not currently bounding HII regions, boundary clouds have similar SFEs. Since evolved clouds likely represent SFEs that boundary clouds could obtain if their gas remained bound, the only impact of the HII region was to relocate gas (and hence the star formation), rather than to trigger a new wave of star formation. Though, a small fraction of the most evolved clouds in the boundaries of HII regions have increased SFEs and are able to form larger stars. The overall implication of this, along with the fact that only only 20% of clouds (both in mass and number) are presently in the boundaries of HII regions, is that triggered star formation does not govern the star formation rate of the Milky Way. In the context of the G316.75 ridge, these results imply that only 2/3 of HII regions are able to unbind their gas while 1/3 of molecular clouds that form HII regions remain bound. Therefore the inefficiency of stellar feedback measured within the G316.75 ridge is not uncommon in the Milky Way.

Combined together, the two studies I present depict a picture where the role of stellar feedback seems at odds with the collective wisdom. My studies show that the impact of stellar feedback from massive stars on their parent/surrounding clouds is relatively minor. While feedback certainly plays a key role in limiting the global SFEs in the Milky way to 1% (Murray 2011), it seems now clear that once dense molecular gas has formed, very little can be done to prevent it from forming stars. On the other hand, even when HII regions do compress existing clouds, their impact seems to accelerate star formation at later stages. These results have strong implications as to how feedback is implemented in cosmological and galaxy-scale simulations. In particular, simulations reaching parsec-scale resolutions by using star-formation recipes (i.e., isotropic subgrid implementations of stellar feedback) might have to be revised to account for reduced impact of stellar feedback has on non-spherical molecular clouds.

6.3 FUTURE WORK

6.3.1 SMALL-SCALE IMPACT OF FEEDBACK ON G316.75

While I was able to investigate the impact of feedback on the cloud scale, the angular resolution of the public datasets limited our ability to investigate the impact of stellar feedback on the core scale. But even at low angular resolution, the data points towards an evolutionary gradient of young stellar objects running along the spine of G316.75 (i.e., temperature and H_2 column density gradients present from the south of the ridge to the north of the ridge, see Fig. 4.4). This gradient is likely caused by the compression and heating of the ridge by the high-mass stars currently present (see Fig. 4.8 to see velocity gradients indicative of compressed gas) (Fukuda & Hanawa 2000; Ginsburg et al. 2017). These effects, in combination, can enhance the number of high-mass stars that will form by compressing the gas and increasing the Jeans length sequentially, as a function of the distance away from the high-mass stars. Therefore, these data allow us to investigate whether the presence of high-mass stars can internally trigger the formation of larger stars (i.e., if the core mass function changes as a function of distance away from the ionising source).

In order to do this, high angular resolution data (typically a couple thousand AU which is $\sim 1''$ at the distance of G316.75) are needed so that one can probe the properties (i.e., mass) of individual cores and to determine whether the clumps are further fragmented. A project containing the data necessary to perform this study already exists on the ALMA archive, which became publicly available in January 2020. The data consists of 12m/ACA, 1.3 mm (PI: Wang, project: 2016.1.00909.S) observations of continuum data at $1''$ over the entire ridge. Therefore, with this data I will investigate the core mass function present in the ridge, in relation to its position relative to the high-mass stars.

It was also found that the balance of kinetic to gravitational energy throughout the entire ridge is constant despite the presence of at least 2 O-stars (Watkins et al. 2019). In fact, the only distinguishing feature between the active and quiescent regions is that the balance of kinetic to gravitational energy varies more in the active region with a dex of 0.6 compared to 0.3 in the quiescent region (see Fig. 4.19). Therefore the mechanism driving the observed large-scale velocity dispersion (i.e., its kinetic energy) of the G316.75 ridge has to be global to the ridge. Since ionising and radiative feedback from the high-mass stars present in the active region cannot be the

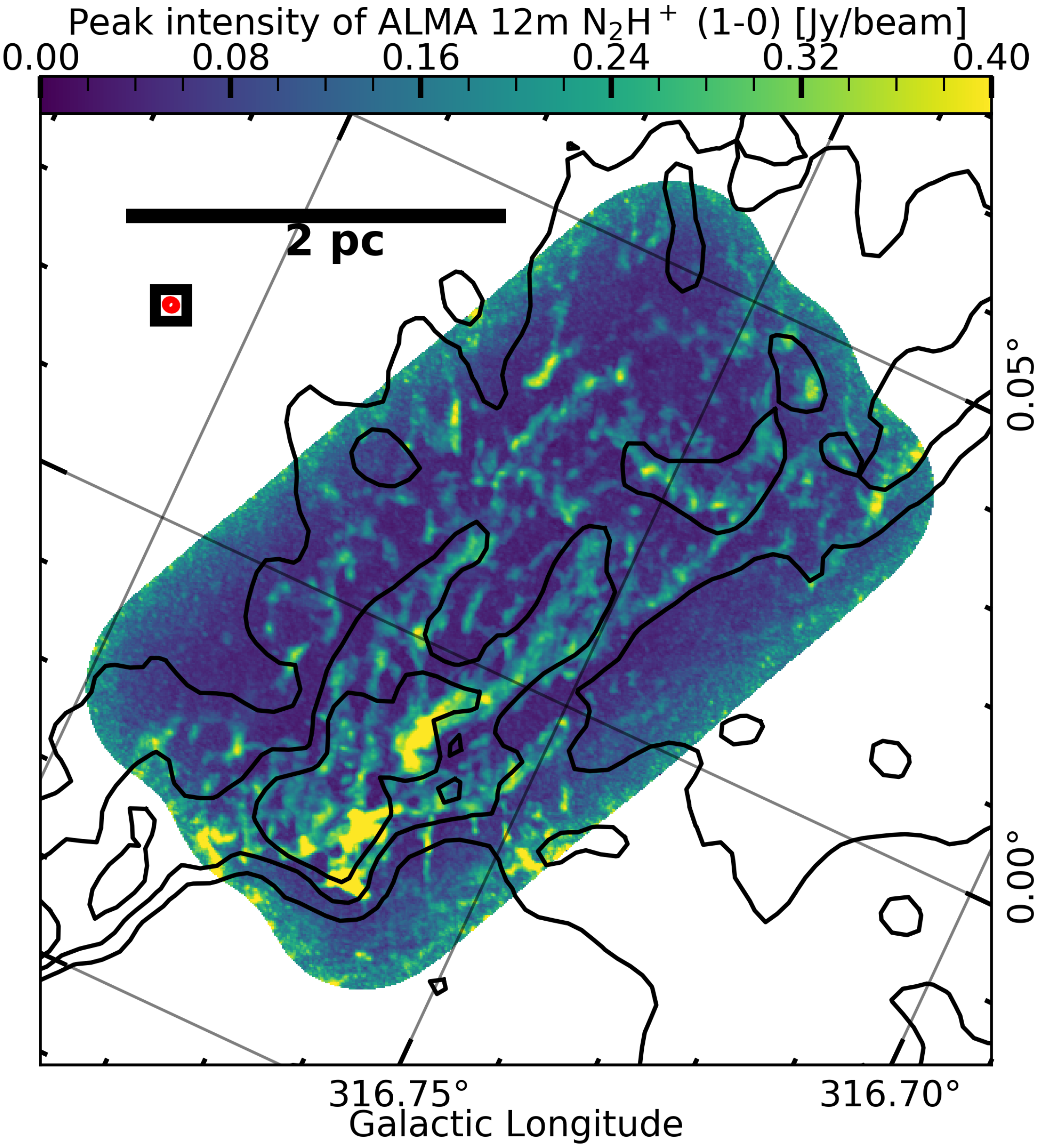

Figure 6.1. Peak intensity of N_2H^+ (1–0) from data taken with ALMA 12m data. Black contours depicts H_2 column density at 400, 800 and 1600 cm^{-2}. Area shown here covers the quiescent part of the ridge, just above the active part.

cause, other possible mechanisms could be outflow feedback from a large population of low-mass protostars (Krumholz et al. 2012) present throughout the entire ridge, or could be caused by the global collapse of the ridge, which would convert potential energy into kinetic energy (Peretto et al. 2014; Hacar et al. 2017; Williams et al. 2018). If the energy balance of the entire ridge is set by gravitational contraction via collapse and fragmentation, it should translate into specific kinematic signatures in the dense gas (e.g., accelerating velocity gradients in position velocity space coinciding with an increase in velocity dispersion, infall signatures in optically thick tracers, such as HCO^+ (1–0)).

To view these signatures, I successfully applied for 12m/ACA/TP cycle 6 data, of N_2H^+ (1–0) an optically thin gas tracer to map the velocity of G316.75 at 0.05 pc (3.5″) resolution for its ability to trace cold, dense gas. With these data, the dynamics of the underlying density structure can be resolved and I can search for coherent velocity gradients converging towards cores (which will be identified using the Wang et al dataset—see above). When concurrent with an increasing an velocity dispersion (which indicates the conversion of gravitational potential energy into kinetic energy), such gradients have in the past been interpreted to signify the fragmentation/collapse of star-forming filaments (Peretto et al. 2014; Hacar et al. 2017; Williams et al. 2018). Calculating the contribution of such motions to the observed ridge-scale kinetic energy would show if gravitational contraction can explain the energy balance of G316.75. I note that part of this dataset was already observed (PI: Linz, project 2013.1.01029.S), using 12m ALMA data. However, the Linz dataset only observed the quiescent part of the ridge and did not include ACA or TP observations, resulting in a large amount of missing zero-spacing measurements. This made the data unusable. Yet after plotting the product file received with the data on Fig. 6.1, one can see that a wealth of sub-filaments. Potentially, this indicates that large-scale motions along the filaments are what drives the observed large-scale velocity dispersion. The ALMA data regarding this project has been delivered and partly reduced. In Fig. 6.2, the initial reduction

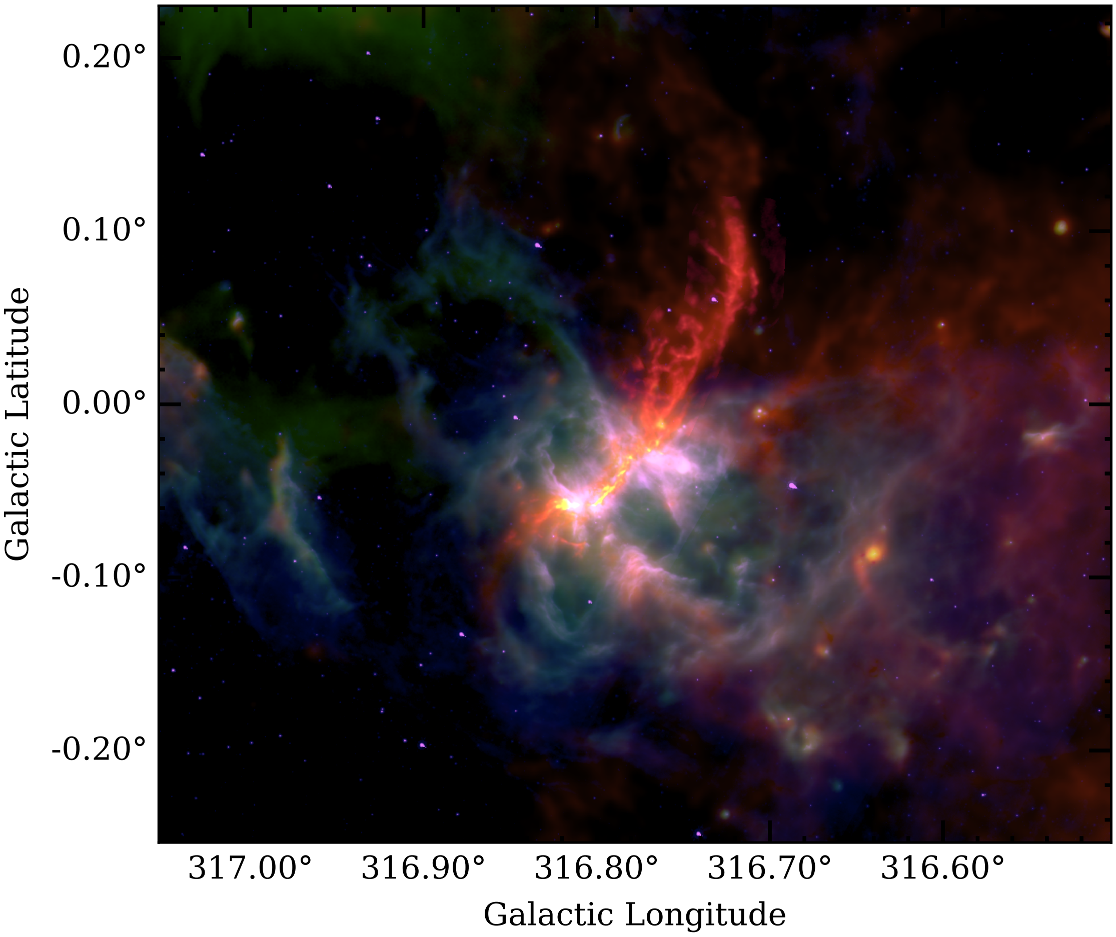

Figure 6.2. RGB image of G316.75 showing the fully combined integrated intensity of N_2H^+ (1–0) taken with ALMA (red+Yellow) over-plotted onto of Fig. 1.7. Blue and pink: *Spitzer* 8μm; Green: *Herschel* 70 μm; orange: *Herschel* 250 μm.

of the fully combined N_2H^+ (1–0) has been shown over-plotted on top of Fig. 1.7. Here, the sub-filaments present in the previous figure can now be fully traced and I plan to work on this dataset in the immediate future.

6.3.2 TRIGGERED STAR FORMATION

The work presented in Chapter 5 represents ongoing work in Watkins, E., J., Peretto, N. & Zavagno, A. in prep. Therefore it is a work in progress and I will be adding additional analysis in the near future, the first of which is to use the ∼1000 distance/velocity values that has been assigned to the HII regions in the WISE catalogue (Anderson et al. 2014b). I will use these measurements to estimate the number of molecular clouds within the sample that have been wrongly assigned, allowing to estimate the error introduced. Secondly, with a distance measurement available, I will calculate the dynamical ages of a subsample of HII regions. This will allow me to link the age of the HII regions to the evolutionary stage of the boundary clouds along with any changes in the SFE.

Bibliography

Agladze, N. I., Sievers, A. J., Jones, S. A., Burlitch, J. M., & Beckwith, S. V. W. 1996, The Astrophysical Journal, 462, 1026

Aguirre, J. E., Ginsburg, A. G., Dunham, M. K., et al. 2011, The Astrophysical Journal Supplement Series, 192, 4

Alves, J. F., Lada, C. J., & Lada, E. A. 2001, Nature, 409, 159

Anderson, G. E., Gaensler, B. M., Kaplan, D. L., et al. 2014a, The Astrophysical Journal Supplement Series, 212, 13

Anderson, L. D., Bania, T. M., Balser, D. S., et al. 2014b, The Astrophysical Journal Supplement Series, 212, 1

André, P. 2011, in Encyclopedia of Astrobiology, ed. M. Gargaud, R. Amils, J. C. Quintanilla, H. J. Cleaves, W. M. Irvine, D. L. Pinti, & M. Viso (Berlin, Heidelberg: Springer Berlin Heidelberg), 1549–1553

André, P., Di Francesco, J., Ward-Thompson, D., et al. 2014, Protostars and Planets VI, 27

André, P., Men'shchikov, A., Bontemps, S., et al. 2010a, Astronomy & Astrophysics, 518, L102

André, P., Men'shchikov, A., Bontemps, S., et al. 2010b, Astronomy & Astrophysics, 518, L102

André, P. & Montmerle, T. 1994, The Astrophysical Journal, 420, 837

Appenzeller, I. & Tscharnuter, W. 1987, The Astrophysical Journal, 319, 850

Arce, H. G., Borkin, M. A., Goodman, A. A., Pineda, J. E., & Beaumont, C. N. 2011, The Astrophysical Journal, 742, 105

Arce, H. G., Borkin, M. A., Goodman, A. A., Pineda, J. E., & Halle, M. W. 2010, The Astrophysical Journal, 715, 1170

Arzoumanian, D., André, P., Didelon, P., et al. 2011, Astronomy & Astrophysics, 529, L6

Arzoumanian, D., André, P., Könyves, V., et al. 2019, Astronomy and Astrophysics, 621, A42

Ballesteros-Paredes, J., Hartmann, L., & Vázquez-Semadeni, E. 1999, The Astrophysical Journal, 527, 285

Bally, J. & Lane, A. P. 1982, The Astrophysical Journal, 257, 612

Bally, J., Langer, W. D., Stark, A. A., & Wilson, R. W. 1987, The Astrophysical Journal, 312, L45

Barnard, E. E. 1919, The Astrophysical Journal, 49, 1

Barnes, P. J., Muller, E., Indermuehle, B., et al. 2015, The Astrophysical Journal, 812, 6

Battersby, C., Bally, J., & Svoboda, B. 2017, The Astrophysical Journal, 835, 263

Beaumont, C. N., Goodman, A. A., Kendrew, S., Williams, J. P., & Simpson, R. 2014, The Astrophysical Journal Supplement Series, 214, 3

Beckwith, S. V. W., Sargent, A. I., Chini, R. S., & Guesten, R. 1990, The Astronomical Journal, 99, 924

Bergin, E. A., Ciardi, D. R., Lada, C. J., Alves, J., & Lada, E. A. 2001, The Astrophysical Journal, 557, 209

Bernstein, R. A., Freedman, W. L., & Madore, B. F. 2002, The Astrophysical Journal, 571, 85

Bertoldi, F. 1989, The Astrophysical Journal, 346, 735

Beuther, H., Ragan, S. E., Johnston, K., et al. 2015, Astronomy & Astrophysics, 584, A67

Beuther, H., Schilke, P., Sridharan, T. K., et al. 2002, Astronomy and Astrophysics, 383, 892

Beuther, H., Semenov, D., Henning, T., & Linz, H. 2008, The Astrophysical Journal Letters, 675, L33

Binder, B. A. & Povich, M. S. 2018, The Astrophysical Journal, 864, 136

Bisbas, T. G., Tanaka, K. E. I., Tan, J. C., Wu, B., & Nakamura, F. 2017, The Astrophysical Journal, 850, 23

Bisbas, T. G., Wünsch, R., Whitworth, A. P., Hubber, D. A., & Walch, S. 2011, The Astrophysical Journal, 736, 142

Black, J. H. & van Dishoeck, E. F. 1987, The Astrophysical Journal, 322, 412

Bohlin, R. C., Savage, B. D., & Drake, J. F. 1978, The Astrophysical Journal, 224, 132

Bondi, H. & Hoyle, F. 1944, Monthly Notices of the Royal Astronomical Society, 104, 273

Bonnell, I. A., Bate, M. R., Clarke, C. J., & Pringle, J. E. 2001, Monthly Notices of the Royal Astronomical Society, 323, 785

Bontemps, S., André, P., Terebey, S., & Cabrit, S. 1996, Astronomy and Astrophysics, 311, 858

Bontemps, S., Motte, F., Csengeri, T., & Schneider, N. 2010, Astronomy & Astrophysics, 524, A18

Braiding, C., Wong, G. F., Maxted, N. I., et al. 2018/ed, Publications of the Astronomical Society of Australia, 35

Bronfman, L., Nyman, L.-A., & May, J. 1996, Astronomy and Astrophysics Supplement Series, 115, 81

Bruhweiler, F. C., Gull, T. R., Kafatos, M., & Sofia, S. 1980, The Astrophysical Journal, 238, L27

Burton, M. G., Braiding, C., Glueck, C., et al. 2013/ed, Publications of the Astronomical Society of Australia, 30

Calabretta, M. R., Staveley-Smith, L., & Barnes, D. G. 2014, Publications of the Astronomical Society of Australia, 31

Caratti o Garatti, A., Stecklum, B., Linz, H., Garcia Lopez, R., & Sanna, A. 2015, Astronomy and Astrophysics, 573, A82

Carey, S. J., Noriega-Crespo, A., Price, S. D., et al. 2005, 207, 63.33

Carruthers, G. R. 1970, The Astrophysical Journal, 161, L81

Castor, J., McCray, R., & Weaver, R. 1975, The Astrophysical Journal, 200, L107

Caswell, J. L. & Haynes, R. F. 1987, Astronomy and Astrophysics, 171, 261

Chandrasekhar, S. & Fermi, E. 1953, The Astrophysical Journal, 118, 116

Chawner, H., Marsh, K., Matsuura, M., et al. 2019, Monthly Notices of the Royal Astronomical Society, 483, 70

Churchwell, E., Babler, B. L., Meade, M. R., et al. 2009, Publications of the Astronomical Society of the Pacific, 121, 213

Churchwell, E., Povich, M. S., Allen, D., et al. 2006, The Astrophysical Journal, 649, 759

Clark, P. C., Bonnell, I. A., & Klessen, R. S. 2008, Monthly Notices of the Royal Astronomical Society, 386, 3

Clarke, S. D. & Whitworth, A. P. 2015, Monthly Notices of the Royal Astronomical Society, 449, 1819

Crowther, P. A., Caballero-Nieves, S. M., Bostroem, K. A., et al. 2016, Monthly Notices of the Royal Astronomical Society, 458, 624

Currie, M. J., Berry, D. S., Jenness, T., et al. 2014, Astronomical Data Analysis Software and Systems XXIII, 485, 391

Cyganowski, C. J., Brogan, C. L., Hunter, T. R., et al. 2014, The Astrophysical Journal Letters, 796, L2

Dale, J. E., Ercolano, B., & Bonnell, I. A. 2012, Monthly Notices of the Royal Astronomical Society, 427, 2852

Dale, J. E., Ercolano, B., & Bonnell, I. A. 2015, Monthly Notices of the Royal Astronomical Society, 451, 987

Dalgarno, A. & McCray, R. A. 1972, Annual Review of Astronomy and Astrophysics, 10, 375

Dalgleish, H. S., Longmore, S. N., Peters, T., et al. 2018, Monthly Notices of the Royal Astronomical Society, 478, 3530

Dame, T. M., Ungerechts, H., Cohen, R. S., et al. 1987, ApJ, 322, 706

Danby, G., Flower, D. R., Valiron, P., Schilke, P., & Walmsley, C. M. 1988, Monthly Notices of the Royal Astronomical Society, 235, 229

Dawson, J. R., McClure-Griffiths, N. M., Wong, T., et al. 2013, The Astrophysical Journal, 763, 56

de Jong, T., Boland, W., & Dalgarno, A. 1980, Astronomy and Astrophysics, 91, 68

Deb, S., Kothes, R., & Rosolowsky, E. 2018, Monthly Notices of the Royal Astronomical Society, 481, 1862

Deharveng, L., Lefloch, B., Zavagno, A., et al. 2003, Astronomy and Astrophysics, 408, L25

Deharveng, L., Zavagno, A., Samal, M. R., et al. 2015, Astronomy & Astrophysics, 582, A1

Deharveng, L., Zavagno, A., Schuller, F., et al. 2009, Astronomy and Astrophysics, 496, 177

Dobashi, K., Shimoikura, T., Katakura, S., Nakamura, F., & Shimajiri, Y. 2019, Publications of the Astronomical Society of Japan

Dobbs, C. L. 2008, Monthly Notices of the Royal Astronomical Society, 391, 844

Dobbs, C. L., Burkert, A., & Pringle, J. E. 2011, Monthly Notices of the Royal Astronomical Society, 413, 2935

Drabek-Maunder, E., Hatchell, J., Buckle, J. V., Di Francesco, J., & Richer, J. 2016, Monthly Notices of the Royal Astronomical Society, 457, L84

Duarte-Cabral, A., Bontemps, S., Motte, F., et al. 2013, Astronomy and Astrophysics, 558, A125

Duarte-Cabral, A., Chrysostomou, A., Peretto, N., et al. 2012, Astronomy and Astrophysics, 543, A140

Dunham, M. M., Crapsi, A., Evans, II, N. J., et al. 2008, The Astrophysical Journal Supplement Series, 179, 249

Dunham, M. M., Stutz, A. M., Allen, L. E., et al. 2014, arXiv

Dyson, J. E. & Williams, D. A. 1980, Physics of the Interstellar Medium

Eddington, A. S. 1926, Proceedings of the Royal Society of London. Series A, Containing Papers of a Mathematical and Physical Character, 111, 424

Eddington, A. S. 1937, The Observatory, 60, 99

Elmegreen, B. G. 2000, The Astrophysical Journal, 530, 277

Elmegreen, B. G. 2007, The Astrophysical Journal, 668, 1064

Elmegreen, B. G., Kimura, T., & Tosa, M. 1995, The Astrophysical Journal, 451, 675

Elmegreen, B. G. & Lada, C. J. 1977, The Astrophysical Journal, 214, 725

Evirgen, C. C., Gent, F. A., Shukurov, A., Fletcher, A., & Bushby, P. J. 2019, Monthly Notices of the Royal Astronomical Society, 488, 5065

Fatuzzo, M. & Adams, F. C. 2008, The Astrophysical Journal, 675, 1361

Faure, A., Varambhia, H. N., Stoecklin, T., & Tennyson, J. 2007, MNRAS, 382, 840

Fazio, G. G., Hora, J. L., Allen, L. E., et al. 2004, The Astrophysical Journal Supplement Series, 154, 10

Federrath, C. 2013, Monthly Notices of the Royal Astronomical Society, 436, 3167

Ferland, G. J., Chatzikos, M., Guzmán, F., et al. 2017, arXiv

Fernández-López, M., Arce, H. G., Looney, L., et al. 2014, The Astrophysical Journal, 790, L19

Ferrière, K. M. 2001, Reviews of Modern Physics, 73, 1031

Field, G. B., Goldsmith, D. W., & Habing, H. J. 1969, The Astrophysical Journal, 155, L149

Foster, J. B., Jackson, J. M., Barnes, P. J., et al. 2011, The Astrophysical Journal Supplement Series, 197, 25

Foster, J. B., Rathborne, J. M., Sanhueza, P., et al. 2013, Publications of the Astronomical Society of Australia, 30, 18

Frank, A., Ray, T. P., Cabrit, S., et al. 2014, in Protostars and Planets VI (University of Arizona Press)

Fukuda, N. & Hanawa, T. 2000, The Astrophysical Journal, 533, 911

Fukui, Y., Ohama, A., Kohno, M., et al. 2018, Publications of the Astronomical Society of Japan, 70, S46

Fuller, G. A. & Myers, P. C. 1992, The Astrophysical Journal, 384, 523

Geen, S., Hennebelle, P., Tremblin, P., & Rosdahl, J. 2016, Monthly Notices of the Royal Astronomical Society, 463, 3129

Giannetti, A., Leurini, S., König, C., et al. 2017, Astronomy & Astrophysics, 606, L12

Ginsburg, A., Goddi, C., Kruijssen, J. M. D., et al. 2017, The Astrophysical Journal, 842, 92

Goorvitch, D. 1994, The Astrophysical Journal Supplement Series, 95, 535

Gould, R. J. & Salpeter, E. E. 1963, The Astrophysical Journal, 138, 393

Grudić, M. Y. & Hopkins, P. F. 2018, arXiv

Grudić, M. Y., Hopkins, P. F., Faucher-Giguère, C.-A., et al. 2018, Monthly Notices of the Royal Astronomical Society, 475, 3511

Hacar, A., Alves, J., Burkert, A., & Goldsmith, P. 2016, Astronomy & Astrophysics, 591, A104

Hacar, A., Alves, J., Tafalla, M., & Goicoechea, J. R. 2017, Astronomy & Astrophysics, 602, L2

Haid, S., Walch, S., Seifried, D., et al. 2018, arXiv

Harju, J., Lehtinen, K., Booth, R. S., & Zinchenko, I. 1998, Astronomy and Astrophysics Supplement Series, 132, 211

Haworth, T. J., Tasker, E. J., Fukui, Y., et al. 2015, Monthly Notices of the Royal Astronomical Society, 450, 10

Hayashi, C. 1961, Publications of the Astronomical Society of Japan, 13, 450

Hayward, C. C. & Hopkins, P. F. 2017, Monthly Notices of the Royal Astronomical Society, 465, 1682

Hennemann, M., Motte, F., Schneider, N., et al. 2012, Astronomy & Astrophysics, 543, L3

Henyey, L. G., Lelevier, R., & Levée, R. D. 1955, Publications of the Astronomical Society of the Pacific, 67, 154

Hernandez, A. K., Tan, J. C., Caselli, P., et al. 2011, The Astrophysical Journal, 738, 11

Herschel, W. 1785, Philosophical Transactions of the Royal Society of London Series I, 75, 213

Heywood, I., Camilo, F., Cotton, W. D., et al. 2019, Nature, 573, 235

Hildebrand, R. H. 1983, Quarterly Journal of the Royal Astronomical Society, 24, 267

Hill, T., Motte, F., Didelon, P., et al. 2011, Astronomy & Astrophysics, 533, A94

Hirashita, H. & Kuo, T.-M. 2011, Monthly Notices of the Royal Astronomical Society, 416, 1340

Ho, P. T. P. & Townes, C. H. 1983, Annual Review of Astronomy and Astrophysics, 21, 239

Howard, A. D. P., Whitworth, A. P., Marsh, K. A., et al. 2019, Monthly Notices of the Royal Astronomical Society, 489, 962

Hoyle, F. 1953, The Astrophysical Journal, 118, 513

Inoue, T., Hennebelle, P., Fukui, Y., et al. 2018, Publications of the Astronomical Society of Japan, 70, S53

Iwasaki, K., Inutsuka, S.-i., & Tsuribe, T. 2011, The Astrophysical Journal, 733, 17

Jackson, J. M., Rathborne, J. M., Foster, J. B., et al. 2013, Publications of the Astronomical Society of Australia, 30, e057

Jeans, J. H. 1902, Philosophical Transactions of the Royal Society of London Series A, 199, 1

Juvela, M. 1996, Astronomy and Astrophysics Supplement Series, 118, 191

Kainulainen, J., Ragan, S. E., Henning, T., & Stutz, A. 2013, Astronomy and Astrophysics, 557, A120

Kendrew, S., Beuther, H., Simpson, R., et al. 2016, The Astrophysical Journal, 825, 142

Kim, J.-G., Kim, W.-T., & Ostriker, E. C. 2018, The Astrophysical Journal, 859, 68

Klessen, R. S. & Burkert, A. 2000, The Astrophysical Journal Supplement Series, 128, 287

Könyves, V., André, P., Men'shchikov, A., et al. 2015, Astronomy and Astrophysics, 584, A91

Koch, E. W. & Rosolowsky, E. W. 2016, Astrophysics Source Code Library, ascl:1608.009

Koyama, H. & Inutsuka, S.-I. 2000, The Astrophysical Journal, 532, 980

Kreckel, K., Ho, I.-T., Blanc, G. A., et al. 2019, The Astrophysical Journal, 887, 80

Körtgen, B., Seifried, D., Banerjee, R., Vázquez-Semadeni, E., & Zamora-Avilés, M. 2016, Monthly Notices of the Royal Astronomical Society, 459, 3460

Kruijssen, J. M. D., Schruba, A., Chevance, M., et al. 2019, Nature, 569, 519

Krumholz, M. R. 2018, Monthly Notices of the Royal Astronomical Society, 480, 3468

Krumholz, M. R., Bate, M. R., Arce, H. G., et al. 2014, Protostars and Planets VI, 243

Krumholz, M. R., Klein, R. I., & McKee, C. F. 2012, The Astrophysical Journal, 754, 71

Krumholz, M. R. & McKee, C. F. 2005, The Astrophysical Journal, 630, 250

Krumholz, M. R., McKee, C. F., & Klein, R. I. 2005, The Astrophysical Journal Letters, 618, L33

Krumholz, M. R. & Tan, J. C. 2007, The Astrophysical Journal, 654, 304

Kuiper, R. & Hosokawa, T. 2018, Astronomy and Astrophysics, 616, A101

Lada, C. J., Lombardi, M., & Alves, J. F. 2010, The Astrophysical Journal, 724, 687

Lamers, H. J. G. L. M., Cassinelli, J. P., & Cassinelli, J. 1999, Introduction to Stellar Winds (Cambridge University Press)

Langer, W. D. & Penzias, A. A. 1990, The Astrophysical Journal, 357, 477

Larson, R. B. 1969, Monthly Notices of the Royal Astronomical Society, 145, 271

Larson, R. B. 1985, Monthly Notices of the Royal Astronomical Society, 214, 379

Lee, E. J., Miville-Deschênes, M.-A., & Murray, N. W. 2016, The Astrophysical Journal, 833, 229

Lee, Y.-N. & Hennebelle, P. 2016, Astronomy and Astrophysics, 591, A31

Leitherer, C., Robert, C., & Drissen, L. 1992, The Astrophysical Journal, 401, 596

Lim, B., Sung, H., Bessell, M. S., et al. 2018, Monthly Notices of the Royal Astronomical Society, 477, 1993

Liu, T., Lacy, J., Li, P. S., et al. 2017, The Astrophysical Journal, 849, 25

Longmore, S. N. & Burton, M. G. 2009, Publications of the Astronomical Society of Australia, 26, 439

Longmore, S. N., Burton, M. G., Barnes, P. J., et al. 2007, Monthly Notices of the Royal Astronomical Society, 379, 535

Longmore, S. N., Burton, M. G., Keto, E., Kurtz, S., & Walsh, A. J. 2009, Monthly Notices of the Royal Astronomical Society, 399, 861

Longmore, S. N., Walsh, A. J., Purcell, C. R., et al. 2017, Monthly Notices of the Royal Astronomical Society, 470, 1462

Lucy, L. B. & Solomon, P. M. 1970, The Astrophysical Journal, 159, 879

Lundgren, A. 2012, ALMA Cycle 1 Technical Handbook, Version 1.0

Marsh, K. A., Whitworth, A. P., & Lomax, O. 2015, Monthly Notices of the Royal Astronomical Society, 454, 4282

Martín-Hernández, N. L., Vermeij, R., & van der Hulst, J. M. 2005, Astronomy & Astrophysics, 433, 205

Mauch, T., Murphy, T., Buttery, H. J., et al. 2003, Monthly Notices of the Royal Astronomical Society, 342, 1117

Maud, L. T., Moore, T. J. T., Lumsden, S. L., et al. 2015, Monthly Notices of the Royal Astronomical Society, 453, 645

McKee, C. F. & Ostriker, J. P. 1977, The Astrophysical Journal, 218, 148

McKee, C. F. & Tan, J. C. 2003, The Astrophysical Journal, 585, 850

Mills, B. Y. 1981, Proceedings of the Astronomical Society of Australia, 4, 156

Minier, V., Tremblin, P., Hill, T., et al. 2013, Astronomy & Astrophysics, 550, A50

Molet, J., Brouillet, N., Nony, T., et al. 2019, Astronomy & Astrophysics, 626, A132

Molinari, S., Schisano, E., Elia, D., et al. 2016, Astronomy and Astrophysics, 591, A149

Molinari, S., Swinyard, B., Bally, J., et al. 2010a, Astronomy & Astrophysics, 518, L100

Molinari, S., Swinyard, B., Bally, J., et al. 2010b, Publications of the Astronomical Society of the Pacific, 122, 314

Monsch, K., Pineda, J. E., Liu, H. B., et al. 2018, The Astrophysical Journal, 861, 77

Motte, F., Bontemps, S., & Louvet, F. 2018, Annual Review of Astronomy and Astrophysics, 56, null

Motte, F., Bontemps, S., Schilke, P., et al. 2007, Astronomy and Astrophysics, 476, 1243

Muench, A. A., Lada, E. A., Lada, C. J., & Alves, J. 2002, The Astrophysical Journal, 573, 366

Murray, N. 2011, The Astrophysical Journal, 729, 133

Murray, N. & Rahman, M. 2010, The Astrophysical Journal, 709, 424

Myers, A. T., McKee, C. F., Cunningham, A. J., Klein, R. I., & Krumholz, M. R. 2013, The Astrophysical Journal, 766, 97

Myers, P. C., Ladd, E. F., & Fuller, G. A. 1991, The Astrophysical Journal Letters, 372, L95

Nagasawa, M. 1987, Progress of Theoretical Physics, 77, 635

Nakamura, F. 2015, EAS Publications Series, 75-76, 123

Nakamura, F. & Li, Z.-Y. 2011, The Astrophysical Journal, 740, 36

Natta, A., Testi, L., Calvet, N., et al. 2007, in Protostars and Planets V

Nguyen, T., Baouche, S., Congiu, E., et al. 2018, Astronomy & Astrophysics, 619, A111

Nguyen Luong, Q., Motte, F., Hennemann, M., et al. 2011, Astronomy and Astrophysics, 535, A76

Nishiyama, K. & Nakai, N. 2001, Publications of the Astronomical Society of Japan, 53, 713

Orkisz, J. H., Peretto, N., Pety, J., et al. 2019, arXiv e-prints, 1902, arXiv:1902.02077

Ossenkopf, V. & Henning, T. 1994, Astronomy and Astrophysics, 291, 943

Oster, L. 1961, RvMP, 33, 525

Osterbrock, D. E. 1989, Astrophysics of Gaseous Nebulae and Active Galactic Nuclei

Ostriker, J. 1964, The Astrophysical Journal, 140, 1056

Owocki, S. P. & Puls, J. 1999, The Astrophysical Journal, 510, 355

Padoan, P., Pan, L., Haugbølle, T., & Nordlund, t. A. 2016, The Astrophysical Journal, 822, 11

Pagani, L., Pardo, J.-R., Apponi, A. J., Bacmann, A., & Cabrit, S. 2005, Astronomy & Astrophysics, 429, 181

Palmeirim, P., Zavagno, A., Elia, D., et al. 2017, Astronomy and Astrophysics, 605, A35

Panagia, N. 1973, Astronomical Journal, 78, 929

Panagia, N. & Walmsley, C. M. 1978, Astronomy and Astrophysics, 70, 411

Panopoulou, G. V., Psaradaki, I., Skalidis, R., Tassis, K., & Andrews, J. J. 2017, Monthly Notices of the Royal Astronomical Society, 466, 2529

Parker, Q. A., Phillipps, S., Pierce, M. J., et al. 2005, Monthly Notices of the Royal Astronomical Society, 362, 689

Peñaloza, C. H., Clark, P. C., Glover, S. C. O., & Klessen, R. S. 2018, Monthly Notices of the Royal Astronomical Society, 475, 1508

Peimbert, M., Peimbert, A., & Delgado-Inglada, G. 2017, Publications of the Astronomical Society of the Pacific, 129, 082001

Peretto, N. & Fuller, G. A. 2009, Astronomy & Astrophysics, 505, 405

Peretto, N., Fuller, G. A., André, P., et al. 2014, Astronomy & Astrophysics, 561, A83

Peretto, N., Fuller, G. A., Duarte-Cabral, A., et al. 2013, Astronomy and Astrophysics, 555, A112

Peretto, N., Fuller, G. A., Plume, R., et al. 2010, Astronomy and Astrophysics, 518, L98

Peretto, N., Lenfestey, C., Fuller, G. A., et al. 2016, Astronomy and Astrophysics, 590, A72

Peters, T., Klessen, R. S., Mac Low, M.-M., & Banerjee, R. 2010, The Astrophysical Journal, 725, 134

Pirogov, L., Zinchenko, I., Caselli, P., & Johansson, L. E. B. 2007, Astronomy & Astrophysics, 461, 523

Pirogov, L., Zinchenko, I., Caselli, P., Johansson, L. E. B., & Myers, P. C. 2003, Astronomy & Astrophysics, 405, 639

Plunkett, A. L., Arce, H. G., Corder, S. A., et al. 2015, The Astrophysical Journal, 803, 22

Portegies Zwart, S. F., McMillan, S. L., & Gieles, M. 2010, Annual Review of Astronomy and Astrophysics, 48, 431

Purcell, C. R., Balasubramanyam, R., Burton, M. G., et al. 2006, Monthly Notices of the Royal Astronomical Society, 367, 553

Purcell, C. R., Longmore, S. N., Walsh, A. J., et al. 2012, Monthly Notices of the Royal Astronomical Society, 426, 1972

Ragan, S., Henning, T., Krause, O., et al. 2012, Astronomy & Astrophysics, 547, A49

Ragan, S. E., Henning, T., Tackenberg, J., et al. 2014, Astronomy & Astrophysics, 568, A73

Reed, B. C. 2001, Publications of the Astronomical Society of the Pacific, 113, 537

Reid, M. J., Menten, K. M., Zheng, X. W., et al. 2009, The Astrophysical Journal, 700, 137

Rigby, A. J., Peretto, N., Adam, R., et al. 2018, A&A, 615, A18

Rosen, A. L., Lopez, L. A., Krumholz, M. R., & Ramirez-Ruiz, E. 2014, Monthly Notices of the Royal Astronomical Society, 442, 2701

Rosolowsky, E. W., Pineda, J. E., Kauffmann, J., & Goodman, A. A. 2008, The Astrophysical Journal, 679, 1338

Rowan-Robinson, M., Lock, T. D., Walker, D. W., & Harris, S. 1986, MNRAS, 222, 273

Roy, A., André, P., Palmeirim, P., et al. 2014, Astronomy and Astrophysics, 562, A138

Samal, M. R., Deharveng, L., Zavagno, A., et al. 2018, Astronomy & Astrophysics, 617, A67

Sanhueza, P., Contreras, Y., Wu, B., et al. 2019, The Astrophysical Journal, 886, 102

Sanhueza, P., Jackson, J. M., Zhang, Q., et al. 2017, The Astrophysical Journal, 841, 97

Sano, H., Enokiya, R., Hayashi, K., et al. 2018, Publications of the Astronomical Society of Japan, 70

Schöier, F. L., van der Tak, F. F. S., van Dishoeck, E. F., & Black, J. H. 2005, Astronomy and Astrophysics, 432, 369

Schisano, E., Molinari, S., Elia, D., et al. 2019, arXiv e-prints, 1912, arXiv:1912.04020

Schisano, E., Rygl, K. L. J., Molinari, S., et al. 2014, The Astrophysical Journal, 791, 27

Schneider, S. & Elmegreen, B. G. 1979, The Astrophysical Journal Supplement Series, 41, 87

Schuller, F., Menten, K. M., Contreras, Y., et al. 2009, Astronomy & Astrophysics, 504, 415

Scoville, N. Z. & Hersh, K. 1979, The Astrophysical Journal, 229, 578

Scoville, N. Z. & Solomon, P. M. 1974, The Astrophysical Journal, 187, L67

Seifried, D., Walch, S., Haid, S., Girichidis, P., & Naab, T. 2018, The Astrophysical Journal, 855, 81

Shaver, P. A. & Goss, W. M. 1970a, Australian Journal of Physics Astrophysical Supplement, 14, 77

Shaver, P. A. & Goss, W. M. 1970b, Australian Journal of Physics Astrophysical Supplement, 14, 133

Shaver, P. A., McGee, R. X., Newton, L. M., Danks, A. C., & Pottasch, S. R. 1983, Monthly Notices of the Royal Astronomical Society, 204, 53

Shaver, P. A., Retallack, D. S., Wamsteker, W., & Danks, A. C. 1981, Astronomy and Astrophysics, 102, 225

Shirley, Y. L. 2015, Publications of the Astronomical Society of the Pacific, 127, 299

Shu, F. H. 1977, The Astrophysical Journal, 214, 488

Smith, M. W. L., Eales, S. A., Gomez, H. L., et al. 2012, ApJ, 756, 40

Smith, R. J., Glover, S. C. O., Bonnell, I. A., Clark, P. C., & Klessen, R. S. 2011, Monthly Notices of the Royal Astronomical Society, 411, 1354

Smith, R. J., Longmore, S., & Bonnell, I. 2009, Monthly Notices of the Royal Astronomical Society, 400, 1775

Solomon, P. M., Rivolo, A. R., Barrett, J., & Yahil, A. 1987, The Astrophysical Journal, 319, 730

Sousbie, T. 2011, Monthly Notices of the Royal Astronomical Society, 414, 350

Spitzer, L. 1956, The Astrophysical Journal, 124, 20

Spitzer, L. 1978, A Wiley-Interscience Publication

Spitzer, Jr., L. 1949, The Astrophysical Journal, 109, 337

Stahler, S. W., Shu, F. H., & Taam, R. E. 1980, The Astrophysical Journal, 241, 637

Stecher, T. P. & Williams, D. A. 1967, The Astrophysical Journal, 149, L29

Sternberg, A., Hoffmann, T. L., & Pauldrach, A. W. A. 2003, The Astrophysical Journal, 599, 1333

Sternberg, A., Petit, F. L., Roueff, E., & Bourlot, J. L. 2014, The Astrophysical Journal, 790, 10

Strömgren, B. 1939, The Astrophysical Journal, 89, 526

Suchkov, A. A. & Shchekinov, Y. A. 1984, Soviet Astronomy Letters, 10, 13

Svoboda, B. E., Shirley, Y. L., Traficante, A., et al. 2019, arXiv e-prints, arXiv:1908.10374

Szűcs, L., Glover, S. C. O., & Klessen, R. S. 2014, Monthly Notices of the Royal Astronomical Society, 445, 4055

Szűcs, L., Glover, S. C. O., & Klessen, R. S. 2016, Monthly Notices of the Royal Astronomical Society, 460, 82

Tasker, E. J. & Tan, J. C. 2009, The Astrophysical Journal, 700, 358

Thompson, M. A., Urquhart, J. S., Moore, T. J. T., & Morgan, L. K. 2012, Monthly Notices of the Royal Astronomical Society, 421, 408

Thompson, T. A. & Krumholz, M. R. 2016, Monthly Notices of the Royal Astronomical Society, 455, 334

Townes, C. H. & Schawlow, A. L. 1975, Microwave spectroscopy., by Townes, C. H.; Schawlow, A. L.. New York, NY (USA): Dover Publications, 698 p.

Traficante, A., Fuller, G. A., Smith, R. J., et al. 2018, Monthly Notices of the Royal Astronomical Society, 473, 4975

Tremblin, P., Anderson, L. D., Didelon, P., et al. 2014, Astronomy and Astrophysics, 568, A4

Tricco, T. S., Price, D. J., & Laibe, G. 2017, Monthly Notices of the Royal Astronomical Society: Letters, 471, L52

Trumpler, R. J. 1930, Lick Observatory Bulletin, 420, 154

Tsitali, A. E., Belloche, A., Commerçon, B., & Menten, K. M. 2013, Astronomy & Astrophysics, 557, A98

Urquhart, J. S., König, C., Giannetti, A., et al. 2018, Monthly Notices of the Royal Astronomical Society, 473, 1059

Vacca, W. D., Garmany, C. D., & Shull, J. M. 1996, The Astrophysical Journal, 460, 914

van Dishoeck, E. F. & Black, J. H. 1986, The Astrophysical Journal Supplement Series, 62, 109

Vasyunina, T., Linz, H., Henning, T., et al. 2011, Astronomy & Astrophysics, 527, A88

Vig, S., Ghosh, S. K., Ojha, D. K., & Verma, R. P. 2007, Astronomy & Astrophysics, 463, 175

Vázquez-Semadeni, E., Gómez, G. C., Jappsen, A.-K., Ballesteros-Paredes, J., & Klessen, R. S. 2009, The Astrophysical Journal, 707, 1023

Vázquez-Semadeni, E., Zamora-Avilés, M., Galván-Madrid, R., & Forbrich, J. 2018, Monthly Notices of the Royal Astronomical Society, 479, 3254

Wakelam, V., Bron, E., Cazaux, S., et al. 2017, Molecular Astrophysics, 9, 1

Walch, S. & Naab, T. 2015, Monthly Notices of the Royal Astronomical Society, 451, 2757

Walch, S., Whitworth, A. P., Bisbas, T. G., Hubber, D. A., & Wünsch, R. 2015, Monthly Notices of the Royal Astronomical Society, 452, 2794

Walsh, A. J., Bertoldi, F., Burton, M. G., & Nikola, T. 2001, Monthly Notices of the Royal Astronomical Society, 326, 36

Walsh, A. J., Breen, S. L., Britton, T., et al. 2011, Monthly Notices of the Royal Astronomical Society, 416, 1764

Walsh, A. J., Burton, M. G., Hyland, A. R., & Robinson, G. 1998, Monthly Notices of the Royal Astronomical Society, 301, 640

Wareing, C. J., Pittard, J. M., & Falle, S. a. E. G. 2017, Monthly Notices of the Royal Astronomical Society, 470, 2283

Watkins, E. J., Peretto, N., Marsh, K., & Fuller, G. A. 2019, Astronomy and Astrophysics, 628, A21

Weidner, C. & Vink, J. S. 2010, Astronomy & Astrophysics, 524, A98

Weingartner, J. C. & Draine, B. T. 2001, ApJ, 548, 296

Werner, M. W., Roellig, T. L., Low, F. J., et al. 2004, The Astrophysical Journal Supplement Series, 154, 1

Whitworth, A., Lomax, O., Balfour, S., et al. 2018, Publications of the Astronomical Society of Japan, 70

Whitworth, A. P., Bhattal, A. S., Chapman, S. J., Disney, M. J., & Turner, J. A. 1994, Monthly Notices of the Royal Astronomical Society, 268, 291

Whitworth, A. P., Marsh, K. A., Cigan, P. J., et al. 2019, MNRAS, 489, 5436

Williams, G. M., Peretto, N., Avison, A., Duarte-Cabral, A., & Fuller, G. A. 2018, Astronomy and Astrophysics, 613, A11

Wilson, T. L., Rohlfs, K., & Hüttemeister, S. 2009, Tools of Radio Astronomy

Wright, E. L., Eisenhardt, P. R. M., Mainzer, A. K., et al. 2010, The Astronomical Journal, 140, 1868

Xu, J.-L., Xu, Y., Yu, N., et al. 2017, The Astrophysical Journal, 849, 140

Yang, A. Y., Thompson, M. A., Tian, W. W., et al. 2018a, arXiv

Yang, A. Y., Thompson, M. A., Urquhart, J. S., & Tian, W. W. 2018b, The Astrophysical Journal Supplement Series, 235, 3

Yang, B., Stancil, P. C., Balakrishnan, N., & Forrey, R. C. 2010, The Astrophysical Journal, 718, 1062

Yorke, H. W. & Sonnhalter, C. 2002, The Astrophysical Journal, 569, 846

Zavagno, A., Pomarès, M., Deharveng, L., et al. 2007, Astronomy & Astrophysics, 472, 835

Zinnecker, H., McCaughrean, M., & Rayner, J. 1997, 182, 198

Zweibel, E. G. 2013, Physics of Plasmas, 20, 055501